UNIVERZITA PALACKÉHO V OLOMOUCI
PŘÍRODOVĚDECKÁ FAKULTA

Katedra Optiky

Prostorová modulace světla v metodách digitální optiky

Mgr. Jaromír Běhal

Disertační práce předložena k získání titulu
Doktor Filosofie

Školitel: prof. RNDr. Zdeněk Bouchal, Dr.

Olomouc 2020

PALACKY UNIVERSITY OLOMOUC
FACULTY OF NATURAL SCIENCES

Department of Optics

Spatial light modulation in methods of digital optics

Mgr. Jaromír Běhal

A Thesis presented for the degree of
Doctor of Philosophy

Supervisor: prof. RNDr. Zdeněk Bouchal, Dr.

Olomouc 2020

Abstrakt

Tato disertační práce je založena na třech originálních publikacích [1–3] a shrnuje hlavní výsledky dosažené v průběhu mého doktorského studia. Každý ze studovaných problémů přímo využívá principů digitální holografie ať už v kontextu designu experimentálního uspořádání, optimálního využití prezentované metody, či jako nástroje pro studium a kvantifikaci studovaných efektů. Digitální holografie je zobrazovací metoda využívající záznamu optického pole digitálním senzorem a následné numerické rekonstrukce. Takto získaný obraz nese informaci o komplexní amplitudě a typicky slouží pro mapování reliéfu povrchu nebo měření optické tloušťky.

První blok práce poskytuje stručný úvod do oblasti kvantitativního fázového zobrazení s důrazem na digitální holografii. U vybraných témat je dále uveden současný stav problematiky. Druhý blok shrnuje vlastní přínos v podobě dosažených výsledků. Předložená disertační práce rozvíjí metodiku volby optimálních experimentálních parametrů pro pozorování zvětšeného obrazu vzorku v bezčočkové koherentní digitální holografické mikroskopii. Dále je v práci studována možnost vzniku otisku buněk ve fotorefraktivním materiálu s využitím fotolitografických principů. Tento přístup může být v budoucnu využitý pro diagnostické účely či provázání optických vlastností materiálových vzorků a živých buněk. Následně je v práci popsán princip korekce fázového pozadí s důrazem na využití metody dvojité expozice, která pro svou funkci nevyžaduje znalost numerického modelu. Tento přístup slouží pro svou jednoduchost a přesnost též jako referenční metoda. Kvalita dosažené fázové kompenzace je diskutována pro rozdílné experimentální podmínky.

Abstract

The presented thesis is based on three original publications [1–3] and summarizes the main results achieved during my Ph.D. studies. Each of the discussed problems exploits digital holographic principles, whether in the context of the experimental arrangement design, optimal implementation of the presented method, or as an instrument to study and quantify the investigated effects. Digital holography is an imaging technique consisting of recording the interference field by the digital sensor, followed by the subsequent numerical reconstruction process. The retrieved image provides a complex amplitude, typically exploited for three-dimensional relief mapping or optical thickness measurements.

The introduction and the contemporary state of research related to the discussed problems are presented in the first part of the thesis. The primary outcomes are then summarized in the second part of the thesis. The thesis initially proposes the methodology for an optimal choice of the experimental parameters suitable for observing the enlarged image in the lensless coherent digital holographic microscopy. A further ambition aims to study the possibility of fixing parameters of cells into photorefractive material, adopting the principles of photolithography. The approach may be exploited for diagnostics or the interconnection of optical properties of materials and living cells. Moreover, the thesis presents the concept of phase-background compensation, emphasizing the double-exposure method. Such an approach is easy to implement without the need for the numerical model while providing accurate results; thus, ordinarily serves as a reference. Here, the optimal use of the method is discussed for various experimental conditions.

Acknowledgements

Firstly, I would like to thank my supervisor for guidance during my studies. I am thankful to the leading management of the Department of Optics for their patience. I want to extend my thanks to laboratory colleagues for inspiring discussions and sharing their know-how. I am grateful to other members of the Department of Optics for various support, especially appreciating their friendly attitude. I am thankful to all my colleagues I met abroad during my stay at the Institute of Applied Sciences and Intelligent Systems (ISASI-CNR) in Pozzuoli for great collaboration and the possibility to learn from them a lot. Further, I would like to thank the 4.007-crew for their friendly attitude, creative environment, and much more. Special thanks belong to Pepa, Dominik, Honza, Mirek, Robert, Martin, Martina, Ivo, Michal.

Finally, warmest thanks go to my family for their continuous unlimited support, love, and care.

Declaration

I declare I wrote this Ph. D. thesis ***Spatial light modulation in methods of digital optics*** on my own. To the best of my knowledge and belief, it contains no material previously published by another person. This thesis is based on three original publications [1–3]. My contribution to these publications consists of the simulations, experimental realizations, data processing, and participating in writing the manuscripts. This thesis uses only the resources cited in the Bibliography section.

I agree with the further use of this thesis according to the requirements of Palacky University and the Department of Optics.

In Olomouc, ...

.....

Jaromír Běhal

List of symbols and abbreviations

1D, 2D, 3D	one-dimensional, two-dimensional, three-dimensional
a_j, A_j	amplitude
AD_s, AD_i	lateral resolution in the object space and the image space
α, α_j	angular inclination
BE	collimation and focusing lenses
BS, BS_j	Beam Splitter
β	lateral magnification
CC	Correlation Coefficient
CCD	Charge-Coupled Device
CMOS	Complementary Metal–Oxide–Semiconductor
γ	longitudinal magnification
DH	Digital Holography
DHM	Digital Holographic Microscopy
δ	rotation angle
Δ	pinhole-sample distance
Δf	distance between focal points
$\Delta\Phi$, $\Delta\Phi_j$	phase difference
Δn_j	refractive-index change
Δx, Δy	lateral shear
$\Delta z_j, \Delta z_j^i$	defocusing distances and longitudinal resolution
E_j	electric field intensity
η	orientation angle of local axis in the SWP aperture
f, f_j	focal distance or paraxial image distance
F_j	focal point
FID	Field Iris Diaphragm
FOV	Field Of View
FS	Focal Shift
FWHM	Full Width at Half Maximum
Φ_j	phase
h	height
H	holographic record
$\mathfrak{h}$	impulse response
$\mathfrak{H}$	transfer function
He-Ne	Helium-Neon

HWP, HWP$_j$	Half-Wave Plate
I, I_j	intensity
k	wave number
K	Strehl coefficient
κ, κ_j	coefficient
L$_j$	Lens
LED	Light-Emitting Diode
$LiNbO_3$	lithium niobate
LP, LP$_j$	Linear Polarizer
λ	wavelength
Λ_i^+, Λ_i^-	half width of axial PSF in the image space
M, M$_j$	Mirror
MO, MO$_j$	Microscope Objective
n, n_j	refractive index
$\lvert n_i \rvert$, N_i	Fresnel number in the image space
NA, NA_i	Numerical Aperture in the object space and the image space
ν_j	spatial frequencies
OPD	Optical Path Difference
p_{CCD}	pixel size of the camera
PBS, PBS$_j$	Polarizing Beam Splitter
PD	Petri Dish
PL	PhotoLithography
PR	PhotoRefractive
PSF	Point Spread Function
Q_j	asymmetry coefficient
QPI	Quantitative Phase Imaging
QWP	Quarter-Wave Plate
r, φ	polar coordinates
r_j	absolute value of position vector
$r_\perp$, $r_{\perp j}$	absolute value of transversal position vector
r_{13}	electrooptic coefficient
R	refocusing coefficient
RBC	Red Blood Cell
RD	Rotating Diffuser
ρ, φ	polar coordinates
ρ_N	normalized radial coordinate
ρ_h	aperture radius of a point interference record
ρ_m	radial coordinate in the plane of SLM
ρ_p	pinhole radius
S, C, A, F, D	aberration coefficients
SD	Shearing Device
SF	Spatial Filter
SLM	Spatial Light Modulator
SMF	Single Mode optical Fibre

SWP	S-wave plate
σ, σ_j	standard deviation
t, t_j, T	transmission or aperture functions
$\mathbb{T}$, T_j	Jones matrix and its elements
TC	Tamura Coefficient
TL	Tube Lens
θ_j	constant phase shift
U, U_j	complex amplitudes
W	wavefront aberration function
x, x_j; $\overline{x}$	cartesian coordinates; translation
y, y_j; $\overline{y}$	cartesian coordinates; translation
z, z_j	cartesian coordinates

Contents

Chapter 1

Goals of the thesis

This chapter presents mostly experimental outcomes based on the three original publications [1–3], which profit from the advantages of powerful imaging technique called digital holography. Its imaging performance consists of two consecutive operations, recording the interference field and the subsequent numerical reconstruction process. The retrieved complex amplitude carries the information of both the amplitude and the phase distributions as a result. In this thesis, the digital holography serves as a subject of interest itself or as an instrument for analyzing and quantifying the investigated effects.

The theoretical part of the thesis introduces the background of the quantitative phase imaging with an emphasis on the digital holographic microscopy and contemporary state of research related to the presented topics in chapter 2. Description of the main methods used in the thesis, as well as the experimental background, are the subjects of chapter 3. The following part introduces the experiments which aim to extend the boundaries of the studied possibilities further. Chapters $4-6$ are based on the scientific articles mentioned above and present the achieved results. Chapter 7 presents Jones matrix reconstruction by methods of digital holography in the specific experimental configuration. Subsequently, Chapter 8 includes a summarization of the topics. Chapters $4-7$ are briefly introduced in the following text.

Results achieved in chapter 4 develop the methodology for the optimal choice of the experimental parameters suitable for observing the enlarged image in the lens-less coherent digital holographic microscopy. Initially, the imaging performance of a coherent magnified in-line digital holographic microscopy is described. Here the enlarged specimen's image is achieved in numerical post-processing by a mismatch between parameters of the reference and the reconstruction waves. The residual effects, coupled with this approach, are considered, which may result in undesirable effects caused by holographic aberrations and asymmetry of the point spread function. A trade-off between the influence

of holographic aberrations and diffraction effects is, therefore, taken into account. The analysis provides an optimal combination of experimental parameters and range of the applicable magnifications, while the holographic aberrations reach an acceptable level, and the point spread function remains symmetrical. Theoretical predictions are verified experimentally by reconstructing the three-dimensional point spread functions of point interference records and the image of the line resolution target. Chapter 4 is based on publication: [1] J. Běhal and Z. Bouchal, "Optimizing three-dimensional point spread function in lensless holographic microscopy," *Optics Express*, vol. 25, pp. 29026–29042, 2017.

A further ambition is presented in chapter 5, which aims to study the possibility of fixing parameters of living micro-objects into the material, exploiting the principles of photolithography. The approach may be further used for diagnostics or the interconnection of optical properties of materials and living cells. Digital holographic microscopy serves here for both, as a tool for realizing and investigating the photolithographic performance, simultaneously. The particular aim is to imprint the structure of red blood cells into the biocompatible and photo-activable substrate. In this case, the illuminating-light profile is shaped while passing through the cells. Hence, such a biolensing effect enables photolithographic writing. Experimentally, red blood cells settle down on the surface of the photorefractive $LiNbO_3$ crystal, which acts as a photoresist. After the sedimentation process is complete, the appropriately polarized laser light illuminates the specimen for suitable exposure time. At the same time, local changes arise inside the refractive index material during the process. Refractive index distribution shows that focusing properties of red blood cells can be directly transferred into the crystal depending on which type of the cells is employed. Similarities and differences between the imprints and cells are discussed for discocytes and spherocytes, respectively. Chapter 5 is based on publication: [2] L. Miccio, J. Behal, M. Mugnano, P. Memmolo, B. Mandracchia, F. Merola, S. Grilli, and P. Ferraro, "Biological lenses as a photomask for writing laser spots into ferroelectric crystals," *ACS Applied Bio Materials*, vol. 2, no. 11, pp. 4675–4680, 2019.

Moreover, chapter 6 extends the concept of phase-background compensation, emphasizing the double-exposure method. This easy-to-implement approach provides accurate results, hence may serve as a reference method. Notably, the performance of common-path self-referencing geometries is analyzed. Such off-axis experimental arrangements with the enhanced temporal stability enable long-time measurements and advantageous implementation of the double-exposure method for the suppression of phase defects in the recording plane. Conditions required for optimal application of the double-exposure method are discussed and experimentally approved. Processing the duplicated field of view, which often

arises in the self-referencing geometries, is also taken into account. Quality of the achieved phase correction is also discussed and demonstrated experimentally. Chapter 6 is based on publication: [3] J. Běhal, "Quantitative phase imaging in common-path cross-referenced holographic microscopy using double-exposure method," *Scientific Reports*, vol. 9, no. 9801, 2019.

Chapter 7 presents the polarization-sensitive imaging employing digital holography. A single-shot polarization reconstruction is based on principles of the angular multiplexing achieved by mixing two orthogonally polarized reference waves with the signal beam. The adopted experimental configuration represents the Mach-Zehnder interferometer with the incorporated Sagnac interference module in the reference arm for the simultaneous generation of the two tilted reference waves. The proof-of-principle experiment is focused on quantifying the enhanced temporal stability of the polarization reconstruction compared to the quantitative phase imaging, for the first time, according to our knowledge. Furthermore, the imaging ability is qualitatively performed using the sample generating spatially dependent polarization-state distribution.

Chapter 2

Background and contemporary state of research

2.1 Background

Many material or biological materials exhibit weak absorption in the visible spectral region. Low-contrast images produced without staining the samples, which differ just slightly from the surrounding medium in terms of color and absorbance, were a challenging problem in optical microscopy. However, according to Abbe's imaging theory, the image formation can be considered as an interference process which consists of superposed waves emerging from various angles. Based on this principle, the first label-free technique called the phase-contrast microscopy was invented in the 1930s by Zernike [4–6]. The enhanced quality of weakly absorbing objects was obtained by phase modulation inserted on a light scattered by the sample and an unscattered light. The contrast was depicted in areas with different optical path differences (OPDs) as a change in the light intensity. Later in the 1950s, the differential interference contrast microscopy was invented by Nomarski [7]. The phase contrast was achieved by separating, laterally shearing, and projecting mutually coherent orthogonal polarization components of light. This method solved the problem with the bright diffraction halo present in the Zernike's phase-contrast microscopy [8]. Nowadays, both techniques, the phase-contrast microscopy, and the differential interference contrast microscopy, respectively, widely used in biomedical laboratories, are of significant importance, although the information provided is mostly qualitative [9].

Besides, it is more than 80 years these days, since Dennis Gabor, primarily motivated by needs to improve the resolution in the electron microscopy, has realized that the full optical field can be recorded and subsequently reconstructed. The ability to record the whole complex amplitude consequently led to the invention of holography in the 1940s [10]. Further implementation of holography became more practical after the invention of

the laser, and the imaging performance enhancement by the effective zero-order and the twin image suppression [11].

A combination of the methods mentioned above resulted in the invention of quantitative phase imaging (QPI), which consequently enables to retrieve the phase delay of the complex wavefield. This intrinsic property carries information about the sample, which interacts with the passing through light. It is suitable for label-free studying of the weakly absorbing objects as well as reflected surfaces with the nanoscale sensitivity in OPD measurement.

Even though imaging is generally considered a complicated interference process, the phase retrieval methods are often classified as interferometric or non-interferometric, depending on the nature of recorded patterns. Most of the phase retrieval methods are based on the interferometric approach. Here, the complex wavefield originating from the sample is mixed with a second mutually coherent, well-defined optical beam. The output intensity contains fringes encoding the information, which deterministically enables direct selection of the required phase-contrast measure. In a lack of added fringes, originating from mixing the signal information with the second coherent beam, alternative non-interferometric approaches were established [12, 13]. They assume the fringe-less image as an interferogram itself where amplitude and phase are coupled mathematically to the defocused images. Non-interferometric methods are categorized into two significant groups, iterative and deterministic, respectively. The iterative algorithms mostly employ the four-step closed-loop Gerchberg-Saxton algorithm, which was first introduced in 1972 [14]. The deterministic algorithms are usually based on finding the solution to the transport of intensity equation [15].

The mature methods of QPI have found many applications in material engineering and surface profilometry for decades [16, 17]. However, surprisingly, there were just a few interferometry-based applications in biology and medicine until the 2000s [18–21]. The rapid growth of biomedical applications in the following years has been stimulated by the invention of high-resolution cameras and improved computational power and memory of modern computers. Direct access to the particularly significant phase delay of the wavefield interacting with the object enabled the measurement of the thickness and the refractive index spatial distributions, respectively. It provides morphological and biochemical information about individual cells, e.g., dry mass and dry density [22, 23], biovolume, sphericity, surface area, and other parameters relevant to the biosample's morphological properties [24]. Besides, QPI is widely used nowadays from high-resolution topography of structured surfaces [25, 26] to label-free imaging of the living biomedical samples [27].

The QPI can be advantageously implemented by digital holography (DH), where the phase is restored from the interference pattern whose modulation depends on the OPD of the two mutually coherent waves, the well-defined reference wave and the signal wave scat-

tered by the specimen, respectively. The optically recorded interference pattern is further numerically processed to retrieve a full complex amplitude of the observed sample.

Elementary arrangements to perform the DH are feasible without additional optics. For instance, light source, pinhole, and camera are enough to build the original Gabor's DH configuration [27]. It is important to note that with this approach, the sample must remain relatively sparse to maintain the clean reference wave for holographic reconstruction [28]. The lens-less DH enables us to make very compact devices useful for outdoor measurements [29]. However, also more bulky arrangements providing lens less DH are commonly used for laboratory applications [30]. Moreover, the imaging performance of lens-less DH can be upgraded and enhanced in the context of the achieved magnifications or quality of the created image by inserting additional components into the optical path. Both lens-less and lens-based DH configurations commonly exploit in-line or off-axis geometries.

In in-line holography, the signal and the reference waves are collinear. Spectra of all the holographic parts overlap, thus additional techniques must be applied to separate the desired term. Temporal phase-shifting, for example, requires recording and processing multiple interference records with the different phase shifts introduced between the interfering waves [31, 32]. Contrary, in off-axis holography, the additional spatial carrier frequency is inserted between the signal and the reference waves. The term of interest is then extracted from a single holographic record by the angular-spectrum processing [33]. The main advantages and disadvantages of the approaches are apparent. In-line geometries employ the full range of the detector's sampling limit in contrast to off-axis holography, where just part of the detector's capacity is exploited [34]. On the other hand, real-time experiments are limited by the camera's exposure time in off-axis holography. Contrary, in in-line holography, an additional limitation is determined by recording multiple snapshots. Nevertheless, both approaches are widely used depending on the application requirements. It should be noted that in recent years, even single-shot phase-shifting in-line DH approaches with the space-division multiplexing by the designed segmented detectors were introduced. However, the resolution achieved is still reduced compared to standard in-line DH, as expected [35].

Both in-line and off-axis DH configurations can be categorized according to properties of the interferometer incorporated. Geometries, where the signal and the reference waves pass through the separated arms, provide variability in the experimental realization, easy access into each of the arms, and a clean reference wave [36], but the setups are often bulky and sensitive to external vibrations. In contrast, in configurations with the common-path interferometer, the signal and the reference waves pass through a single arm and share identical optical components. Hence, the common-path arrangements inherently achieve enhanced temporal stability compared to the geometries with independent arms [37, 38]. The temporal stability, i.e., the ability to maintain phase difference introduced between the

signal and the reference waves for a specified time interval, is thus the highest in interferometers with a common-path geometry. Based on the advantage of common-path DH, lab-on-chip devices with incorporated microfluidic channels were recently built and successfully tested [39, 40], for example.

2.2 Selected advanced techniques of digital holography

The advantages of DH are that it permits variability in the experimental realization and the numerical postprocessing [41]. DH provides the classical phase-contrast images [42], compensation of phase aberrations [43], tracking and isolating the particles [44, 45], implementation of autofocusing algorithms [46], enlarging the depth of focus [47, 48], multi-wavelength imaging [49], formation of the synthetic aperture [50], polarization-sensitive imaging, and many others.

The DH allows the imaging of various samples. Phase objects distinctly modulate the phase of the illumination wave while the amplitude remains almost unchanged. On the other hand, absorbing specimens significantly influence the amplitude of the transmitted light, and partially transparent objects modulate both the amplitude and the phase distributions, respectively. Due to the features mentioned, diverse approaches for autofocusing and tracking the samples were proposed. Different criteria were implemented to achieve the optimal autofocusing, including the integrated amplitude [51], the contrast-texture measure [52], i.e., Tamura coefficient (TC) [53], the sparsity measure, i. e. Gini's index [54], the sparsity of the Fresnelet bases [55], the weighted Fourier spectrum, and the variance. The total sums of gradients and Laplacians were also used to calculate the cumulated edge detection [56]. Recently, the combined approaches, namely Gini of the gradient and Tamura of the gradient, seem to be sufficiently applicable for various types of the samples [46]. DHM hence represents a powerful tool for autofocusing and particle tracking [45], and as a consequence, velocity, density, and temperature distributions can be evaluated [57]. DH also enables particle detection [58], particle location, and size determination from a single interference record based on the tomographic principles [59, 60].

Realistic experimental conditions and phase defects influence the quality of the reconstructed complex field, considering the nature of DH. For example, phase distortions can be reduced directly in the setup by inserting proper optical components to achieve the curvature compensation or to realize the telecentric imaging of the specimen [43]. Moreover, the direct access to complex amplitude enables compensating phase inhomogeneities in the plane of the detector by fitting or deducting the reference phase map [61–63]. Various methods used for a surface fitting were proposed, including the second-order or the

higher-order fitting models [62, 64], the fitting by Zernike's polynomials [65, 66], or the principal component analysis [67], which simplifies two-dimensional (2D) phase unwrapping into the one-dimensional (1D) computational problem. Several techniques require a sample-free blank area close to the sample for the surface analysis and further extrapolation of the phase map, assuming identical background phase distribution in the region of interest [62]. Other techniques exploit fitting the whole field of view in spite that the accuracy achieved may be influenced by the topographic distribution of the sample [64, 65]. Generally, the particular method suitable for phase correction has to be chosen based on the application requirements. As an example of various possibilities, tilt can be compensated by multiplying the reconstructed phase by a numerical reference wave [61, 68], the angular spectrum shift [69], counting the period of interference fringes [70], or surface fitting methods [63]. Besides, tilt suppression methods still received significant attention in the last decade [71–75].

Some applications of DH exploit two or more wavelengths [49] for the angular multiplexing [76, 77], the color-sensitive imaging [78–80] by a single-color camera [81], the dispersion measurement of living cells [82], the phase unwrapping [76], the spatial noise reduction [36], or to isolate the physical thickness from the refractive index distributions [83–85]. Decoupling the refractive index and the thickness distributions, respectively, is possible by acquiring two interference records, which correspond to the same sample immersed in two various surrounding solutions with the same osmolarities but with different refractive indexes [83, 84]. However, the decoupling can be obtained even from a single interference record, without manipulating the sample, just using the highly dispersive surrounding medium [85]. Moreover, the wrapping procedure in multi-wavelength holography is simplified by synthesizing wavelength much longer than either of the two probing wavelengths [76]. The same trajectory thus provides a smaller OPD compared to each of the original wavelengths. This procedure reduces the number of phase wraps present in the field of view (FOV). In opposite, wavelength shorter than either of the two wavelengths can also be synthesized, which enables higher accuracy in OPD measurement [36].

Though the DH is a coherence-based technique, applications employing the broadband light were also developed. The three-dimensional (3D) fluorescence holographic imaging was initially proposed in 1997 [86] and further improved in the following years [87]. To ensure a small OPD and to keep interference in the broadband illumination [88], the common-path arrangements were successfully used. The spatial light modulator was advantageously implemented as a splitting device for incoherent correlation imaging, based on the fact that every point source is self-spatially coherent [89]. Although these methods combine bright-field microscopy and interferometry, they are not appropriate for retrieving the quantitative phase information of the specimen. A combination of fluorescence microscopy and DHM

for QPI was implemented in 2006 for the first time [90].

The true QPI can be categorized depending on the used illumination as coherent and incoherent. The spatial noise, known as speckle, appears in coherent-light imaging. It originates from diffraction on rough surfaces, optical inhomogeneities, or multiple parasitic reflections that mutually interfere. The images captured hence contain typical grain structured inhomogeneities in both the amplitude and the phase distributions. Various methods to reduce the coherent noise were proposed [43], including the implementation of low-coherence sources, averaging the multiple interference records, or numerical processing of a single interference record. Besides, in monochromatic light imaging, a single shot approach was established to reduce the influence of speckle. This technique is based on dynamical variations of the spatial coherence to get partially spatial coherent illumination before the interferometer. The averaging required is achieved during the camera exposure time [51, 91–93]. Other methods based on monochromatic imaging require more records to achieve noise suppression, including the variable angular illumination [94] or moving diffusers [95]. Moreover, multiple interference records with uncorrelated speckle patterns can be obtained by the slight object rotation [96], translation [97], or translation of the camera [98, 99]. Contrary, multi-wavelength [36, 100] or broadband light [101] interferometry provides a low spatial noise with a more homogeneous background intrinsically because of the speckle contributions from various wavelengths mutually average. Broadband light interferometry also reduces the added noise because just light emerging from a small section of the object interferes [102]. Hence, the multiple-reflection interference reduces as a consequence. Feasible experimental implementation of a nonmonochromatic DH is possible by a spatial filtration of the light-emitting diode (LED) source [103–105] with precisely adjusted optical components.

As mentioned before, principles of off-axis holography enable exploitation of the angular multiplexing [50] for the multi-color imaging, the super-resolution imaging, the multi-polarization imaging, and the tomographic phase microscopy, for example. Moreover, the full field high-resolution performance of DHM was further improved [106] by adopting the synthetic-aperture principles to study the material [107] and biological [108, 109] samples. The method was implemented, providing an angular, angular-wavelength, or angular-polarization multiplexing. Besides, various components to enhance the synthetic aperture were proposed, such as diffraction gratings [110–114], spatial light modulators [115–120], pinhole mask [121], microlenses array [109], Fresnel prism [122], or moveable camera to enlarge the acquired FOV [110, 123].

2.3 Contemporary state of research

It was introduced that DH is a sophisticated, powerful imaging tool allowing to measure the complex amplitude of light interacting with the sample, which brings out quantitative information on both the amplitude and the phase distributions, respectively. In the following text, the introduction and the contemporary state of research related to problems discussed in the publications:

[1] J. Běhal and Z. Bouchal, "Optimizing three-dimensional point spread function in lensless holographic microscopy," *Optics Express*, vol. 25, pp. 29026–29042, 2017,

[2] L. Miccio, J. Behal, M. Mugnano, P. Memmolo, B. Mandracchia, F. Merola, S. Grilli, and P. Ferraro, "Biological lenses as a photomask for writing laser spots into ferroelectric crystals," *ACS Applied Bio Materials*, vol. 2, no. 11, pp. 4675–4680, 2019,

[3] J. Běhal, "Quantitative phase imaging in common-path cross-referenced holographic microscopy using double-exposure method," *Scientific Reports*, vol. 9, no. 9801, 2019,

are present. All the topics are motivated by the exploitation of digital holography to optical microscopy, which is called digital holographic microscopy (DHM).

Firstly, the design of the three-dimensional (3D) point spread function (PSF) is discussed, including holographic aberrations and the focal shift (FS) effect. The topic is in the Thesis further extended to a lens-less Gabor's holographic configuration where the magnified aberration-free imaging is required. According to our knowledge, the description of the FS effect appears for the first time in this context. Furthermore, currently established topics the bio-photolithography (bio-PL) and employment of the living samples as optical elements are present. Notably, recent works focused on the biolensing effect of red blood cells (RBCs) are reviewed with the intent to use the cells as optical elements for photolithographic writing into lithium niobate ($LiNbO_3$) substrate. DHM serves here as an instrument to study and quantify the performance. Besides, recent works focused on describing the experimental configurations used for a single-shot common-path self-referencing DHM are summarized. In the following text of the Thesis, the optimal implementation of the double-exposure method used to eliminate the phase background in the common-path self-referencing DHM is discussed. Finally, the polarization imaging by DH is introduced with an emphasis on the Jones matrix reconstruction.

2.3.1 Three-dimensional point spread function

Elementary imaging criteria adopted for evaluating the quality of imaging performance in classical optical imaging theory were preferably defined for two-dimensional objects. The full three-dimensional imaging became possible after the invention of confocal mi-

croscopy [124], and it has been further developed in modern imaging techniques, including digital holographic microscopy [125], Fourier ptychographic microscopy [126], or super-resolution localization microscopy [127, 128], for example. Properties of 3D imaging are also crucial in laser manipulations [129] and particle tracking applications [44]. The intensity image of a point object is called a point spread function and is traditionally used to estimate the quality of the imaging performance provided by imaging systems. The 3D PSF is commonly determined by calculating the diffraction of a convergent spherical wave truncated by the lens aperture. Multiple exact approaches, including Rayleigh-Sommerfeld and Fresnel-Kirchhoff diffraction theories, were formulated, and the paraxial and Debye approximations used for the investigation of the optical performance. To apply these approximations correctly, the specific imaging conditions must be considered. In optical systems with a low numerical aperture, where apodization, polarization, and aberrations are not essential, the paraxial approximation is well applicable. In high-aperture optical systems, the Debye approximation is used successfully. It represents the focused light field as a superposition of plane waves whose propagation vectors fall inside the cone given by the aperture angle. Paraxial elaboration of the Debye approximation provides the 3D PSF with a symmetrical distribution of the axial intensity. This result is correct only when the Fresnel number of the focusing arrangement is much higher than unity [130] but fails in systems with a low Fresnel number, where the axial intensity exhibits asymmetry, and its maximum is shifted away from the geometric focus, toward the aperture [131–135]. The effect was experimentally verified in work [136] and cannot be explained by the Debye approximation.

Focal shift effect

In the works devoted to light focusing on the optical systems with a low value of the Fresnel number, an asymmetric axial profile of the PSF, and the shift of the intensity maximum out of the paraxial image plane received considerable attention. The features mentioned originate from truncating the wave-field by finite-size apertures or equivalently from the finite value of the Fresnel number [137]. The shift of the intensity maximum out of focus is in the literature called the focal shift. The effect was first noticed in connection with non-uniform beams. Mainly it was found that the intensity maximum of focused Gaussian beam is shifted towards the focusing lens relative to the position of geometrical focus [138]. Later, more detailed studies have found that this shift depends on the truncation parameter (ratio between aperture radius of the imaging lens and width of the Gaussian beam) and the Gaussian Fresnel number assigned to the width of the incident beam [139].

The focal shift was studied in connection with various types of optical fields includ-

ing, spherical wave [135], Gaussian beam [140], Bessel beams [141], Lorentz–Gauss beams [142], flat-topped beams [143], degrees of spatial coherence [144], apodization functions, e.g., in noncentral obscured pupils [145], axially super resolving apertures, or generally in any diffracting pupil [146]. Besides, in the case of selected apodization apertures, further effect rises, which may lead to complications in distinguishing between the truth-focal spot and a new emerging high-intensity spot. It is called the focal-switch and is again a consequence of the diffraction [146]. Both effects, focal shift, and focal switch appear when the Fresnel number is low enough. Hence they have not received substantial attention in light imaging applications with standard optical components. More than in the direct imaging with typical lenses, the FS effect appears while using the micro-optical elements [147–155] or in the performance of the magnified lens-less DH [1, 156].

2.3.2 Bio-photolithography

Photolithography is a well-established sophisticated technology for the fabrication of 3D relief structures. Three components are needed to realize PL: light source, physical mask or optical elements, and photoresist. The process enables to transfer of the pattern imposed by the mask to photoresist employing the light illumination [157–159]. Recently, PL became appropriate also for purposes of biotechnology where PL allowed to realize scaffolds for biological applications, for example, in tissue engineering [160, 161]. Besides, a new PL approach was established that utilizes biological samples as a photomask itself. It was demonstrated that direct cell PL could be realized to modify the surface of PDMS to enhance the efficiency of the cell-imprinting based experiments [162]. Moreover, DNA molecules that behave as biophotomasks enable specific patterning on PVDF membranes [163]. PL throughout living samples or biomolecules is hence part of a broader contest where the paradigm is the employment of the natural interactions between living samples and light, thus integrating them as active optical elements [164–166]. The bio-PL requires higher demands to select the proper substrate as a photoresist. It has to function in close contact with the sample without subsequent intoxication of living tissue. Such materials are called biocompatible. Lithium niobate is an excellent example of the material utilized for wide-field of optical applications, which is also biocompatible [167] and was currently employed for interfacing biological samples [168].

Lithium niobate as a photoresist

Generally, $LiNbO_3$ is a promising material utilized due to its various properties [169]. The high transparency from the visible to the near-infrared spectral regions (0.3-5 μm), optical homogeneity, and high refractive index (≈ 2.2) allow exploitation of the $LiNbO_3$ for op-

tical applications. As an example, 3D optical surfaces, including lenses and axicons, can be milled by ion beam into $LiNbO_3$ despite its fragility [170]. Besides, numerous properties enable to implement the $LiNbO_3$ in optics and photonics [171], including second-order nonlinearity, uniaxial optical anisotropy, acousto-optic effect, linear electro-optic effect, bulk photovoltaic effect, and photorefractive effect. Charge transport models of the photorefractive and ferroelectric crystals were also widely characterized in the literature [169,171,172]. The properties mentioned enable the creation of holographic memories [173] and manufacturing optical elements, e.g., negative lens-like structures [174] and patterning diffraction gratings [175, 176] and waveguides [177] in both regimes with the pulse [178, 179] and continuous [176] lasers, respectively. The material was used as a photovoltaic tweezer to trap and manipulate particles on the surface of the crystal with a single beam or periodical patterns [180–182].

Moreover, recently, $LiNbO_3$ was employed for electrophoretic and dielectrophoretic trapping [168, 183–186]. It was demonstrated that $LiNbO_3$ has an active role in cellular adhesion and migration processes due to the electric charge patterns induced by the photovoltaic effect [167, 187–191].

2.3.3 Red blood cells as optical elements

Interactions between light and living samples, to integrate them as active optical elements [164–166], have opened remarkable opportunities in recent research. Some examples are the biolasing, i.e., the generation of laser light into single cells [192,193], and the realization of specific photonic structures utilizing bacteria suspensions [194,195]. In this context, the living cells can act as optofluidic lenses [196] supplementing true optical elements. Notably, red blood cells lacking any internal organelles were treated as transparent phase objects with corresponding magnification and focal length [196]. The mentioned biolens property was found to be an optical fingerprint utilized for diagnostic purposes. Indeed, a set of selected optical biomarkers was regarded to be able to discriminate different anemias with similar morphologies. Also, the correlation of such biomarkers with mechanical stress of RBC's membrane was demonstrated [197–200]. Furthermore, tracking of the biolens focal point in a microfluidic channel enabled the tomographic reconstruction of the RBC surface profile [201]. It was also demonstrated that RBCs could be trapped separately or chained one after another, forming the optical chain at the probe tip [202]. Various types, discocyte, and spherical-like RBCs were further used for the dynamic scanning to image a membrane of the investigated cell. Besides, recently, even the Talbot effect was demonstrated to characterize the ensemble of the self-assembled and synthetic array of RBCs [203].

2.3.4 Common-path off-axis digital holography

In-line holographic microscopes with incorporated common-path interferometer guarantee improved temporal stability intrinsically. However, an overlap of the useful information with the zero-order and the twin image makes a correct image restoration from a single-shot interference record impossible. Hence, multiple phase-shifted interference records must be processed to overcome this deterioration, limiting the observation of the dynamically evolving phenomena. A single-shot phase reconstruction is feasible in off-axis holographic arrangements where the real and the virtual images separate by filtering in the Fourier domain [34]. However, the conventional two-beam off-axis geometries with Michelson or Mach Zehnder interferometer are very sensitive to external vibrations causing the loss of temporal stability.

A single-shot holographic reconstruction maintaining the high temporal stability is feasible in common-path lateral-shearing setups where the interfering signal and reference waves share identical components, thus providing nearly the same optical path. In methods with a replicated field of view, various types of shearing devices were used to achieve the duplication, including a beam splitter [204–208], a thick glass plate [209–218], a Wollaston prism [219], a calcite crystal [220], a Fresnel biprism [221, 222], and gratings [37, 90, 223–226]. In self-referencing techniques [37, 204–207, 209, 212, 214, 219, 222, 226, 227], a part of the beam unscattered by the sample acts directly as a reference wave. Here, only half of the field of view is exploited. Hence the methods are appropriate for imaging the sparse objects. On the other hand, one of the beams produced can be additionally filtered in the Fourier plane to create an isolated reference beam with reduced information about the object [90, 216, 222–224]. This approach enables imaging more dense samples but requires a precise alignment of the added optical components. Indeed, both techniques presented were implemented with the Sagnac interferometer [38, 228] incorporated, which allows continuous adjustment of the angle introduced between the interfering waves in advance. Moreover, the quasi common-path self-referencing DH can be achieved even in a lack of the shearing device, e.g., by the additional mirror, which reflects part of the sample-free object beam on itself to achieve the self-referencing [210, 229]. The approach enables to exploit the full field of view while remaining the temporal stability enhanced.

2.3.5 Polarization-sensitive digital holography

The direction of the oscillating vectorial electric field of light is characterized by the polarization, which is sensitive to environments introducing the optical anisotropy. Such materials variously influence individual components of the electrical field vector. The polarized light microscopy is a commonly used technique to quantify the optical anisotropy. The

polarization-sensitive imaging is useful for measuring the stress inside material and biological samples and imaging the internal structures of cells and tissues without the need for additional contrast agents. The intensity-based polarization imaging can be classified as compensator-based and polarimetric-based. The compensator-based methods eliminate the specimen-induced phase difference by setting the compensator parameters [230]. The polarimetric-based methods process multiple images captured under various polarization modulation conditions of light to retrieve the specimen's polarization properties [231–233]. Further methods advantageously exploit the principles of QPI to extract the polarization properties of the sample simultaneously with the complex amplitude.

The idea of using the holography for the polarization-sensitive imaging was initially proposed in the 1960s by Lohmann [234]. Based on this principle, a single-shot method for recovering the polarization state distribution by DH was implemented in the 1990s [235]. Here, the mutually orthogonal reference waves were mixed with the signal wave in the three-arm Mach-Zehnder interferometer. Hence the amplitude, phase, and polarization-state distributions were obtained simultaneously [236, 237]. The polarimeter based on the principle of angular multiplexing was also tested and introduced [238]. Moreover, the generalized approach of the polarization-sensitive imaging by DH for the Jones matrix reconstruction was proposed [239]. This technique, called Jones phase microscopy, requires the illumination by mutually orthogonally polarized beams, which are mixed with the orthogonally polarized reference beams to retrieve the whole Jones matrix of the specimen. Later, even the Stokes holography was proposed [240] in a similar context. Besides, the common-path off-axis DHM was used for purposes of Jones phase microscopy, ensuring the high temporal stability of the system [241]. Authors utilized an optical chopper for switching between the polarization modes of the illumination light, 2D diffraction grating for replicating the FOV, and specially designed filter placed in the Fourier plane. The spatial filter ensures the homogeneity of the reference wave and separation of the duplicated signal waves, subsequently projected by locally placed orthogonally-oriented linear polarizers. The Jones-matrix of liquid crystal droplets used as a specimen was retrieved in order of tens of milliseconds to prove the method's application potential. Another experimental arrangement providing a partially common-path geometry was introduced [242] by implementing ordinary optical components. Here, the Sagnac interferometer was used to generate orthogonally polarized reference beams.

Furthermore, a single-shot reconstruction of a Jones matrix by DH was first introduced in the paper [243]. Two independent laser sources were used in the experimental realization to assure the incoherent summarization of the optical beams in the camera plane. Each of the laser sources passed through its 2D diffraction grating to introduce spatial frequencies before entering the Mach-Zehnder interferometer with specially designed filters to achieve

the suppression of unwanted diffraction orders. Another application of a single-shot Jones matrix reconstruction by digital holography was obtained by the angular multiplexing and spatial separation at the detector's plane [244], enabling the use of the full dynamical range of the sensor despite its partial spatial exploitation. Recently, the work [242] was extended to a single-shot Jones matrix reconstruction [245] method, where the specimen was additionally illuminated by two tilted orthogonally polarized beams.

Chapter 3

Methods and tools

This chapter summarizes the main theoretical and experimental methods exploited in the Thesis. The first part introduces the performance of holographic reconstruction. In particular, the image of a point source in lens-less DH is studied with emphasis on the achieved paraxial imaging parameters, the presence of the focal shift effect, and the influence and quantification of holographic aberrations. The second part discusses phase-background compensation with an emphasis on the correction by the double-exposure. Special effort is paid to describe the use of the double-exposure method in the performance of common-path lateral-shearing self-referencing DHM. Furthermore, focusing properties of healthy and spherical-shape RBCs are studied together with the intensity-based writing into photorefractive materials. The final part presents the polarization-sensitive imaging and Jones matrix reconstruction by digital holography. Most of the methods are also included in the following publications:

[1] J. Běhal and Z. Bouchal, "Optimizing three-dimensional point spread function in lensless holographic microscopy," *Optics Express*, vol. 25, pp. 29026–29042, 2017,

[2] L. Miccio, J. Behal, M. Mugnano, P. Memmolo, B. Mandracchia, F. Merola, S. Grilli, and P. Ferraro, "Biological lenses as a photomask for writing laser spots into ferroelectric crystals," *ACS Applied Bio Materials*, vol. 2, no. 11, pp. 4675–4680, 2019,

[3] J. Běhal, "Quantitative phase imaging in common-path cross-referenced holographic microscopy using double-exposure method," *Scientific Reports*, vol. 9, no. 9801, 2019.

3.1 Holographic terms and their separation

Digital holography is a technique based on the coherence properties of light. The interference field created by mutually coherent signal wave U_s and reference wave U_r captured by

the quadratic detector can be written in the following form

$$H = |U_s + U_r|^2 = |U_s|^2 + |U_r|^2 + U_s^* U_r + U_s U_r^*. \tag{3.1}$$

The interference pattern includes four terms, which are known as two dc terms $|U_s|^2$ and $|U_r|^2$, and complex conjugated images marked as $U_s^* U_r$ and $U_s U_r^*$, respectively.

When reconstructing one of the desired images $U_s^* U_r$ or $U_s U_r^*$ from the interference record (3.1), the remaining terms cause undesired blurring. This problem was diminished, proposing various approaches in which the dc term was subtracted [246]. The basic ones exploit deducting a mean intensity of the holographic record [247] or high-pass filtering the Fourier spectra [248]. Separate snapshots of the reference wave or both the signal and the reference waves can further reduce the influence of inhomogeneities modulated on the reference wave, in spite that requirements on the temporal stability of the experimental setup increase. In-line DH configurations solve the problem by processing three or more interference records with different phase shifts introduced between the signal and the reference waves [31]. For example, a set of three phase-shifted holographic snapshots with subsequent phase-steps $2/3\pi$ is expressed as

$$H_j = |U_s|^2 + |U_r|^2 + U_s^* U_r \exp\{i\theta_j\} + U_s U_r^* \exp\{-i\theta_j\}, \tag{3.2}$$

where $j = \{1, 2, 3\}$, $\theta_j = \{0, 2/3\pi, 4/3\pi\}$, and the term of interest is further achieved as [41]

$$U_s U_r^* = \frac{1}{3} H_1 - \frac{1 - i\sqrt{3}}{6} H_2 - \frac{1 + i\sqrt{3}}{6} H_3. \tag{3.3}$$

The required phase shifts were implemented applying a piezoelectric transducer [31], a spiral phase plate [249], geometric phase optical elements [250], a liquid crystal variable retarder [251] or a spatial light modulator [252–256]. In off-axis holography, the overlapping problem was solved successfully by introducing high enough spatial carrier frequency between the signal and the reference waves. It ensures the spectral separation of the terms, although the resolution of the imaging system may decrease. If the high-enough spatial carrier frequency $\sin\alpha/\lambda$ is introduced on the reference wave along the x-axis, the recorded holographic pattern reaches the form

$$H = |U_s + U_r \exp(ik_x x)|^2 = |U_s|^2 + |U_r|^2 + U_s^* U_r \exp(ik_x x) + U_s U_r^* \exp(-ik_x x), \tag{3.4}$$

where $k_x = k \sin\alpha$, $k = 2\pi/\lambda$, and the selection of $U_s^* U_r$ or $U_s U_r^*$ in the Fourier domain is feasible. Applying the techniques mentioned allows separation of the useful holographic term for further numerical processing, e.g., the reconstruction of either a virtual or real

image.

3.2 Complex-amplitude propagation

The image reconstruction in DH is usually provided by the reconstruction wave of the identical wavelength as that used in the experiment. The recorded interference pattern situated in the plane $z = 0$ of lateral coordinates x, y diffracts the illumination light, and the numerical refocusing can be applied by calculating the first Rayleigh-Sommerfeld diffraction integral [257, 258]. In this case, the image complex amplitude U_i evaluated at the lateral position x_i, y_i and located in the distance z_i from the interference record is expressed as

$$U_i(x_i, y_i; z_i) = \frac{z_i}{i\lambda} \iint_{-\infty}^{\infty} t(x, y) \frac{\exp\{\mathrm{sgn}(z_i) ikr_i\}}{r_i^2} \mathrm{d}x\mathrm{d}y. \tag{3.5}$$

Here $r_i = \sqrt{(x_i - x)^2 + (y_i - y)^2 + z_i^2}$, sgn is a signum function, and t is a complex function which describes the transformation of the reconstructing wave by the transmission aperture function imposed in the recording plane. The numerical requirements needed for direct calculation of the integral (3.5) increase rapidly with the increasing pattern dimensions. Thus equivalent forms of the diffraction integral (3.5) may be adopted for its faster evaluation. For example, rewriting the integral (3.5) into the convolution form

$$U_i(x_i, y_i; z_i) = \iint_{-\infty}^{\infty} t(x, y) \mathfrak{h}(x_i - x, y_i - y; z_i) \mathrm{d}x\mathrm{d}y = t * \mathfrak{h} = \mathcal{F}^{-1}\{\mathcal{F}\{t\}\mathcal{F}\{\mathfrak{h}\}\} \tag{3.6}$$

may be advantageous, including the 2D convolution operator $*$, 2D Fourier transform $\mathcal{F}$, and the impulse response of free space $\mathfrak{h}(u, v; z_i) = \dfrac{z_i}{i\lambda} \dfrac{\exp\left\{\mathrm{sgn}(z_i) ik\sqrt{u^2 + v^2 + z_i^2}\right\}}{u^2 + v^2 + z_i^2}$.

Besides, the angular spectrum approach of a free-space propagation leads to the analogous form of the Rayleigh-Sommerfeld integral (3.5)

$$U_i(x_i, y_i; z_i) = t * \mathfrak{h} = \mathcal{F}^{-1}\{\mathcal{F}\{t\}\mathfrak{H}\}, \tag{3.7}$$

where the function $\mathfrak{H}(\nu_x, \nu_y) = \exp\left\{ikz_i\sqrt{1 - (\lambda\nu_x)^2 - (\lambda\nu_y)^2}\right\}$ for $\sqrt{\nu_x^2 + \nu_y^2} \leq 1/\lambda$ and $\mathfrak{H}(\nu_x, \nu_y) = 0$ for $\sqrt{\nu_x^2 + \nu_y^2} > 1/\lambda$ represents the transfer function of free space with spatial frequencies ν_x, ν_y. The free-space propagation described by the above equations enables the numerical refocusing of the complex amplitude imposed, e.g., for the reconstruction of the holographic image.

3.3 Three-dimensional point spread function

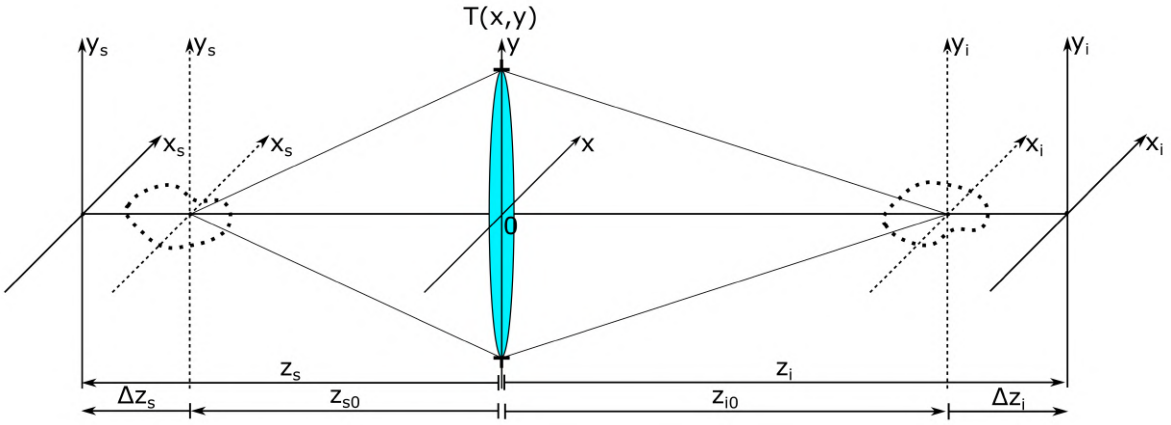

Figure 3.1: Geometry of the optical imaging system represented by a single thin lens.

Linear optical systems can be fully described by specifying the responses of point objects positioned in the object space [257]. When a 2D imaging under coherent illumination is considered in the optical imaging systems, the formed complex image field $U_i(x_i, y_i; z_i)$ can be written in the form

$$U_i(x_i, y_i; z_i) = \iint_{-\infty}^{\infty} U_s(x_s, y_s; z_s)\overline{\mathfrak{h}}(x_i, y_i, x_s, y_s)\mathrm{d}x_s\mathrm{d}y_s, \tag{3.8}$$

where $\overline{\mathfrak{h}}$ represents 2D amplitude point spread function. This approach can be generalized directly to 3D imaging if the first Born approximation is valid, i.e., if the superposition principle holds, which neglects secondary diffraction in the volume of a semi-transparent thick object [259]. The entire field $U_i(x_i, y_i, z_i)$ is evaluated by integration through the sample $U_s(x_s, y_s, z_s)$, including the axial coordinate. Therefore,

$$U_i(x_i, y_i, z_i) = \iiint_{-\infty}^{\infty} U_s(x_s, y_s, z_s)\overline{\mathfrak{h}}(x_i, y_i, z_i, x_s, y_s, z_s)\mathrm{d}x_s\mathrm{d}y_s\mathrm{d}z_s, \tag{3.9}$$

where $\overline{\mathfrak{h}}(x_i, y_i, z_i, x_s, y_s, z_s)$ represents a 3D image-field distribution of a single point scatterer called 3D amplitude point spread function [259]. For example, 3D amplitude point

spread function for thin-lens imaging in the Fresnel approximation is expressed in the form

$$\begin{aligned}\overline{\mathfrak{h}}(x_i, y_i, z_i, x_s, y_s, z_s) =& \frac{\exp\{ik(z_i - z_s)\}}{\lambda^2 z_i z_s} \exp\left\{ik\frac{x_i^2 + y_i^2}{2z_i}\right\} \exp\left\{-ik\frac{x_s^2 + y_s^2}{2z_s}\right\} \times \\ & \iint_{-\infty}^{\infty} T(x_i, y_i) \exp\left\{ik\frac{x^2 + y^2}{2}\left(-\frac{1}{z_s} + \frac{1}{z_i} - \frac{1}{f}\right)\right\} \times \\ & \exp\left\{-ik\left[\left(-\frac{x_s}{z_s} + \frac{x_i}{z_i}\right)x + \left(-\frac{y_s}{z_s} + \frac{y_i}{z_i}\right)y\right]\right\} \mathrm{d}x\mathrm{d}y,\end{aligned} \tag{3.10}$$

where the transmittance function of a thin lens is assumed as $\exp\{-ik(x^2 + y^2)/(2f)\}$, and T defines its finite aperture. Generally, the distances z_s and z_i are expressed as

$$z_s = z_{s0} + \Delta z_s, \quad z_i = z_{i0} + \Delta z_i, \tag{3.11}$$

where z_{s0} and z_{i0} satisfy the lens law

$$\frac{1}{z_{i0}} - \frac{1}{z_{s0}} = \frac{1}{f}, \tag{3.12}$$

and Δz_s, Δz_i are defocusing distances in the object space and the image space, respectively (Fig. 3.1). If the $\Delta z_s, \Delta z_i$ are small in meaning that relations

$$\frac{1}{z_s} \approx \frac{1}{z_{s0}}\left(1 - \frac{\Delta z_s}{z_{s0}}\right), \quad \frac{1}{z_i} \approx \frac{1}{z_{i0}}\left(1 - \frac{\Delta z_i}{z_{i0}}\right) \quad x_i = \beta x_s, \quad y_i = \beta y_s, \quad \beta = \frac{z_{i0}}{z_{s0}} \approx \frac{z_i}{z_s}, \tag{3.13}$$

are satisfied, the equation (3.9) reaches the convolution form

$$\begin{aligned}U_i(x_i, y_i, \Delta z_i) =& \frac{\exp\{ik(z_{i0} - z_{s0})\}}{\lambda^2 z_{i0} z_{s0}} \exp\left\{-ik\frac{x_i^2 + y_i^2}{2\beta f}\right\} \exp\{ik\Delta z_i\} \times \\ & \iiint_{-\infty}^{\infty} \widehat{U}_s(x_s, y_s, \Delta z_s) \overline{\mathfrak{h}}(x_i - \beta x_s, y_i - \beta y_s, \Delta z_i - \beta^2 \Delta z_s) \mathrm{d}x_s \mathrm{d}y_s \mathrm{d}\Delta z_s,\end{aligned} \tag{3.14}$$

where

$$\overline{\mathfrak{h}}(u, v, w) = \iint_{-\infty}^{\infty} T(x, y) \exp\left\{ik\frac{x^2 + y^2}{2z_{i0}^2} w\right\} \exp\left\{-ik\frac{1}{z_{i0}}(xu + yv)\right\} \mathrm{d}x\mathrm{d}y, \tag{3.15}$$

with $\widehat{U}_s(x_s, y_s, \Delta z_s) = U_s(x_s, y_s, \Delta z_s) \exp\{-ik\Delta z_s\}$ representing the effective object function. The shape of the 3D amplitude point spread function (3.15) does not depend on the point object's coordinates but scaled differences between the object and image coordinates. This 3D space-invariant property (3.14) enables to exploit the constant lateral and

longitudinal magnifications, β and β^2, to describe the thin-lens imaging. However, the 3D convolution relation of the image formation (3.14) holds only if the simplified conditions (3.13) are fulfilled.

Image of the point objects expressed in terms of the 3D amplitude point spread function or square of its absolute value, called 3D point spread function, are parameters essential for describing the image formation and were studied in the context of digital holography [260–262].

3.4 Lens-less Gabor holography of point sources

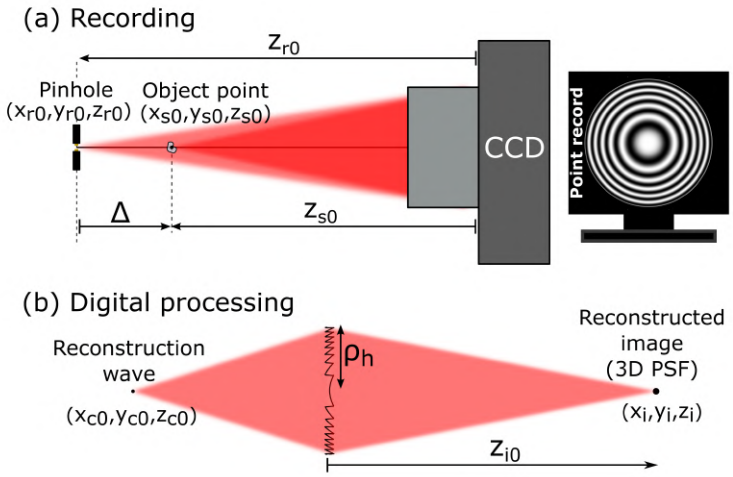

Figure 3.2: Optical scheme for evaluation of the three-dimensional point spread function in lens-less digital holographic microscopy: (a) in-line recording geometry, (b) reconstruction geometry.

Here, the imaging performance of coherent digital holography is studied adopting the lens-less in-line geometry [27] from Fig. 3.2, demonstrating both recording and numerical reconstruction of a point interference record. Laser light of the wavelength λ passes through a pinhole of few micrometers in the diameter, creating the source of divergent reference wave U_r. The reference wave illuminates a point-like object which consequently generates a divergent signal wave U_s. The waves U_r and U_s mutually interfere, creating the point interference image (3.1) captured by a camera. The record achieved is illuminated by a virtual reconstruction wave U_c and the image is obtained by enumerating the free propagation of light diffracted at the interference structure. The complex function t in (3.5) thus represents interaction between the reconstructing wave U_c and the record (3.1),

$$t(x, y) = T(x, y)U_c|U_s + U_r|^2, \tag{3.16}$$

where the aperture function T defines a finite area. In real experiments, this area is given by an overlap achieved by interfering divergent waves U_s and U_r or active area of the used detector. Optionally, when the virtual image $U_s U_r^*$ is separated, the complex function t is given as

$$t(x,y) = T(x,y) A_s A_r A_c \exp\{i[-\mathrm{sgn}(z_{s0})\Phi_s + \mathrm{sgn}(z_{r0})\Phi_r - \mathrm{sgn}(z_{c0})\Phi_c]\}, \tag{3.17}$$

where A_j and Φ_j, $j = \{r, s, c\}$, are amplitudes and phases of the signal, the reference and the reconstruction waves.

When the waves considered are treated as perfectly spherical and originate from the positions x_{j0}, y_{j0}, z_{j0}, $j = \{r, s, c\}$ marking the coordinates of a pinhole, an off-axis point scatterer, and a virtual source, respectively, the amplitudes and phases within the recording plane relative to the phase at the origin can be written as

$$A_j = \frac{a_j}{r_j}, \quad \Phi_j = k(r_j - r_{j0}), \quad j = \{r, s, c\}, \tag{3.18}$$

where $r_j = \sqrt{(x_{j0} - x)^2 + (y_{j0} - y)^2 + z_{j0}^2}$, $r_{j0} = \sqrt{x_{j0}^2 + y_{j0}^2 + z_{j0}^2}$ and a_j are constant amplitudes.

3.4.1 Paraxial optical parameters

The Fresnel approximation of spherical waves provides an accuracy sufficient for describing the experiments implemented with a low numerical aperture [16]. The spherical waves are, in this case, considered as paraboloidal. Hence, the signal, the reference, and the reconstruction waves (3.18) reach the form

$$\Phi_j = k\left(\frac{x^2 + y^2}{2z_{j0}} - \frac{x x_{j0} + y y_{j0}}{z_{j0}}\right), \quad j = \{r, s, c\}. \tag{3.19}$$

To modify the diffraction integral (3.5) the Fresnel approximation is applied in the phase term, while a rough approximation $r_i \approx |z_i|$ is used for the amplitude. The following discussion can be simplified, considering the pinhole localized on the optical axis, $\sqrt{x_{r0}^2 + y_{r0}^2} = 0$. By omitting parts that do not influence the shape of the reconstructed intensity image of the point source and applying the complex function (3.17), the complex amplitude (3.5), can be considered as a Fourier transform of the aperture function T multiplied by a quadratic phase term,

$$U_i \propto \frac{1}{z_i} \iint_{-\infty}^{\infty} T(x,y) \exp\left\{ik\frac{\Omega(x^2 + y^2)}{2}\right\} \exp\{-i2\pi(x\nu_x + y\nu_y)\}\mathrm{d}x\mathrm{d}y, \tag{3.20}$$

where Ω and the spatial frequencies ν_x, ν_y are given as

$$\Omega = \frac{1}{z_i} - \frac{1}{z_{s0}} + \frac{1}{z_{r0}} - \frac{1}{z_{c0}}, \quad \nu_x = \frac{1}{\lambda}\left(\frac{x_i}{z_i} - \frac{x_{s0}}{z_{s0}} - \frac{x_{c0}}{z_{c0}}\right), \quad \nu_y = \frac{1}{\lambda}\left(\frac{y_i}{z_i} - \frac{y_{s0}}{z_{s0}} - \frac{y_{c0}}{z_{c0}}\right).$$

The focused image is reconstructed considering that the quadratic phase term vanishes. The condition required, $\Omega = 0$, is achieved for the reconstruction distance $z_i = z_{i0}$ determined as

$$\frac{1}{z_{i0}} = \frac{1}{z_{c0}} - \frac{\Delta}{z_{r0}(z_{r0} + \Delta)}, \tag{3.21}$$

where $\Delta = z_{s0} - z_{r0}$. Assuming the unlimited aperture of the record (T =const.), the geometric image given by the Dirac delta function is reconstructed, $U_i \propto \delta(\nu_x, \nu_y)$. The lateral coordinates of this point image are $x_i = x_{i0} = \beta x_{s0} + (z_{i0}/z_{c0})x_{c0}$ and $y_i = y_{i0} = \beta y_{s0} + (z_{i0}/z_{c0})y_{c0}$, where β is the lateral magnification given by

$$\beta = \frac{\mathrm{d}x_{i0}}{\mathrm{d}x_{s0}} = \frac{\mathrm{d}y_{i0}}{\mathrm{d}y_{s0}} = \frac{z_{i0}}{z_{r0} + \Delta}. \tag{3.22}$$

To be complete the longitudinal magnification of the imaging performance is given as

$$\gamma = \frac{\mathrm{d}z_{i0}}{\mathrm{d}z_{s0}} = \left(\frac{z_{i0}}{z_{r0} + \Delta}\right)^2 = \beta^2. \tag{3.23}$$

3.4.2 Diffraction-limited three-dimensional point spread function

The diffraction-limited 3D intensity distribution is studied if the point image is evaluated in the radial coordinates (ν_x, ν_y) and the defocused axial image plane, $z_i = z_{i0} + \Delta z_i$. Considering the circularly bounded holographic record with the finite radius ρ_h, the 3D PSF must be evaluated numerically, hovewer, the transversal cross-section through the 3D PSF reconstructed in the distance z_{i0} given by (3.21) can be calculated analytically. The normalized radial PSF defined as $I = |U_i(\sqrt{\nu_x^2 + \nu_y^2}, \Delta z_i = 0)|^2$ being unitary in its maximum, $I\left(\sqrt{\nu_x^2 + \nu_y^2} = 0, \Delta z_i = 0\right) = 1$, is expressed as

$$I\left(\sqrt{\nu_x^2 + \nu_y^2}, \Delta z_i = 0\right) = 4\,\mathrm{jinc}^2\left(\pi\rho_h\sqrt{\nu_x^2 + \nu_y^2}\right), \tag{3.24}$$

where $\mathrm{jinc}(x) = J_1(x)/x$, $J_1(x)$ is the Bessel function of a first kind and a first order. The condition needed to achieve the first minimum, i.e., an argument of the function reaches the value ≈ 3.8, defines the radius of Airy disc in the form

$$AD_i = \sqrt{(x_i - x_{i0})^2 + (y_i - y_{i0})^2} = 0.61\frac{\lambda}{NA_i}, \quad NA_i = \frac{\rho_h}{|z_{i0}|}, \tag{3.25}$$

where NA_i is the image numerical aperture.

Moreover, if the axial profile of the 3D PSF is investigated ($\sqrt{\nu_x^2+\nu_y^2}=0$), the diffraction integral has also an analytical solution. The normalized axial intensity defined as $I=|U_i(\sqrt{\nu_x^2+\nu_y^2}=0,\Delta z_i)|^2$ being unitary in the paraxial image plane, $I(\sqrt{\nu_x^2+\nu_y^2}=0,\Delta z_i=0)=1$, can be obtained in the form

$$I\left(\sqrt{\nu_x^2+\nu_y^2}=0,q\right)=\left(1-\frac{q}{\pi n_i}\right)^2\operatorname{sinc}^2\left(\frac{q}{2}\right),\quad q=\frac{\pi n_i\Delta z_i}{z_{i0}+\Delta z_i},\quad n_i=\frac{\rho_h^2}{\lambda z_{i0}}. \tag{3.26}$$

The function q behaves nonlinearly in Δz_i. The term before the sinc function leads to the shift of the intensity maximum out of the geometric focus, while the argument of the sinc function causes asymmetry of the intensity profile.

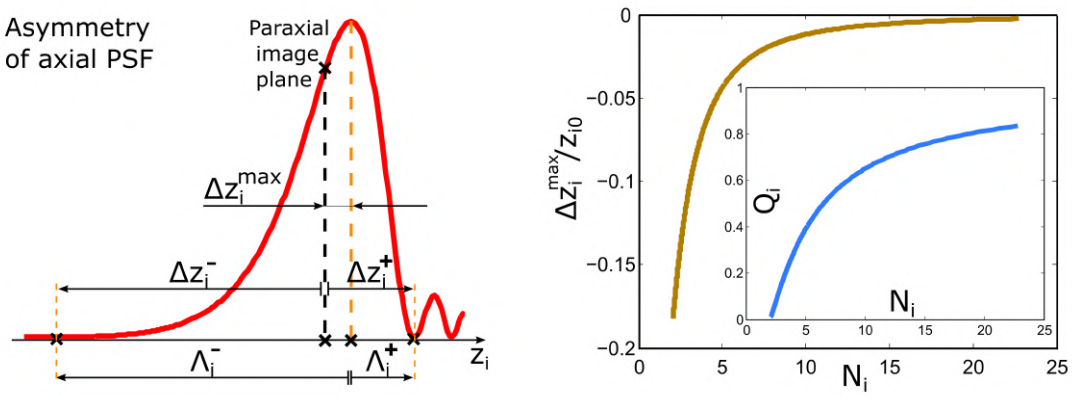

Figure 3.3: Asymmetric axial PSF with geometrical parameters used for the detailed analysis and the quantitative evaluation of the focal shift effect ($\Delta z_i^{max}/z_{i0}$) and the axial asymmetry in the image space (Q_i) as a function of the Fresnel number N_i.

Both effects, illustrated in Fig. 3.3, are influenced by the geometry of experiments and their evaluation is feasible adopting the Fresnel number $N_i=|n_i|$. The axial intensity (3.26) exhibits periodical changes and reaches zero values when the condition $q=2m\pi$, $m=\pm1,\pm2,\ldots$ is satisfied. The asymmetry of the axial intensity profile is evaluated by the positions of the nearest zero points Δz_i^+ and Δz_i^- related to $m=\pm1$ (Fig. 3.3),

$$\Delta z_i^+=\frac{2z_{i0}}{n_i-2},\quad \Delta z_i^-=-\frac{2z_{i0}}{n_i+2}. \tag{3.27}$$

Distribution of the axial intensity reaches its maximum in the position displaced from the paraxial image plane towards the recording plane. The position of the intensity maximum is calculated as a solution of a transcendental equation originating from the condition

$\mathrm{d}I/\mathrm{d}q = 0$ [135],

$$\tan\left(\frac{q}{2}\right) = \frac{q}{2}\left(1 - \frac{q}{\pi n_i}\right), \tag{3.28}$$

and the root q_{max} of the equation (3.28) must be obtained numerically. The position of the intensity maximum Δz_i^{max} is then determined by

$$\Delta z_i^{max} = \frac{z_{i0} q_{max}}{\pi n_i - q_{max}}. \tag{3.29}$$

Half-widths of the central intensity peak Λ_i^+ and Λ_i^- are given by the first zero points of the oscillating axial intensity that are closest to the intensity maximum,

$$\Lambda_i^+ = \Delta z_i^+ - \Delta z_i^{max}, \quad \Lambda_i^- = \Delta z_i^- - \Delta z_i^{max}. \tag{3.30}$$

Meaning of the defined geometrical symbols is evident from the illustration in Fig. 3.3. To quantify the axial asymmetry of the PSF in the image space the coefficient Q_i defined as

$$Q_i = \left|\frac{\Lambda_i^+}{\Lambda_i^-}\right| \tag{3.31}$$

can be used (Fig. 3.3). Examination of the axial PSF in the object space is also feasible by implementation of the longitudinal magnification γ (3.23). Asymmetry coefficients in the image space Q_i and the object space Q_s are identical in case when the constant longitudinal magnification is used, $Q_s = Q_i$. However, in the exact analysis, the positions of the intensity maximum and the nearest zero points of the oscillating axial intensity are transformed into the object space with different values of γ. Hence Q_s and Q_i are slightly different in the object space and the image space.

The equations mentioned above can be compared to the results achieved by the paraxial Debye approximation. When an investigation of the axial profile in proximity to the paraxial image plane is considered the approximation $|\Delta z_i| \ll |z_{i0}|$ is adopted leading to the modified form of the (3.26)

$$I\left(\sqrt{\nu_x^2 + \nu_y^2} = 0, q_D\right) = \mathrm{sinc}^2\left(\frac{q_D}{2}\right), \quad q_D = \frac{\pi n_i \Delta z_i}{z_{i0}}, \quad n_i = \frac{\rho_h^2}{\lambda z_{i0}}. \tag{3.32}$$

Contrary to the case (3.26), the function q_D is linear in Δz_i. Thus the axial PSF is symmetrical relative to the focal plane and without the focal shift effect, naturally. The axial intensity also varies periodically and takes zero when $q_D = 2m\pi$, where $m = \pm 1, \pm 2, \ldots$.

The relations (3.27) in this case reach the form

$$\Delta z_{iD}^{+} = -\Delta z_{iD}^{-} = \frac{2z_{i0}}{n_i}. \tag{3.33}$$

Symmetrical distribution in the image space (3.31), $Q_{iD} = 1$, is determined, which is equivalent to the result obtained using the paraxial Debye approximation. The condition for the Debye approximation to hold is that the Fresnel number $N_i = |n_i|$ is much larger than unity which also can be noticed comparing the relations (3.27) and (3.33). However, this condition may conflict with the paraxial approximation under some circumstances, and the results achieved may provide incorrect predictions comparing to the experiment [259]. Particularly, the intensity shapes obtained from the equations (3.26) and (3.32), including the functions q and q_D, respectively, vary when N_i reaches low values. Moreover, even the condition to hold the axial-space invariance $1/z_i = 1/(z_{i0} + \Delta z_i) \approx 1/z_{i0}$ is violated when N_i is low because the axial PSF becomes broad. Hence, the convolution form (3.14) describing the 3D image formation cannot be used in this case.

3.4.3 Holographic aberrations

When the conditions required for applying the paraxial approximation are satisfied and the virtual complex image is being reconstructed, the obtained paraboloidal phase matches the phase of the wave converging at the paraxial image point with the coordinates $x_i = x_{i0} = \beta x_{s0} + (z_{i0}/z_{c0})x_{c0}$, $y_i = y_{i0} = \beta y_{s0} + (z_{i0}/z_{c0})y_{c0}$ and $z_i = z_{i0}$. When experimental parameters exceed requirements of the paraxial approximation, the phase of $U_s U_r^*$ determined by the interference of spherical waves generally no longer matches the spherical wave. The differences that appear are known as holographic aberrations. The third-order holographic aberrations are described by the Taylor expansion applied to the phase Φ_j given by (3.18), in which only first three terms are included [263]. A phase of the aberrated waves can be written as

$$\Phi_j = \Phi_j^{(1)} - \Phi_j^{(3)}, \quad \Phi_j^{(1)} = k\frac{r_{\perp j}^2 - r_{\perp j0}^2}{2z_{j0}}, \quad \Phi_j^{(3)} = k\frac{r_{\perp j}^4 - r_{\perp j0}^4}{8z_{j0}^3}, \tag{3.34}$$

where $r_{\perp j} = \sqrt{(x_{j0} - x)^2 + (y_{j0} - y)^2}$, $r_{\perp j0} = \sqrt{x_{j0}^2 + y_{j0}^2}$ and $j = \{s, r, c, i\}$ are considered. Matching the first-order terms in z_j as $\Phi_i^{(1)} = -\Phi_r^{(1)} + \Phi_s^{(1)} + \Phi_c^{(1)}$, from which the image distance z_{i0} (3.21) and the lateral magnification (3.22) can be derived, ensure that the paraxial imaging conditions are satisfied.

The optical path difference between the reference wavefront and the equiphase surface given by the complex holographic term expresses the holographic wave aberrations. The

third-order aberrations in z_j, are calculated as

$$W = \frac{1}{k}\left(-\Phi_i^{(3)} - \Phi_r^{(3)} + \Phi_s^{(3)} + \Phi_c^{(3)}\right). \tag{3.35}$$

The investigation of holographic aberrations is further simplified when considering the pinhole and the source of the reconstruction wave are placed on the optical axis ($x_{j0} = y_{j0} = 0$, for $j = \{r, c\}$) and the source of the signal wave is located on the x-axis ($y_{j0} = 0$ for $j = \{s, i\}$). Using the polar coordinates (ρ, φ) in the recording plane, $x = \rho\cos\varphi$, $y = \rho\sin\varphi$, the third-order terms can be rewritten to the form

$$\begin{aligned}\frac{1}{k}\Phi_j^{(3)} &= A_{j040}\rho^4 + A_{j131}x_{j0}\rho^3\cos\varphi + A_{j222}x_{j0}^2\rho^2\cos^2\varphi + \\ &+ A_{j220}x_{j0}^2\rho^2 + A_{j311}x_{j0}^3\rho\cos\varphi, \qquad j = \{s, r, c, i\},\end{aligned} \tag{3.36}$$

where the used coefficients are given as

$$A_{j040} = \frac{1}{8z_{j0}^3}, \quad A_{j131} = -4A_{j040}, \quad A_{j222} = 4A_{j040}, \quad A_{j220} = 2A_{j040}, \quad A_{j311} = -4A_{j040}.$$

Substituting (3.36) into (3.35) and using the normalized radial coordinate $\rho_N = \rho/\rho_h$, where ρ_h is the radius of the circularly bounded interference record, the total holographic aberration is given by

$$W = S\rho_N^4 + C\rho_N^3\cos\varphi + A\rho_N^2\cos^2\varphi + F\rho_N^2 + D\rho_N\cos\varphi, \tag{3.37}$$

where the coefficients S, C, A, F and D represent spherical aberration, coma, astigmatism, field curvature and distortion, respectively, and can be written as

$$\begin{aligned} S &= -\frac{\rho_h^4}{8}\left(\frac{1}{z_{i0}^3} + \frac{1}{z_{r0}^3} - \frac{1}{z_{s0}^3} - \frac{1}{z_{c0}^3}\right), & C &= \frac{x_{s0}\rho_h^3}{2}\left(\frac{\beta}{z_{i0}^3} - \frac{1}{z_{s0}^3}\right), \\ A &= -\frac{x_{s0}^2\rho_h^2}{2}\left(\frac{\beta^2}{z_{i0}^3} - \frac{1}{z_{s0}^3}\right), & F &= \frac{1}{2}A, & D &= \frac{x_{s0}^3\rho_h}{2}\left(\frac{\beta^3}{z_{i0}^3} - \frac{1}{z_{s0}^3}\right). \end{aligned} \tag{3.38}$$

When the reconstruction wave matches the reference wave ($z_{c0} = z_{r0}$), the phases of the waves mutually eliminate each other in the reconstructed complex function (3.17) and the signal wave is fully recovered. In this case, the aberration-free image with the unitary magnification (3.22) is obtained ($z_i = z_{i0} = z_{s0}$, $\beta = 1$, hence $S = C = A = F = D = 0$). However, when the reconstructing wave differs from the reference wave ($z_{c0} \neq z_{r0}$) the influence of holographic aberrations have to be taken into account.

3.4.4 Strehl ratio

Holographic aberrations can be assessed fully numerically, but a sufficient estimation is possible even with the Strehl ratio K achievable by simplified calculations [264]. Assuming a circular aperture with the radius ρ_h, polar coordinates (ρ, φ), the normalized radial coordinate $\rho_N = \rho/\rho_h$, and a wave aberration W, the Strehl ratio is defined as

$$K = \left| \frac{\int_0^{2\pi} \int_0^1 \exp\{ikW\} \rho_N \mathrm{d}\rho_N \mathrm{d}\varphi}{\int_0^{2\pi} \int_0^1 \rho_N \mathrm{d}\rho_N \mathrm{d}\varphi} \right|^2 . \tag{3.39}$$

By expanding the complex exponential in a power series and retaining the first three terms, the approximate expression of the Strehl ratio valid for small aberrations is obtained as

$$K = 1 - k^2[\langle W^2 \rangle - \langle W \rangle^2], \tag{3.40}$$

where $\langle W^2 \rangle$ and $\langle W \rangle$ are defined by the formulas

$$\langle W^2 \rangle = \frac{1}{\pi} \int_0^{2\pi} \int_0^1 W^2 \rho_N \mathrm{d}\rho_N \mathrm{d}\varphi, \qquad \langle W \rangle = \frac{1}{\pi} \int_0^{2\pi} \int_0^1 W \rho_N \mathrm{d}\rho_N \mathrm{d}\varphi.$$

When studying an influence of the third-order spherical aberration $W = S\rho_N^4$ in the paraxial image plane, the Strehl ratio (3.40) is then obtained as

$$K = 1 - \frac{4}{45} k^2 S^2. \tag{3.41}$$

The precision in the image reconstruction can be significantly enhanced considering the wave aberration $W' = W + R\rho_N^2$ with the refocusing coefficient R. The optimal focusing is achieved when the Strehl ratio K for the wave aberration W' is calculated as a function of R and the condition $\mathrm{d}K/\mathrm{d}R = 0$ providing its extremum is applied. The Strehl ratio in the optimal image plane then results in

$$K = 1 - k^2[\langle W^2 \rangle - \langle W \rangle^2 - 12\langle W\rho_N^2 \rangle + 12\langle W \rangle \langle \rho_N^2 \rangle .] \tag{3.42}$$

Especially, in case of the spherical aberration $W = S\rho_N^4$ the relation (3.42) reaches the form

$$K = 1 - \frac{1}{180} k^2 S^2. \tag{3.43}$$

As a result of the equations mentioned above, the decrease of Strehl ratio calculated for a spherical aberration is approximately $16\times$ smaller after optimal refocusing (3.43) related to

the paraxial image plane (3.41).

3.5 Correction of the phase background

The enlargement required for observing small specimens can be adjusted, positioning the object related to a pinhole in Gabor holography (3.22). Similarly, in lens-less digital in-line holographic microscopy, the magnification is set by varying the light-source-sample and light-source-camera distances. Still, the range of applicable lateral magnifications is often limited [30, 265]. In microscopic applications, the enlargement is preferably achieved by additional optics, which form the image close to the detector plane. Direct observation of the magnified specimen's image before capturing the interference record is advantageous and allows pre-screening the FOV. However, additional optics may induce other phase-background defects, deteriorating the reconstructed image [63]. Luckily the direct access to the full complex amplitude enables us to compensate for various phase inaccuracies.

Typical phase distortions influencing the holographic performance include a tilt and a parabolic curvature. When the microscope lens with the focal distance f_{MO} creates an enlarged image in the detector plane with the coordinates (x, y), the background-phase curvature induced by the microscope objective can be obtained by analyzing the thin-lens imaging performance in the Fresnel approximation (3.14) as [43, 257]

$$\exp\left\{-ik\frac{x^2+y^2}{2\beta_{MO}f_{MO}}\right\}, \tag{3.44}$$

where β_{MO} is the lateral magnification achieved. Moreover, a tilt introduced in the off-axis geometries or a residual tilt between the interfering waves in in-line holographic configurations appears in the form

$$\exp\left\{-ik(x\sin\alpha_x + y\sin\alpha_y)\right\}, \tag{3.45}$$

where $\alpha_x,\ \alpha_y$ are residual angular inclinations. The phase defects induced can be compensated physically, i.e., directly in the optical setup, or numerically in the post-processing.

3.5.1 Physical compensation methods

Physical compensation methods allow the elimination of the selected phase-background defects directly in the experimental setup, for example, by inserting additional components into the optical path [43]. The wavefront curvature induced by the magnifying microscope lens can be compensated by adding the second microscope objective with identical param-

eters into the reference arm [266]. The background phase is reduced sufficiently, just if the curvatures of both waves are equal. In this case, two identical parabolic waves interfere, creating the straight interference fringes in the detector plane. Indeed, when the interference record of two parabolic waves $U_{P1} \propto \exp\left\{ik\frac{x^2+y^2}{2f_1}\right\}$ and $U_{P2} \propto \exp\left\{ik\frac{x^2+y^2}{2f_2}\right\}$ is recorded, and the valuable holographic term $U_{P1}U_{P2}^*$ is separated, the obtained phase background

$$\arg\{U_{P1}U_{P2}^*\} = k\frac{x^2+y^2}{2}\left(\frac{1}{f_1}-\frac{1}{f_2}\right) \tag{3.46}$$

vanishes just if $f_1 = f_2$. Another possibility for the quadratic phase compensation is to adopt a telecentric imaging system instead of a single microscope objective [267]. The tube lens compensates the quadratic phase induced by the microscope objective as a result of the afocal arrangement. In the case of plane reference wave and precisely calibrated imaging system, two plane waves interfere in the interferometer's output plane, leading to a quadratic-phase-free background.

3.5.2 Numerical compensation methods

Despite the excellent properties of physical compensation methods, some residual phase defects may appear, e.g., due to requirements on the precise adjustment of the optical components, higher-order distortions, or low temporal stability of the interferometer used. Fortunately, the direct access to complex amplitude enables to subtract the irregularities even during the numerical processing.

The curvature compensation achieved by adding the microscope objective referred to in

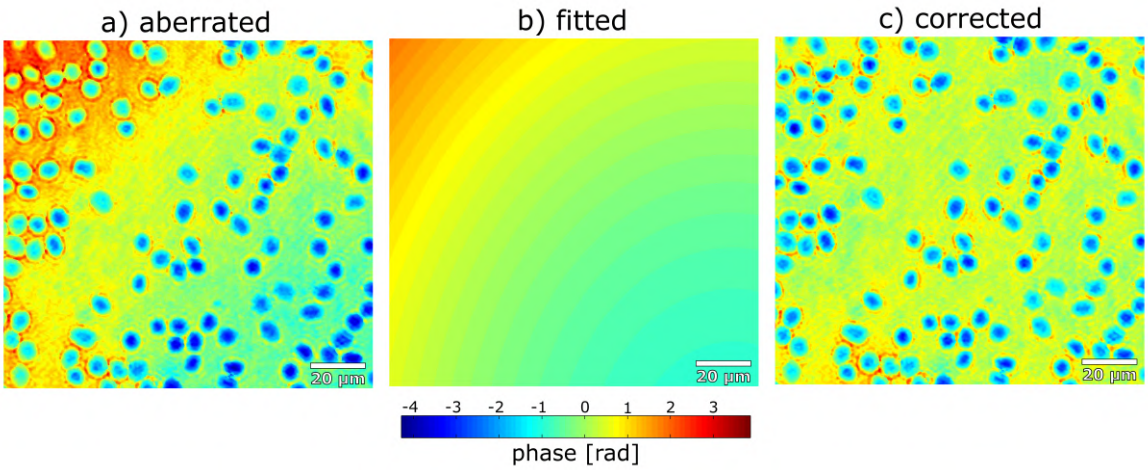

Figure 3.4: Background phase corrected by fitting. (a) Unwrapped quantitative phase image including the specimen superimposed on the slowly varying background phase. (b) Fitted background. (c) Corrected phase map.

the previous text is not often optimal. In typical cases, additional numerical compensation must be used. One possibility is to use the surface fitting approach, where the fitted phase is estimated and subsequently deducted from the original phase map to eliminate the phase deterioration. For instance, the reconstructed phase influenced by a residual tilt and curvature may be fitted by a function $g(x, y) = \kappa_1 x^2 + \kappa_2 y^2 + \kappa_3 x + \kappa_4 y + \kappa_5$, where x, y are cartesian coordinates in the detector plane, and κ_j, $j = \{1, 2, 3, 4, 5\}$ are the coefficients wanted. In the case of compact objects, whose dimensions are much smaller comparing the entire FOV, whose phase varies faster than the background (Fig. 3.4a), it can be assumed that the sample's phase distribution is superimposed on the slowly changing background phase. Hence the total phase map can be fitted to achieve the background-phase compensation [64, 65]. The surface obtained by the fitting (Fig. 3.4b) is then deducted from the initial phase-map leading to the correction of the original phase image (Fig. 3.4c).

3.5.3 Double-exposure method

Various types of phase inhomogeneities without the need of their exact knowledge can be eliminated utilizing the double exposure method [61]. The method is based on processing two interference records, with and without the sample, respectively (Fig. 3.5). The phase image restored from the pattern acquired with the specimen reveals a background-phase degradation, making the quantitative phase assessment of the image difficult (Fig. 3.5b). Hence, the sample is moved out of the field of view to take the reference snapshot (Fig. 3.5c). The phase map restored (Fig. 3.5d) is then subtracted from the original phase image. By this operation, the phase image of the cell is obtained in which the phase background approaches the zero phase level (Fig. 3.5e). Indeed, the approach enables correction of the background phase without requirements on a priori knowledge of the numerical model. However, it neglects image distortions in the recording plane and the influence of aberrations introduced by the specimen. Nevertheless, even partial correction of aberrations introduced by the sample was proposed under specific circumstances by processing the original holographic record [63].

In presence of the specimen the signal and the reference waves U_s and U_r interfere, creating the holographic record (3.1). The signal and the reference waves comprised in the reconstructed term $U_s U_r^*$ are expressed as

$$U_s = A_s \exp[i\Phi_s + i\Phi_{Ws}], \quad U_r = A_r \exp[i\Phi_r + i\Phi_{Wr}], \tag{3.47}$$

where A_s, A_r are amplitudes, Φ_s, Φ_r are desired phases and terms Φ_{Ws}, Φ_{Wr} correspond to the undesired phase defects. Recording the reference holographic pattern without the

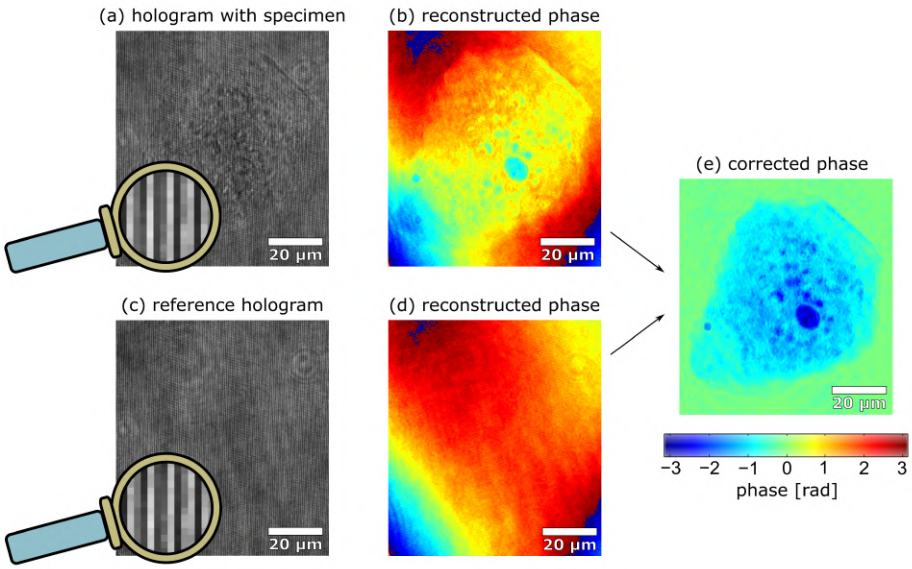

Figure 3.5: Background phase corrected by the double-exposure method exploiting the reference interference record. (a) Interference record including the specimen. (b) Quantitative phase image of the specimen reconstructed from the record. (c) Reference snapshot recorded without the specimen. (d) Quantitative phase map reconstructed from the reference record. (e) Corrected quantitative phase image of the cell.

specimen enables reconstruction of the term $U_{s0}U_{r0}^{*}$, where

$$U_{s0} = A_{s0}\exp[i\Phi_{Ws0}], \quad U_{r0} = A_{r0}\exp[i\Phi_{Wr0}]. \tag{3.48}$$

The numerical correction of the background phase is then obtained as

$$\arg\left\{\frac{U_s U_r^{*}}{U_{s0}U_{r0}^{*}}\right\} = \Phi_s - \Phi_r + [(\Phi_{Ws} - \Phi_{Wr}) - (\Phi_{Ws0} - \Phi_{Wr0})]. \tag{3.49}$$

If the unchanged optical parameters are guaranteed between capturing both snapshots, terms in the square brackets (3.49) disappear, and just the phase difference $\Phi_s - \Phi_r$ is restored.

3.6 Common-path lateral-shearing self-referencing digital holographic microscopy

The signal and the reference waves in the DH configurations with the common-path interferometer pass through a single-arm and share identical optical components. Hence the temporal stability of the system is enhanced by comparing the geometries with two spatially

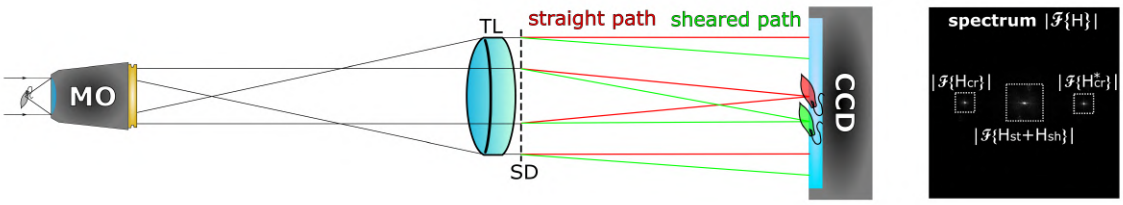

Figure 3.6: Illustration of straight and sheared optical paths in standard microscope supplemented by a shearing device. microscope objective (MO), tube lens (TL), shearing device (SD), camera (CCD). Typical Fourier amplitude spectrum on the right part of the figure.

independent arms. The signal and the reference waves in a common-path lateral-shearing self-referencing DHM, leave a standard microscope arrangement with a microscope objective (MO) and a tube lens (TL). The lateral shear required between the straight and sheared copies of the FOV (Fig. 3.6) is achieved by inserting a proper optical component, called a shearing device (SD), between the TL and detector (CCD). Various types of shearing devices were used to achieve the lateral shear, such as a beam splitter [208], a thick glass plate [218], a Wollaston prism [219], a calcite crystal [220], a Fresnel biprism [222], or gratings [226]. The choice of suitable shearing device depends on the requirements of a particular application. The spatial frequency introduced between the interfering paths advantageously enables a single-shot holographic reconstruction ideal for the real-time experimental observations.

In case of the coherent monochromatic illumination with the wavelength λ and the lateral shear collinear to the x-axis, the off-axis holographic record is described by the modified equation (3.4) as

$$H = |U_s(x) + U_r(x) + [U_s(x - \Delta x) + U_r(x - \Delta x)] \exp(-ik_x x)|^2 , \tag{3.50}$$

where $U_s(x)$, $U_r(x)$, and $U_s(x - \Delta x)$, $U_r(x - \Delta x)$ are the signal and the reference waves passing through the straight and the sheared optical paths, $k_x = k \sin \alpha$, $k = 2\pi/\lambda$, α defines angular inclination of the waves, and Δx indicates a lateral shear at the detector plane. The whole record (3.50) can be rewritten into the form

$$H = H_{st} + H_{sh} + H_{cr} \exp(-ik_x x) + H^*_{cr} \exp(ik_x x), \tag{3.51}$$

where

$$\begin{aligned} H_{st} &= |U_s(x) + U_r(x)|^2, \\ H_{sh} &= |U_s(x - \Delta x) + U_r(x - \Delta x)|^2, \\ H_{cr} &= [U_s(x - \Delta x) + U_r(x - \Delta x)]\,[U_s^*(x) + U_r^*(x)]. \end{aligned}$$

Terms H_{st}, H_{sh} are common holographic interference patterns originating from the straight path and the sheared path, and H_{cr} is a pattern created by interference between the mutually tilted straight and sheared waves. Filtering the H_{cr} in the Fourier domain enables the efficient isolation and reconstruction of the valuable complex amplitude from a single-shot record, in principle. Typical Fourier spectrum, including three spatially separated diffraction orders, is presented on the right part of Fig. 3.6, where the valuable Fourier terms $\mathcal{F}\{H_{cr}\}$ and $\mathcal{F}\{H_{cr}^*\}$ are modulated on the spatial carrier frequencies (3.51).

3.6.1 Double-exposure method in common-path lateral-shearing self-referencing digital holographic microscopy

The enhanced temporal stability of the common-path lateral-shearing holographic system enables the advantageous utilization of the double-exposure method for the background-phase correction. The restored term H_{cr} (3.51) contains four interfering parts. The terms of interest that contain information about the signal wave emanating from the sheared optical path $U_s(x - \Delta x)U_r^*(x)$ and the straight optical path $U_s^*(x)U_r(x - \Delta x)$ are available for numerical processing. The term $U_r(x - \Delta x)U_r^*(x)$ originates from the sheared and straight reference wave and is exploited for eliminating the phase imperfections of the optical path. The term $U_s(x - \Delta x)U_s^*(x)$ created by the sheared and straight signal waves can be neglected because the signal waves do not spatially overlap in the observed field of view in real experiments. To demonstrate a phase reconstruction from the holographic records the complex amplitude of the signal and reference waves is expressed as,

$$U_s(x) = A_s(x)\exp[i\Phi_s(x) + i\Phi_{Ws}(x)], \tag{3.52}$$

$$U_r(x) = A_r(x)\exp[i\Phi_r(x) + i\Phi_{Wr}(x)], \tag{3.53}$$

where $A_s(x)$, $A_r(x)$, and $\Phi_s(x)$, $\Phi_r(x)$ denote amplitudes, and phases of the signal and the reference waves, and $\Phi_{Ws}(x)$, $\Phi_{Wr}(x)$ are phase defects modulated on the signal and reference waves at the output of the optical arrangement. Using well-separated holographic terms the signal wave originating from the sheared and the straight optical path is recon-

structed while eliminating the systematic phase defects,

$$\Delta\Phi_{sh}(x-\Delta x) = \arg\left\{\frac{U_s(x-\Delta x)U_r^*(x)}{U_r(x-\Delta x)U_r^*(x)}\right\}, \tag{3.54}$$

$$\Delta\Phi_{st}(x) = \arg\left\{\frac{U_s^*(x)U_r(x-\Delta x)}{U_r^*(x)U_r(x-\Delta x)}\right\}. \tag{3.55}$$

The final phase retrieved from (3.54) and (3.55) is expressed as

$$\Delta\Phi_{sh}(x-\Delta x) = \Delta\Phi(x-\Delta x) + \Delta\Phi_{Wsr}(x-\Delta x), \tag{3.56}$$

$$\Delta\Phi_{st}(x) = -\Delta\Phi(x) - \Delta\Phi_{Wsr}(x), \tag{3.57}$$

with $\Delta\Phi(x) = \Phi_s(x) - \Phi_r(x)$ and $\Delta\Phi_{Wsr}(x) = \Phi_{Ws}(x) - \Phi_{Wr}(x)$. Experimentally, when the double-exposure method is applied, the term $U_r(x-\Delta x)U_r^*(x)$ used for the background-phase correction is obtained from a reference record taken without the sample. The terms in the numerator and the denominator of (3.54) and (3.55) thus origin from the snapshots captured with and without the sample, respectively. To effectively correct the phase background, the two records must be captured while maintaining the experimental conditions except for the presence of the sample. In such the case, $\Delta\Phi_{Wsr}(x) = \Delta\Phi_{Wsr}(x-\Delta x) = 0$ and the terms $\Delta\Phi(x-\Delta x)$ and $\Delta\Phi(x)$ are restored, respectively.

3.7 Red blood cells as biolenses

One of the topics presented in this Thesis exploits the focusing properties of RBCs. This biolensing effect was discovered and firstly demonstrated in [196], where RBCs were treated as transparent phase objects with corresponding magnification and focal length. The attribute mentioned corresponds to the fingerprint, which enables to discriminate various morphological types of the RBCs. For example, healthy RBCs surrounded by an environ-

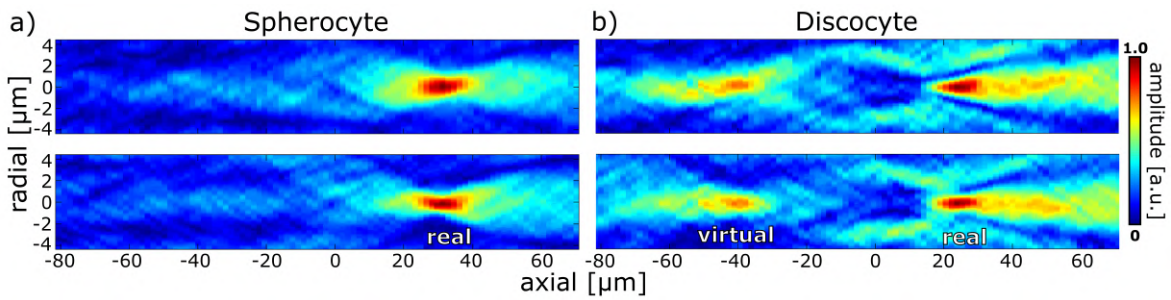

Figure 3.7: Absolute value of complex amplitude. Cross-sections through mutually orthogonal planes including the optical axis in case of a) Spherocyte, b) Discocyte.

ment with a hypotonic osmolarity change the shape fluently from disc-like RBCs (Discocytes) to spherical-like RBCs (Spherocytes). Amplitude cross-sections through two mutually orthogonal planes, including the optical axis, in the case of such RBCs whose interference patterns were measured experimentally, and the amplitudes were calculated numerically (3.7), are illustrated in the Fig. 3.7. Spherocytes include just one real focal point (Fig. 3.7a), while Discocytes produce both the real and the virtual focal spots (Fig. 3.7b) due to a convex-concave profile of the cells. The transparency and presence of focal spots can be advantageously utilized for localization or tracking the cells [45].

Various objects can be successfully localized, exploiting the contrast properties. The contrast is a measure characterizing the distribution of the bright and dark values in the image I. It can be evaluated in the meaning of the Tamura-coefficient approximation [53] defined as

$$TC = \sqrt{\frac{\sigma_I}{\langle I \rangle}}, \tag{3.58}$$

where $\langle I \rangle$ and σ_I are the mean value and standard deviation of the distribution evaluated, respectively.

Absorbing objects often maximize the contrast, while transparent phase-like structures minimize the contrast in the sample's plane. The situation is illustrated in Fig. 3.8 where the TC is calculated for three different samples (line target, Spherocytes, and Discocytes) using distributions of absolute values of complex amplitude obtained by the numerical propagation (3.7). In the case of line target, the position with the highest contrast corresponds to

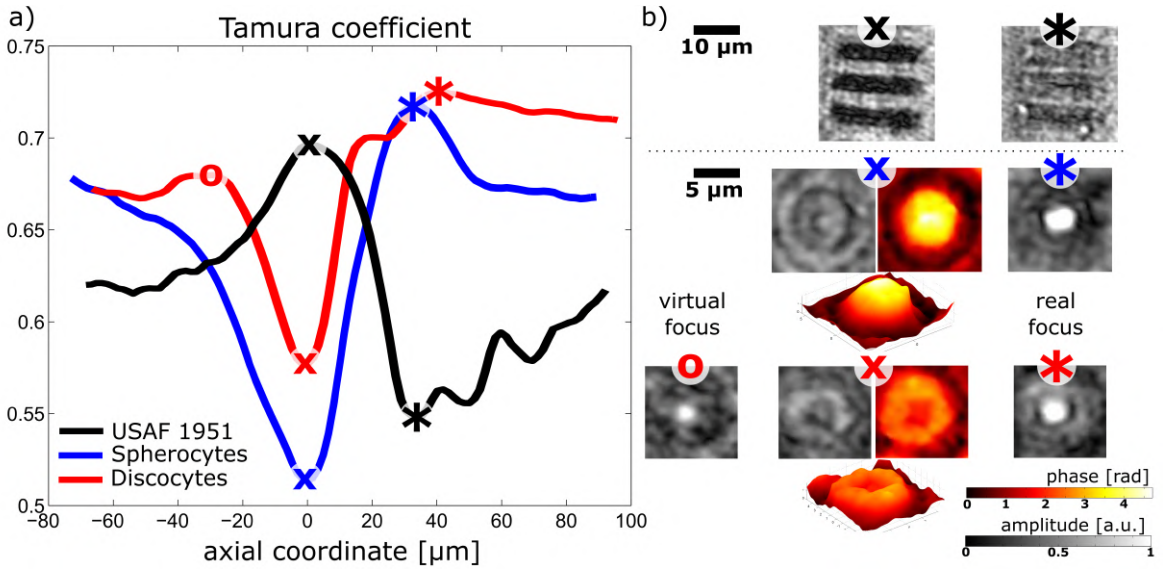

Figure 3.8: Tamura coefficient calculated for resolution line target and ∼10 Spherocytes and ∼10 Discocytes. Corresponding examples of selected amplitude images for line target USAF 1951, spherocytes and discocytes.

a sharp image of the lines, while strong blurring is obtained in the location of the lowest contrast (black line and symbols). The lowest value of the TC in the case of cells corresponds to the plane where the cells are seeded (blue and red lines). In addition, the contrast phase profile is obtained in this plane (Fig. 3.8). The TC-profile of Spherocytes includes one distinct maximum, which corresponds to the real focal point of the Spherocytes (blue line and blue symbols). The two focal planes of Discocytes are also distinguishable in the profile of TC (red line and red symbols). The properties mentioned are successfully implemented for localization or tracking the objects [45].

3.8 Intensity-based writing into the photorefractive materials

Charge transport models of the photorefractive (PR) crystals achieved substantial attention in the literature [169, 171, 172]. Although the PR effect was discovered in 1966 [268], the interaction of PR materials with various light fields still achieve significant attention from both theoretical and experimental point of view, respectively [176, 183, 269]. PR effect can be understood as a light-induced change of the refractive index distribution. Electrons released by ionized donors are transported and retrapped by acceptors in a different place. A charge redistribution between the illuminated and dark areas is build up as a consequence. Subsequently, the generated internal electric field changes the refractive index distribution via the electrooptic effect. The PR effect is theoretically described by Kukhtarev–Vinetskii formulation [270,271] from which it is possible to derive the generated steady-state intrinsic electric-intensity field E_{sc}. The closed-form formula of the E_{sc} for circularly symmetric beams ($I = I(r)$), which are of significant application importance in optics, reaches the form [272]

$$E_{sc}(r,\varphi) = E_0\sqrt{\frac{1+I_\infty}{1+I}}\{2\cos^2\varphi - \cos 2\varphi\sqrt{\frac{1+I}{1+I_\infty}} - \\ - \frac{2}{r^2}\left(\cos 2\varphi + r\cos^2\varphi\frac{\mathrm{d}\ln\sqrt{1+I}}{\mathrm{d}r}\right)\int_0^r \rho\left(1-\sqrt{\frac{1+I(\rho)}{1+I_\infty}}\right)\mathrm{d}\rho\}, \tag{3.59}$$

where (r,φ) are polar coordinates, E_0 is the transverse dc internal field in the crystal, I is intensity profile of the illumination beam, and I_∞ is an intensity value if $r \to \infty$, $I_\infty = \lim_{r\to\infty} I(r)$. The equation (3.59) reaches a scalar form because the released electric charges tend to migrate along the crystal axis ($c-$axis), which is assumed to be parallel to $z-$coordinate. As an example, the intensity of the bright Gaussian beam of width w ex-

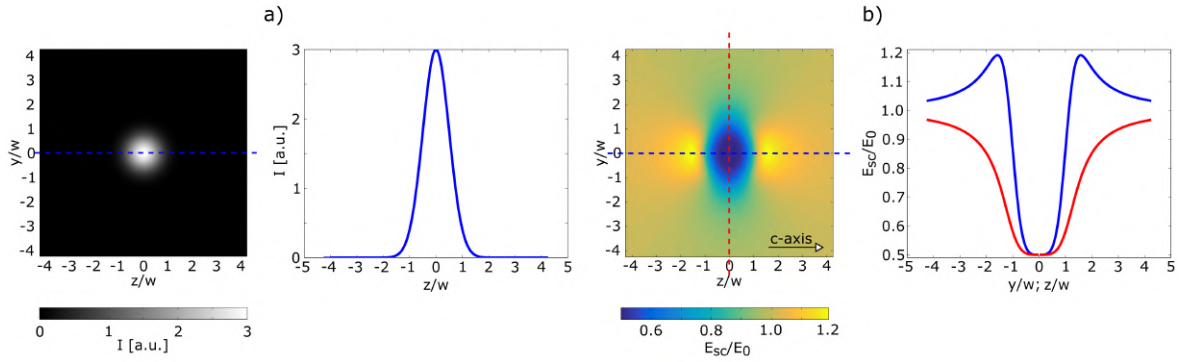

Figure 3.9: a) Intensity profile of the illuminating Gaussian beam. b) Intrinsic electric field induced in photorefractive crystal (3.59). Simulations are made for $I = I_\infty + I_0 \exp\{-2r^2/w^2\}$, $I_\infty = 0$ W m^{-2}, $I_0 = 3$ W m^{-2}, $E_0 = 1$ V m^{-1}, $w = 30$ μm.

pressed in the form $I = I_\infty + I_0 \exp\{-2r^2/w^2\}$ is assumed (Fig. 3.9a). The induced intrinsic electric field E_{sc} predicted by the equation (3.59) is illustrated in Fig. 3.9b. The results are obtained for equal parameters, as in [272], specified in the caption of the figure. A radially symmetric beam induces a radially asymmetric electric field E_{sc}, which is effectively generated for illumination beams polarized parallel to the $c-$axis (extraordinary waves). On the other hand, orthogonally polarized illumination beams (ordinary waves) do not effectively modify the intrinsic electric field.

The final refractive-index change measured by the ordinary polarized wave, for example, is finally calculated according to the equation for linear electrooptic effect as [169]

$$\Delta n_o = -0.5 n_o^3 r_{13} E_{sc}, \tag{3.60}$$

where n_o is the ordinary refractive index, and r_{13} is the corresponding electrooptic coefficient.

3.9 Direct Jones matrix reconstruction in digital holography

Polarization is an elementary property of the electromagnetic field describing its vectorial character. The spatio-temporal orientation of the electric vector evaluated in the plane perpendicular to the propagation direction (propagation along z-axis), is in the case of the plane wave characterized by the polarization ellipse given as [273]

$$\left(\frac{\mathrm{Re}\{U_x\}}{A_x}\right)^2 + \left(\frac{\mathrm{Re}\{U_y\}}{A_y}\right)^2 - 2\frac{\mathrm{Re}\{U_x\}\,\mathrm{Re}\{U_y\}}{A_x A_y}\cos(\Phi_y - \Phi_x) = \sin^2(\Phi_y - \Phi_x), \tag{3.61}$$

where $\mathrm{Re}\{...\}$ is a real part, A_x, A_y are amplitudes, and Φ_x, Φ_y are phases of the transversal scalar complex amplitudes U_x, U_y. In special cases, the elliptical polarization degenerates to the linear polarization ($\Phi_y - \Phi_x = m\pi$, where m is an integer) or the circular polarization ($A_x = A_y$, $\Phi_y - \Phi_x = 2(m+1)\pi/2$, where m is an integer). When the m is odd, the circular polarization is left-hand, and when m is even or zero, the polarization is considered as right-handed, respectively. The polarization ellipse is characterized by the two angles representing the principal axis orientation ($\in [-\pi/2, \pi/2]$) and the ellipticity ($\in [-\pi/4, \pi/4]$), which is given by the arctangent of the minor/major axis ratio.

The polarized light is advantageously characterized by the Jones matrix formalism developed in the 1940s [274]. Jones vector of the optical beam propagated along the z-axis is written as

$$\mathbf{U} = \begin{bmatrix} U_x \\ U_y \end{bmatrix} = \begin{bmatrix} A_x \exp(i\Phi_x) \\ A_y \exp(i\Phi_y) \end{bmatrix}. \tag{3.62}$$

The Jones matrix of an arbitrary object transforming the polarization state is defined as

$$\mathbb{T} = \begin{bmatrix} T_{xx} & T_{xy} \\ T_{yx} & T_{yy} \end{bmatrix}, \tag{3.63}$$

where $T_{xx}, T_{xy}, T_{yx}, T_{yy}$ are complex elements in general. Elements of the matrix can be obtained directly from the measurement provided by the two orthogonal polarization states of the illuminating light. For example, when the measurement is sequentially performed by the diagonal ($\mathbf{U^d}$) and antidiagonal ($\mathbf{U^a}$) illumination, given as

$$\mathbf{U^d} = \frac{1}{\sqrt{2}} \begin{bmatrix} 1 \\ 1 \end{bmatrix}, \quad \mathbf{U^a} = \frac{1}{\sqrt{2}} \begin{bmatrix} 1 \\ -1 \end{bmatrix}, \tag{3.64}$$

and the corresponding output polarization states

$$\overline{\mathbf{U}}^{\mathbf{d}} = \mathbb{T}\mathbf{U^d}, \quad \overline{\mathbf{U}}^{\mathbf{a}} = \mathbb{T}\mathbf{U^a} \tag{3.65}$$

are measured, the required elements of the Jones matrix $\mathbb{T}$ are recovered as

$$\mathbb{T} = \begin{bmatrix} T_{xx} & T_{xy} \\ T_{yx} & T_{yy} \end{bmatrix} = \frac{1}{\sqrt{2}} \begin{bmatrix} \overline{U}_x^d + \overline{U}_x^a & \overline{U}_x^d - \overline{U}_x^a \\ \overline{U}_y^d + \overline{U}_y^a & \overline{U}_y^d - \overline{U}_y^a \end{bmatrix}. \tag{3.66}$$

Till now, the exploitation of the DH was considered working for the scalar waves. However, each of the components in equation (3.62) can be mixed with the mutually coherent equally polarized beam generating the scalar interference field. The polarization imaging is consequently possible by measuring the phase differences for multiple polarization modes.

Especially, the horizontally $\overline{\mathbf{U}}_{\mathbf{r1}}$ and vertically polarized reference waves $\overline{\mathbf{U}}_{\mathbf{r2}}$ are considered, which are simultaneously mixed with the arbitrarily polarized signal wave $\overline{\mathbf{U}}_{\mathbf{s}}$, given as

$$\overline{\mathbf{U}}_{\mathbf{r1}} = \begin{bmatrix} \overline{U}_{r1,x} \\ 0 \end{bmatrix}, \quad \overline{\mathbf{U}}_{\mathbf{r2}} = \begin{bmatrix} 0 \\ \overline{U}_{r2,y} \end{bmatrix}, \quad \overline{\mathbf{U}}_{\mathbf{s}} = \begin{bmatrix} \overline{U}_{s,x} \\ \overline{U}_{s,y} \end{bmatrix}. \tag{3.67}$$

In this case, two interference fields are created and summarized incoherently. When significant spatial frequencies are introduced between the interfering waves, the correct single-shot reconstruction is feasible, providing the complex amplitudes $\overline{U}_{s,x}\overline{U}^{*}_{r1,x}$, and $\overline{U}_{s,y}\overline{U}^{*}_{r2,y}$. For the known parameters of the reference waves, even the complex amplitudes $\overline{U}_{s,x}$ and $\overline{U}_{s,y}$ are additionally obtained, and the polarization-state distribution is recovered. Reconstruction of the Jones matrix is possible when the sample is illuminated by orthogonally polarized waves. When diagonally and antidiagonally polarized illumination beams are used, the output Jones vectors $\overline{\mathbf{U}}^{\mathbf{d}}_{\mathbf{s}}$ and $\overline{\mathbf{U}}^{\mathbf{a}}_{\mathbf{s}}$ are reconstructed, and the Jones matrix, determined by equation (3.66), is recovered.

Chapter 4

Optimizing three-dimensional point spread function in lens-less digital holographic microscopy

This chapter is based on the following publication:

[1] J. Běhal and Z. Bouchal, "Optimizing three-dimensional point spread function in lensless holographic microscopy," *Optics Express*, vol. 25, pp. 29026–29042, 2017.

In this chapter, the main interest is paid to analyze experimentally the deterioration of the 3D PSF, whose intensity maximum is displaced axially out of the paraxial image plane. This unwanted effect is studied as a consequence of the diffraction or holographic aberrations in the performance of a magnified lens-less phase-shifting DH where the magnification is obtained due to the mismatch between the reference and the reconstruction waves. The range of experimental parameters and magnifications that trade-off the influence of both effects are predicted theoretically and verified experimentally as the main result.

4.1 Optical performance of Gabor digital holography

The diffraction-limited point image is reconstructed when the conditions for the paraxial approximation are fulfilled. In the case of the circular aperture, the radius of the Airy disc (3.25) is given as $AD_i = 0.61\lambda/NA_i$ where $NA_i = \rho_h/|z_{i0}|$. When considering the pinhole and a source of the reconstruction wave placed on the optical axis ($x_{j0} = y_{j0} = 0$, for $j = \{r, c\}$), the lateral resolution in the object space is obtained using the lateral magnification β (3.22), $AD_s = AD_i/|\beta|$. Hence AD_s is inversely proportional to $NA_i|\beta| = \rho_h/(z_{r0} - \Delta)$, which is independent of z_{c0}. The theoretical lateral resolution in the object space thus remains unchanged when the different reconstruction waves are used. If the point interference record is bounded by the light area arising from the illumination of the reference wave, the radius ρ_h is given by the radius of pinhole ρ_p as $\rho_h = 0.61\lambda|z_{r0}|/\rho_p$.

The resolution in the object space is expressed in the form

$$AD_s = \rho_p \left(1 - \frac{\Delta}{|z_{r0}|}\right), \tag{4.1}$$

where $\Delta > 0$ in the investigated in-line holographic geometry. On the other hand, the Fresnel number of the image space depends on the basic experimental parameters but also changes with the reconstruction geometry. For limiting cases of the reconstruction, it can be written as

$$N_i = \frac{0.61^2 \lambda \kappa}{\rho_p A D_s}, \tag{4.2}$$

where $\kappa = |z_{r0}|$ for the reconstruction wave exactly matched to the reference wave ($z_{c0} = z_{r0}$), while $\kappa = \Delta$ for the plane wave reconstruction ($z_{c0} \to -\infty$). In experiments, $|z_{r0}| \gg \Delta$ and the high N_i is reached with common geometrical parameters when reconstructing with $z_{c0} = z_{r0}$, guaranteeing symmetrical profile of the axial PSF. Additionally, the diffraction-limited image is obtained despite the reconstruction provide the unitary lateral magnification $\beta = 1$. If the zooming is achieved by the mismatch between the parameters of the reconstruction and reference waves ($z_{c0} \neq z_{r0}$), the axial asymmetry of the PSF and holographic aberrations appear even when the ideal spherical waves are considered.

The reconstruction wave originating from a virtual source placed at the distances $z_{c0} \in (-\infty, z_{r0})$ from the recording plane is examined to obtain the magnified image. The largest lateral magnification is for the established experimental parameters Δ and z_{r0} achieved for a plane wave reconstruction ($z_{c0} \to -\infty$). Axial symmetry of the PSF and the object space resolution are enhanced when increasing the pinhole-sample distance Δ [relations (4.1) and (4.2)]. However demands on the correct sampling provided by the detector increase strongly. Considering the Nyquist-Shannon sampling theorem for the reconstruction using $z_{c0} \to -\infty$, the largest specimen to pinhole distance Δ permissible for the pixel size p_{CCD} is determined by the condition

$$\Delta \leq \frac{|z_{r0}| A D_s}{1.22 p_{CCD}}. \tag{4.3}$$

Both the holographic aberrations and diffraction effects leading to the axially asymmetric profile of PSF must be included in the analysis to investigate how the real imaging meets the theoretically predicted object space resolution limit (4.1)

4.1.1 Influence of holographic spherical aberration

The PSF deterioration due to the spherical aberration is taken into account to optimize the discussed holographic performance. The off-axis aberrations are then assessed to determine

the acceptable field of view. If the spherical aberration is evaluated in the paraxial image plane ($z_i = z_{i0}$), the coefficient S (3.38) in a case of the plane wave reconstruction ($z_{c0} \to -\infty$) can be written as

$$S = \frac{3}{8}\frac{\rho_h^4}{z_{s0}z_{r0}z_{i0}} = -\frac{3}{8}\frac{\rho_h^4\Delta}{z_{r0}^2(z_{r0}+\Delta)^2}\,. \tag{4.4}$$

The higher values of Δ improve the theoretical lateral resolution (4.1) and ensure symmetry of the axial PSF, but, unfortunately, since Δ is positive and z_{r0} negative, the degradation due to spherical aberration increases significantly with larger Δ as is seen in (4.4). To examine the influence of the spherical aberration, the Strehl ratio approximation is further adopted. The range of Strehl ratio $K \geq 0.8$ in the optimal image plane (3.43) is used to ensure the high imaging quality, resulting in the requirement of a weak holographic spherical aberration limited by $|S| \leq 6/k$. To achieve the desired values of K in the optimal image plane, the condition for the combination of basic experimental parameters can be obtained using (4.4) as

$$z_{r0}^2\Delta\left(1+\frac{z_{r0}}{\Delta}\right)^2 \geq \frac{2\rho_h^4}{5\lambda}. \tag{4.5}$$

If the radius of the point interference record is determined by the light spot created by the reference wave diffracted on the pinhole with the radius ρ_p, the combination of the parameters ensuring the imaging with $K \geq 0.8$ is rewritten as

$$\frac{\Delta}{z_{r0}^2}\left(1+\frac{z_{r0}}{\Delta}\right)^2 \geq \frac{\lambda^3}{18\rho_p^4}. \tag{4.6}$$

The specified experimental parameters λ, z_{r0}, ρ_p, or ρ_h hence enable to derive by employing the inequalities (4.5) and (4.6) the applicable range of values, which ensures the reconstructed image is not deteriorated by the spherical aberration at an optimal image plane.

4.2 Simulations

Before the measurement was realized, the aberration deterioration and axial asymmetry of the PSF was evaluated depending on the experimental parameters by adopting the criteria imposed. In all demonstrated results, the monochromatic plane wave ($\lambda = 633$ nm) was considered as a reconstruction wave. The pinhole-detector distance $z_{r0} = -43.5$ mm, the pinhole radius $\rho_p = 2.75$ µm, and the camera's pixel size $p_{CCD} = 7.4$ µm are used in the simulations. The dependence of the Strehl ratio K on Δ evaluated in the optimal plane (3.43) is plotted in Fig. 4.1 (black line), together with the diffraction-limited resolution (4.1) in the object space AD_s (green line), the resolution limit obtained by sampling conditions (4.3)

(thin black line), the coefficient of asymmetry Q_s (red line) and the coefficient of spherical aberration S (3.38) (blue line). The asymmetry coefficient in the object space Q_s is calculated precisely by applying the variable longitudinal magnification to transform the required distances from the image to the object space. The range of the pinhole-sample distance $\Delta \in [0, 10\ \mathrm{mm}]$ is limited by the sampling condition determined for CCD QImaging Retiga 4000R. For the highest value of Δ, the best theoretical lateral resolution $AD_s \approx 3.3\lambda$ is obtained. Lateral resolution AD_s improves linearly with increasing Δ. The asymmetry and aberration coefficients Q_s and S exhibit mutually opposite changes. For small values of Δ, the coefficient Q_s rapidly decreases, indicating a strong asymmetry of the axial PSF. In contrast, spherical aberration coefficient S is low, so the Strehl ratio K is almost unity. The situation is just the opposite when Δ is large. The axial symmetry of the PSF with the coefficient $Q_s \approx 1$ is achieved. At the same time, the spherical aberration increases, and the Strehl ratio drops sharply. Axial symmetry of the PSF and nearly aberration-free imaging are guaranteed if both the asymmetry coefficient and the Strehl ratio are close

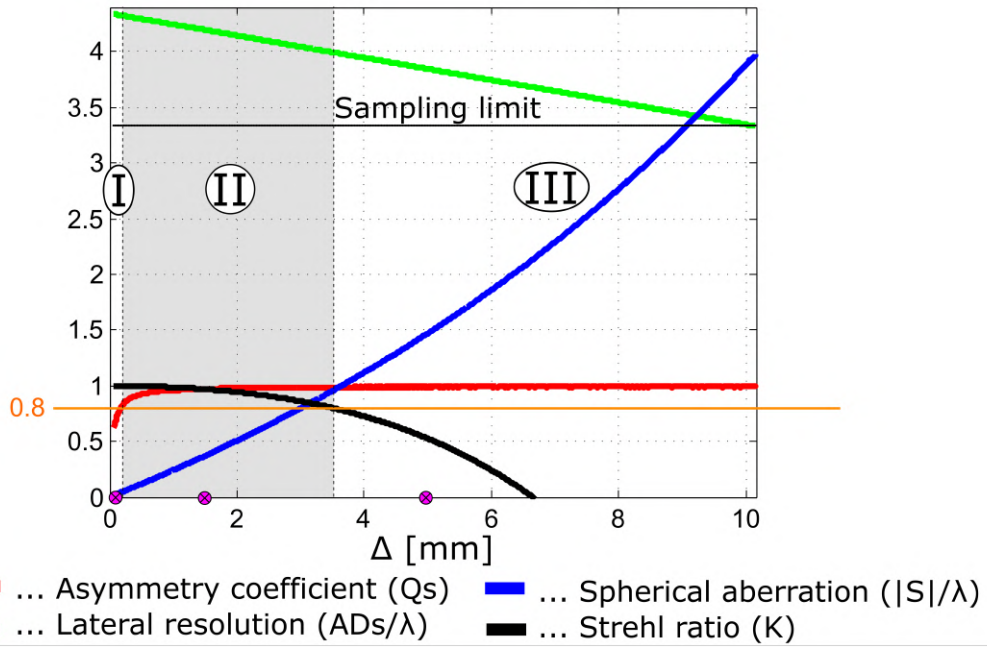

Figure 4.1: Dependence of the indicators of imaging performance on the pinhole to object distance Δ (evaluation performed for $z_{r0} = -43.5$ mm and $\rho_p = 2.75$ µm): object space diffraction-limited lateral resolution in multiples of λ, AD_s (green line), resolution limit in multiples of λ given by sampling conditions for CCD QImaging Retiga 4000R (thin black line), asymmetry coefficient, Q_s (red line), Strehl ratio for optimal image plane, K (black line) and coefficient of spherical aberration in multiples of λ, S (blue line). Ranges of parameters: I-axially asymmetric PSF, II-symmetric nearly diffraction-limited PSF ($Q_s \geq 0.8$, $K \geq 0.8$), III-strong spherical aberration.

to unity. With the conditions $Q_s \geq 0.8$ and $K \geq 0.8$, the range of applicable positions Δ can be determined for the fixed parameters z_{r0} and ρ_p defining three different areas in Fig. 4.1 marked as I, II, and III. Area I represents the parameters resulting in diffraction-limited imaging with the axial asymmetry of the PSF. Area II determines almost aberration-free performance with nearly symmetrical 3D PSF. Area III indicates imaging significantly deteriorated by the spherical aberration. The optimal area II is defined by the limit values of the sample to pinhole distance $\Delta = 0.17$ mm and $\Delta = 3.5$ mm and corresponding lateral magnifications $\beta = 257$ and $\beta = 12.5$, respectively. The experiments carried out with the parameters belonging to the individual areas of Fig. 4.1 (marked by violet points) provide results that closely match the theoretical predictions.

4.3 Experimental setup

The experimental arrangement implemented to demonstrate the imaging performance is illustrated in Fig. 4.2. The light beam emanated from the unpolarized helium-neon (He-Ne) laser (10 mW, $\lambda = 633$ nm) is spatially filtered by the single-mode fiber (Thorlabs P1-630A-FC-2, mode field diameter 3.6-5.3 mm) and collimated by the lens L_1 (achromatic doublet Thorlabs AC254-150-A, diameter 25.4 mm, focal length 150 mm). The beam generated passes through a linear polarizer (LP), a half-wave plate (HWP), and a beam splitter (BS) towards the reflective spatial light modulator (SLM, Hamamatsu X10468, 800×600, pixel size 20 µm). Two different phase masks are simultaneously displayed on the SLM, providing the converging and diverging lenses through a random pixel selection [254, 255], e.g., of the focal lengths $\pm f_m$. Moreover, three different constant phase shifts θ_j are sequentially added to the phase creating the converging lens for purposes of the phase-shifting (3.3), so the phase functions t_j are given as

$$t_j = \exp\left\{-\frac{ik\rho_m^2}{2f_m} + i\theta_j\right\} + \exp\left\{\frac{ik\rho_m^2}{2f_m}\right\}, \quad j = \{1, 2, 3\}, \tag{4.7}$$

where ρ_m is the radial polar coordinate at the SLM plane and $\theta_1 = 0$, $\theta_2 = 2\pi/3$, and $\theta_3 = 4\pi/3$. Consequently, the SLM enables splitting the input collimated beam into two slightly convergent/divergent waves, which are further transformed by a lens L_2 of the focal length f_d. Since the focal lengths $f_m \gg f_d$ are used, two focal points F_{r0} and F_{s0} are formed behind the lens L_2, whose mutual distance Δf is approximately determined as $\Delta f = 2f_d^2/f_m$. When implementing the lens L_2 with the focal distance $f_d = 38.1$ mm (achromatic doublet Edmund # $49-775$, diameter 12.7 mm), the separation of the focal points Δf may be varied in the range $1-10$ mm when the focal lengths of the converging/diverging lenses created on

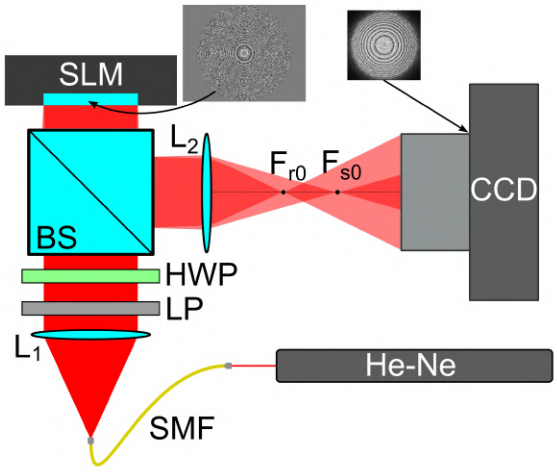

Figure 4.2: In-line holographic setup used for reconstruction of the 3D PSFs and image of the resolution target in testing an optimal design of geometric parameters: SMF...single-mode fiber, collimating lens (L_1), beam splitter (BS), linear polarizer (LP), half-wave plate (HWP), spatial light modulator (SLM) creating converging/diverging lenses with varying focal lengths, imaging lens (L_2).

the SLM are changed from ± 2900 mm to ± 290 mm. The focal points F_{r0} and F_{s0} represent sources of reference and signal waves that interfere and form a point interference record captured by a CCD (QImaging Retiga 4000R, 2048×2048 pixels, chip size 15×15 mm^2). The spacing of the focal points then corresponds to the distance between the pinhole and the sample, $\Delta \leftrightarrow \Delta f$. To ensure the experimental conditions are closely related to the lens-less digital in-line holography, almost perfect reference and signal waves must emerge from the focal points F_{r0} and F_{s0}. This requirement was achieved by the optimized design of the optical system carried out using Oslo Premium software. With the optical components used, the diffraction-limited light spots with a diameter of about 5 µm were obtained at the focal points F_{r0} and F_{s0}. For the apertures used, the optical system worked as aberration-free. The geometric image of the fiber created with the magnification determined by the lenses L_1 and L_2 was almost three times smaller than the diffraction spot. During the measurements, the SLM flexibility was advantageously utilized for positioning the spots F_{s0} and F_{r0} and achieving the mechanical free phase-shifting of the interfering waves (3.4). By recording and processing three mutually phase-shifted interference patterns, a complex holographic term corresponding to the virtual image was obtained (3.3), and the 3D PSF reconstructed numerically. When restoring the image of the resolution target, only one convergent lens was displayed on the SLM that created the reference wave in combination with the lens L_2. The signal wave was hence created by diffraction of the reference wave on the resolution target.

4.4 Results

The experimental results are shown in Fig. 4.3, Fig. 4.4, Fig. 4.5. The positions of spots F_{s0}, F_{r0} (Fig. 4.3) determine the parameters corresponding to the Gabor holographic geometry, including the pinhole-camera distance z_{r0}, the pinhole-sample distance Δ, and the pinhole radius ρ_p (Fig. 4.1). In all three cases, the same position of the reference spot $z_{r0} = -43.5$ mm was used, and the plane wave reconstruction of the PSF was done using the point interference records with the same radius $\rho_h = 6.1$ mm. In the individual cases, the distance Δ corresponds to $\Delta = 0.1$ mm, 1.5 mm, and 4.9 mm, respectively. The settings considered provide nearly identical theoretical lateral resolutions in the object space $AD_s = 2.7$ µm, 2.65 µm, and 2.4 µm. When considering the paraxial Debye approximation, the obtained PSFs are symmetrical of the analytical form given by (3.32). The half-widths of the longitudinal spots determined by the first zero points of the sinc function transformed into the object space by utilizing the axial magnification (3.23) are comparable in all three cases as $\Delta z^{+}_{sD} = \Delta z^{+}_{iD}/\gamma = 64$ µm, 60 µm, and 56 µm, respectively, where Δz^{+}_{iD} is given by (3.33). Although the demonstrated image reconstructions provide nearly the same theoretical values of the lateral and the longitudinal resolutions in the paraxial Debye approximation, significant differences are found when the 3D PSFs are experimentally implemented and correctly evaluated. The 3D PSFs are shown in Fig. 4.3, Fig. 4.4, Fig. 4.5 and can be assigned, according to the effects influencing their shape, to the areas I, II, III in Fig. 4.1.

The PSF in Fig. 4.3 belongs to area I in Fig. 4.1. It was obtained by processing the records acquired with parameters $\rho_h = 6.1$ mm, $z_{r0} = -43.5$ mm, and $\Delta = 0.1$ mm (left violet dot in Fig. 4.1). Here, the paraxial lateral and longitudinal resolutions $AD_s = 2.7$ µm and $\Delta z^{+}_{sD} = 64$ µm were obtained by combining a low numerical aperture in the image space ($NA_i = 0.0003$) with extremely large lateral and longitudinal magnifications ($\beta = 435$, $\gamma = \beta^2$). The influence of holographic aberrations is negligible due to the low value of NA_i. On the other hand, a low value of the Fresnel number ($N_i = 3.1$) indicates a significant influence of diffraction effects, causing an asymmetry of the axial PSF. The asymmetric axial PSF (blue line) was reconstructed from experimentally acquired interference records by the direct implementation of (3.5). The numerical simulations were performed to confirm the accordance of experimental results, including the recording with parameters of the real experiment and the reconstruction. The results obtained in the precise nonparaxial approach are illustrated by a red line while the use of the paraxial approximation corresponds to a black dashed line.

The PSF in Fig. 4.4 belongs to area II in Fig. 4.1. It was obtained by reconstructing the records acquired with optimally selected parameters $\rho_h = 6.1$ mm, $z_{r0} = -43.5$ mm, and

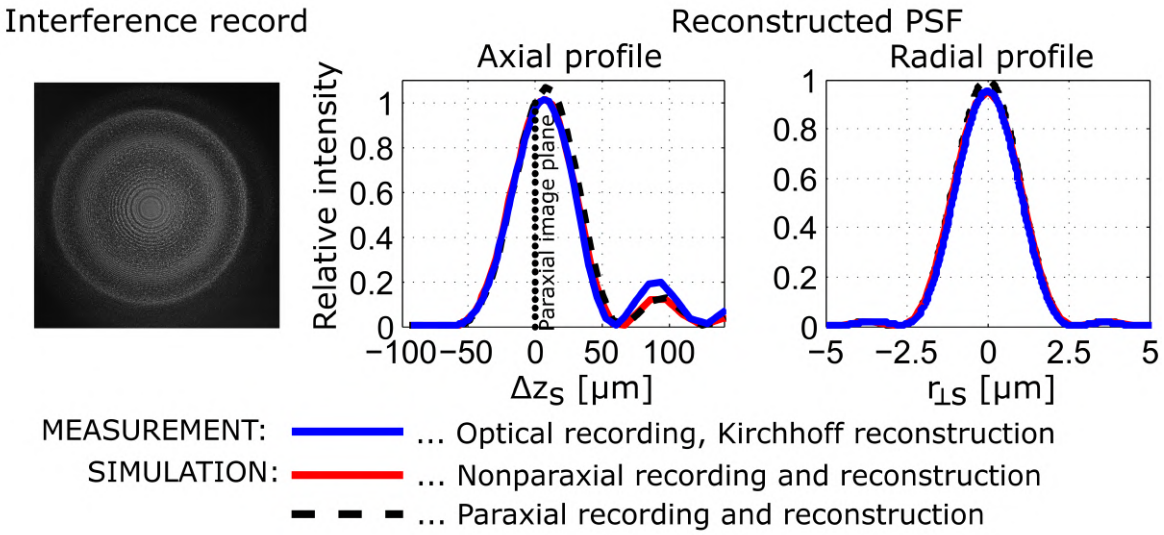

Figure 4.3: Diffraction-limited axially asymmetric PSF reconstructed by the plane wave from three phase-shifted point interference records taken with the geometric parameters belonging to the area I in Fig. 4.1 ($\rho_h = 6.1$ mm; $z_{r0} = -43.5$ mm; $\Delta = 0.1$ mm). The axial and radial PSF profiles obtained from experimental data were transformed into the object space and compared with numerical simulations of the pattern recording and reconstruction.

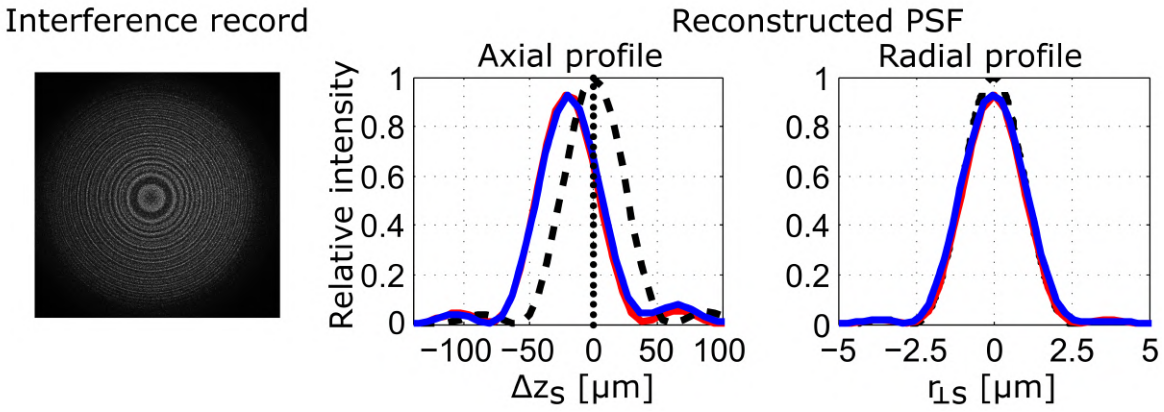

Figure 4.4: Symmetric low-aberration PSF reconstructed by the plane wave from three phase-shifted point interference records taken with the geometric parameters belonging to the area II in Fig. 4.1 ($\rho_h = 6.1$ mm; $z_{r0} = -43.5$ mm; $\Delta = 1.5$ mm).

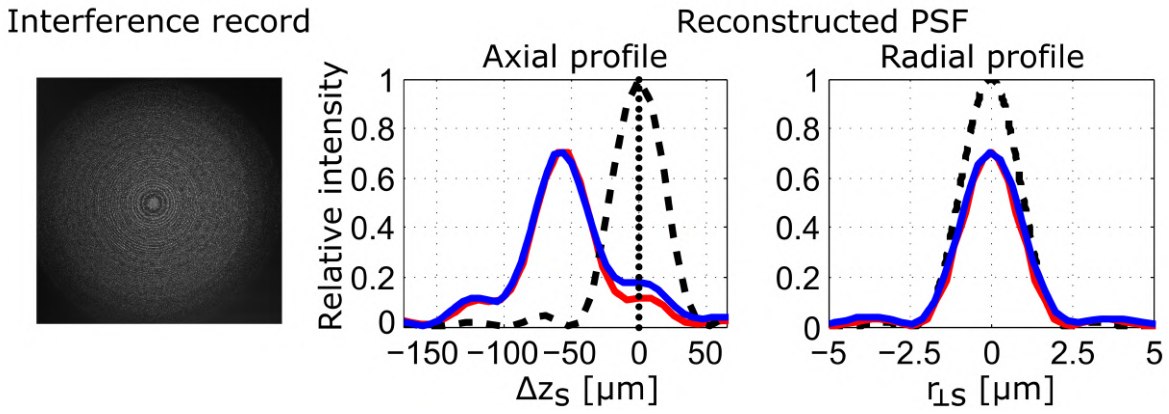

Figure 4.5: PSF deteriorated by a strong holographic aberration and reconstructed by the plane wave from three phase-shifted point interference records taken with the geometric parameters belonging to the area III in Fig. 4.1 ($\rho_h = 6.1$ mm; $z_{r0} = -43.5$ mm; $\Delta = 4.9$ mm).

$\Delta = 1.5$ mm (middle violet dot in Fig. 4.1). Here, the paraxial lateral and the longitudinal resolutions $AD_s = 2.65$ μm and $\Delta z_{sD}^{+} = 60$ μm were achieved by an appropriate combination of the image numerical aperture ($NA_i = 0.005$) and the lateral and the longitudinal magnifications ($\beta = 29$, $\gamma = \beta^2$). High enough value of the Fresnel number ($N_i = 48.3$) ensures nearly symmetrical axial PSF while the spherical aberration remains small enough to provide nearly diffraction-limited imaging. The condition (4.6) is satisfied, ensuring the Strehl ratio is high enough ($K \geq 0.8$).

The PSF shown in Fig. 4.5 belongs to area III in Fig. 4.1 ($\rho_h = 6.1$ mm, $z_{r0} = -43.5$ mm, $\Delta = 4.9$ mm, right violet dot in Fig. 4.1). It corresponds to the paraxial lateral and the longitudinal resolutions $AD_s = 2.4$ μm and $\Delta z_{sD}^{+} = 56$ μm obtained with the high image space aperture ($NA_i = 0.017$) and the low lateral and longitudinal magnifications ($\beta = 8.9$, $\gamma = \beta^2$). The high value of the Fresnel number ($N_i = 172$) confirms that the asymmetrical PSF is not present. However the spherical aberration appears, making both the lateral and longitudinal PSF profiles deteriorated. The experimental PSF (blue line) is again in a good agreement with the PSF obtained in the numerical model (red line) in which both the holographic recording and reconstruction were simulated in the nonparaxial approach.

Additional measurement was realized in the arrangement displayed in Fig. 4.2 with a positive line resolution target. In this case, the distance z_{r0} between the camera and the reference focus F_{r0} remained fixed, $z_{r0} = -46.4$ mm. Three interference patterns that correspond to the three distinct positions of the resolution target relative to the reference focus $\Delta = 0.7$ mm, $\Delta = 3$ mm, and $\Delta = 10$ mm, were recorded. Numerical reconstructions were accomplished by applying the monochromatic plane wave. Different positioning of the sample corresponds to various combinations of the reached magnification and the image

space numerical aperture. The theoretical resolution, the radius of Airy disc in the object space, is obtained as $AD_s = 0.61\lambda|z_{i0}|/(\rho_h\beta)$. It means that if the ρ_h remains fixed, the object space resolution improves with the smaller $|z_{i0}|/\beta$ ratio. In the settings imposed, the reconstruction distances and the lateral magnifications reach values $z_{i0} = -3029$ mm, -671 mm, -169 mm, and $\beta = 66.3, 15.5, 4.6$, respectively. The $|z_{i0}|/\beta$ ratio decreases in each of the examined cases, giving values $|z_{i0}|/\beta = 45.7, 43.4$, and 36.7.

The smallest group present in the target includes the lines of the 2.5 µm widths. Each of the reconstructions is shown in Fig. 4.6, where the enlarged cutout of the finest line group is present together with profiles of the average visibility of horizontal and vertical

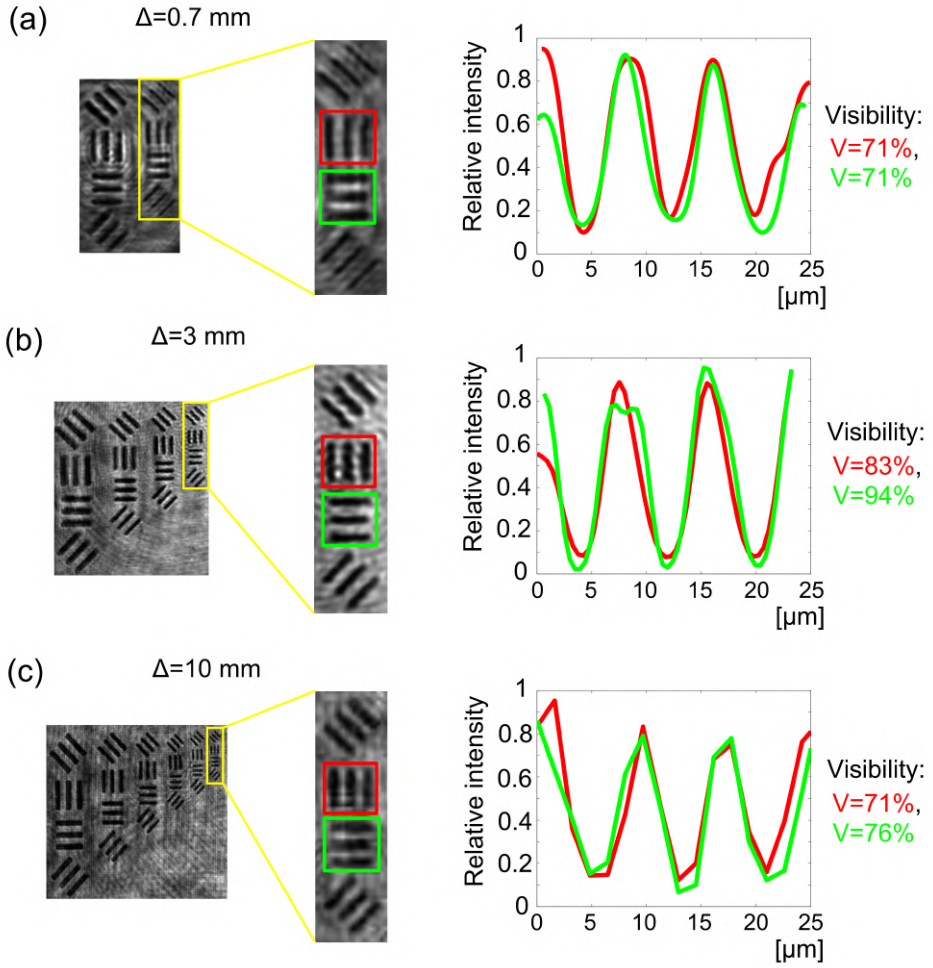

Figure 4.6: Plane wave reconstructions of the resolution target verifying an optimal choice of geometric parameters for recording: (a) aberration-free imaging with reduced diffraction-limited lateral resolution ($z_{r0} = -46.4$ mm, $\Delta = 0.7$ mm), (b) low-aberration imaging with optimal lateral resolution ($z_{r0} = -46.4$ mm, $\Delta = 3$ mm), (c) imaging with resolution reduced by holographic aberrations ($z_{r0} = -46.4$ mm, $\Delta = 10$ mm).

lines calculated in the marked square areas. The reconstruction of the line target with the experimental setting providing a high lateral magnification and the low image space numerical aperture is shown in Fig. 4.6a. In this case, the lateral resolution is limited by the $|z_{i0}|/\beta$ ratio, which is the highest of all the three cases. Moreover, the axial asymmetry of the PSF occurs with these parameters. The reconstruction in Fig. 4.6b belongs to the optimal configuration of experimental parameters where the image is nearly unaffected by the holographic aberrations. The resolution achieved meets the theoretical limit. In this case, the axial PSF provides practically perfect symmetry. Even a combination of the geometrical parameters in case of the reconstruction shown in Fig. 4.6c reaches the smallest $|z_{i0}|/\beta$ ratio predicting the best theoretical resolution, the influence of spherical aberration forbids its practical realization. The reduced lateral resolution and deteriorated axial profile of the PSF are achieved, as was discussed in the text mentioned above.

Chapter 5

Red blood cells as photomask for photorefractive writing into lithium niobate

This chapter is based on the following publication:

[2] L. Miccio, J. Behal, M. Mugnano, P. Memmolo, B. Mandracchia, F. Merola, S. Grilli, and P. Ferraro, "Biological lenses as a photomask for writing laser spots into ferroelectric crystals," *ACS Applied Bio Materials*, vol. 2, no. 11, pp. 4675–4680, 2019.

As was introduced, red blood cells may behave as a sort of biolenses with optical parameters determined by their shape. This chapter demonstrates the exploitation of the biolensing effect to modulate the optical properties of the photo-activated and biocompatible substrate. Thus, performing the optical bio-photolithography as a consequence. The chapter notably presents the possibility of imprinting information about red blood cells into the iron-doped x-cut $LiNbO_3$ crystal. The results achieved prove that various optical properties of discocytes and spherical-like RBCs imprint different phase discontinuities, which are characterized by the complex-amplitude propagation.

5.1 Experimental setup

Fig. 5.1a illustrates a Mach-Zehnder holographic microscope, and the scheme in Fig. 5.1b represents the optical bio-PL performed by an array of RBCs. Here, linearly polarized laser light (Melles Griot, $\lambda = 473$ nm, 15 mW, 0.67 mm beam diameter) is attenuated by an arrangement consisting of the half-wave plate HWP_1 and the linear polarizer LP_1, maintaining the output polarization. The sample illuminated by the laser light is placed in the signal arm of the interferometer on the vertical stage made of a beam splitter BS_1 and mirrors M_1 – M_3. The microscope objective MO_1 (Nikon, $20\times/0.30$) images the sample placed

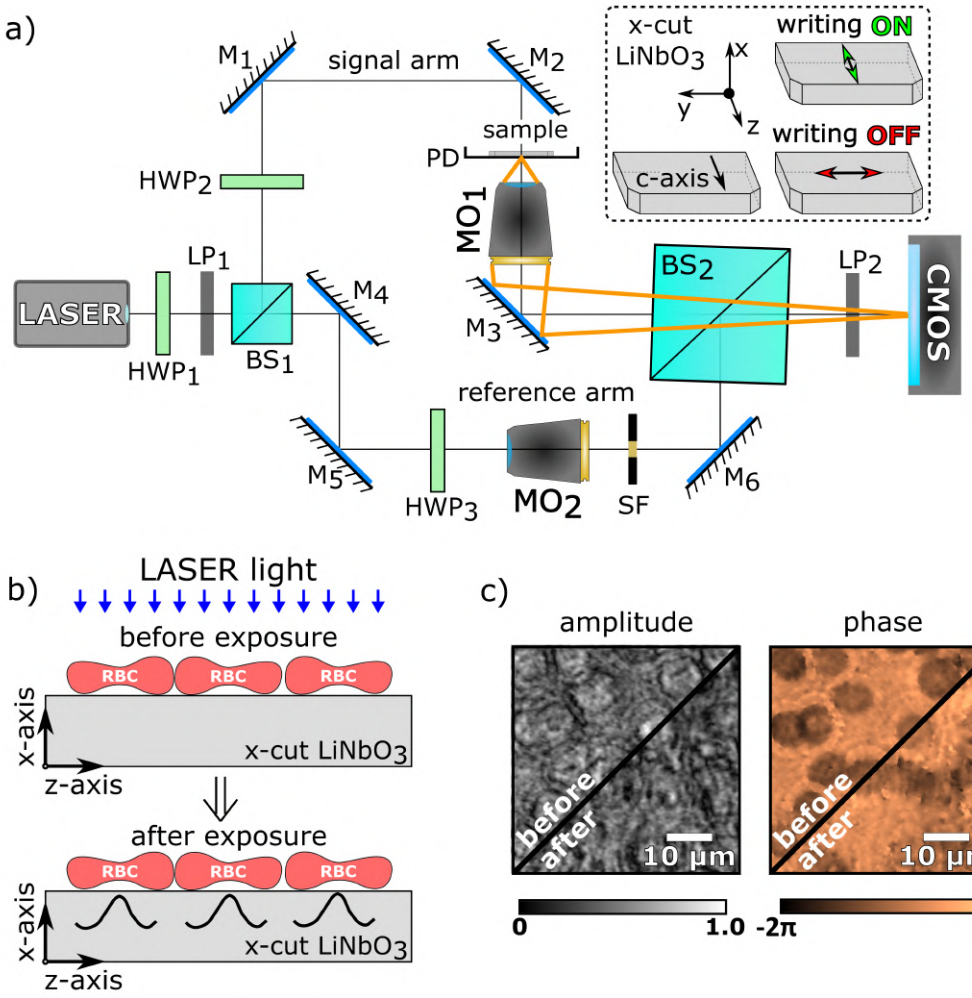

Figure 5.1: (a) Sketch of the experimental setup. Inserted image defines the coordinate system of the crystal and writing ON and writing OFF modes. Microscope objective (MO), half wave plate (HWP), mirror (M), linear polarizer (LP), beam Splitter (BS), Petri dish (PD). (b) Schematic view of bio-PL by RBC biolenses. (c) Quantitative phase map due to bio-PL writing on $LiNbO_3$, before and after exposure including RBCs.

in a Petri Dish (PD) onto the conventional CMOS chip (1280×1024 pixels, 5.3 μm square pixels). Lateral magnification of the optical arrangement $43\times$ was measured by a standard amplitude resolution target (USAF 1951). Phase curvature induced by the objective MO_1 (3.44) is compensated experimentally by the module placed in the reference arm, which consists of the spatial filter (SF) and the microscope objective MO_2 (Newport, $20\times$), generating the parabolic wave of comparable curvature as MO_1 (3.46). The off-axis geometry is achieved by mixing the signal and the reference waves on the second beam splitter BS_2. The half-wave plate HWP_1 adjusts the polarization direction related to the sample plane. The half-wave plate HWP_2 ensures the collinearity of the output polarization states, and the linear polarizer LP_2 filters out the undesired residual polarization component. An x-cut

iron-doped $LiNbO_3$ (Altechna, Fe:$LiNbO_3$ dopant level 0.05 %, 500µm thickness in x-axis, 10×10 mm in y-z plane) is placed into the PD, adopting the coordinate system from Fig. 5.1a. The optical arrangement works in two modalities, i.e., writing-on mode (polarization adjusted collinearly to the z-axis) and writing-off mode (polarization adjusted perpendicular to the z-axis). It is possible to easily switch between the two modalities by $90°$ rotation of the linear laser light polarization. Writing-on mode allows the local modification of the refractive index while writing-off mode does not modify the refractive index, respectively. In the writing-off condition, it is possible to illuminate and analyze the $LiNbO_3$ sample using the same laser light without inducing the refractive index changes.

5.2 Sample preparation

Human blood obtained from a healthy volunteer was centrifuged twice. Firstly, to separate RBCs at the bottom of the sterile tube from the plasma and buffy coat. Then the RBC pellet was washed with a saline solution in sterile water and centrifuged again. The isolated RBCs obtained were dispersed in physiological saline solution to maintain the osmotic pressure of the RBCs. In this way, discocytes were prepared. The isolated RBCs were further diluted in a hypotonic saline solution to get the cell swelling, hence obtaining the spherocytes. As a result of the preparation process, the discocytes and spherical-like RBCs were prepared and subsequently seeded on the crystal for the laser illumination. Technical details of the sample preparation are present in the article [2].

5.3 Measurement

The camera records the interference field originating from mixing a mutually coherent object beam passing through the sample, and a separate reference wave. The interference patterns are recorded at different times and then numerically processed to retrieve the sample's complex amplitude, including quantitative phase maps.

Fig. 5.1c illustrates the amplitude and phase of the sample before and after the writing process. On the left-upper part of the phase map, the phase shift introduced by a few RBCs settled on the crystal is visible. The color-map goes from -2π to 0, and the image is retrieved in the writing-off mode. The cells exhibit a negative phase due to the adopted coordinate system (Fig. 5.1a). Then the laser light polarization is switched in the writing-on mode for 15 minutes. At the end of the process, the laser polarization is turned-off again. Another interference record is captured, and the corresponding phase map is shown on the right-bottom part of Fig. 5.1c. In this case, the measured phase map is the integral contribution of

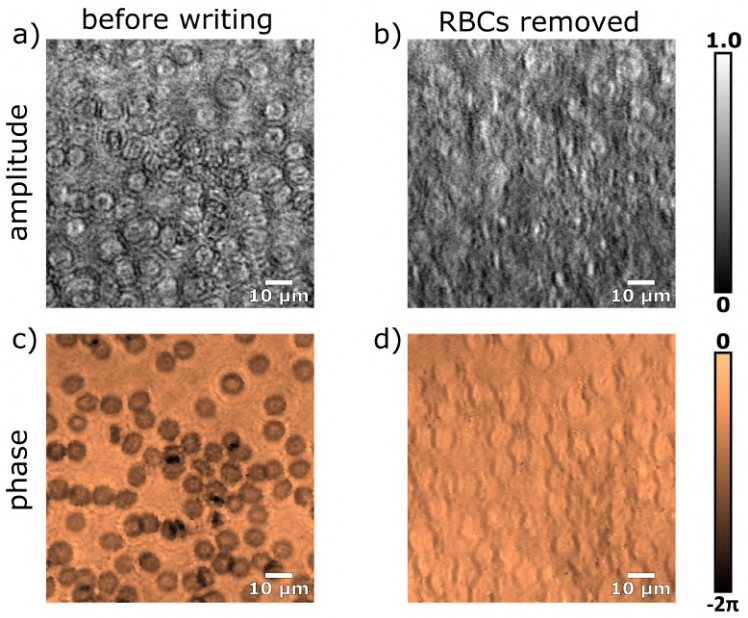

Figure 5.2: Reconstructed amplitude and phase of discocytes and the corresponding imprints. a), c) Cells before writing. b), d) Imprinted structures without cells.

the phase shift of RBCs and local inhomogeneity induced inside the $LiNbO_3$. The timing of the writing process was calibrated as it depends on laser intensity. The higher the intensity, the shorter the time needed for producing relevant refractive index changes into the crystal. Or similarly, when the intensity of the illumination light is preserved, more changes in the refractive index distribution appear with the increasing exposure time. More details of the calibration procedure are described in the article [2].

The measurements were conducted on both types of RBCs, discocytes, and spherocytes, respectively. Initially, the light in the writing-off mode (Fig. 5.1a) illuminated the RBCs seeded on the top surface of the crystal, hence the first interference record close to the image plane was recorded before the PL writing started. In Fig. 5.2a, and Fig. 5.2c, retrieved amplitude and quantitative phase maps are reported. Further, the optical power was set to 120 µW, and the polarization was adjusted in the writing-on mode (Fig. 5.1a) to imprint the cell structures into the crystal. The sample was exposed for 15 minutes in the case of discocytes and 4 minutes in the case of spherocytes, respectively. After this procedure, the polarization was switched again into the writing-off mode. The sample was taken out from the signal arm. The RBCs were removed out of the surface of the crystal. Petri dish with the cleaned crystal was then placed back into the object plane of the microscope objective MO_1. The imprinted structures were localized in the identical FOV, and subsequently, the corresponding interference record was captured. Fig. 5.2b, and Fig. 5.2d show the amplitude and

the phase maps of the crystal without RBCs. The imprinted structures were imaged under writing-off-mode illumination of lower optical power, to minimize the possible deterioration.

5.4 Data processing, results and discussion

The useful holographic term was reconstructed, and the phase-background removed by fitting the entire FOV (Fig. 3.4). The obtained complex amplitude was further propagated using the angular spectrum method (3.7). The data presented in Fig. 5.3 and Fig. 5.4 were derived from the cell's properties and their corresponding imprints in the identical FOV.

The cells were localized using their focusing properties [196]. The radial coordinates of the amplitude maxima were found in the plane of the highest contrast calculated using the TC (3.58) in the entire FOV [45]. The obtained amplitude profiles in x-y and x-z planes are shown in Fig. 5.3a, and Fig. 5.4a. The zero axial coordinates correspond to the plane

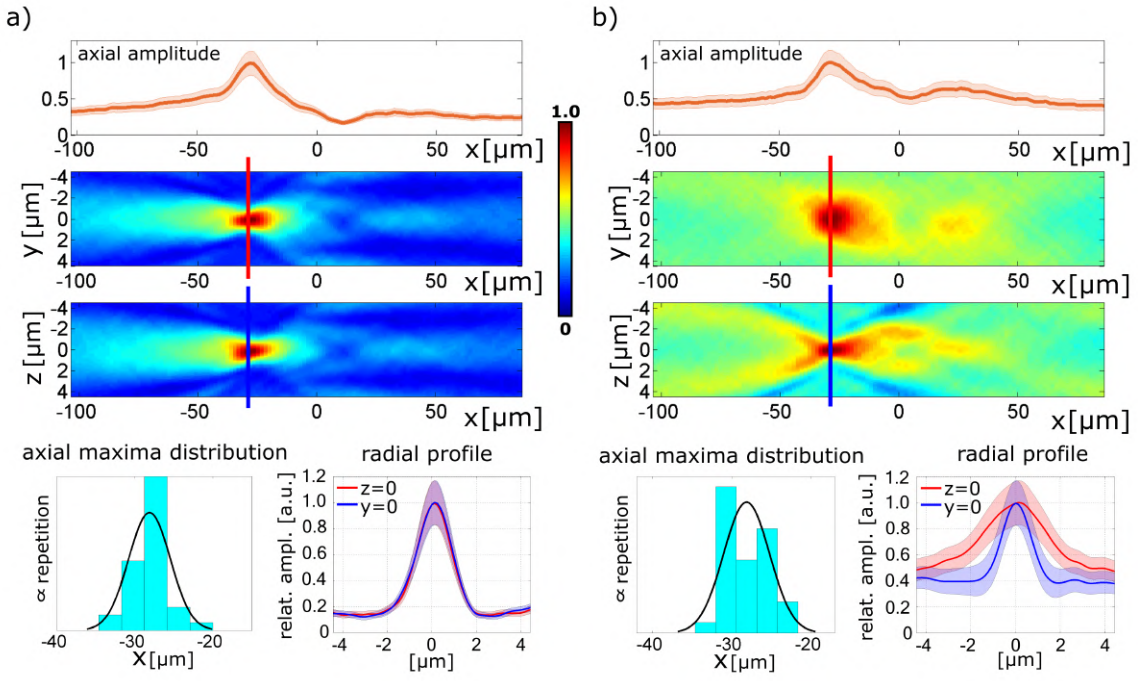

Figure 5.3: Average data obtained from 35 spherocytes and corresponding imprints. a) Axial amplitude and 2D amplitude plots in x-y and x-z planes of the cells with the real focal distance -28 ± 3 µm. b) Axial amplitude and 2D amplitude plots in x-y and x-z planes of the corresponding imprints with the real focal distance -28 ± 3 µm. Histograms represent focal-plane distribution for the real focal distance by means of the highest value of the axial amplitude [equal x-axis range 25 µm]. The radial profiles are the intersections through the marked lines. The error curves are calculated from the ensemble of 35 cells as a range of one standard deviation.

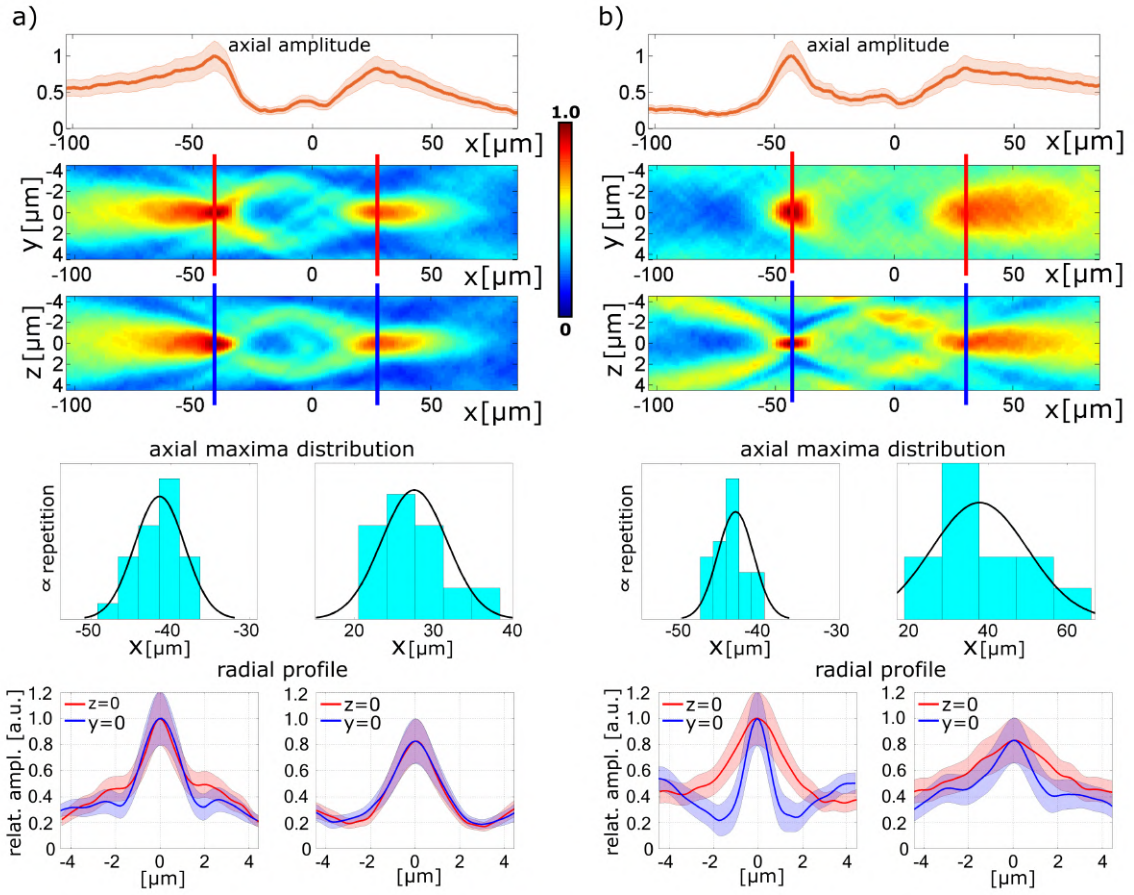

Figure 5.4: Average data obtained from 24 discocytes and corresponding imprints. a) Axial amplitude and 2D amplitude plots in x-y and x-z planes of the cells with the real focal distance -42 ± 3 μm and the virtual focal distance 27 ± 5 μm. b) Axial amplitude and 2D amplitude plots in x-y and x-z planes of the corresponding imprints with the real focal distance -42 ± 2 μm and the virtual focal distances 39 ± 12 μm. Histograms represent focal-plane distribution for the real and the virtual focal distances by means of the highest value of the axial amplitude [equal x-axis range 25 μm in all cases except virtual foci of the imprints (60 μm)]. The radial profiles are the intersections through the marked lines. The error curves are calculated from the ensemble of 24 cells as a range of one standard deviation.

of the lowest local value of TC calculated in the plotted area (not shown in the figures), which not necessarily correspond to the local minimum of the amplitude profile. Each cell's focal distance was estimated as a position of the highest value of its axial amplitude. Histograms inserted in the figures represent the real and virtual focal distance distributions of the selected cells with the calculated values -28 ± 3 μm for the real foci in the case of spherical-like RBCs while, in case of discocytes, -42 ± 3 μm for the real foci and 27 ± 5 μm for the virtual foci (Fig. 5.3a, Fig. 5.4a).

In the adopted coordinate system, the real focus of the cells and the structures are situ-

ated in the negative part of the propagation axis. The interference records of the imprinted structures without RBCs were processed similarly as the interference records of the RBCs due to similar focusing properties. The obtained average amplitude profiles in x-y and x-z planes for spherical-like RBCs and discocytes are plotted in Fig. 5.3b and Fig. 5.4b, respectively. Spherical-like cells and their imprints contain just one significant focal point. The position of the real foci of 35 spherical-like cells -28 ± 3 µm is equal to the position of the real foci of the corresponding imprints -28 ± 3 µm. In the case of discocytes, it can be observed that imprints exhibit bi-focal properties, thus replicating the intrinsic double-focal property of discocytes. The external toroidal shape of the discocyte is responsible for the real-focus, while the central part produces a negative focus. The real and the virtual foci for 24 discocytes were found as -42 ± 3 µm and 27 ± 5 µm, respectively. The real and the virtual foci of the imprints were established as -42 ± 2 µm and 39 ± 12 µm. Real focal distances exhibit comparable standard deviations for the cells and the imprints, whereas the position of virtual focal distances of the imprints is blurred. Nevertheless, the absolute distance between both focal points in the case of the discocytes and the imprints is equal in a range of the calculated standard deviations. All the mentioned values are summarized in the Tab. 5.1.

Amplitudes of the imprints exhibit asymmetrical behavior in x-y and x-z planes in both cases because the imprinted structures are also asymmetrical (Fig. 5.2b, Fig. 5.2d), even though amplitude plots of cells are symmetrical. This effect appears due to light-induced spatial distribution of the electric charges generated in PR materials by inhomogeneous illumination distribution [183, 269]. The asymmetry of the focal spots in the radial plane is characterized by a coefficient $\chi \in [0, 1]$ calculated as a ratio of two full widths at half maxima (FWHMs) in mutually orthogonal planes, i.e., x-y and y-z planes in our case, thus

$$\chi = \min\left\{\frac{\mathrm{FWHM}_{x-y}}{\mathrm{FWHM}_{x-z}}, \frac{\mathrm{FWHM}_{x-z}}{\mathrm{FWHM}_{x-y}}\right\}. \tag{5.1}$$

		Real foci (values in µm)			Virtual foci (values in µm)		
		position	FM_{x-y}	FM_{y-z}	position	FM_{x-y}	FM_{y-z}
Disco. (24 cells)	cells	-42 ± 3	1.5 ± 0.3	1.7 ± 0.3	27 ± 5	1.8 ± 0.3	1.9 ± 0.3
	imprints	-42 ± 2	2.4 ± 0.5	1.0 ± 0.3	39 ± 12	4.0 ± 1.1	2.0 ± 0.8
Spher. (35 cells)	cells	-28 ± 3	1.4 ± 0.2	1.4 ± 0.2	/	/	/
	imprints	-28 ± 3	3.4 ± 0.6	1.6 ± 0.4	/	/	/

Table 5.1: Characteristics in the focal regions for RBCs and the corresponding imprinted structures. FWHMs (denoted as FM_{x-y} and FM_{y-z}) are calculated from the intensity profiles.

The real focal spots of the cells exhibit symmetrical behavior in both cases, discocytes ($\chi \approx 0.9$), and spherical-like cells ($\chi \approx 1.0$), as expected. In contrast, the imprints in the case of discocytes ($\chi \approx 0.4$) and spherical-like RBCs ($\chi \approx 0.4$) are significantly asymmetrical (Fig. 5.3, Fig. 5.4). Indeed, even values achieved in the virtual focal spots confirm the symmetry of discocytes ($\chi \approx 1.0$) and the asymmetry of the imprints ($\chi \approx 0.5$).

To be complete, the full 3D shape of the imprinted structure in case of discocytes looks similar to the shape of the focal spots produced inside the z-cut $LiNbO_3$ crystal containing several voxel structures due to different birefringence-induced aberrations for the ordinary and extraordinary polarization eigenmodes [30]. However, the effect observed in Fig. 5.3b is obtained in x-cut $LiNbO_3$, which is voxel free in the area of the focal region, concluding that the reconstructed lobes of imprinted structure correspond to the cell optical properties. The virtual foci structure is not directly written inside the crystal volume but must be obtained by the numerical propagation before the crystal. This fact is also confirmed by the similarity of spherical-like RBCs and the voxels-free imprints (Fig. 5.4).

Besides, numerical simulations are performed to understand the formation of refractive-index distribution induced by RBCs via a PR effect in $LiNbO_3$. In work [272], the steady-state solution of the induced space-charge electric field E_{sc} for radially symmetrical illumination intensities was proposed. Here, the expression (3.59) is adopted to clarify the results observed (Fig. 5.4). Discocytes seeded on top of the crystal modify the profile of the laser-light illumination. Hence, the intensity illuminating surface of the crystal can be in principle obtained by numerical refocusing the reconstructed complex-amplitude map (Fig. 5.2a,c) of ~ 3 µm. The distribution calculated is approximately radially symmetrical due to the shape of RBCs and can be roughly expressed as

$$I = \kappa_1 \left(\kappa_2 \exp\left\{\kappa_3 r^8\right\} + \kappa_4 \exp\left\{\kappa_5 r^2\right\} + \kappa_6 \exp\left\{\kappa_7 r^2\right\}\right) + \kappa_8, \tag{5.2}$$

where r is a radial coordinate, and $\kappa_j, j = \{1, ..., 8\}$ are real coefficients. The defocused intensity distribution of the selected discocyte is illustrated in Fig. 5.5d, together with its approximate form (Fig. 5.5a) obtained according to equation (5.2). Coefficients $\kappa_j, j = \{1, ..., 8\}$ are specified in the caption of the figure. The coefficients κ_1, κ_8 were subsequently changed (in contrast to Fig. 5.5a) to 300 and 150, respectively, to approximately estimate real experimental conditions. Hence, the peak intensity of the light illuminating the crystal's surface reaches ~ 300 W m^{-2}. The formula obtained for I is further substituted into the equation (3.59) to predict the intrinsic electric field E_{sc} induced by space-charge distribution inside the crystal. Finally, the refractive-index map predicted by the

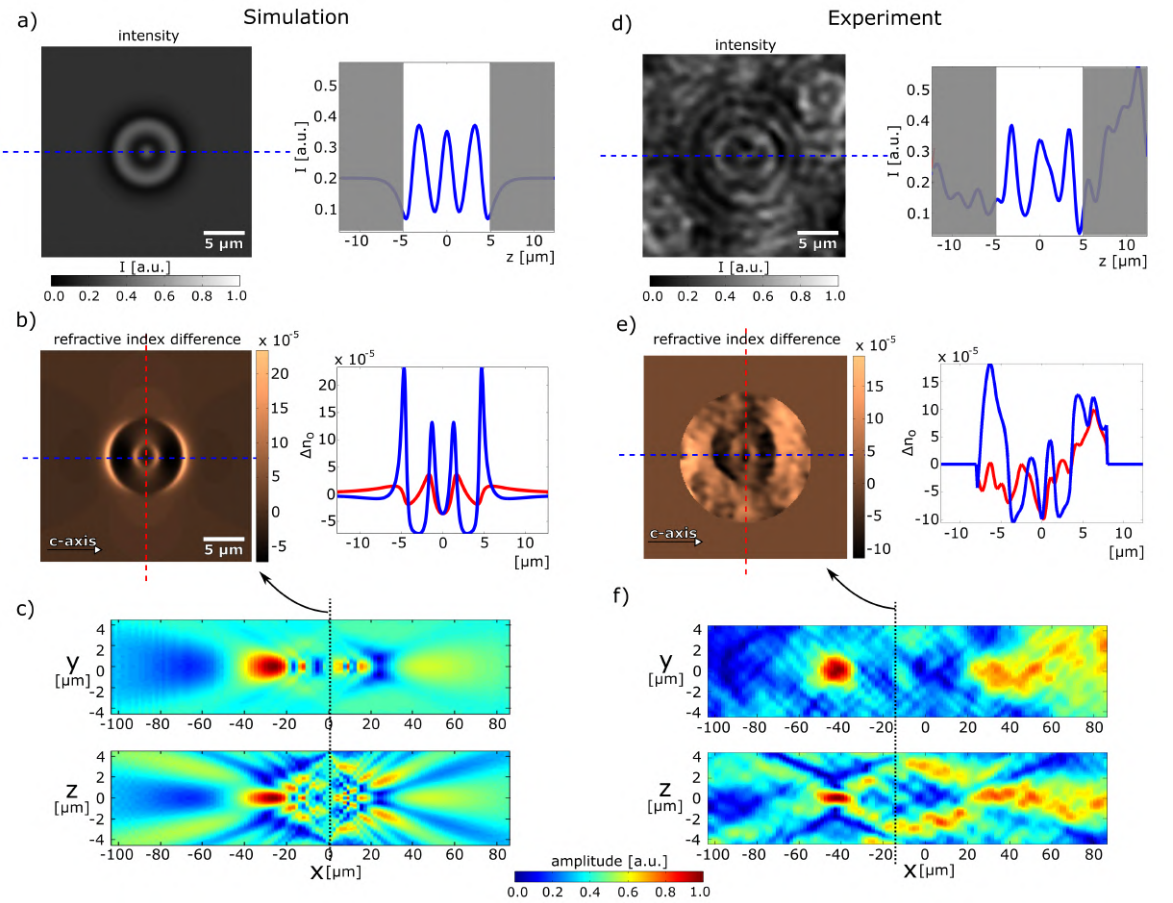

Figure 5.5: Parameters af the selected RBC and the corresponding imprint. a) Theoretical intensity profile illuminating the surface of the iron-doped x-cut $LiNbO_3$ crystal of parameters (5.2) $\kappa_1 = 0.38, \kappa_2 = 1.9, \kappa_3 = -1.5 \cdot 10^{43}, \kappa_4 = -2.9, \kappa_5 = -9.9^{11}, \kappa_6 = 1.4, \kappa_7 = -9.9^{12}, \kappa_8 = 0.20$. (Physical units of the coefficients are omitted for simplicity). b) Evaluated refractive-index distribution according to (5.3) with maintained parameters except $\kappa_1 = 300$ and $\kappa_1 = 150$ due to experimental conditions, $n_o = 2.35$, $r_{13} = 11$ pm V^{-1}, $E_0 = 20$ kV cm^{-1}. c) Cross-sections through the amplitude obtained by numerical propagation. d) Intensity profiles obtained by processing the experimenal data (refocusing the reconstructed complex amplitude of the RBC of $\sim$ 3 µm). e) Experimentally obtained refractive-index distribution. f) Cross-sections through the amplitude obtained by numerical propagation.

measurement is calculated according to

$$\Delta n_o = -0.5 n_o^3 r_{13} (E_0 - E_{sc}), \tag{5.3}$$

because the measurements were performed with illumination polarized orthogonally to the $c-$axis=$z-$axis, where $n_o = 2.35$, $r_{13} = 11$ pm V^{-1}, and E_0 is estimated as 20 kV cm^{-1}, which lies in the range of expected values [169]. Predicted distribution of the induced

refractive-index is illustrated in Fig. 5.5b with corresponding plots through the horizontal and vertical coordinates. The central part reaches local minimum followed by two symmetrically displaced local maxima, two local minima and two maxima in a periphery. Cross-sections through the amplitude, similar to those observed in Fig. 5.4b, were subsequently calculated by numerical propagation of the phase profile corresponding to the derived refractive-index map (Fig. 5.5c). Furthermore, amplitude cross-sections through the complex amplitude of the measured imprint are illustrated in Fig. 5.5f. The theoretical predictions (Fig. 5.5c) are in good accordance with the experimental measurements (Fig. 5.5f), although positions of the amplitude maxima are mutually shifted in the $z-$direction of ~ 15 μm. Hence, the simulated refractive-index distribution (Fig. 5.5b) was compared to the correspondingly shifted experimental one (Fig. 5.5e).

For detailed quantitative evaluation, more precise optical measurements, including speckle-free homogeneous illumination, should be provided with an in-depth characterization of the used crystal. Here approximate characteristics of Fe:$LiNbO_3$ were used to evaluate the theoretical photorefractive change induced by the living RBC (Fig. 5.5). Moreover, temporarily stable optical illumination, together with an accurately defined beam profile, should be used to study the interaction of light and photorefractive material. However, the theoretical model of the proposed interaction was out of the scope of this work. In our case, living cells, dynamically evolved systems [223, 275], were used as optical elements that fluctuate in their positions and induced optical properties. To prove the possibility of imprinting structures of cells into the photorefractive material and to study the possibility of their mutual distinguishing was the primary motivation of this work. Both of the properties were proved satisfyingly.

Chapter 6

Optimized implementation of the double-exposure method in common-path self-referencing digital holographic microscopy

This chapter is based on the following publication:

[3] J. Běhal, "Quantitative phase imaging in common-path cross-referenced holographic microscopy using double-exposure method," *Scientific Reports*, vol. 9, no. 9801, 2019.

This chapter presents the optimized implementation of the double-exposure method, emphasizing the uniformity and the minimization of residual phase imperfections in common-path self-referencing DHM. The required holographic terms are retrieved from single-shot records. Quantitative phase maps obtained are further processed to reduce phase defects originating from the imperfections of the optical path. Firstly, common-path lateral-shearing self-referencing DHM is implemented in a microscope configuration supplemented by a Sagnac interferometer to achieve duplication and further shearing of the waves. Utilization of the averaging process, which enhances the precision of QPI reconstruction, applicable in the methods with a doubled FOV, is also presented. The calibration measurements are provided, and the application potential is demonstrated by the imaging of biological samples, including the cheek and sperm cells. Moreover, another common-path self-referencing DHM is realized in a microscope arrangement with the added mirror to obtain the self-referencing. The initial measurements are performed, and the optimized implementation of the double-exposure method is demonstrated by imaging the glass beads.

6.1 Arrangement with Sagnac interferometer

Common-path lateral-shearing self-referencing DHM was realized in the microscope arrangement with incorporated Sagnac interferometer operating as a fluently adjustable shearing device (Fig. 6.1a). The monochromatic light beam emerging from unpolarized He-Ne laser (10 mW, $\lambda = 633$ nm) is coupled into a single-mode optical fiber by collimation and focusing optics. The spatially filtered light arising from the fiber is captured by an aspheric lens L_0 and focused in proximity to a rotating diffuser (RD). The light scattered

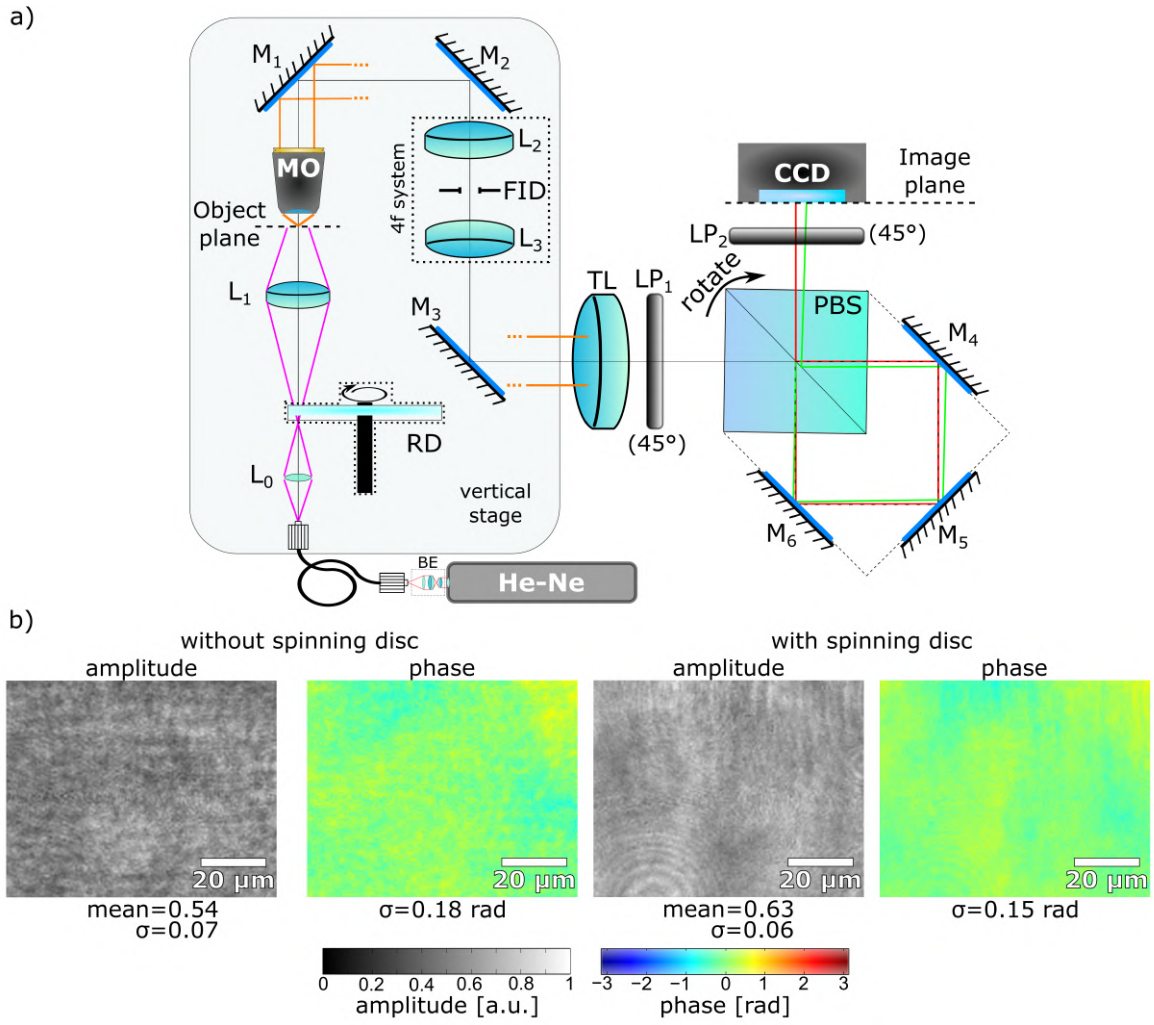

Figure 6.1: a) Setup for implementation of the common-path lateral-shearing self-referencing digital holographic microscopy with the incorporated Sagnac interferometer used as a shearing device. Collimation and focusing lenses (BE), aspheric lens (L_0), rotating diffuser (RD), condenser lens (L_1), microscope objective (MO), mirrors (M_1-M_4), relay lenses (L_2, L_3), field iris diaphragm (FID), tube lens (TL), linear polarizers (LP_1, LP_2), polarizing beam splitter (PBS), camera (CCD). b) Reconstructed amplitudes and phases without and with the rotating diffuser in the same area, respectively.

by RD is condensed by lens L_1 and subsequently illuminates the studied specimen. Using a microscope objective MO (UPlanFL N, NA $= 0.75$) and a tube lens TL (achromatic doublet, effective focal distance 400 mm) the specimen's magnified image (lateral magnification $89\times$) is created on a CCD (Retiga 4000R, 7.4 µm pixel size, 2048×2048 pixels). Relay lenses L_2 and L_3 (both achromatic doublets, effective focal distance 50 mm) are used to image the field iris diaphragm (FID) to the CCD plane.

The Sagnac interferometer module is situated between the TL and the CCD. It contains a polarizing beam splitter (PBS), three mirrors M_4-M_6, and two diagonally oriented linear polarizers LP_1 and LP_2 in the input and the output of the PBS to enhance the contrast of interference fringes created at the CCD. The lateral shear Δx between the interfering waves is adjusted by a slight rotation of the PBS, which is illustrated in Fig. 6.1a. The used tube lens (focal distance 400 mm) enables easy access to the Sagnac module built with optical components of commonly available parameters. In case when coupling the microscope objective with the standard tube lenses (focal distance ≈ 200 mm) is required, dimensions of PBS and used mirrors (M_4-M_6) should decrease correspondingly.

6.1.1 Initial measurements

The distance between the light spot created by the lens L_0 and the rotating diffuser allows the adjustment of spatial coherence of illuminating light and reducing speckle noise in the image plane when imaging the sample [91,276]. To demonstrate speckle suppression, measurements with and without the spinning diffuser were realized where required complex amplitudes were restored from the off-axis interference records. Phase maps were further unwrapped and fitted by the second-order polynomial to remove residual phase offsets, tilts, and curvatures. Amplitude and phase maps are illustrated in Fig. 6.1b. The amplitude obtained when the diffuser is out of the action exhibit less homogeneous distribution (standard deviation $\sigma = 0.07$, σ to mean ratio: 0.14) than the case when the diffuser spins (standard deviation $\sigma = 0.06$, σ to mean ratio: 0.10). Phases exhibit similar behavior as amplitudes, i.e., phase-map is less homogeneous (standard deviation $\sigma = 0.18$ rad) compared to the case with the spinning diffuser (standard deviation $\sigma = 0.15$ rad). Results obtained follow experimental results observed in work [93], where background speckle suppression was studied in common-path lateral-shearing self-referencing DHM.

Moreover, the temporal stability of the system was measured without the presence of any specimen. Period of interference fringes was adjusted to three pixels of the CCD, and a sequence of 240 snapshots was recorded for 2 minutes (the detector rate of 2 Hz). Each of the saved interference records was filtered in the Fourier space, and a phase map was further restored. The standard deviation calculated in the area 8.3×8.3 µm^2 was determined as

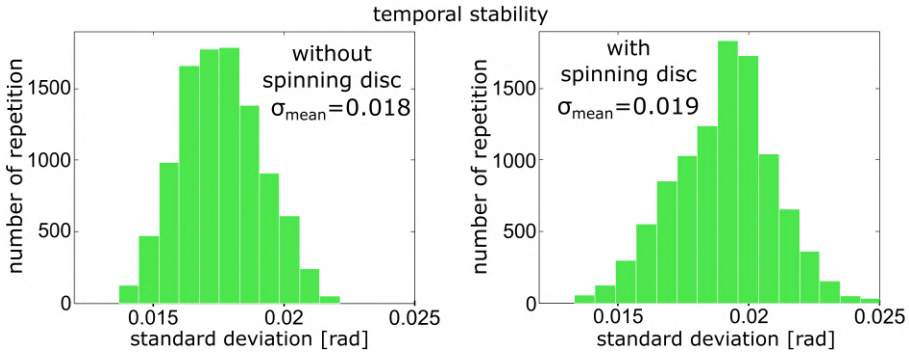

Figure 6.2: Measurement of the temporal stability carried out with and without rotating diffuser.

$\sigma_{mean} = 0.018$ rad in a case when the rotating diffuser was inactive. The measurement realized with the rotating diffuser results in the standard deviation value of $\sigma_{mean} = 0.019$ rad, meaning that the diffuser spins have low importance on the temporal stability of the system. The results obtained are illustrated in Fig. 6.2. Accuracy of the imaging performance was studied by the quantitative phase resolution target USAF 1951 with multiple heights in the range from ~ 50 nm to ~ 350 nm with the ~ 50 nm steps. The measurement was done in three square areas of the target, with the ground-truth heights 59 nm, 218 nm, and 384 nm (Fig. 6.3). The phase stroke is determined by comparing the phase restored from a single-shot recording with the phase of the background obtained by the reference interference record. The height profile is evaluated according to the equation $h(x) = \Delta\Phi_{st}(x)/[k(n-1)]$, where the refractive index of the glass $n = 1.52$ for the used wavelength is employed. The phase steps in three areas of the resolution target transformed into the heights are shown in Fig. 6.3a. Firstly, the standard deviations obtained from the measurement in the square areas of 8.3×8.3 μm^2 using the ground-truth heights 59 nm, 218 nm and 384 nm are evaluated as 7 nm, 18 nm and 28 nm, respectively. The abrupt oscillations close to the sharp edges of the square phase areas influence the quality of the reconstructed phase and are apparent from the cross-sections illustrated in Fig. 6.3b. Elementary numerical simulations were accomplished to investigate this behavior. Firstly square areas of phase delay corresponding to the known ground-truth heights and refractive index $n = 1.52$ for wavelength $\lambda = 633$ nm were defined reaching values 0.30 rad for height 59 nm, 1.13 rad for height 218 nm, and 1.98 rad for height 384 nm, respectively. Imposed complex amplitudes were Fourier transformed, filtered by the circular aperture of radius NA/λ, which corresponds to the theoretical resolution limit of the imaging system, inverse Fourier transformed, and the obtained phase maps were converted to heights. Cross-sections, through the results obtained, are illustrated in Fig. 6.3d, together with the initially imposed height steps. The oscillations are evident close to the sharp edges. The effect achieves the highest magnitude

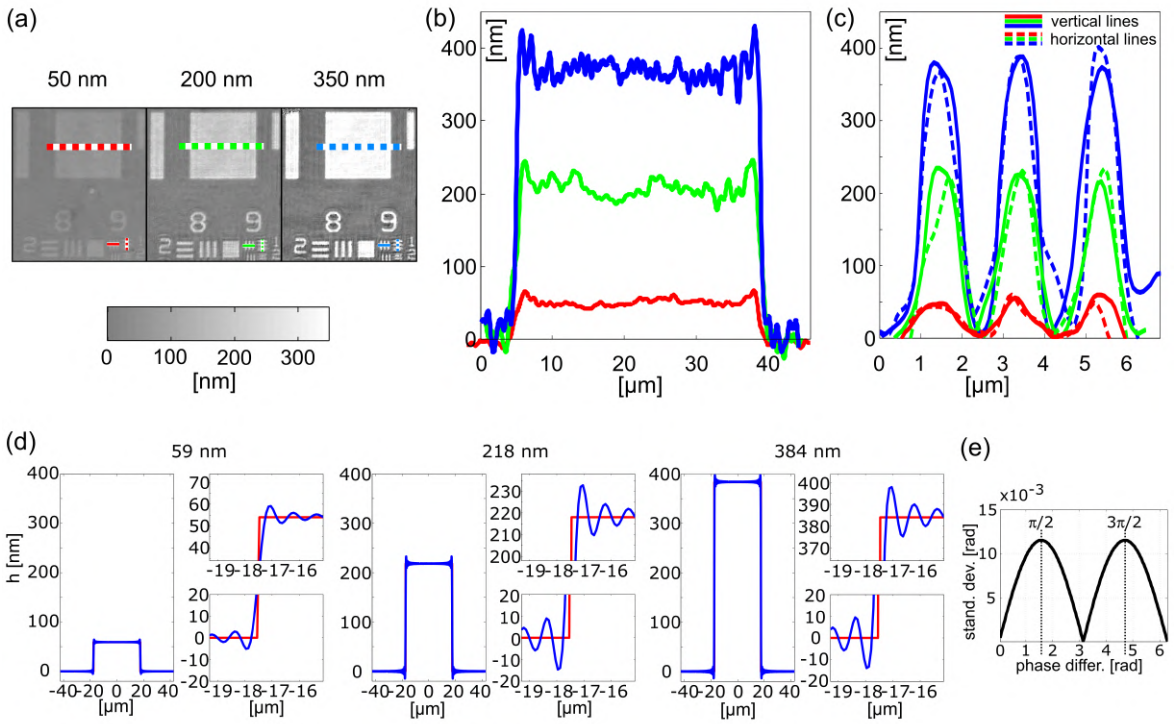

Figure 6.3: Evaluation of common-path lateral-shearing self-referencing digital holographic microscopy accuracy by the quantitative phase resolution target USAF 1951. (a) Gray level maps with the ground-truth heights 59 nm, 218 nm and 384 nm. (b) Cross-sections along thick dashed lines. (c) Cross-sections along thin solid and dashed lines passing through the group 9 and element 1 of the USAF target (linewidth 0.98 µm). (d) Simulations of low-pass filtering the complex amplitudes belonging to ground-truth heights 59 nm, 218 nm, and 384 nm, respectively. The radius of the circular filtering function NA/λ corresponds to the theoretical resolution limit of the coherent imaging system. (e) Standard deviations evaluated inside the reconstructed square area for initial phase steps in a range of 0 to 2π radians.

when the phase delay induced by the step imposed reaches odd multiples of $\pi/2$, as shown in Fig. 6.3e, where the standard deviation is evaluated inside the square area. To sum up, the oscillations in proximity to the sharp edges appear as a result of filtering out the high spatial frequencies of the resolution target. These simulations confirm that oscillations in a case of the 384 nm height step are more significant than in a case of the 59 nm height step, respectively (Fig. 6.3b). Furthermore, cross-sections plotted in Fig. 6.3c demonstrate that the phase resolution remains preserved even for a group of 0.98 µm width lines of the resolution target.

6.1.2 Results and discussion

For practical utilization of the method, cheek cells as a specimen were used. The cells were taken from inside the mouth by a toothpick, diluted in a drop of water, and sandwiched between the ground glass and the cover glass. The interference record of a single cheek cell was stored. Subsequently, the reference snapshot was recorded after the cell was moved away from the FOV by mechanically translating the stage. The phase-maps were retrieved from corresponding records and mutually deducted to eliminate the phase background. The reconstructed doubled phase images, with a flat background reaching the zero phase value, are shown in Fig. 6.4a.

Results obtained by the double-exposure method were compared to the polynomial background phase fitting (Fig. 6.4b). The reconstructed phase was unwrapped and fitted by the second-order polynomial to reduce residual offsets, tilts, and curvatures. The phase map corrected by fitting is compared to the result achieved by the double-exposure method in the same area (16.6×24.9 μm^2) in proximity to the observed cell reaching the standard deviations $\sigma_{mean} = 0.208$ rad and $\sigma_{mean} = 0.066$ rad, respectively. These results confirm an efficient background phase correction in the experimental configuration considered. Although the background phase can be fitted by higher-order polynomials or more sophisticated mathematical models, local phase inhomogeneities can barely be suppressed. As an example, multiple reflections from optical surfaces cause local ring-like interference circles, which deteriorate the overall sample phase-map. These local defects influence both amplitude and phase distributions (Fig. 6.4b) and are effectively eliminated by the double-exposure method (Fig. 6.4b).

Homogeneity of the phase background is examined by quantifying the changes of standard deviations when expanding the region for evaluation. The standard deviations calculated in two small laterally displaced areas of the size 4.2×4.2 μm^2 are established as 0.030 rad and 0.038 rad, respectively. When the areas are enlarged from 4.2×4.2 μm^2 to 12.5×12.5 μm^2, the standard deviations are increased to 0.057 rad and 0.059 rad revealing irregularity of the phase background. The inhomogeneity of phase background is illustrated by blue and green histograms associated with the smaller and larger regions. In addition to the enlarged standard deviations, even a shift of mean values is evident comparing the histograms of smaller and larger areas. The indicated inhomogeneity of the background phase in Fig. 6.4a is a consequence of a mechanical translation of the specimen to achieve the empty FOV when recording the reference snapshot. The shape of the phase background changes when the specimen is mechanically removed, thus $\Delta\Phi_{Wsr}(x - \Delta x) \neq 0$ and $\Delta\Phi_{Wsr}(x) \neq 0$ [see relations (3.56) and (3.57)]. Consequently, the remaining phase nonuniformities influence the quality of the phase background, even the double-exposure method

is applied (Fig. 6.4a).

The correction of the phase background is much more accurate when the specimen is removed without external mechanical interventions. The approach mentioned is feasible to demonstrate in the experiment with a semen sample diffused in water and sandwiched between the ground and the cover glass. The stage was slightly tilted from a horizontal position to achieve moving of the specimen by flowing a surrounding medium. In this case,

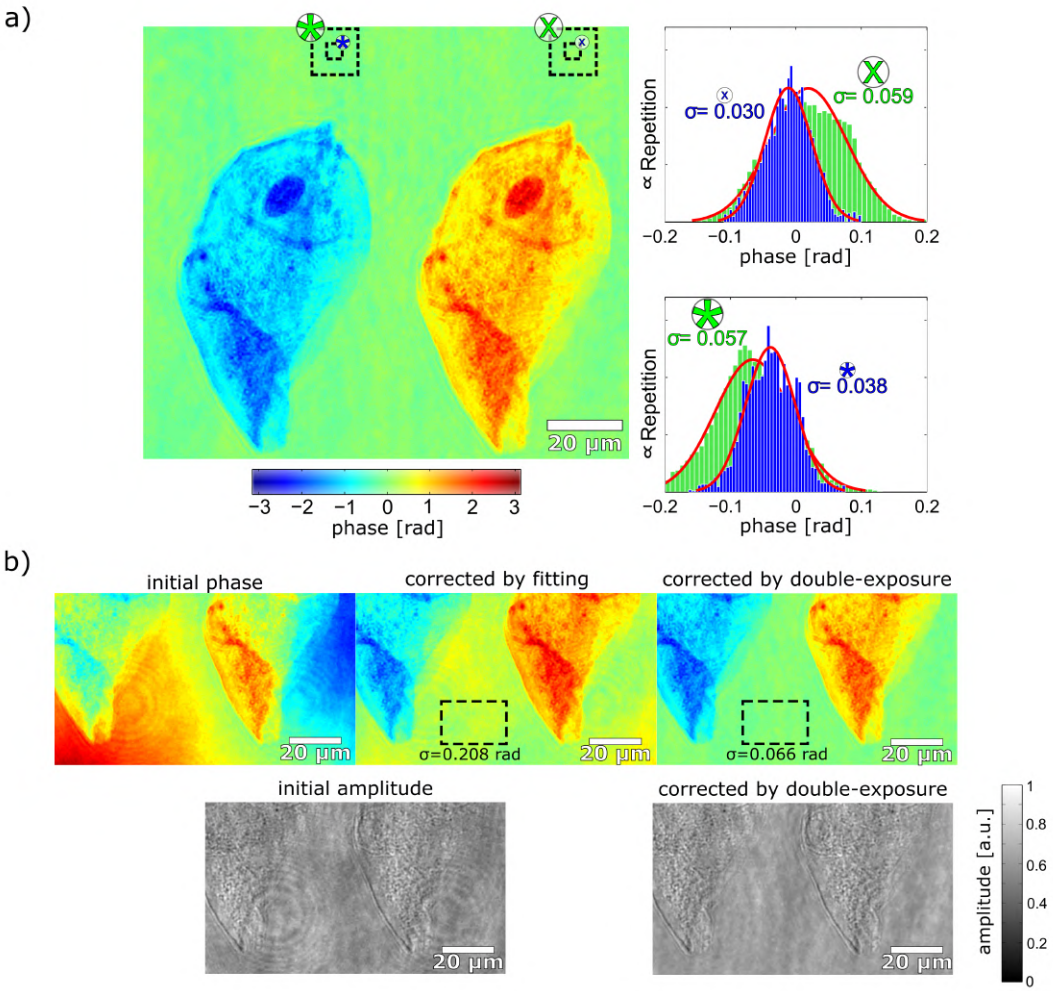

Figure 6.4: a) Quantitative phase image of the cheek cell with demonstration of nonuniformity of the phase background in the two laterally displaced areas. The standard deviations were increased from 0.038 rad to 0.057 rad and from 0.030 rad to 0.059 rad when evaluation areas expanded from 4.2×4.2 µm^2 (blue line histograms) to 12.5×12.5 µm^2 (green line histograms). b) Comparison of background phase correction achieved by fitting and double-exposure method. Standard deviations calculated in dashed rectangles embedded (16.6×24.9 µm^2) reach values 0.208 rad and 0.066 rad, respectively. Local circ-like structures originating from multiple reflections are effectively eliminated in both amplitude and phase distributions by double-exposure method.

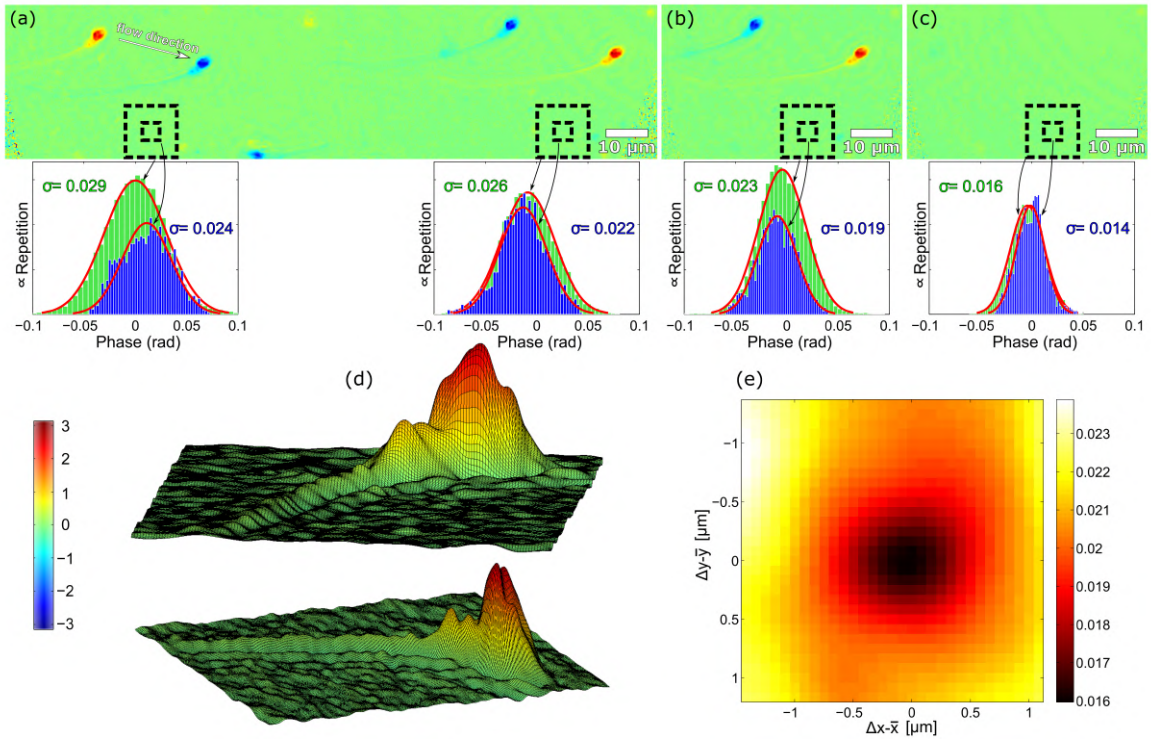

Figure 6.5: Quantitative phase imaging of the sperm cell. (a) Doubled phase image of the cell with demonstration of the background uniformity. The standard deviation is less dependent on the size and lateral position of the evaluation areas than in the previous case (size of areas 4.2×4.2 μm^2 and 12.5×12.5 μm^2). (b) The phase image with decreased standard deviation provided by the averaging procedure. (c) The phase map of imperfections added by the cross-referenced waves and standard deviations calculated in the marked areas. (d) Surface plot of the cell. (e) Standard deviation of $[\Delta\Phi_{st}(x,y) + \Delta\Phi_{sh}(x - \Delta x + \overline{x}, y - \Delta y + \overline{y})]/2$ when eliminating the lateral shear Δx in x-direction and Δy in y-direction.

the reference interference record can be captured after the sample is freely removed outside of FOV. The doubled phase images of the semen cell restored from the records appear on the opposite sides of the FOV in Fig. 6.5a. The standard deviations calculated in two laterally displaced areas of the size 4.2×4.2 μm^2, providing values of 0.024 rad and 0.022 rad. When expanding the areas from 4.2×4.2 μm^2 to 12.5×12.5 μm^2, the values of standard deviation stayed practically unchanged, 0.029 rad and 0.026 rad, respectively. The homogeneity of phase background is well illustrated by the blue and the green histograms associated with the smaller area and the larger area, respectively (Fig. 6.5a). Note that the range of the values displayed is different compared to Fig. 6.4a.

The fact that the field of view in common-path lateral-shearing DHM is reduced intrinsically can be exploited to enhance the imaging performance. Quality of the quantitative phase image restored is further improved when the straight and the sheared images

$\Delta\Phi_{st}(x)$ and $\Delta\Phi_{sh}(x-\Delta x)$ are present in the FOV. The lateral shear between the duplicated images is eliminated during the numerical processing, hence averaging of the phases $-\Delta\Phi_{st}(x)$ and $+\Delta\Phi_{sh}(x)$ is possible to carry out. Significant advantages of the averaging are demonstrated in measurement with the sperm specimen, where both doubled images of the cell fit inside the FOV. The result obtained after applying the averaging procedure is shown in Fig. 6.5b with the standard deviation of the background decreased to 0.019 rad and 0.023 rad, in the regions studied, respectively. The quasi-surface plot of the phase image restored, including the sperm cell, is available in Fig. 6.5d, where the homogeneous background enables clear recognition of the sperm-cell tail.

The terms $+\Delta\Phi_{st}(x)$ and $+\Delta\Phi_{sh}(x-\Delta x)$ contain identical information about the sample [except the sign minus in the equations (3.56) and (3.57)] but differ in residual phase imperfections rising from the sheared and the straight cross-reference waves, respectively. The feature mentioned was exploited when numerically eliminating a lateral shear. The sheared image is localized, shifted towards the straight image by $\overline{x}$, and both areas are averaged. The lateral shear is canceled when a standard deviation of the averaged image $[\Delta\Phi_{st}(x)+\Delta\Phi_{sh}(x-\Delta x+\overline{x})]/2$ reaches its minimum (i. e., in case when $\overline{x}=\Delta x$) because the information about the sample is just reduced. This property is evaluated by a standard deviation calculated inside the larger area 12.5×12.5 μm^2 without the cells (Fig. 6.5e). The lateral shear is canceled with precision $\propto$ 0.08 μm, which is lower than the radius of Airy disc $\propto$ 0.5 μm in the object space. After removing the lateral shear, the phase differences $+\Delta\Phi_{st}(x)$ and $+\Delta\Phi_{sh}(x)$ can be averaged which enables to estimate the amount of phase fluctuations added into the area of interest by the straight and the sheared reference waves, passing through the surrounding medium. Fig. 6.5c illustrates the result with the standard deviations of the background 0.014 rad and 0.016 rad, which simultaneously estimate the precision of the quantitative phase reconstruction in the evaluation areas. These values converted into OPD result in 1.4 nm and 1.6 nm, respectively. These imperfections can be minimized, and the common-path lateral shearing self-referencing DHM imaging performance further enhanced in microfluidic applications using channels. Here the reference record can be captured without mechanical movements, and the straight and the sheared reference waves pass through the areas out of the channel without the surrounding medium. This implementation reduces the added phase fluctuations naturally.

6.2 Arrangement with additional mirror

Another example of a quasi-common-path experimental arrangement is illustrated in Fig. 6.6a. Instead of incorporating the shearing device replicating FOV, just an additional mirror

is used to create an off-axis geometry by reflecting a part of the object beam on itself. Particularly, He-Ne laser ($10\mathrm{mW}$, $\lambda = 633$ nm) is coupled into a single-mode fiber by collimation and focusing optics (BE). Light emerging from the fiber illuminates the sample whose magnified image (lateral magnification $25\times$) is created close to the camera's chip (CCD, Retiga 4000R, 7.4 μm pixel size, 2048×2048 pixels) by the microscope objective (MO). The mirror (M) positioned in the image space of the MO reflects part of initially unemployed light for self-referencing. Hence, off-axis geometry is achieved by mixing both mutually coherent optical fields with fluent adjustment of the fringe period allowed by a tilt of the mirror M.

Firstly, 240 interference images without any specimen were recorded for 120 seconds (the detector rate of 2 Hz) to test the temporal stability of the system. The saved images were numerically processed to reconstruct phase maps of the corresponding complex amplitudes. The average standard deviation evaluated in the region of the entire camera chip $\sim 600 \times 600$ μm^2 reaches $\sigma_{mean} = 0.028$ rad. Histogram of the values obtained is illustrated in Fig. 6.6b.

It can be noticed in the experiment with phase target USAF 1951 (Fig. 6.6c), that phase background contains residual curvatures even when the spatial carrier frequency is eliminated because the interfering waves are of close, however unequal, curvatures. Hence, the unwrapped phase background can be corrected accurately by the second-order polynomial fitting (Fig. 6.6c). Although the phase background is fixed, the higher-frequency fringes originating from parasitic interference of multiple reflections remain preserved. The residual fringes are eliminated more effectively by the double-exposure method with the reference acquisition obtained when the target is translated out of the field of view. The average profile of fringes inside the highlighted area is plotted in Fig. 6.6c and reaches standard deviations $\sigma = 0.15$ rad in case of the map corrected by fitting and $\sigma = 0.11$ rad in the case of the double-exposure method, respectively. Furthermore, the height profile is evaluated according to equation $h(x) = \Delta\Phi_{st}(x)/[k(n-1)]$, where the refractive index of the glass $n = 1.52$ is used. Plots through the square, line group 6 element 2, and line group 7 element 6 of the resolution target transformed into the heights are also shown in Fig. 6.6d (black solid lines). Oscillations near sharp edges appear again as a result of filtering out the high spatial frequencies of the resolution target by the optical system. The height calculated in the area of $\sim 30 \times 30$ μm^2 inside the large square of the phase target reaches 304 ± 21 nm. Subsequently, the heights of different line groups of comparable lateral dimensions present in mutually distant areas were evaluated. Especially, height of the line group 6 element 1 and line group 6 element 2 (highlighted by dotted rectangles in Fig. 6.6d) achieve similar results 308 ± 27 nm and 296 ± 24 nm, respectively.

The tiniest lines, plotted in Fig. 6.6d, and Fig. 6.3c, are of similar percent of resolution

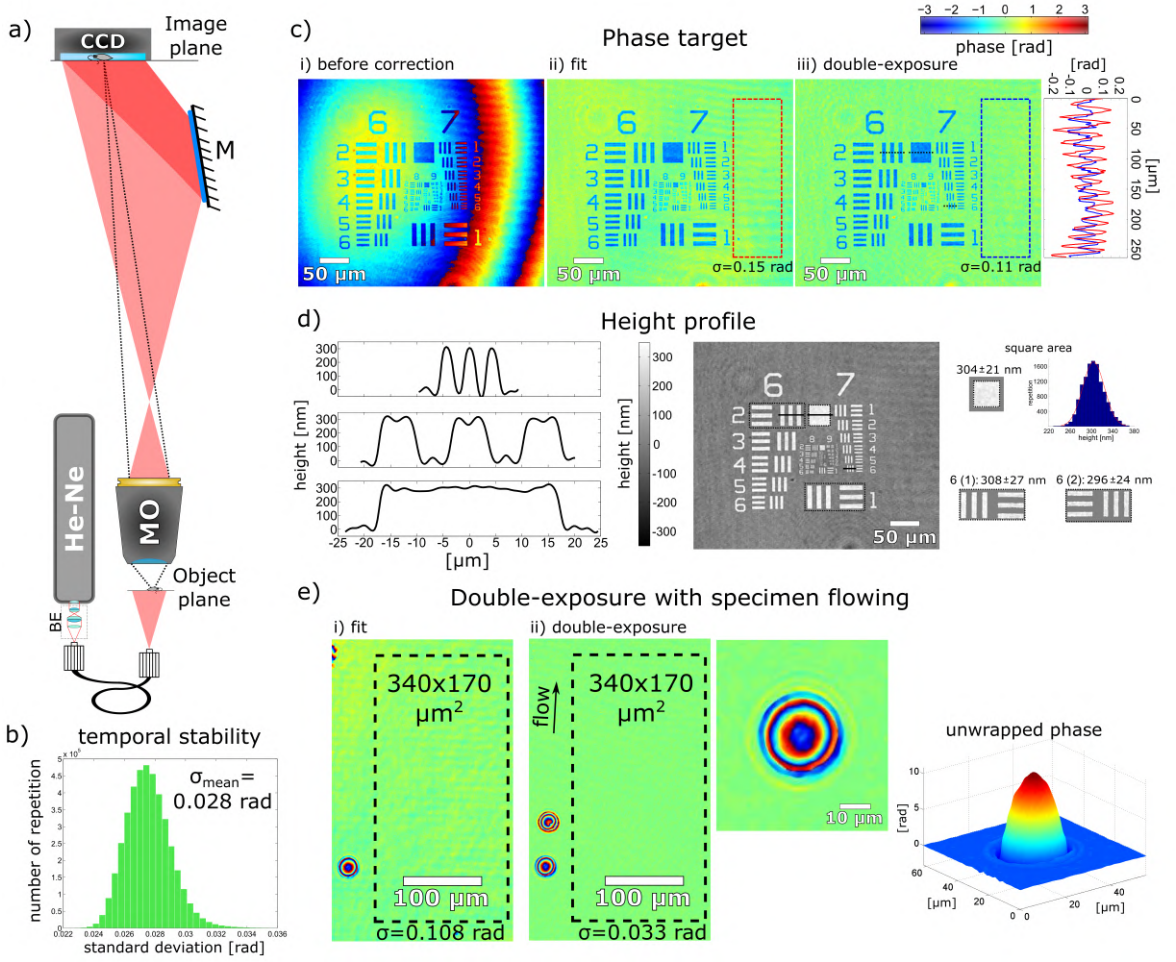

Figure 6.6: a) Experimental arrangement. Collimation and focusing lenses (BE), microscope objective (MO), a mirror (M), and camera (CCD). b) Temporal stability evaluated in the area of $\sim 600 \times 600$ μm^2 from a 2-minute interference record captured by frequency of 2 Hz. c) Phase target USAF 1951. i) The reconstructed phase before correction. ii) Phase corrected by the second-order polynomial fitting. iii) Phase corrected by double-exposure method. d) Reconstructed height map with plots along the marked lines. Ground-truth height of the target is 321 nm. e) Comparison of the double-exposure method with second-order polynomial fitting in case of a self-moving sample.

limit of the incorporated microscope objective ($\sim$ 43% in case of Fig. 6.3c and $\sim$ 48% in case of Fig. 6.6d). Lines of the group 7 element 6 also reach round-off shape as those reconstructed in Fig. 6.3c. However, their shape is more smooth, perhaps due to simple, straightforward geometry of the used experimental configuration.

The correction of phase background is even more efficient when the sample observed is self-moving or driven by the flow. In such the case, both interference records with and without the sample, respectively, can be recorded without external mechanical manipulation by the sample. The approach mentioned is demonstrated in the experiment with glass beads

($10 - 30$ μm, Polyscience, #07688) diffused in distilled water and sandwiched between the ground and the cover glass. The stage was slightly tilted from a horizontal position to achieve moving of the specimen by flowing in the flow. In this case, the reference snapshot can be captured after the sample is freely removed outside of the FOV. The reconstructed phase is illustrated in Fig. 6.6e, where the background phase homogeneity is evaluated in the area of the size 340×170 μm^2, where the standard deviation reaches $\sigma = 0.033$ rad. The predictable shape of the background phase map also enables its more sufficient correction by a second-order polynomial fitting, in comparison to Fig. 6.4b. Initially, the phase is unwrapped, fitted, corrected, and the result obtained is illustrated in the left part of Fig. 6.6e. Furthermore, the standard deviation $\sigma = 0.108$ rad is obtained inside the same area, as in the case of the double-exposure method, which enables the direct comparison of results obtained by both approaches. Hence, the reference snapshot captured without mechanical interventions enables efficient correction of the whole background phase. Therefore the double-exposure method is used as a reference to confirm the effectiveness of other phase-compensation methods [65, 66, 277]. The conclusions reached in the current experimental arrangement are in good accordance with the results achieved in the previous experiment, where the Sagnac interferometer was used as a shearing device.

Chapter 7

Polarization-sensitive digital holographic imaging with enhanced temporal stability

Enhanced temporal stability of the common-path Sagnac interferometer, discussed in the previous chapter, is utilized for generation of the temporarily correlated beams. The experimental arrangement, being examined (sketched in Fig. 7.1), basically represents a digital holographic microscope with the Mach-Zehnder interferometer with the incorporated polarization-sensitive Sagnac module in the reference arm for generation of two orthogonally polarized reference beams. This idea was firstly introduced in the work [242]. However detailed analysis of the setup have not been discussed yet, according to our knowledge. The experimental configuration presented served for imaging homogeneous anisotropic samples producing uniform polarization distribution (linear polarizer, quarter-wave plate), except residual deviations from the expected values. Here, the temporal stability is quantified and the ability of reconstructing spatially variable polarization states confirmed by imaging the S-wave plate, which is a half-wave plate with the spatially-dependent orientation of the local axis.

7.1 Experimental setup

Experimental arrangement is illustated in the Fig. 7.1, where the beam from an unpolarized He-Ne laser (10 mW, $\lambda = 633$ nm) is coupled into a single-mode optical fiber, decoupled, collimated by the lens L_0, and polarized along the horizontal direction related to the optical table by a linear polarizer (LP). The beam generated is divided into two paths by the first beam splitter (BS_1) of the Mach-Zehnder interferometer. The lenses L_1 and L_2 placed in the reference arm serve as a beam expander followed by the Sagnac module which consists of the polarizing beam splitter (PBS_1) and three mirrors (M_1-M_3). The half-wave plate (HWP_1)

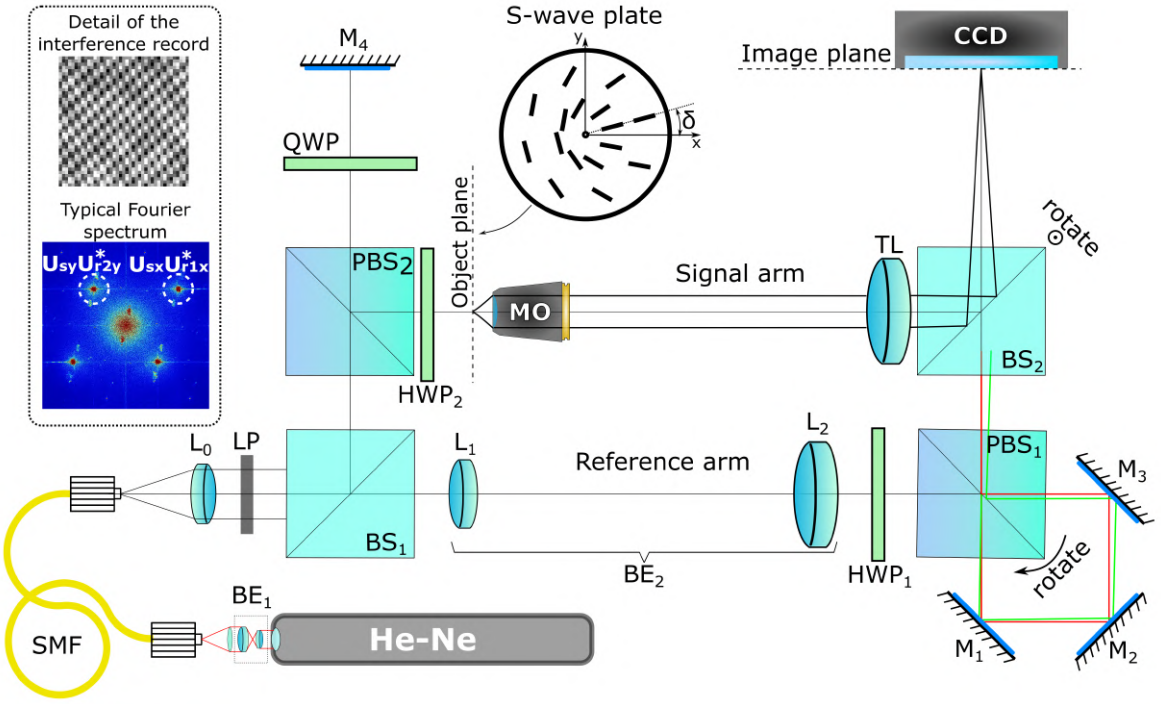

Figure 7.1: Mach-Zehnder configuration with the Sagnac interferometer incorporated in the reference arm to perform the polarization-sensitive imaging by DH. Beam expander and focusing lens (BE_1), single mode fiber (SMF) collimating lens (L_0), linear polarizer (LP), beam splitter (BS_1, BS_2), beam expander (BE_2), half-wave plate (HWP_1, HWP_2), polarizing beam splitter (PBS_1, PBS_2), mirrors (M_1-M_4), quarter-wave plate (QWP), microscope objective (MO), tube lens (TL), camera (CCD). The detail of the interference record and a typical Fourier spectrum are set in the inset figure. Arrows in proximity to PBS_1 and BS_2 point out the tilt direction clockwise and toward the reader, respectively. Lines in the aperture of the S-wave plate indicate orientation of the local axis.

balance the intensity ratio between the output orthogonally polarized beams. A slight rotation of the PBS_1 induces a tilt between the noninterfering but temporarily correlated output beams which leave the Mach-Zehnder interferometer after the transmission through the last beam splitter (BS_2). The polarizing beam splitter (PBS_2), quarter wave (QWP) and mirror (M_4) serve as OPD compensator in the signal arm, and the half-wave plate (HWP_2) adjusts the linear polarization direction of the beam illuminating the specimen. The sample is imaged by the microscope objective (MO, Olympus, $4\times$ Plan N, NA$= 0.1$) and the tube lens (TL, achromatic doublet, effective focal distance 100 mm) into the camera plane (CCD, Retiga 4000R, 7.4 µm pixel size, 2048×2048 pixels) with the lateral magnification $2.2\times$. The optical beams formed in the signal and the reference arm are mixed by the BS_2 which introduce spatial carrier frequency between the signal beam and the reference waves. As a result the horizontal component of the signal wave interferes with the horizontally polarized reference beam while the vertical component of the signal wave interferes with the

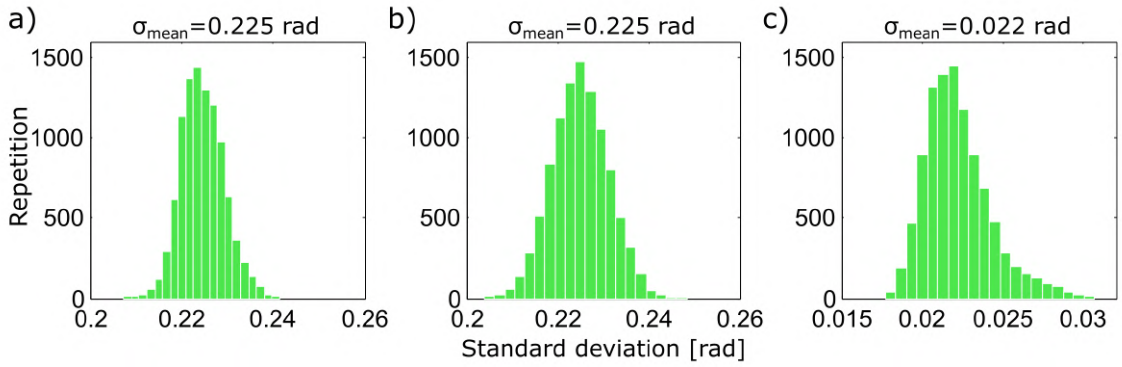

Figure 7.2: Simultaneously measured temporal stability of the: a) QPI performed by the horizontally polarized component, b) QPI performed by the vertically polarized component, c) polarization-state reconstruction. The calculations were accomplished in the area of 0.3×0.3 mm^2 from the 240 interference records captured by the 2 Hz frequency.

vertically polarized reference beam. Both the interference fields are incoherently summed and detected by the CCD. An example of the recorded checkerboard like structure and the Fourier spectrum are shown in the inset in Fig. 7.1.

7.2 Measurements and results

In the arrangement described, the horizontal and vertical components of the signal wave, interfere with the horizontal and vertical reference waves, respectively. Hence the temporal stability of the interferometer can be evaluated for both polarizations simultaneously. Particularly, a diagonal polarization of the signal wave was adjusted, and a sequence of 240 interference records was measured during 120 seconds with the frequency 2 Hz without any sample incuded in the signal arm. The phase map corresponding to the horizontal component was retrieved from 240 records, and the standard deviation was evaluated in the area of 0.3×0.3 mm^2 as 0.225 rad (Fig. 7.2a). Moreover, the equal set of interference records enabled to calculate the temporal stability of the vertical polarization with the identical standard deviation of 0.225 rad (Fig. 7.2b). Hence, both distributions reach similar parameters. Indeed, temporal stability of the polarization-state reconstruction by the digital holography, i.e., a standard deviation of the phase differences induced between the horizontal and the vertical polarization components, reaches 0.022 rad (Fig. 7.2c). The Mach-Zehnder configuration determines the stability of the quantitative phase imaging independently for the horizontal and vertical polarization. However, their fluctuations are mutually correlated due to the Sagnac interferometer providing an order of magnitude improvement of the temporal stability in the polarization imaging compared to the temporal stability of QPI in horizontal and vertical components in Mach-Zehnder interferometer

separately. To sum up, the presented arrangement can be advantageously used for the polarization imaging by DH with an enhanced temporal stability.

Known object producing the spatially variable polarization distribution was used as a specimen to test the practical utilization of the method. Specifically, a structured HWP-like component with a spatially-dependent orientation of the local fast axis, called S-wave plate (SWP), was used. Jones matrix of the SWP of a unitary topological charge is mathematically expressed as

$$\mathbb{T}_{SWP}(\delta) = \begin{bmatrix} \cos(\varphi+\delta) & \sin(\varphi+\delta) \\ \sin(\varphi+\delta) & -\cos(\varphi+\delta) \end{bmatrix}, \tag{7.1}$$

where the orientation of local axis η in the circular aperture of the SWP satisfies equation $\eta = \varphi/2$ with the azimuthal coordinate $\varphi \in [0, 2\pi]$. δ is the rotation angle between the horizontal axis of the system and the position, where the SWP local-axis orientation is collinear to the radial direction. The situation is illustrated in Fig. 7.1. This component is usually used for the generation of radially or azimuthally polarized beams from the linearly polarized illumination or optical vortices from the circularly polarized light.

The SWP used (RCP-632-04) was placed into the object plane of the MO and two inde-

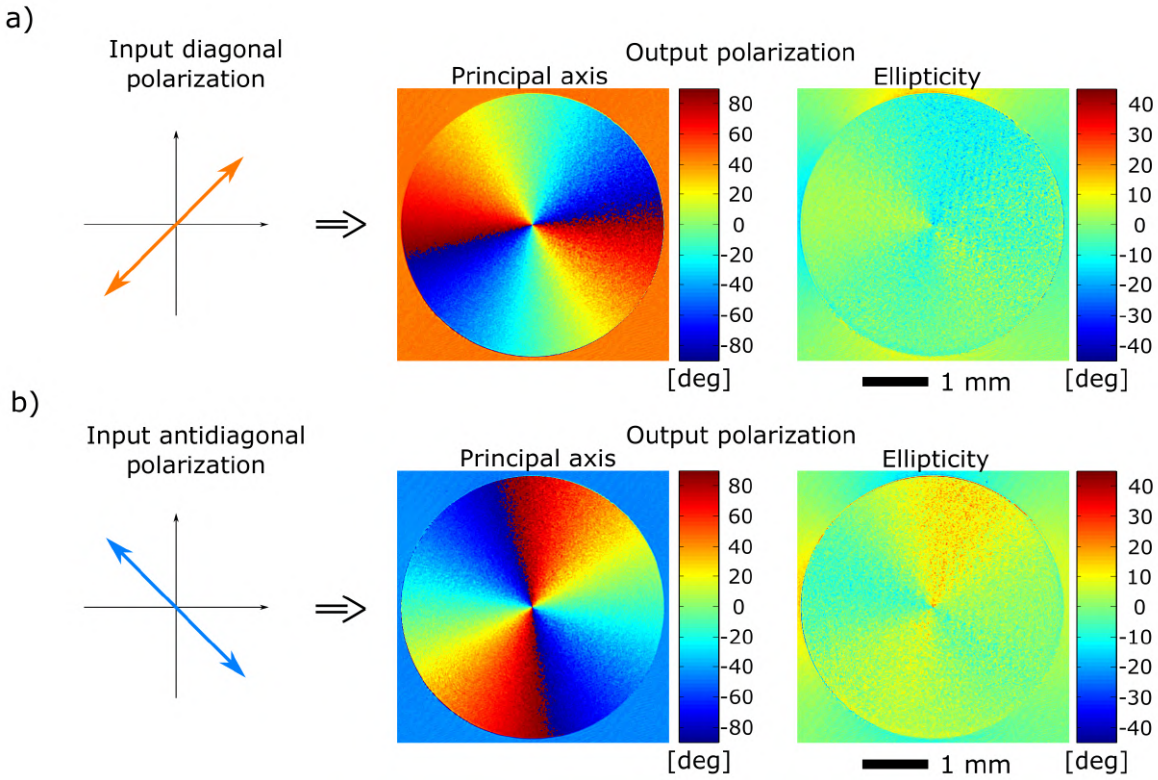

Figure 7.3: Principal axis orientation and ellipticity of the reconstructed output polarization states for diagonally (a) and antidiagonally (b) polarized input illumination beam.

pendent interference patterns were recorded, corresponding to the diagonal and antidiagonal illumination, respectively. Firstly, the interference pattern under the diagonal illumination was captured, numerically processed, and the output Jones vector $\overline{\mathbf{U}}_{\mathbf{s}}^{\mathbf{d}}$ was retrieved as a result. Secondly, the same process was repeated for antidiagonally polarized illumination. Parameters of the reconstructed polarization states $\overline{\mathbf{U}}_{\mathbf{s}}^{\mathbf{d}}$ and $\overline{\mathbf{U}}_{\mathbf{s}}^{\mathbf{a}}$ are visualized in Fig. 7.3.

Subsequently, the Jones matrix of the SWP was reconstructed directly from the $\overline{\mathbf{U}}_{\mathbf{s}}^{\mathbf{d}}$ and $\overline{\mathbf{U}}_{\mathbf{s}}^{\mathbf{a}}$ by applying equation (3.66). The absolute values of the complex amplitudes are illustrated in Fig. 7.4a, which are compared to the theoretical predictions. The correlation coefficients (CCs) of the T_{xx}, T_{xy}, T_{yx}, and T_{yy} are calculated to estimate the similarity reaching the values 0.91, 0.97, 0.96, and 0.95, respectively. Phases of the Jones-matrix elements (Fig. 7.4b) are also compared calculating the CCs with the results 0.93, 0.93, 0.93, and 0.94, respectively. All the CCs are obtained from the evaluations provided inside the whole square areas, except phases of T_{xy}, T_{yx}, where CCs are calculated from the area inside the circular aperture of the SWP. Phases obtained in the area out of this aperture are irrelevant for the quantification because the retrieved amplitudes reach zero levels.

To be complete, two Sagnac modules were additionally exploited in a configuration used for a single-shot Jones matrix reconstruction [245]. The first module was incorporated in the signal arm to simultaneously generate two orthogonally polarized mutually tilted illuminating beams, while the second was situated in the reference arm to generate two orthogonally polarized mutually tilted reference beams as in [242]. The working principle was proved, however, based on the synthetic-aperture principle, mutually tilted illumination beams provide imaging from different parts of the spatial-frequency spectral domain. Hence the method may provide insufficient results for the selected applications.

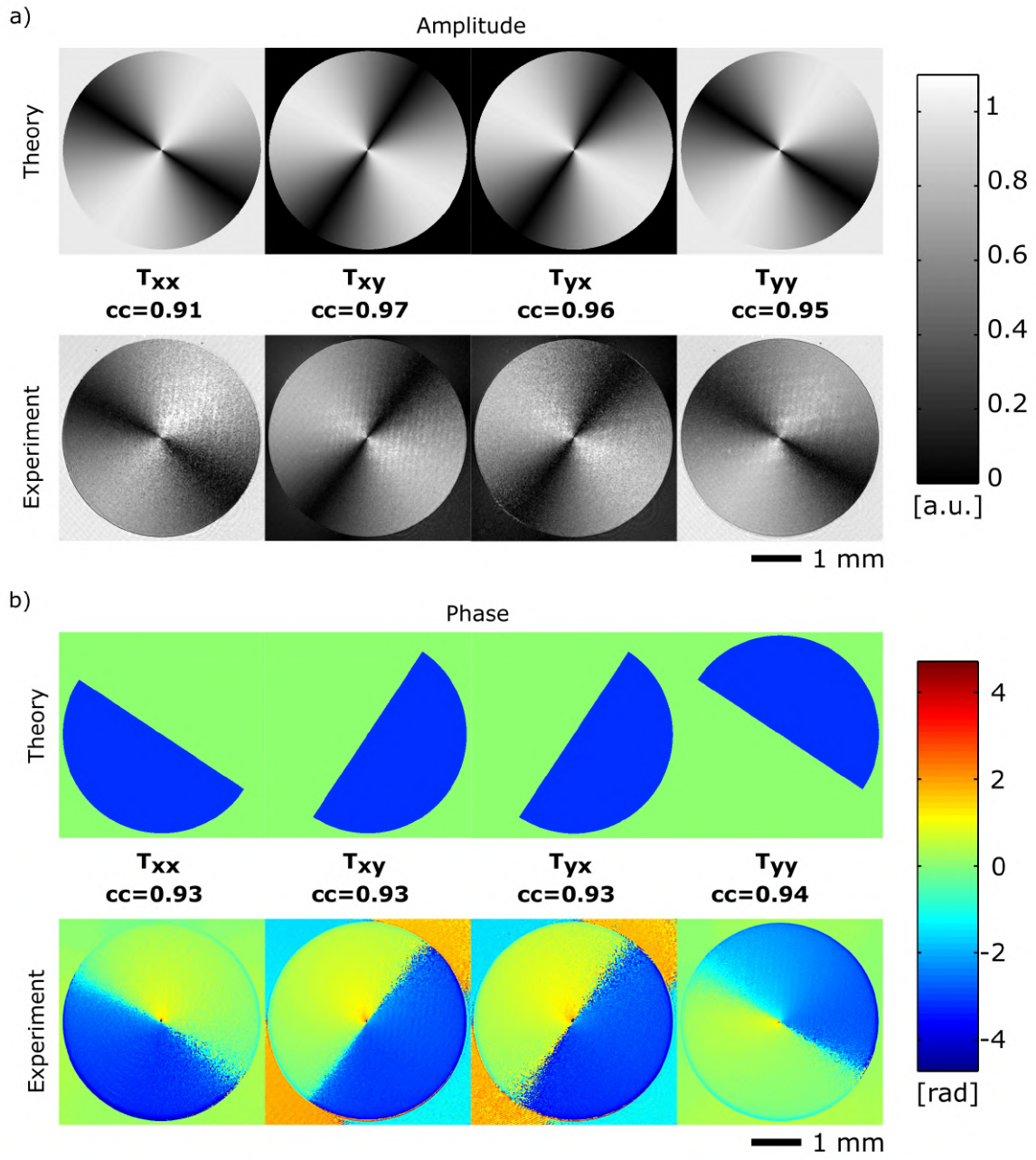

Figure 7.4: Jones matrix of the SWP. The upper rows represent the theoretical predictions and the bottom rows represent the reconstructions obtained by processing the experimantal data. a) Absolute values of the T_{xx}, T_{xy}, T_{yx}, and T_{yy} with the corresponding correlation coefficients (CCs) 0.91, 0.97, 0.96, and 0.95, respectively. b) Phases of the T_{xx}, T_{xy}, T_{yx}, and T_{yy} with the corresponding CCs 0.93, 0.93, 0.93, and 0.94, respectively. All the CCs are evaluated in the displayed areas except the phases of T_{xy}, T_{yx}, which are evaluated just in the circular aperture of the SWP. Phase values out of the aperture are irrelevant because the amplitudes from a) are close to zero.

Chapter 8

Conclusion

In this thesis, the primary outcomes of my Ph.D. studies were discussed. All the investigated problems benefit from and further develop the advantages of digital holography, which serves as a subject of investigation itself as well as an instrument to study and quantify the observed phenomena.

The main goals of the thesis were overviewed in chapter 1. In chapter 2, the digital holography was briefly introduced with emphasis on its extension to optical microscopy. Besides, the contemporary state of research related to the topics discussed was also proposed. Chapter 3 describes used methods, including the separation of holographic terms, holographic reconstruction process, the performance of the lens-less Gabor-like digital holography, the selected background-phase compensation methods, common-path lateral-shearing self-referencing digital holographic microscopy, optical properties of red blood cells, and intensity based writing into the photorefractive material. Chapter 4, chapter 5, chapter 6, and chapter 7 are based on the three original scientific publications [1–3] and present their outcomes, which are summarized in the following text.

In chapter 4, based on publication [1], the imaging performance of the magnified lens-less coherent digital holographic microscopy was investigated. The primary intent aimed to provide experimental parameters appropriate for observing the specimen's enlarged image while preserving the quality of the imaging performance. Initially, a three-dimensional point spread function was designed considering deteriorations originating from the influence of holographic aberrations and the diffraction effects, respectively. The desired magnification was achieved by the mismatch between the parameters of the reference and the reconstruction waves. It was shown that plane wave holographic reconstructions with the expected comparable theoretical resolutions produce very different results based on the various experimental adjustments. In this context, the focal shift effect and asymmetry of the axial point spread function was discussed for the first

time in the digital holography according to our best knowledge. The combination of a low Fresnel number and high magnifications in image space cause the axial asymmetry, and intensity maximum shifted out of the paraxial image plane. In contrast, higher Fresnel numbers and lower magnifications enlarge the deterioration of the three-dimensional point spread function by the spherical aberration. The theoretical criteria were formulated to assess the influence of both effects and were further used to optimize the holographic reconstruction. Indeed, the predictions were approved experimentally by the reconstructed three-dimensional point spread functions from the point holographic records and the measurements realized with the line resolution target.

In chapter 5, based on publication [2], the living cells were employed as optical elements to perform the photolithography into the photoactivable and biocompatible substrate. The main ambition was to create and fix the optical fingerprints of the biological specimen whose properties correlate with its morphology into such material. Notably, red blood cells, lacking any internal organelles, were successfully employed as biolenses. The standard off-axis digital holography arrangement was used, which served simultaneously as an instrument for the realization and characterization of the bio-photolithographic performance. Cells seeded on the top of the x-cut lithium niobate crystal were exposed directly. The structures inside the crystal arose without changing its topography, just reversibly modifying the refractive index distribution. The structures were further investigated through the propagation of a complex amplitude. Similarities and differences between the cells and corresponding imprints were analyzed concerning the anisotropy of the photorefractive effect. Besides, disc-like and spherical-like red blood cells were used due to their different morphologies. The results obtained confirmed the replication of a single layer of both cell types. Hence, exhibiting bi-focal and mono-focal structures for disc-like and spherical-like cells, respectively.

Chapter 6, based on publication [3], proposed the phase-background compensation employing the double-exposure method. Notably, its implementation in common-path self-referencing digital holographic microscopy was introduced, suggesting the optimal concept of phase-background elimination with emphasis on reducing the residual phase defects. Thus the performance of the double-exposure method was extended, whose practical utilization was demonstrated observing various samples. The first experiment was realized in the configuration with a microscope objective, a tube lens, and an integrated Sagnac interferometer used as a shearing device duplicating the field of view. Here, interference of the signal and the reference waves with their replicas were utilized for a single-shot holographic reconstruction, whose phase background was further corrected in

the post-processing procedure. The averaging process of the duplicated phase images also contributed to improving the quality of the final reconstruction. The analysis concluded that the advantageous implementation of the double-exposure method is possible when imaging the self-moving or driven-by-a-flow sparse specimens. It was found that further enhancement of the reconstructed phase-map is feasible in microfluidic applications. The second investigated experimental arrangement represented quasi-common-path geometry. Instead of incorporating the shearing device replicating field of view, just an additional mirror was used to create an off-axis geometry by reflecting a part of the initially unemployed object beam on itself. Firstly, calibration measurements verifying the accuracy of the quantitative reconstruction and the high temporal stability of the interferometer were approved. Furthermore, the experimental measurements with glass beads as a specimen confirmed the previous conclusions valid for optimal implementation of the double-exposure method.

Finally, in chapter 7, the polarization-sensitive imaging by digital holography performed in the Mach-Zehnder experimental arrangement with the incorporated Sagnac module was presented. The method exploited the angular multiplexing principles in the off-axis geometry, and it was realized using common optical elements. Improvement of the temporal stability in the polarization-state reconstruction was quantified and compared to the standard Mach-Zehnder configuration of the identical parameters used for the quantitative phase imaging. Moreover, the imaging capacity was mostly qualitatively tested in measurements carried with the sample generating the spatially variable polarization state distribution. Quantifying the accuracy of this proof-of-concept arrangement is a subject of future experiments.

Chapter 9

Stručné shrnutí v češtině

Předložená práce shrnuje hlavní výsledky dosažené během mého doktorského studia. Všechny studované problémy využívají principů digitální holografie, ať už v kontextu designu vlastního experimentálního uspořádání, nebo jako nástroje pro studium a kvantifikaci studovaných jevů.

V úvodní kapitole jsou vytyčeny hlavní cíle práce. V kapitole 2 je stručně uvedena digitální holografie s důrazem na její aplikace v optické mikroskopii. Dále je diskutován současný stav problematiky. V kapitole 3 jsou zavedeny metody a nástroje potřebné k popisu holografického zobrazovaní včetně separace holografických členů, rekonstrukce holografického obrazu, zobrazování v bezčočkové Gaborově konfiguraci, vybraných metod používaných pro korekci fázového pozadí, mimoosovou digitální holografii se společnou optickou cestou, optické vlastnosti červených krvinek a vznik intenzitou indukovaných nehomogenit ve fotorefraktivních materiálů. Kapitoly $4-7$ vychází z publikací [1–3] a shrnují hlavní dosažené výsledky stručně uvedené v následujícím textu.

Kapitola 4, která je založená na publikaci [1], se zabývá zobrazením v bezčočkové koherentní digitální holografické mikroskopii. Hlavním přínosem práce je nalezení experimentálních parametrů, které umožňují pozorování zvětšeného obrazu s přípustným vlivem holografických aberací a co nejlepší zachovanou rozlišovací schopností. Nejprve byla studována trojrozměrná bodová rozptylová funkce s uvážením vlivu holografických aberací a difrakčních efektů. V tomto kontextu byly poprvé studovány asymetrie axiální bodové rozptylové funkce a posun maxima osová intenzity mimo paraxiální obrazovou rovinu v digitální holografii. Zvětšení nezbytné pro pozorování mikroskopických objektů zde bylo získáno nesouladem mezi parametry referenční a rekonstrukční vlny. Digitální rekonstrukce byla speciálně provedena pro případ rovinné rekonstrukční vlny se zjištěním, že různá volba experimentálních parametrů vede k odlišným výsledkům, a to i v případě srovnatelné teoretické rozlišovací meze. Kombinace nízké hodnoty Fresnelova čísla a rela-

tivně velkého zvětšení v obrazovém prostoru vedou k asymetrii PSF v důsledku difrakce, zatímco vysoké hodnoty Fresnelova čísla a relativně malého zvětšení způsobují degradaci odrazu sférickou aberací. Rozmezí přípustných hodnot experimentálních parametrů bylo určeno pomocí numerických simulací a aproximativních kritérií. Teoretické predikce byly též experimentálně ověřeny rekonstrukcí trojrozměrné bodové rozptylové funkce z bodových holografických záznamů a rekonstrukcí plošného předmětu – amplitudového čárového testu.

V další části práce, která je založená na publikaci [2], bylo studováno využití živých buněk jako optických elementů pro fotolitografický zápis do fotorefraktivního a biokompatibilního materiálu. Hlavním cílem bylo vytvoření a fixace otisků biologického vzorku, s rozdílnými optickými vlastnostmi v závislosti na jejich morfologické stavbě. Jelikož lze červeným krvinkám přiřadit například ohniskovou vzdálenost a zvětšení, naskytla se otázka, zda je možné využít těchto buněk jako optických elementů pro vytvoření fotolitografického otisku. Vrstva krvinek proto byla nanesena na lithium niobátový krystal a exponována laserovým světlem. Otisky krvinek vznikly v krystalu díky lokální modifikaci indexu lomu světla bez změny topologie povrchu. Vlastnosti buněk a struktur byly studované numerickým šířením komplexní amplitudy, která byla rekonstruovaná z interferenčního obrazce zaznamenaného ve standardním dvoucestném digitálním holografickém uspořádání s mimoosovou geometrií. Analogie a rozdíly mezi optickými vlastnostmi krvinek a vzniklých otisků byly analyzovány s uvážením anisotropie fotorefraktivního efektu v lithium niobátovém krystalu. Krvinky diskovitého a sférického tvaru byly dále použity pro jejich odlišnou morfologii. Dosažené výsledky prokazují, že vzniklé struktury vykazují obdobné fokusační vlastnosti, jako původní buňky – v obou případech. A tak vykazují jedno-ohniskovou strukturu v případě sférických a dvoj-ohniskovou v případně diskovitých červených krvinek.

Kapitola 6, která je založená na publikaci [3], prezentuje optimální využití metody dvojí expozice v interferometrech se společnou optickou cestou a mimoosovou geometrií. Tato metoda je založena na zpracování dvou holografických záznamů a umožňuje kompenzaci fázového pozadí bez znalosti jeho přesného numerického modelu. Hlavní přínos této práce spočívá v určení podmínek pro zvýšení kvality rekonstruované fáze s důrazem na potlačení nehomogenit zbytkového fázového pozadí. Praktické využití metody dvojité expozice bylo zkoumáno při pozorování různých vzorků. První experiment byl realizovaný v konfiguraci s objektivem a tubusovou čočkou doplněnou o Sagnacův interferometr, který duplikoval zorné pole a zaváděl střih mezi interferujícími vlnami. Vzniklé duplikované zorné pole bylo u řídkých vzorků též využito pro vylepšení kvality rekonstruovaného obrazu. Analýza

dat zjistila, že implementace metody dvojí expozice je výhodná v aplikacích s pohybujícími se či plovoucími řídkými vzorky. Další vylepšení je dále myslitelné v aplikacích s mikrofluidními kanálky. Druhé experimentální uspořádání reprezentovalo geometrii bez duplikovaného zorného pole s blízkými optickými cestami. Místo komponenty zavádějící střih zde bylo použito přídavné zrcátko. To zajišťovalo mimoosovou geometrii smícháním signální vlny s původně nevyužitou částí předmětového zorného pole. Kalibrační měření potvrdila vysokou časovou stabilitu konfigurace a správnost fázové rekonstrukce. Praktické využití metody bylo konkrétně demonstrováno v měřeních se skleněnými kuličkami a potvrdilo závěry získané z předchozího experimentálního uspořádání se Sagnacovým interferometrem.

Kapitola 7 se zabývá polarizačně citlivým zobrazením s využitím principů digitální holografie. Experimentální uspořádání využívá mimoosové geometrie Mach-Zehnderova interferometru se Sagnacovým modulem vloženým do referenčního ramene. Princip metody spočívá v nekoherentním skládání dvou ortogonálně polarizovaných optických polí, které (každé zvlášť) reprezentují skalární interferenční záznamy. U rekonstrukce polarizačního stavu je prokázaná zvýšená časová stabilita vzhledem k časové stabilitě kvantitativního fázového zobrazování provedeného ve standardním Mach-Zehnderově interferometru shodných optických parametrů. Metoda je převážně kvalitativně testována s využitím anizotropního vzorku jako předmětu, který generuje prostorově závislé rozložení polarizace. Přesnost rekonstrukce tohoto 'proof-of-principle' experimentálního uspořádání bude předmětem následujících zkoumání.

Bibliography

[1] J. Běhal and Z. Bouchal, "Optimizing three-dimensional point spread function in lensless holographic microscopy," *Optics Express*, vol. 25, pp. 29026–29042, 2017.

[2] L. Miccio, J. Behal, M. Mugnano, P. Memmolo, B. Mandracchia, F. Merola, S. Grilli, and P. Ferraro, "Biological lenses as a photomask for writing laser spots into ferroelectric crystals," *ACS Applied Bio Materials*, vol. 2, no. 11, pp. 4675–4680, 2019.

[3] J. Běhal, "Quantitative phase imaging in common-path cross-referenced holographic microscopy using double-exposure method," *Scientific Reports*, vol. 9, no. 9801, 2019.

[4] F. Zernike and F. J. M. Stratton, "Diffraction theory of the knife-edge test and its improved form, the phase-contrast method," *Monthly Notices of the Royal Astronomical Society*, vol. 94, pp. 377–384, 1934.

[5] F. Zernike, "Phase contrast, a new method for the microscopic observation of transparent objects," *Physica*, vol. 9, pp. 686–698, 1942.

[6] F. Zernike, "How I discovered phase contrast," *Science*, vol. 121, no. 3141, pp. 345–349, 1955.

[7] G. Nomarski, "Dispositif oculaire à contraste de phase pour microscope," *Journal De Physique Et Le Radium*, vol. 11, 1950.

[8] C. Edwards, B. Bhaduri, T. Nguyen, B. G. Griffin, H. Pham, T. Kim, G. Popescu, and L. L. Goddard, "Effects of spatial coherence in diffraction phase microscopy," *Optics Express*, vol. 22, pp. 5133–5146, 2014.

[9] C. L. Curl, C. J. Bellair, P. J. Harris, B. E. Allman, A. Roberts, K. A. Nugent, and L. M. Delbridge, "Quantitative phase microscopy: A new tool for investigating the structure and function of unstained live cells," *Clinical and Experimental Pharmacology and Physiology*, vol. 31, pp. 896–901, 2004.

[10] D. Gabor, "A new microscopic principle," *Nature*, vol. 161, no. 4098, pp. 777–778, 1948.

[11] E. N. Leith and J. Upatnieks, "New techniques in wavefront reconstruction," *Journal of the Optical Society of America*, vol. 51, p. 1469, 1961.

[12] L. Camacho, V. Micó, Z. Zalevsky, and J. García, "Quantitative phase microscopy using defocusing by means of a spatial light modulator," *Optics Express*, vol. 18, pp. 6755–6766, 2010.

[13] G. Pedrini, W. Osten, and Y. Zhang, "Wave-front reconstruction from a sequence of interferograms recorded at different planes," *Optics Letters*, vol. 30, pp. 833–835, 2005.

[14] R. W. Gerchberg and W. O. Saxton, "A practical algorithm for the determination of phase from image and diffraction plane pictures," *Optik*, vol. 35, pp. 237–246, 1972.

[15] N. Streibl, "Phase imaging by the transport equation of intensity," *Optics Communications*, vol. 49, pp. 6–10, 1984.

[16] T. Kreis, *Handbook of Holographic Interferometry.* Wiley-Vch, 2005.

[17] D. Malacara, *Optical Shop Testing.* John Wiley & Sons, Inc., 2007.

[18] R. Pawluczyk, "Holographic microinterferometer with noise suppression," *Applied Optics*, vol. 28, pp. 3871–3881, 1989.

[19] G. Dunn and D. Zicha, "Dynamics of fibroblast spreading," *Journal of Cell Science*, vol. 108, pp. 1239–1249, 1995.

[20] J. Farinas and A. S. Verkman, "Cell volume and plasma membrane osmotic water permeability in epithelial cell layers measured by interferometry," *Biophysical Journal*, vol. 71, pp. 3511–3522, 1996.

[21] R. J. Cherry, *New Techniques of Optical Microscopy and Microspectroscopy.* Macmillan Education UK, 1991.

[22] R. Barer, "Interference microscopy and mass determination," *Nature*, vol. 169, no. 4296, pp. 366–367, 1952.

[23] H. G. Davies and M. H. F. Wilkins, "Interference microscopy and mass determination," *Nature*, vol. 169, no. 4300, p. 541, 1952.

[24] J. Yoon, K. Kim, H. Park, C. Choi, S. Jang, and Y. Park, "Label-free characterization of white blood cells by measuring 3D refractive index maps," *Biomedical Optics Express*, vol. 6, pp. 3865–3875, 2015.

[25] R. Leach, *Optical Measurement of Surface Topography.* Springer-Verlag, 2011.

[26] M. León-Rodríguez, J. A. Rayas-Alvarez, A. Martínez-García, and R. R. Cordero, "Microtopography and thickness measurement with digital holographic microscopy highlighting and its tomographic capacity," in *Holographic Materials and Optical Systems*, InTech, 2017.

[27] P. Ferraro, A. Wax, and Z. Zalevsky, *Coherent Light Microscopy.* Springer-Verlag, 2011.

[28] A. Ozcan and E. McLeod, "Lensless imaging and sensing," *Annual Review of Biomedical Engineering*, vol. 18, pp. 77–102, 2016.

[29] S. K. Jericho, J. Garcia-Sucerquia, W. Xu, M. H. Jericho, and H. J. Kreuzer, "Submersible digital in-line holographic microscope," *Review of Scientific Instruments*, vol. 77, no. 043706, 2006.

[30] W. Zhou, Y. Yu, and A. Asundi, "Study on aberration suppressing methods in digital micro-holography," *Optics and Lasers in Engineering*, vol. 47, pp. 264–270, 2009.

[31] I. Yamaguchi and T. Zhang, "Phase-shifting digital holography," *Optics Letters*, vol. 22, pp. 1268–1270, 1997.

[32] T. Zhang and I. Yamaguchi, "Three-dimensional microscopy with phase-shifting digital holography," *Optics Letters*, vol. 23, pp. 1221–1223, 1998.

[33] E. Cuche, P. Marquet, and C. Depeursinge, "Simultaneous amplitude-contrast and quantitative phase-contrast microscopy by numerical reconstruction of fresnel off-axis holograms," *Applied Optics*, vol. 38, pp. 6994–7001, 1999.

[34] E. Sánchez-Ortiga, A. Doblas, G. Saavedra, M. Martínez-Corral, and J. Garcia-Sucerquia, "Off-axis digital holographic microscopy: practical design parameters for operating at diffraction limit," *Applied Optics*, vol. 53, pp. 2058–2066, 2014.

[35] T. Tahara, Y. Awatsuji, K. Nishio, S. Ura, T. Kubota, and O. Matoba, "Comparative analysis and quantitative evaluation of the field of view and the viewing zone of single-shot phase-shifting digital holography using space-division multiplexing," *Optical Review*, vol. 17, pp. 519–524, 2010.

[36] J. Di, J. Zhang, T. Xi, C. Ma, and J. Zhao, "Improvement of measurement accuracy in digital holographic microscopy by using dual-wavelength technique," *Journal of Micro/Nanolithography, MEMS, and MOEMS*, vol. 14, no. 041313, 2015.

[37] W.-C. Hsu, J.-W. Su, T.-Y. Tseng, and K.-B. Sung, "Tomographic diffractive microscopy of living cells based on a common-path configuration," *Optics Letters*, vol. 39, pp. 2210–2213, 2014.

[38] C. Ma, Y. Li, J. Zhang, P. Li, T. Xi, J. Di, and J. Zhao, "Lateral shearing common-path digital holographic microscopy based on a slightly trapezoid sagnac interferometer," *Optics Express*, vol. 25, pp. 13659–13667, 2017.

[39] Z. S. Ballard, Y. Zhang, and A. Ozcan, "Off-axis holography and micro-optics improve lab-on-a-chip imaging," *Light: Science & Applications*, vol. 6, no. e17105, 2017.

[40] V. Bianco, B. Mandracchia, V. Marchesano, V. Pagliarulo, F. Olivieri, S. Coppola, M. Paturzo, and P. Ferraro, "Endowing a plain fluidic chip with micro-optics: a holographic microscope slide," *Light: Science & Applications*, vol. 6, no. e17055, 2017.

[41] M. K. Kim, *Digital Holographic Microscopy*. Springer, 2011.

[42] L. Miccio, A. Finizio, R. Puglisi, D. Balduzzi, A. Galli, and P. Ferraro, "Dynamic DIC by digital holography microscopy for enhancing phase-contrast visualization," *Biomedical Optics Express*, vol. 2, pp. 331–344, 2011.

[43] Y. Liu, Z. Wang, and J. Huang, "Recent progress on aberration compensation and coherent noise suppression in digital holography," *Applied Sciences*, vol. 8, no. 444, 2018.

[44] X. Yu, J. Hong, C. Liu, and M. K. Kim, "Review of digital holographic microscopy for three-dimensional profiling and tracking," *Optical Engineering*, vol. 53, no. 112306, 2014.

[45] P. Memmolo, L. Miccio, M. Paturzo, G. D. Caprio, G. Coppola, P. A. Netti, and P. Ferraro, "Recent advances in holographic 3D particle tracking," *Advances in Optics and Photonics*, vol. 7, pp. 713–755, 2015.

[46] Y. Zhang, H. Wang, Y. Wu, M. Tamamitsu, and A. Ozcan, "Edge sparsity criterion for robust holographic autofocusing," *Optics Letters*, vol. 42, pp. 3824–3827, 2017.

[47] M. Matrecano, M. Paturzo, A. Finizio, and P. Ferraro, "Enhancing depth of focus in tilted microfluidics channels by digital holography," *Optics Letters*, vol. 38, pp. 896–898, 2013.

[48] M. Matrecano, M. Paturzo, and P. Ferraro, "Extended focus imaging in digital holographic microscopy: a review," *Optical Engineering*, vol. 53, no. 112317, 2014.

[49] B. Tayebi, J. hyun Kim, and J.-H. Han, "Review on multi-wavelength quantitative phase microscopy," in *2016 4th International Winter Conference on Brain-Computer Interface (BCI)*, IEEE, 2016.

[50] M. Rubin, G. Dardikman, S. K. Mirsky, N. A. Turko, and N. T. Shaked, "Six-pack off-axis holography," *Optics Letters*, vol. 42, pp. 4611–4614, 2017.

[51] F. Dubois, C. Schockaert, N. Callens, and C. Yourassowsky, "Focus plane detection criteria in digital holography microscopy by amplitude analysis," *Optics Express*, vol. 14, pp. 5895–5908, 2006.

[52] H. Tamura, S. Mori, and T. Yamawaki, "Textural features corresponding to visual perception," *IEEE Transactions on Systems, Man, and Cybernetics*, vol. 8, pp. 460–473, 1978.

[53] P. Memmolo, C. Distante, M. Paturzo, A. Finizio, P. Ferraro, and B. Javidi, "Automatic focusing in digital holography and its application to stretched holograms," *Optics Letters*, vol. 36, pp. 1945–1947, 2011.

[54] P. Memmolo, M. Paturzo, B. Javidi, P. A. Netti, and P. Ferraro, "Refocusing criterion via sparsity measurements in digital holography," *Optics Letters*, vol. 39, pp. 4719–4722, 2014.

[55] M. Liebling and M. Unser, "Autofocus for digital fresnel holograms by use of a fresnelet-sparsity criterion," *Journal of the Optical Society of America A*, vol. 21, pp. 2424–2430, 2004.

[56] P. Langehanenberg, B. Kemper, D. Dirksen, and G. von Bally, "Autofocusing in digital holographic phase contrast microscopy on pure phase objects for live cell imaging," *Applied Optics*, vol. 47, pp. D176–D182, 2008.

[57] B. Skarman, J. Becker, and K. Wozniak, "Simultaneous 3D-PIV and temperature measurements using a new CCD-based holographic interferometer," *Flow Measurement and Instrumentation*, vol. 7, pp. 1–6, 1996.

[58] S. Murata and N. Yasuda, "Potential of digital holography in particle measurement," *Optics & Laser Technology*, vol. 32, pp. 567–574, 2000.

[59] M. Adams, T. M. Kreis, and W. P. O. Jueptner, "Particle size and position measurement with digital holography," in *Optical Inspection and Micromeasurements II* (C. Gorecki, ed.), vol. 3098, SPIE, 1997.

[60] T. M. Kreis, W. P. O. Jueptner, and J. Geldmacher, "Digital holography: methods and applications," in *International Conference on Applied Optical Metrology* (P. K. Rastogi and F. Gyimesi, eds.), vol. 3407, SPIE, 1998.

[61] P. Ferraro, S. D. Nicola, A. Finizio, G. Coppola, S. Grilli, C. Magro, and G. Pierattini, "Compensation of the inherent wave front curvature in digital holographic coherent microscopy for quantitative phase-contrast imaging," *Applied Optics*, vol. 42, pp. 1938–1946, 2003.

[62] T. Colomb, E. Cuche, F. Charrière, J. Kühn, N. Aspert, F. Montfort, P. Marquet, and C. Depeursinge, "Automatic procedure for aberration compensation in digital holographic microscopy and applications to specimen shape compensation," *Applied Optics*, vol. 45, pp. 851–863, 2006.

[63] T. Colomb, J. Kühn, F. Charrière, C. Depeursinge, P. Marquet, and N. Aspert, "Total aberrations compensation in digital holographic microscopy with a reference conjugated hologram," *Optics Express*, vol. 14, pp. 4300–4306, 2006.

[64] Y.-Z. Zhang, D.-Y. Wang, Y.-X. Wang, and S.-Q. Tao, "Automatic compensation of total phase aberrations in digital holographic biological imaging," *Chinese Physics Letters*, vol. 28, no. 114209, 2011.

[65] L. Miccio, D. Alfieri, S. Grilli, P. Ferraro, A. Finizio, L. D. Petrocellis, and S. D. Nicola, "Direct full compensation of the aberrations in quantitative phase microscopy of thin objects by a single digital hologram," *Applied Physics Letters*, vol. 90, no. 041104, 2007.

[66] Y. Liu, Z. Wang, J. Li, J. Gao, and J. Huang, "Total aberrations compensation for misalignment of telecentric arrangement in digital holographic microscopy," *Optical Engineering*, vol. 53, no. 112307, 2014.

[67] C. Zuo, Q. Chen, W. Qu, and A. Asundi, "Phase aberration compensation in digital holographic microscopy based on principal component analysis," *Optics Letters*, vol. 38, pp. 1724–1726, 2013.

[68] E. Cuche, F. Bevilacqua, and C. Depeursinge, "Digital holography for quantitative phase-contrast imaging," *Optics Letters*, vol. 24, pp. 291–293, 1999.

[69] E. Cuche, P. Marquet, and C. Depeursinge, "Spatial filtering for zero-order and twin-image elimination in digital off-axis holography," *Applied Optics*, vol. 39, pp. 4070–4075, 2000.

[70] H.-J. Cho, D.-C. Kim, Y.-H. Yu, S. Shin, and W. Jung, "Tilt aberration compensation using interference patterns in digital holography," *Journal of the Optical Society of Korea*, vol. 13, pp. 451–455, 2009.

[71] W. Qu, C. O. Choo, Y. Yu, and A. Anand, "Microlens characterization by digital holographic microscopy with physical spherical phase compensation," *Applied Optics*, vol. 49, pp. 6448–6454, 2010.

[72] Q. Fan, H. Yang, G. Li, and J. Zhao, "Suppressing carrier removal error in the fourier transform method for interferogram analysis," *Journal of Optics*, vol. 12, no. 115401, 2010.

[73] H. Cui, D. Wang, Y. Wang, J. Zhao, and Y. Zhang, "Phase aberration compensation by spectrum centering in digital holographic microscopy," *Optics Communications*, vol. 284, pp. 4152–4155, 2011.

[74] Y. Du, G. Feng, H. Li, and S. Zhou, "Accurate carrier-removal technique based on zero padding in fourier transform method for carrier interferogram analysis," *Optik*, vol. 125, pp. 1056–1061, 2014.

[75] Y. Liu, Z. Wang, J. Li, J. Gao, and J. Huang, "Phase based method for location of the centers of side bands in spatial frequency domain in off-axis digital holographic microcopy," *Optics and Lasers in Engineering*, vol. 86, pp. 115–124, 2016.

[76] C. J. Mann, P. R. Bingham, V. C. Paquit, and K. W. Tobin, "Quantitative phase imaging by three-wavelength digital holography," *Optics Express*, vol. 16, pp. 9753–9764, 2008.

[77] B. Tayebi, J.-H. Han, F. Sharif, M. R. Jafarfard, and D. Y. Kim, "Compact single-shot four-wavelength quantitative phase microscopy with polarization- and frequency-division demultiplexing," *Optics Express*, vol. 25, pp. 20172–20182, 2017.

[78] B. Javidi, P. Ferraro, S.-H. Hong, S. D. Nicola, A. Finizio, D. Alfieri, and G. Pierattini, "Three-dimensional image fusion by use of multiwavelength digital holography," *Optics Letters*, vol. 30, pp. 144–146, 2005.

[79] P. Ferraro, S. Grilli, L. Miccio, D. Alfieri, S. D. Nicola, A. Finizio, and B. Javidi, "Full color 3-d imaging by digital holography and removal of chromatic aberrations," *Journal of Display Technology*, vol. 4, pp. 97–100, 2008.

[80] P. Memmolo, M. Leo, C. Distante, M. Paturzo, and P. Ferraro, "Coding color three-dimensional scenes and joining different objects by adaptive transformations in digital holography," *Journal of Display Technology*, vol. 11, pp. 854–860, 2015.

[81] T. Tahara, Y. Ito, Y. Lee, P. Xia, J. Inoue, Y. Awatsuji, K. Nishio, S. Ura, T. Kubota, and O. Matoba, "Multiwavelength parallel phase-shifting digital holography using angular multiplexing," *Optics Letters*, vol. 38, pp. 2789–2791, 2013.

[82] N. Lue, J. W. Kang, T. R. Hillman, R. R. Dasari, and Z. Yaqoob, "Single-shot quantitative dispersion phase microscopy," *Applied Physics Letters*, vol. 101, no. 084101, 2012.

[83] B. Rappaz, P. Marquet, E. Cuche, Y. Emery, C. Depeursinge, and P. J. Magistretti, "Measurement of the integral refractive index and dynamic cell morphometry of living cells with digital holographic microscopy," *Optics Express*, vol. 13, pp. 9361–9373, 2005.

[84] B. Rappaz, A. Barbul, F. Charrière, J. Kühn, P. Marquet, R. Korenstein, C. Depeursinge, and P. Magistretti, "Erythrocytes analysis with a digital holographic microscope," in *Novel Optical Instrumentation for Biomedical Applications III* (C. D. Depeursinge, ed.), vol. 6631, SPIE, 2007.

[85] M. R. Jafarfard, S. Moon, B. Tayebi, and D. Y. Kim, "Dual-wavelength diffraction phase microscopy for simultaneous measurement of refractive index and thickness," *Optics Letters*, vol. 39, pp. 2908–2911, 2014.

[86] B. W. Schilling, T.-C. Poon, G. Indebetouw, B. Storrie, K. Shinoda, Y. Suzuki, and M. H. Wu, "Three-dimensional holographic fluorescence microscopy," *Optics Letters*, vol. 22, pp. 1506–1508, 1997.

[87] J. Rosen and G. Brooker, "Non-scanning motionless fluorescence three-dimensional holographic microscopy," *Nature Photonics*, vol. 2, no. 3, pp. 190–195, 2008.

[88] J. Rosen and G. Brooker, "Fluorescence incoherent color holography," *Optics Express*, vol. 15, pp. 2244–2250, 2007.

[89] P. Bouchal and Z. Bouchal, "Concept of coherence aperture and pathways toward white light high-resolution correlation imaging," *New Journal of Physics*, vol. 15, no. 123002, 2013.

[90] Y. Park, G. Popescu, K. Badizadegan, R. R. Dasari, and M. S. Feld, "Diffraction phase and fluorescence microscopy," *Optics Express*, vol. 14, pp. 8263–8268, 2006.

[91] F. Dubois, M.-L. N. Requena, C. Minetti, O. Monnom, and E. Istasse, "Partial spatial coherence effects in digital holographic microscopy with a laser source," *Applied Optics*, vol. 43, pp. 1131–1139, 2004.

[92] Y. Choi, T. D. Yang, K. J. Lee, and W. Choi, "Full-field and single-shot quantitative phase microscopy using dynamic speckle illumination," *Optics Letters*, vol. 36, pp. 2465–2467, 2011.

[93] H. Farrokhi, J. Boonruangkan, B. J. Chun, T. M. Rohith, A. Mishra, H. T. Toh, H. S. Yoon, and Y.-J. Kim, "Speckle reduction in quantitative phase imaging by generating spatially incoherent laser field at electroactive optical diffusers," *Optics Express*, vol. 25, pp. 10791–10800, 2017.

[94] C. Quan, X. Kang, and C. J. Tay, "Speckle noise reduction in digital holography by multiple holograms," *Optical Engineering*, vol. 46, no. 115801, 2007.

[95] J. Garcia-Sucerquia, J. H. Ramírez, and R. Castaneda, "Incoherent recovering of the spatial resolution in digital holography," *Optics Communications*, vol. 260, pp. 62–67, 2005.

[96] J. Herrera-Ramirez, D. A. Hincapie-Zuluaga, and J. Garcia-Sucerquia, "Speckle noise reduction in digital holography by slightly rotating the object," *Optical Engineering*, vol. 55, no. 121714, 2016.

[97] F. Pan, W. Xiao, S. Liu, F. Wang, L. Rong, and R. Li, "Coherent noise reduction in digital holographic phase contrast microscopy by slightly shifting object," *Optics Express*, vol. 19, pp. 3862–3869, 2011.

[98] T. Baumbach, E. Kolenovic, V. Kebbel, and W. Jüptner, "Improvement of accuracy in digital holography by use of multiple holograms," *Applied Optics*, vol. 45, pp. 6077–6085, 2006.

[99] F. Pan, W. Xiao, S. Liu, and L. Rong, "Coherent noise reduction in digital holographic microscopy by laterally shifting camera," *Optics Communications*, vol. 292, pp. 68–72, 2013.

[100] J. Kühn, F. Charrière, T. Colomb, E. Cuche, F. Montfort, Y. Emery, P. Marquet, and C. Depeursinge, "Axial sub-nanometer accuracy in digital holographic microscopy," *Measurement Science and Technology*, vol. 19, no. 074007, 2008.

[101] B. Kemper, S. Stürwald, C. Remmersmann, P. Langehanenberg, and G. von Bally, "Characterisation of light emitting diodes (LEDs) for application in digital holographic microscopy for inspection of micro and nanostructured surfaces," *Optics and Lasers in Engineering*, vol. 46, pp. 499–507, 2008.

[102] L. Martínez-León, G. Pedrini, and W. Osten, "Applications of short-coherence digital holography in microscopy," *Applied Optics*, vol. 44, pp. 3977–3984, 2005.

[103] F. Dubois, L. Joannes, and J.-C. Legros, "Improved three-dimensional imaging with a digital holography microscope with a source of partial spatial coherence," *Applied Optics*, vol. 38, pp. 7085–7094, 1999.

[104] M. León-Rodríguez, R. Rodríguez-Vera, J. A. Rayas, and S. Calixto, "High topographical accuracy by optical shot noise reduction in digital holographic microscopy," *Journal of the Optical Society of America A*, vol. 29, pp. 498–506, 2012.

[105] J. Garcia-Sucerquia, "Noise reduction in digital lensless holographic microscopy by engineering the light from a light-emitting diode," *Applied Optics*, vol. 52, pp. A232–A239, 2012.

[106] J. Zheng, V. Micó, and P. Gao, "Resolution enhancement in phase microscopy: a review," *Preprints*, 2018. 2018030273.

[107] S. A. Alexandrov, T. R. Hillman, T. Gutzler, and D. D. Sampson, "Synthetic aperture fourier holographic optical microscopy," *Physical Review Letters*, vol. 97, no. 168102, 2006.

[108] M. Kim, Y. Choi, C. Fang-Yen, Y. Sung, R. R. Dasari, M. S. Feld, and W. Choi, "High-speed synthetic aperture microscopy for live cell imaging," *Optics Letters*, vol. 36, pp. 148–150, 2011.

[109] A.-H. Phan, J.-H. Park, and N. Kim, "Super-resolution digital holographic microscopy for three dimensional sample using multipoint light source illumination," *Japanese Journal of Applied Physics*, vol. 50, no. 092503, 2011.

[110] V. Mico, Z. Zalevsky, and J. García, "Superresolution optical system by common-path interferometry," *Optics Express*, vol. 14, pp. 5168–5177, 2006.

[111] M. Paturzo and P. Ferraro, "Correct self-assembling of spatial frequencies in super-resolution synthetic aperture digital holography," *Optics Letters*, vol. 34, pp. 3650–3652, 2009.

[112] J. P. Wilde, J. W. Goodman, Y. C. Eldar, and Y. Takashima, "Coherent superresolution imaging via grating-based illumination," *Applied Optics*, vol. 56, pp. A79–A88, 2017.

[113] S. Li, J. Ma, C. Chang, S. Nie, S. Feng, and C. Yuan, "Phase-shifting-free resolution enhancement in digital holographic microscopy under structured illumination," *Optics Express*, vol. 26, pp. 23572–23584, 2018.

[114] S. K. Mirsky and N. T. Shaked, "First experimental realization of six-pack holography and its application to dynamic synthetic aperture superresolution," *Optics Express*, vol. 27, pp. 26708–26720, 2019.

[115] A. Hussain, J. L. Martinez, and J. Campos, "Holographic superresolution using spatial light modulator," *Journal of the European Optical Society: Rapid Publications*, vol. 8, no. 13007, 2013.

[116] A. Hussain, J. L. Martínez, A. Lizana, and J. Campos, "Super resolution imaging achieved by using on-axis interferometry based on a spatial light modulator," *Optics Express*, vol. 21, pp. 9615–9623, 2013.

[117] Q. Lin, D. Wang, Y. Wang, L. Rong, and S. Chang, "Super-resolution imaging in digital holography by using dynamic grating with a spatial light modulator," *Optics and Lasers in Engineering*, vol. 66, pp. 279–284, 2015.

[118] H.-Y. Tu, X.-J. Lai, Y.-C. Lin, and C.-J. Cheng, "Angular- and polarization-multiplexing with spatial light modulators for resolution enhancement in digital holographic microscopy," in *Digital Holography & 3-D Imaging Meeting*, OSA, 2015.

[119] X.-J. Lai, H.-Y. Tu, Y.-C. Lin, and C.-J. Cheng, "Coded aperture structured illumination digital holographic microscopy for superresolution imaging," *Optics Letters*, vol. 43, pp. 1143–1146, 2018.

[120] V. Balasubramani, H.-Y. Tu, X.-J. Lai, and C.-J. Cheng, "Adaptive wavefront correction structured illumination holographic tomography," *Scientific Reports*, vol. 9, no. 10489, 2019.

[121] V. Mico, Z. Zalevsky, P. García-Martínez, and J. García, "Synthetic aperture superresolution with multiple off-axis holograms," *Journal of the Optical Society of America A*, vol. 23, pp. 3162–3170, 2006.

[122] E. Sánchez-Ortiga, M. Martínez-Corral, G. Saavedra, and J. Garcia-Sucerquia, "Enhancing spatial resolution in digital holographic microscopy by biprism structured illumination," *Optics Letters*, vol. 39, pp. 2086–2089, 2014.

[123] L. Martínez-León and B. Javidi, "Synthetic aperture single-exposure on-axis digital holography," *Optics Express*, vol. 16, pp. 161–169, 2008.

[124] M. Gu, *Principles of Three-Dimensional Imaging in Confocal Microscopes*. World Scientific, 1996.

[125] P. Marquet, B. Rappaz, P. J. Magistretti, E. Cuche, Y. Emery, T. Colomb, and C. Depeursinge, "Digital holographic microscopy: a noninvasive contrast imaging technique allowing quantitative visualization of living cells with subwavelength axial accuracy," *Optics Letters*, vol. 30, pp. 468–470, 2005.

[126] G. Zheng, R. Horstmeyer, and C. Yang, "Wide-field, high-resolution fourier ptychographic microscopy," *Nature Photonics*, vol. 7, no. 9, pp. 739–745, 2013.

[127] G. Grover, K. DeLuca, S. Quirin, J. DeLuca, and R. Piestun, "Super-resolution photon-efficient imaging by nanometric double-helix point spread function localization of emitters (SPINDLE)," *Optics Express*, vol. 20, pp. 26681–26695, 2012.

[128] H. D. Lee, S. J. Sahl, M. D. Lew, and W. E. Moerner, "The double-helix microscope super-resolves extended biological structures by localizing single blinking molecules in three dimensions with nanoscale precision," *Applied Physics Letters*, vol. 100, no. 153701, 2012.

[129] K. Dholakia and T. Čižmár, "Shaping the future of manipulation," *Nature Photonics*, vol. 5, no. 6, pp. 335–342, 2011.

[130] E. Wolf and Y. Li, "Conditions for the validity of the debye integral representation of focused fields," *Optics Communications*, vol. 39, pp. 205–210, 1981.

[131] D. A. Holmes, J. E. Korka, and P. V. Avizonis, "Parametric study of apertured focused gaussian beams," *Applied Optics*, vol. 11, p. 565, 1972.

[132] A. Arimoto, "Intensity distribution of aberration-free diffraction patterns due to circular apertures in large F-number optical systems," *Optica Acta: International Journal of Optics*, vol. 23, pp. 245–250, 1976.

[133] M. A. Gusinow, M. E. Riley, and M. A. Palmer, "Focusing in a largeF-number optical system," *Optical and Quantum Electronics*, vol. 9, pp. 465–471, 1977.

[134] J. H. Erkkila and M. E. Rogers, "Diffracted fields in the focal volume of a converging wave," *Journal of the Optical Society of America*, vol. 71, pp. 904–905, 1981.

[135] Y. Li and E. Wolf, "Focal shift in diffracted converging spherical waves," *Optics Communications*, vol. 39, pp. 211–215, 1981.

[136] Y. Li and H. Platzer, "An experimental investigation of diffraction patterns in low-fresnel-number focusing systems," *Optica Acta: International Journal of Optics*, vol. 30, pp. 1621–1643, 1983.

[137] G. P. Karman, M. W. Beijersbergen, A. van Duijl, and J. P. Woerdman, "Creation and annihilation of phase singularities in a focal field," *Optics Letters*, vol. 22, pp. 1503–1505, 1997.

[138] H. Kogelnik, "Imaging of optical modes - resonators with internal lenses," *Bell System Technical Journal*, vol. 44, pp. 455–494, 1965.

[139] Y. Li, "Focal shift formula for focused, apertured gaussian beams," *Journal of Modern Optics*, vol. 39, pp. 1761–1764, 1992.

[140] Y. Li and E. Wolf, "Focal shift in focused truncated gaussian beams," *Optics Communications*, vol. 42, pp. 151–156, 1982.

[141] S. D. Nicola, "On-axis focal shift effects in focused truncated J_0 Bessel beams," *Pure and Applied Optics: Journal of the European Optical Society Part A*, vol. 5, pp. 827–831, 1996.

[142] G. Zhou, "Focal shift of focused truncated Lorentz-Gauss beam," *Journal of the Optical Society of America A*, vol. 25, pp. 2594–2599, 2008.

[143] R. Borghi, M. Santarsiero, and S. Vicalvi, "Focal shift of focused flat-topped beams," *Optics Communications*, vol. 154, pp. 243–248, 1998.

[144] A. T. Friberg, T. D. Visser, W. Wang, and E. Wolf, "Focal shifts of converging diffracted waves of any state of spatial coherence," *Optics Communications*, vol. 196, pp. 1–7, 2001.

[145] J. Ojeda-Castañeda, M. Martínez-Corral, P. Andrés, and A. Pons, "Strehl ratio versus defocus for noncentrally obscured pupils," *Applied Optics*, vol. 33, pp. 7611–7616, 1994.

[146] M. Martínez-Corral and V. Climent, "Focal switch: a new effect in low-Fresnel-number systems," *Applied Optics*, vol. 35, pp. 24–27, 1996.

[147] Y. Yu and H. Zappe, "Effect of lens size on the focusing performance of plasmonic lenses and suggestions for the design," *Optics Express*, vol. 19, pp. 9434–9444, 2011.

[148] Y. Yu and H. Zappe, "Theory and implementation of focal shift of plasmonic lenses," *Optics Letters*, vol. 37, pp. 1592–1594, 2012.

[149] Y. Gao, J. Liu, X. Zhang, Y. Wang, Y. Song, S. Liu, and Y. Zhang, "Analysis of focal-shift effect in planar metallic nanoslit lenses," *Optics Express*, vol. 20, pp. 1320–1329, 2012.

[150] R. Ma, Y. Li, Y. Liu, Z. Yu, X. Long, L. Chen, D. Wu, and H. Ye, "Focal shift of nano-optical lens affected by periodic resonance with substrate," *IEEE Photonics Journal*, vol. 8, pp. 1–9, 2016.

[151] M. M. Shanei, M. Hashemi, D. Fathi, and C. J. Zapata-Rodríguez, "Dielectric metalenses with engineered point spread function," *Applied Optics*, vol. 56, pp. 8917–8923, 2017.

[152] M. Hashemi, A. Moazami, M. Naserpour, and C. J. Zapata-Rodríguez, "Amplitude modulation technique for designing metalenses with apodized and enhanced resolution focal spots," *Optics Communications*, vol. 393, pp. 77–82, 2017.

[153] Y. Jia, "Focal shift in metasurface based lenses," *Optics Express*, vol. 26, pp. 8001–8015, 2018.

[154] D. Y. Lu, X. Cao, K. J. Wang, M. D. He, D. Wang, J. Li, X. M. Zhang, L. Liu, J. H. Luo, Z. Li, J. Q. Liu, L. Xu, W. D. Hu, and X. Chen, "Broadband reflective lens in visible band based on aluminum plasmonic metasurface," *Optics Express*, vol. 26, pp. 34956–34964, 2018.

[155] P. Bouchal, L. Štrbková, Z. Dostál, R. Chmelík, and Z. Bouchal, "Geometric-phase microscopy for quantitative phase imaging of isotropic, birefringent and space-variant polarization samples," *Scientific Reports*, vol. 9, no. 3608, 2019.

[156] J. Běhal, P. Bouchal, P. Schovánek, T. Fordey, and Z. Bouchal, "Axial asymmetry in holographic and incoherent correlation imaging," in *20th Slovak-Czech-Polish Optical Conference on Wave and Quantum Aspects of Contemporary Optics* (J. Müllerová, D. Senderáková, L. Ladányi, and Ľ. Scholtz, eds.), vol. 10142, SPIE, 2016.

[157] C. A. Mack, *Field Guide to Optical Lithography*. SPIE Publications, 2006.

[158] C. Mack, *Fundamental Principles of Optical Lithography*. John Wiley & Sons, Ltd, 2007.

[159] T. Ito and S. Okazaki, "Pushing the limits of lithography," *Nature*, vol. 406, no. 6799, pp. 1027–1031, 2000.

[160] D. Qin, Y. Xia, and G. M. Whitesides, "Soft lithography for micro- and nanoscale patterning," *Nature Protocols*, vol. 5, no. 3, pp. 491–502, 2010.

[161] C.-W. Li and G.-J. Wang, "MEMS manufacturing techniques for tissue scaffolding devices," in *MEMS for Biomedical Applications*, pp. 192–217, Elsevier, 2012.

[162] H. Kavand, H. van Lintel, S. B. Sichani, S. Bonakdar, H. Kavand, J. Koohsorkhi, and P. Renaud, "Cell-imprint surface modification by contact photolithography-based approaches: Direct-cell photolithography and optical soft lithography using PDMS cell imprints," *ACS Applied Materials & Interfaces*, vol. 11, pp. 10559–10566, 2019.

[163] Y. K. Jung, C. Jung, and H. G. Park, "Photopatterned polydiacetylene images using a DNA bio-photomask," *ACS Applied Materials & Interfaces*, vol. 8, pp. 15684–15690, 2016.

[164] Y. Li, X. Liu, X. Yang, H. Lei, Y. Zhang, and B. Li, "Enhancing upconversion fluorescence with a natural bio-microlens," *ACS Nano*, vol. 11, pp. 10672–10680, 2017.

[165] Y. Li, H. Xin, Y. Zhang, H. Lei, T. Zhang, H. Ye, J. J. Saenz, C.-W. Qiu, and B. Li, "Living nanospear for near-field optical probing," *ACS Nano*, vol. 12, pp. 10703–10711, 2018.

[166] A. Kuzyk, R. Jungmann, G. P. Acuna, and N. Liu, "DNA origami route for nanophotonics," *ACS Photonics*, vol. 5, pp. 1151–1163, 2018.

[167] N. C. Carville, L. Collins, M. Manzo, K. Gallo, B. I. Lukasz, K. K. McKayed, J. C. Simpson, and B. J. Rodriguez, "Biocompatibility of ferroelectric lithium niobate and the influence of polarization charge on osteoblast proliferation and function," *Journal of Biomedical Materials Research Part A*, vol. 103, pp. 2540–2548, 2014.

[168] A. Blázquez-Castro, A. García-Cabañes, and M. Carrascosa, "Biological applications of ferroelectric materials," *Applied Physics Reviews*, vol. 5, no. 041101, 2018.

[169] P. Gunter and J. P. Huignard, *Photorefractive Materials and Their Applications*. Springer-Verlag, 2006.

[170] S. Gorelick and A. de Marco, "Refractive micro-lenses and micro-axicons in single-crystal lithium niobate," *Optics Express*, vol. 26, pp. 32324–32331, 2018.

[171] L. Arizmendi, "Photonic applications of lithium niobate crystals," *physica status solidi (a)*, vol. 201, pp. 253–283, 2004.

[172] K. Buse, "Light-induced charge transport processes in photorefractive crystals i: Models and experimental methods," *Applied Physics B: Lasers and Optics*, vol. 64, pp. 273–291, 1997.

[173] V. M. N. Passaro and F. Magno, "Holographic gratings in photorefractive materials: A review," *Laser Physics*, vol. 17, pp. 231–243, 2007.

[174] N. Tarjányi, "Specially shaped negative lens produced in a lithium niobate crystal," *Optical Engineering*, vol. 53, no. 057104, 2014.

[175] V. Mizeikis, "Direct laser writing: Versatile tool for microfabrication of lithium niobate," *Journal of Laser Micro/Nanoengineering*, vol. 7, pp. 345–350, 2012.

[176] L. Vittadello, A. Zaltron, N. Argiolas, M. Bazzan, N. Rossetto, and R. Signorini, "Photorefractive direct laser writing," *Journal of Physics D: Applied Physics*, vol. 49, no. 125103, 2016.

[177] M. Bazzan and C. Sada, "Optical waveguides in lithium niobate: Recent developments and applications," *Applied Physics Reviews*, vol. 2, no. 040603, 2015.

[178] J. Lv, Y. Cheng, W. Yuan, X. Hao, and F. Chen, "Three-dimensional femtosecond laser fabrication of waveguide beam splitters in $LiNbO_3$ crystal," *Optical Materials Express*, vol. 5, pp. 1274–1280, 2015.

[179] J. Qi, P. Wang, Y. Liao, W. Chu, Z. Liu, Z. Wang, L. Qiao, and Y. Cheng, "Fabrication of polarization-independent single-mode waveguides in lithium niobate crystal with femtosecond laser pulses," *Optical Materials Express*, vol. 6, pp. 2554–2559, 2016.

[180] J. Villarroel, H. Burgos, Á. García-Cabañes, M. Carrascosa, A. Blázquez-Castro, and F. Agulló-López, "Photovoltaic versus optical tweezers," *Optics Express*, vol. 19, pp. 24320–24330, 2011.

[181] M. Carrascosa, A. García-Cabañes, M. Jubera, J. B. Ramiro, and F. Agulló-López, "$LiNbO_3$: A photovoltaic substrate for massive parallel manipulation and patterning of nano-objects," *Applied Physics Reviews*, vol. 2, no. 040605, 2015.

[182] A. García-Cabañes, A. Blázquez-Castro, L. Arizmendi, F. Agulló-López, and M. Carrascosa, "Recent achievements on photovoltaic optoelectronic tweezers based on lithium niobate," *Crystals*, vol. 8, no. 65, 2018.

[183] C. Arregui, J. B. Ramiro, Á. Alcázar, Á. Méndez, H. Burgos, Á. García-Cabañes, and M. Carrascosa, "Optoelectronic tweezers under arbitrary illumination patterns: theoretical simulations and comparison to experiment," *Optics Express*, vol. 22, pp. 29099–29110, 2014.

[184] H. Burgos, M. Jubera, J. Villarroel, A. García-Cabañes, F. Agulló-López, and M. Carrascosa, "Role of particle anisotropy and deposition method on the patterning of nano-objects by the photovoltaic effect in $LiNbO_3$," *Optical Materials*, vol. 35, pp. 1700–1705, 2013.

[185] M. Esseling, F. Holtmann, M. Woerdemann, and C. Denz, "Two-dimensional dielectrophoretic particle trapping in a hybrid crystal/PDMS-system," *Optics Express*, vol. 18, pp. 17404–17411, 2010.

[186] L. Miccio, P. Memmolo, S. Grilli, and P. Ferraro, "All-optical microfluidic chips for reconfigurable dielectrophoretic trapping through SLM light induced patterning," *Lab on a Chip*, vol. 12, pp. 4449–4454, 2012.

[187] L. Miccio, V. Marchesano, M. Mugnano, S. Grilli, and P. Ferraro, "Light induced DEP for immobilizing and orienting escherichia coli bacteria," *Optics and Lasers in Engineering*, vol. 76, pp. 34–39, 2016.

[188] R. Rega, O. Gennari, L. Mecozzi, S. Grilli, V. Pagliarulo, and P. Ferraro, "Bipolar patterning of polymer membranes by pyroelectrification," *Advanced Materials*, vol. 28, pp. 454–459, 2016.

[189] V. Marchesano, O. Gennari, L. Mecozzi, S. Grilli, and P. Ferraro, "Effects of lithium niobate polarization on cell adhesion and morphology," *ACS Applied Materials & Interfaces*, vol. 7, pp. 18113–18119, 2015.

[190] C. Christophis, E. A. Cavalcanti-Adam, M. Hanke, K. Kitamura, A. Gruverman, M. Grunze, P. A. Dowben, and A. Rosenhahn, "Adherent cells avoid polarization gradients on periodically poled $LiTaO_3$ ferroelectrics," *Biointerphases*, vol. 8, no. 27, 2013.

[191] D. Kilinc, A. Blasiak, M. A. Baghban, N. C. Carville, A. Al-Adli, R. M. Al-Shammari, J. H. Rice, G. U. Lee, K. Gallo, and B. J. Rodriguez, "Charge and topography patterned lithium niobate provides physical cues to fluidically isolated cortical axons," *Applied Physics Letters*, vol. 110, no. 053702, 2017.

[192] M. C. Gather and S. H. Yun, "Single-cell biological lasers," *Nature Photonics*, vol. 5, no. 7, pp. 406–410, 2011.

[193] A. H. Fikouras, M. Schubert, M. Karl, J. D. Kumar, S. J. Powis, A. D. Falco, and M. C. Gather, "Non-obstructive intracellular nanolasers," *Nature Communications*, vol. 9, no. 4817, 2018.

[194] H. Xin, Y. Li, X. Liu, and B. Li, "Escherichia coli-based biophotonic waveguides," *Nano Letters*, vol. 13, pp. 3408–3413, 2013.

[195] V. Bianco, V. Marchesano, A. Finizio, M. Paturzo, and P. Ferraro, "Self-propelling bacteria mimic coherent light decorrelation," *Optics Express*, vol. 23, pp. 9388–9396, 2015.

[196] L. Miccio, P. Memmolo, F. Merola, P. A. Netti, and P. Ferraro, "Red blood cell as an adaptive optofluidic microlens," *Nature Communications*, vol. 6, no. 6502, 2015.

[197] P. Memmolo, F. Merola, L. Miccio, M. Mugnano, and P. Ferraro, "Investigation on dynamics of red blood cells through their behavior as biophotonic lenses," *Journal of Biomedical Optics*, vol. 21, no. 121509, 2016.

[198] F. Merola, Á. Barroso, L. Miccio, P. Memmolo, M. Mugnano, P. Ferraro, and C. Denz, "Biolens behavior of RBCs under optically-induced mechanical stress," *Cytometry Part A*, vol. 91, pp. 527–533, 2017.

[199] M. Mugnano, P. Memmolo, L. Miccio, F. Merola, V. Bianco, A. Bramanti, A. Gambale, R. Russo, I. Andolfo, A. Iolascon, and P. Ferraro, "Label-free optical marker for red-blood-cell phenotyping of inherited anemias," *Analytical Chemistry*, vol. 90, pp. 7495–7501, 2018.

[200] P. Memmolo, L. Miccio, F. Merola, M. Mugnano, and P. Ferraro, "Hydrodynamic red blood cells deformation by quantitative phase microscopy and zernike polynomials," *Frontiers in Physics*, vol. 7, no. 111, 2019.

[201] F. Merola, P. Memmolo, L. Miccio, R. Savoia, M. Mugnano, A. Fontana, G. D'Ippolito, A. Sardo, A. Iolascon, A. Gambale, and P. Ferraro, "Tomographic flow cytometry by digital holography," *Light: Science & Applications*, vol. 6, no. e16241, 2016.

[202] X. Liu, Y. Li, X. Xu, Y. Zhang, and B. Li, "Red-blood-cell-based microlens: Application to single-cell membrane imaging and stretching," *ACS Applied Bio Materials*, vol. 2, pp. 2889–2895, 2019.

[203] P. Memmolo, L. Miccio, F. Merola, and P. Ferraro, "Talbot effect in self-assembled red blood cells investigated by digital holography," *Journal of Physics: Photonics*, 2020.

[204] W. Qu, Y. Yu, C. O. Choo, and A. Anand, "Digital holographic microscopy with physical phase compensation," *Optics Letters*, vol. 34, pp. 1276–1278, 2009.

[205] W. Qu, K. Bhattacharya, C. O. Choo, Y. Yu, and A. Anand, "Transmission digital holographic microscopy based on a beam-splitter cube interferometer," *Applied Optics*, vol. 48, pp. 2778–2783, 2009.

[206] W. Qu, O. C. Chee, Y. Yu, and A. Anand, "Characterization and inspection of microlens array by single cube beam splitter microscopy," *Applied Optics*, vol. 50, pp. 886–890, 2011.

[207] B. Lam and C. Guo, "Complete characterization of ultrashort optical pulses with a phase-shifting wedged reversal shearing interferometer," *Light: Science & Applications*, vol. 7, no. 30, 2018.

[208] M. León-Rodríguez, J. A. Rayas, R. R. Cordero, A. Martínez-García, A. Martínez-Gonzalez, A. Téllez-Quiñones, P. Yañez-Contreras, and O. Medina-Cázares, "Dual-plane slightly off-axis digital holography based on a single cube beam splitter," *Applied Optics*, vol. 57, pp. 2727–2735, 2018.

[209] A. S. G. Singh, A. Anand, R. A. Leitgeb, and B. Javidi, "Lateral shearing digital holographic imaging of small biological specimens," *Optics Express*, vol. 20, pp. 23617–23622, 2012.

[210] A. Anand, P. Vora, S. Mahajan, V. Trivedi, V. Chhaniwal, A. Singh, R. Leitgeb, and B. Javidi, "Compact, common path quantitative phase microscopic techniques for imaging cell dynamics," *Pramana*, vol. 82, pp. 71–78, 2014.

[211] K.-B. Seo, B.-M. Kim, and E.-S. Kim, "Digital holographic microscopy based on a modified lateral shearing interferometer for three-dimensional visual inspection of nanoscale defects on transparent objects," *Nanoscale Research Letters*, vol. 9, no. 471, 2014.

[212] J. Di, Y. Li, M. Xie, J. Zhang, C. Ma, T. Xi, E. Li, and J. Zhao, "Dual-wavelength common-path digital holographic microscopy for quantitative phase imaging based on lateral shearing interferometry," *Applied Optics*, vol. 55, pp. 7287–7293, 2016.

[213] B.-M. Kim and E.-S. Kim, "Visual inspection of 3-d surface and refractive-index profiles of microscopic lenses using a single-arm off-axis holographic interferometer," *Optics Express*, vol. 24, pp. 10326–10344, 2016.

[214] B.-M. Kim, S.-J. Park, and E.-S. Kim, "Single-shot digital holographic microscopy with a modified lateral-shearing interferometer based on computational telecentricity," *Optics Express*, vol. 25, pp. 6151–6168, 2017.

[215] S. Rawat, S. Komatsu, A. Markman, A. Anand, and B. Javidi, "Compact and field-portable 3D printed shearing digital holographic microscope for automated cell identification," *Applied Optics*, vol. 56, pp. D127–D133, 2017.

[216] P. Vora, V. Trivedi, S. Mahajan, N. Patel, M. Joglekar, V. Chhaniwal, A.-R. Moradi, B. Javidi, and A. Anand, "Wide field of view common-path lateral-shearing digital holographic interference microscope," *Journal of Biomedical Optics*, vol. 22, no. 126001, 2017.

[217] B. Javidi, A. Markman, S. Rawat, T. O'Connor, A. Anand, and B. Andemariam, "Sickle cell disease diagnosis based on spatio-temporal cell dynamics analysis using 3D printed shearing digital holographic microscopy," *Optics Express*, vol. 26, pp. 13614–13627, 2018.

[218] T. O'Connor, A. Doblas, and B. Javidi, "Structured illumination in compact and field-portable 3D-printed shearing digital holographic microscopy for resolution enhancement," *Optics Letters*, vol. 44, pp. 2326–2329, 2019.

[219] K. Lee and Y. Park, "Quantitative phase imaging unit," *Optics Letters*, vol. 39, pp. 3630–3633, 2014.

[220] J. Di, Y. Li, K. Wang, and J. Zhao, "Quantitative and dynamic phase imaging of biological cells by the use of the digital holographic microscopy based on a beam displacer unit," *IEEE Photonics Journal*, vol. 10, pp. 1–10, 2018.

[221] S. Ebrahimi, M. Dashtdar, E. Sánchez-Ortiga, M. Martínez-Corral, and B. Javidi, "Stable and simple quantitative phase-contrast imaging by fresnel biprism," *Applied Physics Letters*, vol. 112, no. 113701, 2018.

[222] V. Singh, S. Tayal, and D. S. Mehta, "Highly stable wide-field common path digital holographic microscope based on a fresnel biprism interferometer," *OSA Continuum*, vol. 1, pp. 48–55, 2018.

[223] G. Popescu, T. Ikeda, R. R. Dasari, and M. S. Feld, "Diffraction phase microscopy for quantifying cell structure and dynamics," *Optics Letters*, vol. 31, pp. 775–777, 2006.

[224] H. Majeed, L. Ma, Y. J. Lee, M. Kandel, E. Min, W. Jung, C. Best-Popescu, and G. Popescu, "Magnified image spatial spectrum (MISS) microscopy for nanometer and millisecond scale label-free imaging," *Optics Express*, vol. 26, pp. 5423–5440, 2018.

[225] L. Puyo, J.-P. Huignard, and M. Atlan, "Off-axis digital holography with multiplexed volume bragg gratings," *Applied Optics*, vol. 57, pp. 3281–3287, 2018.

[226] J. Á. Picazo-Bueno and V. Micó, "Opposed-view spatially multiplexed interferometric microscopy," *Journal of Optics*, vol. 21, no. 035701, 2019.

[227] A. Anand, V. Chhaniwal, and B. Javidi, "Tutorial: Common path self-referencing digital holographic microscopy," *APL Photonics*, vol. 3, no. 071101, 2018.

[228] S. Mahajan, V. Trivedi, P. Vora, V. Chhaniwal, B. Javidi, and A. Anand, "Highly stable digital holographic microscope using sagnac interferometer," *Optics Letters*, vol. 40, pp. 3743–3746, 2015.

[229] V. Chhaniwal, A. S. G. Singh, R. A. Leitgeb, B. Javidi, and A. Anand, "Quantitative phase-contrast imaging with compact digital holographic microscope employing lloyd's mirror," *Optics Letters*, vol. 37, pp. 5127–5129, 2012.

[230] C. C. Montarou and T. K. Gaylord, "Two-wave-plate compensator method for single-point retardation measurements," *Applied Optics*, vol. 43, pp. 6580–6595, 2004.

[231] R. Oldenbourg and G. Mei, "New polarized light microscope with precision universal compensator," *Journal of Microscopy*, vol. 180, pp. 140–147, 1995.

[232] M. Shribak and R. Oldenbourg, "Techniques for fast and sensitive measurements of two-dimensional birefringence distributions," *Applied Optics*, vol. 42, pp. 3009–3017, 2003.

[233] K. Oka and T. Kaneko, "Compact complete imaging polarimeter using birefringent wedge prisms," *Optics Express*, vol. 11, pp. 1510–1519, 2003.

[234] A. W. Lohmann, "Reconstruction of vectorial wavefronts," *Applied Optics*, vol. 4, pp. 1667–1668, 1965.

[235] D. Beghuin, E. Cuche, P. Dahlgren, C. Depeursinge, G. Delacretaz, and R. P. Salathe, "Single acquisition polarisation imaging with digital holography," *Electronics Letters*, vol. 35, pp. 2053–2055, 1999.

[236] T. Colomb, P. Dahlgren, D. Beghuin, E. Cuche, P. Marquet, and C. Depeursinge, "Polarization imaging by use of digital holography," *Applied Optics*, vol. 41, pp. 27–37, 2002.

[237] T. Colomb, E. Cuche, F. Montfort, P. Marquet, and C. Depeursinge, "Jones vector imaging by use of digital holography: simulation and experimentation," *Optics Communications*, vol. 231, pp. 137–147, 2004.

[238] D. N. Naik, R. K. Singh, H. Itou, M. M. Brundavanam, Y. Miyamoto, and M. Takeda, "Single-shot full-field interferometric polarimeter with an integrated calibration scheme," *Optics Letters*, vol. 37, pp. 3282–3284, 2012.

[239] Z. Wang, L. J. Millet, M. U. Gillette, and G. Popescu, "Jones phase microscopy of transparent and anisotropic samples," *Optics Letters*, vol. 33, pp. 1270–1272, 2008.

[240] R. K. Singh, D. N. Naik, H. Itou, Y. Miyamoto, and M. Takeda, "Stokes holography," *Optics Letters*, vol. 37, pp. 966–968, 2012.

[241] Y. Kim, J. Jeong, J. Jang, M. W. Kim, and Y. Park, "Polarization holographic microscopy for extracting spatio-temporally resolved jones matrix," *Optics Express*, vol. 20, pp. 9948–9955, 2012.

[242] N. K. Soni, A. S. Somkuwar, and R. K. Singh, "Jones matrix imaging for transparent and anisotropic sample," in *International Conference on Optics and Photonics 2015* (K. Bhattacharya, ed.), vol. 9654, SPIE, 2015.

[243] X. Liu, B.-Y. Wang, and C.-S. Guo, "One-step jones matrix polarization holography for extraction of spatially resolved jones matrix of polarization-sensitive materials," *Optics Letters*, vol. 39, pp. 6170–6173, 2014.

[244] T. D. Yang, K. Park, Y. G. Kang, K. J. Lee, B.-M. Kim, and Y. Choi, "Single-shot digital holographic microscopy for quantifying a spatially-resolved jones matrix of biological specimens," *Optics Express*, vol. 24, pp. 29302–29311, 2016.

[245] A. V., N. K. Soni, V. R. V., and R. K. Singh, "Anisotropy imaging using polarization and angular multiplexing," in *Quantitative Phase Imaging III* (G. Popescu and Y. Park, eds.), vol. 10074, SPIE, 2017.

[246] Y. Dong and J. Wu, "Space-shifting digital holography with dc term removal," *Optics Letters*, vol. 35, pp. 1287–1289, 2010.

[247] T. M. Kreis, "Suppression of the dc term in digital holography," *Optical Engineering*, vol. 36, pp. 2353–2355, 1997.

[248] L. Xu, "Properties of digital holography based on in-line configuration," *Optical Engineering*, vol. 39, pp. 3214–3219, 2000.

[249] C.-S. Guo, X. Cheng, X.-Y. Ren, J.-P. Ding, and H.-T. Wang, "Optical vortex phase-shifting digital holography," *Optics Express*, vol. 12, pp. 5166–5171, 2004.

[250] B. J. Jackin, C. S. Narayanamurthy, and T. Yatagai, "Geometric phase shifting digital holography," *Optics Letters*, vol. 41, pp. 2648–2651, 2016.

[251] P. Bouchal, R. Čelechovský, and Z. Bouchal, "Polarization sensitive phase-shifting mirau interferometry using a liquid crystal variable retarder," *Optics Letters*, vol. 40, pp. 4567–4570, 2015.

[252] C.-S. Guo, Z.-Y. Rong, H.-T. Wang, Y. Wang, and L. Z. Cai, "Phase-shifting with computer-generated holograms written on a spatial light modulator," *Applied Optics*, vol. 42, pp. 6975–6979, 2003.

[253] V. Micó and J. García, "Common-path phase-shifting lensless holographic microscopy," *Optics Letters*, vol. 35, pp. 3919–3921, 2010.

[254] J. Rosen and G. Brooker, "Digital spatially incoherent fresnel holography," *Optics Letters*, vol. 32, pp. 912–914, 2007.

[255] B. Katz, J. Rosen, R. Kelner, and G. Brooker, "Enhanced resolution and throughput of fresnel incoherent correlation holography (FINCH) using dual diffractive lenses on a spatial light modulator (SLM)," *Optics Express*, vol. 20, pp. 9109–9121, 2012.

[256] V. Micó, Z. Zalevsky, and J. Garcia, "Superresolved common-path phase-shifting digital inline holographic microscopy using a spatial light modulator," *Optics Letters*, vol. 37, pp. 4988–4990, 2012.

[257] J. W. Goodman, *Introduction To Fourier Optics*. McGraw-Hill, 1996.

[258] U. Schnars and W. P. O. Juptner, "Digital recording and numerical reconstruction of holograms," *Measurement Science and Technology*, vol. 13, pp. R85–R101, 2002.

[259] M. Gu, *Advanced Optical Imaging Theory*. Springer-Verlag, 2000.

[260] F. Charrière, A. Marian, T. Colomb, P. Marquet, and C. Depeursinge, "Amplitude point-spread function measurement of high-NA microscope objectives by digital holographic microscopy," *Optics Letters*, vol. 32, pp. 2456–2458, 2007.

[261] Y. Cotte, F. M. Toy, C. Arfire, S. S. Kou, D. Boss, I. Bergoënd, and C. Depeursinge, "Realistic 3d coherent transfer function inverse filtering of complex fields," *Biomedical Optics Express*, vol. 2, pp. 2216–2230, 2011.

[262] P. Bouchal, J. Kapitán, R. Chmelík, and Z. Bouchal, "Point spread function and two-point resolution in fresnel incoherent correlation holography," *Optics Express*, vol. 19, pp. 15603–15620, 2011.

[263] R. W. Meier, "Magnification and third-order aberrations in holography," *Journal of the Optical Society of America*, vol. 55, pp. 987–992, 1965.

[264] V. N. Mahajan, "Strehl ratio for primary aberrations: some analytical results for circular and annular pupils," *Journal of the Optical Society of America*, vol. 72, pp. 1258–1266, 1982.

[265] M. K. Kim, "Principles and techniques of digital holographic microscopy," *Journal of Photonics for Energy*, vol. 1, no. 018005, 2010.

[266] C. J. Mann, L. Yu, C.-M. Lo, and M. K. Kim, "High-resolution quantitative phase-contrast microscopy by digital holography," *Optics Express*, vol. 13, pp. 8693–8698, 2005.

[267] E. Sánchez-Ortiga, P. Ferraro, M. Martínez-Corral, G. Saavedra, and A. Doblas, "Digital holographic microscopy with pure-optical spherical phase compensation," *Journal of the Optical Society of America A*, vol. 28, pp. 1410–1417, 2011.

[268] A. Ashkin, G. D. Boyd, J. M. Dziedzic, R. G. Smith, A. A. Ballman, J. J. Levinstein, and K. Nassau, "Optically-induced refractive index inhomogeneities in LiNbO3 and LiTaO3," *Applied Physics Letters*, vol. 9, no. 1, pp. 72–74, 1966.

[269] C. Bernert, R. Hoppe, F. Wittwer, T. Woike, and C. G. Schroer, "Ptychographic analysis of the photorefractive effect in $LiNbO_3$:Fe," *Optics Express*, vol. 25, pp. 31640–31650, 2017.

[270] T. Volk and M. Wöhlecke, *Lithium Niobate*. Springer-Verlag, 2008.

[271] A. A. Zozulya and D. Z. Anderson, "Propagation of an optical beam in a photorefractive medium in the presence of a photogalvanic nonlinearity or an externally applied electric field," *Physical Review A*, vol. 51, no. 2, pp. 1520–1531, 1995.

[272] G. F. Calvo, F. Agulló-López, M. Carrascosa, M. R. Belić, and W. Królikowski, "Locality vs. nonlocality of $(2 + 1)$-dimensional light-induced space-charge field in photorefractive crystals," *Europhysics Letters (EPL)*, vol. 60, no. 6, pp. 847–853, 2002.

[273] S. Huard, *Polarization of Light.* John Wiley & Sons, 1997.

[274] R. C. Jones, "A new calculus for the treatment of optical systems," *Journal of the Optical Society of America*, vol. 31, pp. 488–493, 1941.

[275] G. Popescu, K. Badizadegan, R. R. Dasari, and M. S. Feld, "Observation of dynamic subdomains in red blood cells," *Journal of Biomedical Optics*, vol. 11, no. 040503, 2006.

[276] M. G. Somekh, C. W. See, and J. Goh, "Wide field amplitude and phase confocal microscope with speckle illumination," *Optics Communications*, vol. 174, pp. 75–80, 2000.

[277] D. Deng, W. Qu, W. He, Y. Wu, X. Liu, and X. Peng, "Off-axis tilt compensation in common-path digital holographic microscopy based on hologram rotation," *Optics Letters*, vol. 42, pp. 5282–5285, 2017.

UNIVERZITA PALACKÉHO V OLOMOUCI
PŘÍRODOVĚDECKÁ FAKULTA

Katedra Optiky

Prostorová modulace světla v metodách digitální optiky

Mgr. Jaromír Běhal

AUTOREFERÁT DISERTAČNÍ PRÁCE

Olomouc 2020

PALACKY UNIVERSITY OLOMOUC
FACULTY OF NATURAL SCIENCES

Department of Optics

Spatial light modulation in methods of digital optics

Mgr. Jaromír Běhal

SUMMARY OF DOCTORAL THESIS

Olomouc 2020

Výsledky prezentované v disertační práci byly získány v rámci prezenčního doktorského studia studijního oboru Optika a optoelektronika (P1703 1701V029) ve studijním programu Fyzika (P1703) na Přírodovědecké fakultě Univerzity Palackého v Olomouci.

Doktorand:	Mgr. Jaromír Běhal
Školitel:	prof. RNDr. Zdeněk Bouchal, Dr. Katedra optiky Přírodovědecká fakulta Univerzita Palackého v Olomouci, ČR
Oponenti:	
Předseda komise:	prof. Mgr. Jaromír Fiurášek, Ph.D. Katedra optiky Přírodovědecká fakulta Univerzita Palackého v Olomouci, ČR

Autoreferát byl rozeslán dne ..... 2020.

Obhajoba se koná dne ..... 2020 v ..... hodin před komisí pro obhajobu disertační práce vědního oboru Fyzika, studijního oboru Optika a optoelektronika na katedře optiky Přírodovědecké fakulty Univerzity Palackého v Olomouci na adrese 17. listopadu 12, 771 46, Olomouc.

S disertační prací je možné se seznámit na studijním oddělení Přírodovědecké fakulty Univerzity Palackého v Olomouci sídlícím na stejné adrese.

Results presented in the Ph.D. thesis were obtained during doctoral study in study field Optics and optoelectronics (P1703 1701V029), study program Physics (P1703), of Faculty of Science, Palacký University Olomouc.

Ph.D. candidate:	Mgr. Jaromír Běhal
Supervisor:	prof. RNDr. Zdeněk Bouchal, Dr. Department of Optics Faculty of Science Palacký University Olomouc, CZ
Reviewers:	

Chairman of the committee:	prof. Mgr. Jaromír Fiurášek, Ph.D. Department of Optics Faculty of Science Palacký University Olomouc, CZ

The summary was sent on ……. 2020.

The defence will take a place on ……. 2020 at ……o'clock in front of the committee for doctoral study program Optics and optoelectronics at the Department of optics, Faculty of Science, Palacký University Olomouc, residing at 17. listopadu 12, 771 46 Olomouc, Czech Republic.

The Ph.D. thesis is available at the study department of Faculty of Science of Palacký University Olomouc, residing at the same address.

Abstrakt

Tato disertační práce je založena na třech originálních publikacích [1–3] a shrnuje hlavní výsledky dosažené v průběhu mého doktorského studia. Každý ze studovaných problémů přímo využívá principů digitální holografie ať už v kontextu designu experimentálního uspořádání, optimálního využití prezentované metody, či jako nástroje pro studium a kvantifikaci studovaných efektů. Digitální holografie je zobrazovací metoda využívající záznamu optického pole digitálním senzorem a následné numerické rekonstrukce. Takto získaný obraz nese informaci o komplexní amplitudě a typicky slouží pro mapování reliéfu povrchu nebo měření optické tloušťky.

Předložená disertační práce rozvíjí metodiku volby optimálních experimentálních parametrů pro pozorování zvětšeného obrazu vzorku v bezčočkové koherentní digitální holografické mikroskopii. Dále je v práci studována možnost vzniku otisku buněk ve fotorefraktivním materiálu s využitím fotolitografických principů. Tento přístup může být v budoucnu využitý pro diagnostické účely či provázání optických vlastností materiálových vzorků a živých buněk. Následně je v práci popsán princip korekce fázového pozadí s důrazem na využití metody dvojité expozice, která pro svou funkci nevyžaduje znalost numerického modelu. Tento přístup slouží pro svou jednoduchost a přesnost též jako referenční metoda. Kvalita dosažené fázové kompenzace je diskutována pro rozdílné experimentální podmínky.

Abstract

The presented thesis is based on three original publications [1–3] and summarizes the main results achieved during my Ph.D. studies. Each of the discussed problems exploits digital holographic principles, whether in the context of the experimental arrangement design, optimal implementation of the presented method, or as an instrument to study and quantify the investigated effects. Digital holography is an imaging technique consisting of recording the interference field by the digital sensor, followed by the subsequent numerical reconstruction process. The retrieved image provides a complex amplitude, typically exploited for three-dimensional relief mapping or optical thickness measurements.

The thesis initially proposes the methodology for an optimal choice of the experimental parameters suitable for observing the enlarged image in the lens-less coherent digital holographic microscopy. A further ambition aims to study the possibility of fixing parameters of cells into photorefractive material, adopting the principles of photolithography. The approach may be exploited for diagnostics or the interconnection of optical properties of materials and living cells. Moreover, the thesis presents the concept of phase-background compensation, emphasizing the double-exposure method. Such an approach is easy to implement without the need for the numerical model while providing accurate results; thus, ordinarily serves as a reference. Here, the optimal use of the method is discussed for various experimental conditions.

Declaration

I declare I wrote this Ph. D. thesis ***Spatial light modulation in methods of digital optics*** on my own. To the best of my knowledge and belief, it contains no material previously published by another person. This thesis is based on three original publications [1–3]. My contribution to these publications consists of the simulations, experimental realizations, data processing, and participating in writing the manuscripts. This thesis uses only the resources cited in the Bibliography section.

I agree with the further use of this thesis according to the requirements of Palacky University and the Department of Optics.

In Olomouc, ...

.....

Jaromír Běhal

Contents

Goals of the thesis

This chapter presents mostly experimental outcomes based on the three original publications [1–3], which profit from the advantages of powerful imaging technique called digital holography. Its imaging performance consists of two consecutive operations, recording the interference field and the subsequent numerical reconstruction process. The retrieved complex amplitude carries the information of both the amplitude and the phase distributions as a result. In this thesis, the digital holography serves as a subject of interest itself or as an instrument for analyzing and quantifying the investigated effects. The thesis introduces the experiments which aim to extend the boundaries of the studied possibilities further. Main outcomes are briefly introduced in the following text.

Results achieved in chapter 1 develop the methodology for the optimal choice of the experimental parameters suitable for observing the enlarged image in the lens-less coherent digital holographic microscopy. Initially, the imaging performance of a coherent magnified in-line digital holographic microscopy is described. Here the enlarged specimen's image is achieved in numerical post-processing by a mismatch between parameters of the reference and the reconstruction waves. The residual effects, coupled with this approach, are considered, which may result in undesirable effects caused by holographic aberrations and asymmetry of the point spread function. A trade-off between the influence of holographic aberrations and diffraction effects is, therefore, taken into account. The analysis provides an optimal combination of experimental parameters and range of the applicable magnifications, while the holographic aberrations reach an acceptable level, and the point spread function remains symmetrical. Theoretical predictions are verified experimentally by reconstructing the three-dimensional point spread functions of point interference records and the image of the line resolution target. Chapter 1 is based on publication: [1] J. Běhal and Z. Bouchal, "Optimizing three-dimensional point spread function in lensless holographic microscopy," *Optics Express*, vol. 25, pp. 29026–29042, 2017.

A further ambition is presented in chapter 2, which aims to study the possibility of fixing parameters of living micro-objects into the material, exploiting the principles of photolithography. The approach may be further used for diagnostics or the interconnection of optical properties of materials and living cells. Digital holographic microscopy serves here

for both, as a tool for realizing and investigating the photolithographic performance, simultaneously. The particular aim is to imprint the structure of red blood cells into the biocompatible and photo-activable substrate. In this case, the illuminating-light profile is shaped while passing through the cells. Hence, such a biolensing effect enables photolithographic writing. Experimentally, red blood cells settle down on the surface of the photorefractive $LiNbO_3$ crystal, which acts as a photoresist. After the sedimentation process is complete, the appropriately polarized laser light illuminates the specimen for suitable exposure time. At the same time, local changes arise inside the refractive index material during the process. Refractive index distribution shows that focusing properties of red blood cells can be directly transferred into the crystal depending on which type of the cells is employed. Similarities and differences between the imprints and cells are discussed for discocytes and spherocytes, respectively. Chapter 2 is based on publication: [2] L. Miccio, J. Behal, M. Mugnano, P. Memmolo, B. Mandracchia, F. Merola, S. Grilli, and P. Ferraro, "Biological lenses as a photomask for writing laser spots into ferroelectric crystals," *ACS Applied Bio Materials*, vol. 2, no. 11, pp. 4675–4680, 2019.

Moreover, chapter 3 extends the concept of phase-background compensation, emphasizing the double-exposure method. This easy-to-implement approach provides accurate results, hence may serve as a reference method. Notably, the performance of common-path self-referencing geometries is analyzed. Such off-axis experimental arrangements with the enhanced temporal stability enable long-time measurements and advantageous implementation of the double-exposure method for the suppression of phase defects in the recording plane. Conditions required for optimal application of the double-exposure method are discussed and experimentally approved. Processing the duplicated field of view, which often arises in the self-referencing geometries, is also taken into account. Quality of the achieved phase correction is discussed and demonstrated experimentally. Chapter 3 is based on publication: [3] J. Běhal, "Quantitative phase imaging in common-path cross-referenced holographic microscopy using double-exposure method," *Scientific Reports*, vol. 9, no. 9801, 2019.

Chapter 4 presents the polarization-sensitive imaging employing digital holography. A single-shot polarization reconstruction is based on principles of the angular multiplexing achieved by mixing two orthogonally polarized reference waves with the signal beam. The adopted experimental configuration represents the Mach-Zehnder interferometer with the incorporated Sagnac interference module in the reference arm for the simultaneous generation of the two tilted reference waves. The proof-of-principle experiment is focused on quantifying the enhanced temporal stability of the polarization reconstruction compared to the quantitative phase imaging, for the first time, according to our knowledge. Furthermore, the imaging ability is qualitatively performed using the sample generating spatially dependent polarization-state distribution.

Chapter 1

Optimizing three-dimensional point spread function in lens-less digital holographic microscopy

This chapter is based on the following publication:

[1] J. Běhal and Z. Bouchal, "Optimizing three-dimensional point spread function in lensless holographic microscopy," *Optics Express*, vol. 25, pp. 29026–29042, 2017.

In this chapter, the main interest is paid to analyze experimentally the deterioration of the 3D PSF, whose intensity maximum is displaced axially out of the paraxial image plane. This unwanted effect is studied as a consequence of the diffraction or holographic aberrations in the performance of a magnified lens-less phase-shifting digital holography (DH) where the magnification is obtained due to the mismatch between the parameters of the reference and the reconstruction waves. The range of experimental parameters and magnifications that trade-off the influence of both effects are predicted theoretically and verified experimentally as the main result.

1.1 Lens-less Gabor holography of point sources

The image reconstruction in DH is usually provided by the reconstruction wave of the identical wavelength as that used in the experiment. The recorded interference pattern situated in the plane $z = 0$ of lateral coordinates x, y diffracts the illumination light, and the numerical refocusing can be applied by calculating the first Rayleigh-Sommerfeld diffraction integral [4,5]. In this case, the image complex amplitude U_i evaluated at the lateral position

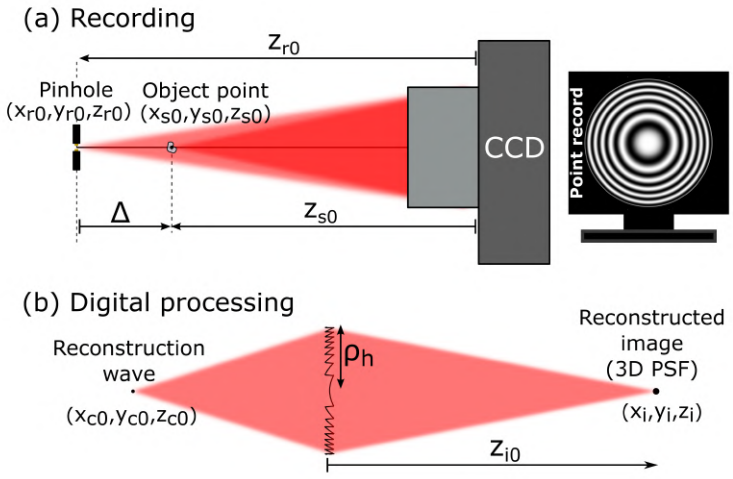

Figure 1.1: Optical scheme for evaluation of the three-dimensional point spread function in lens-less digital holographic microscopy: (a) in-line recording geometry, (b) reconstruction geometry.

x_i, y_i and located in the distance z_i from the interference record is expressed as

$$U_i(x_i, y_i; z_i) = \frac{z_i}{i\lambda} \iint_{-\infty}^{\infty} t(x, y) \frac{\exp\{\mathrm{sgn}(z_i) ikr_i\}}{r_i^2} \mathrm{d}x\mathrm{d}y, \tag{1.1}$$

where $r_i = \sqrt{(x_i - x)^2 + (y_i - y)^2 + z_i^2}$, sgn is a signum function, and t is a complex function which describes the transformation of the reconstructing wave by the transmission aperture function imposed in the recording plane. Here, the imaging performance of coherent digital holography is studied adopting the lens-less in-line geometry [6] from Fig. 1.1, demonstrating both recording and numerical reconstruction of a point interference record. Laser light of the wavelength λ passes through a pinhole of few micrometers in the diameter, creating the source of divergent reference wave U_r. The reference wave illuminates a point-like object which consequently generates a divergent signal wave U_s. The waves U_r and U_s mutually interfere, creating the point interference image captured by a camera. The record achieved is illuminated by a virtual reconstruction wave U_c and the image is obtained by enumerating the free propagation of light diffracted at the interference structure. The complex function t represents interaction between the reconstructing wave U_c and the holographic record,

$$t(x, y) = T(x, y) U_c |U_s + U_r|^2, \tag{1.2}$$

where the aperture function T defines a finite area. In real experiments, this area is given by an overlap achieved by interfering divergent waves U_s and U_r or active area of the used

detector. Optionally, when the virtual image $U_s U_r^*$ is separated, the complex function t is given as

$$t(x,y) = T(x,y)A_sA_rA_c\exp\{i[-\mathrm{sgn}(z_{s0})\Phi_s + \mathrm{sgn}(z_{r0})\Phi_r - \mathrm{sgn}(z_{c0})\Phi_c]\}, \tag{1.3}$$

where A_j and Φ_j, $j = \{r,s,c\}$, are amplitudes and phases of the signal, the reference and the reconstruction waves.

When the waves considered are treated as perfectly spherical and originate from the positions x_{j0}, y_{j0}, z_{j0}, $j = \{r,s,c\}$ marking the coordinates of a pinhole, an off-axis point scatterer, and a virtual source, respectively, the amplitudes and phases within the recording plane relative to the phase at the origin can be written as

$$A_j = \frac{a_j}{r_j}, \quad \Phi_j = k(r_j - r_{j0}), \quad j = \{r,s,c\}, \tag{1.4}$$

where $r_j = \sqrt{(x_{j0}-x)^2 + (y_{j0}-y)^2 + z_{j0}^2}$, $r_{j0} = \sqrt{x_{j0}^2 + y_{j0}^2 + z_{j0}^2}$ and a_j are constant amplitudes.

1.1.1 Paraxial optical parameters

The Fresnel approximation of spherical waves provides an accuracy sufficient for describing the experiments implemented with a low numerical aperture [7]. The spherical waves are, in this case, considered as paraboloidal. Hence, the signal, the reference, and the reconstruction waves (1.4) reach the form

$$\Phi_j = k\left(\frac{x^2+y^2}{2z_{j0}} - \frac{xx_{j0}+yy_{j0}}{z_{j0}}\right), \quad j = \{r,s,c\}. \tag{1.5}$$

To modify the diffraction integral (1.1) the Fresnel approximation is applied in the phase term, while a rough approximation $r_i \approx |z_i|$ is used for the amplitude. The following discussion can be simplified, considering the pinhole localized on the optical axis, $\sqrt{x_{r0}^2 + y_{r0}^2} = 0$. By omitting parts that do not influence the shape of the reconstructed intensity image of the point source and applying the complex function (1.3), the complex amplitude (1.1), can be considered as a Fourier transform of the aperture function T multiplied by a quadratic phase term,

$$U_i \propto \frac{1}{z_i}\iint_{-\infty}^{\infty} T(x,y)\exp\left\{ik\frac{\Omega(x^2+y^2)}{2}\right\}\exp\{-i2\pi(x\nu_x + y\nu_y)\}\mathrm{d}x\mathrm{d}y, \tag{1.6}$$

where Ω and the spatial frequencies ν_x, ν_y are given as

$$\Omega = \frac{1}{z_i} - \frac{1}{z_{s0}} + \frac{1}{z_{r0}} - \frac{1}{z_{c0}}, \quad \nu_x = \frac{1}{\lambda}\left(\frac{x_i}{z_i} - \frac{x_{s0}}{z_{s0}} - \frac{x_{c0}}{z_{c0}}\right), \quad \nu_y = \frac{1}{\lambda}\left(\frac{y_i}{z_i} - \frac{y_{s0}}{z_{s0}} - \frac{y_{c0}}{z_{c0}}\right).$$

The focused image is reconstructed considering that the quadratic phase term vanishes. The condition required, $\Omega = 0$, is achieved for the reconstruction distance $z_i = z_{i0}$ determined as

$$\frac{1}{z_{i0}} = \frac{1}{z_{c0}} - \frac{\Delta}{z_{r0}(z_{r0} + \Delta)}, \tag{1.7}$$

where $\Delta = z_{s0} - z_{r0}$. Assuming the unlimited aperture of the record (T =const.), the geometric image given by the Dirac delta function is reconstructed, $U_i \propto \delta(\nu_x, \nu_y)$. The lateral coordinates of this point image are $x_i = x_{i0} = \beta x_{s0} + (z_{i0}/z_{c0})x_{c0}$ and $y_i = y_{i0} = \beta y_{s0} + (z_{i0}/z_{c0})y_{c0}$, where β is the lateral magnification given by

$$\beta = \frac{\mathrm{d}x_{i0}}{\mathrm{d}x_{s0}} = \frac{\mathrm{d}y_{i0}}{\mathrm{d}y_{s0}} = \frac{z_{i0}}{z_{r0} + \Delta}. \tag{1.8}$$

To be complete the longitudinal magnification of the imaging performance is given as

$$\gamma = \frac{\mathrm{d}z_{i0}}{\mathrm{d}z_{s0}} = \left(\frac{z_{i0}}{z_{r0} + \Delta}\right)^2 = \beta^2. \tag{1.9}$$

1.1.2 Diffraction-limited three-dimensional point spread function

The diffraction-limited 3D intensity distribution is studied if the point image is evaluated in the radial coordinates (ν_x, ν_y) and the defocused axial image plane, $z_i = z_{i0} + \Delta z_i$. Considering the circularly bounded holographic record with the finite radius ρ_h, the 3D PSF must be evaluated numerically, hovewer, the transversal cross-section through the 3D PSF reconstructed in the distance z_{i0} given by (1.7) can be calculated analytically. The normalized radial PSF defined as $I = |U_i(\sqrt{\nu_x^2 + \nu_y^2}, \Delta z_i = 0)|^2$ being unitary in its maximum, $I\left(\sqrt{\nu_x^2 + \nu_y^2} = 0, \Delta z_i = 0\right) = 1$, is expressed as

$$I\left(\sqrt{\nu_x^2 + \nu_y^2}, \Delta z_i = 0\right) = 4\,\mathrm{jinc}^2\left(\pi\rho_h\sqrt{\nu_x^2 + \nu_y^2}\right), \tag{1.10}$$

where $\mathrm{jinc}(x) = J_1(x)/x$, $J_1(x)$ is the Bessel function of a first kind and a first order. The condition needed to achieve the first minimum, i.e., an argument of the function reaches the value ≈ 3.8, defines the radius of Airy disc in the form

$$AD_i = \sqrt{(x_i - x_{i0})^2 + (y_i - y_{i0})^2} = 0.61\frac{\lambda}{NA_i}, \quad NA_i = \frac{\rho_h}{|z_{i0}|}, \tag{1.11}$$

where NA_i is the image numerical aperture.

Moreover, if the axial profile of the 3D PSF is investigated ($\sqrt{\nu_x^2+\nu_y^2}=0$), the diffraction integral has also an analytical solution. The normalized axial intensity defined as $I=|U_i(\sqrt{\nu_x^2+\nu_y^2}=0,\Delta z_i)|^2$ being unitary in the paraxial image plane, $I(\sqrt{\nu_x^2+\nu_y^2}=0,\Delta z_i=0)=1$, can be obtained in the form

$$I\left(\sqrt{\nu_x^2+\nu_y^2}=0,q\right)=\left(1-\frac{q}{\pi n_i}\right)^2\operatorname{sinc}^2\left(\frac{q}{2}\right),\quad q=\frac{\pi n_i\Delta z_i}{z_{i0}+\Delta z_i},\quad n_i=\frac{\rho_h^2}{\lambda z_{i0}}. \tag{1.12}$$

The function q behaves nonlinearly in Δz_i. The term before the sinc function leads to the shift of the intensity maximum out of the geometric focus, while the argument of the sinc function causes asymmetry of the intensity profile.

Both effects, illustrated in Fig. 1.2, are influenced by the geometry of experiments and their evaluation is feasible adopting the Fresnel number $N_i=|n_i|$. The axial intensity (1.12) exhibits periodical changes and reaches zero values when the condition $q=2m\pi$, $m=\pm1,\pm2,\ldots$ is satisfied. The asymmetry of the axial intensity profile is evaluated by the positions of the nearest zero points Δz_i^+ and Δz_i^- related to $m=\pm1$ (Fig. 1.2),

$$\Delta z_i^+=\frac{2z_{i0}}{n_i-2},\quad \Delta z_i^-=-\frac{2z_{i0}}{n_i+2}. \tag{1.13}$$

Distribution of the axial intensity reaches its maximum in the position displaced from the paraxial image plane towards the recording plane. The position of the intensity maximum Δz_i^{max} is calculated as a solution of a transcendental equation originating from the condition $\mathrm{d}I/\mathrm{d}q=0$ [8]. Half-widths of the central intensity peak Λ_i^+ and Λ_i^- are given by the

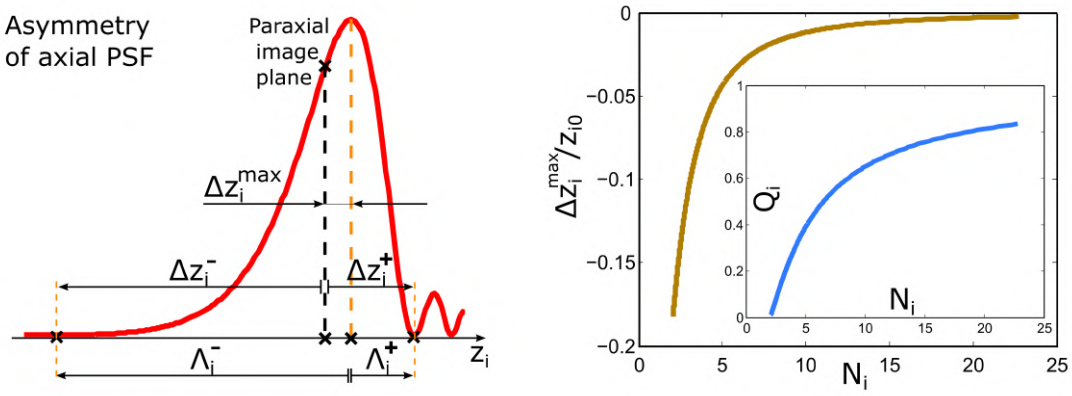

Figure 1.2: Asymmetric axial PSF with geometrical parameters used for the detailed analysis and the quantitative evaluation of the focal shift effect ($\Delta z_i^{max}/z_{i0}$) and the axial asymmetry in the image space (Q_i) as a function of the Fresnel number N_i.

first zero points of the oscillating axial intensity that are closest to the intensity maximum,

$$\Lambda_i^+ = \Delta z_i^+ - \Delta z_i^{max}, \quad \Lambda_i^- = \Delta z_i^- - \Delta z_i^{max}. \tag{1.14}$$

Meaning of the defined geometrical symbols is evident from the illustration in Fig. 1.2. To quantify the axial asymmetry of the PSF in the image space the coefficient Q_i defined as

$$Q_i = \left|\Lambda_i^+ / \Lambda_i^-\right| \tag{1.15}$$

can be used (Fig. 1.2). Examination of the axial PSF in the object space is also feasible by implementation of the longitudinal magnification γ (1.9). Asymmetry coefficients in the image space Q_i and the object space Q_s are identical in case when the constant longitudinal magnification is used, $Q_s = Q_i$. However, in the exact analysis, the positions of the intensity maximum and the nearest zero points of the oscillating axial intensity are transformed into the object space with different values of γ. Hence Q_s and Q_i are slightly different in the object space and the image space.

The equations mentioned above can be compared to the results achieved by the paraxial Debye approximation. When an investigation of the axial profile in proximity to the paraxial image plane is considered the approximation $|\Delta z_i| \ll |z_{i0}|$ is adopted leading to the modified form of the (1.12)

$$I\left(\sqrt{\nu_x^2 + \nu_y^2} = 0, q_D\right) = \mathrm{sinc}^2\left(\frac{q_D}{2}\right), \quad q_D = \frac{\pi n_i \Delta z_i}{z_{i0}}, \quad n_i = \frac{\rho_h^2}{\lambda z_{i0}}. \tag{1.16}$$

Contrary to the case (1.12), the function q_D is linear in Δz_i. Thus the axial PSF is symmetrical relative to the focal plane and without the focal shift effect, naturally. The axial intensity also varies periodically and takes zero when $q_D = 2m\pi$, where $m = \pm 1, \pm 2, \ldots$. The relations (1.13) in this case reach the form

$$\Delta z_{iD}^+ = -\Delta z_{iD}^- = \frac{2 z_{i0}}{n_i}. \tag{1.17}$$

Symmetrical distribution in the image space (1.15), $Q_{iD} = 1$, is determined, which is equivalent to the result obtained using the paraxial Debye approximation. The condition for the Debye approximation to hold is that the Fresnel number $N_i = |n_i|$ is much larger than unity which also can be noticed comparing the relations (1.13) and (1.17). However, this condition may conflict with the paraxial approximation under some circumstances, and the results achieved may provide incorrect predictions comparing to the experiment [9].

1.1.3 Holographic aberrations

When experimental parameters exceed requirements of the paraxial approximation, the phase of $U_s U_r^*$ determined by the interference of spherical waves generally no longer matches the spherical wave. The differences that appear are known as holographic aberrations. The third-order holographic aberrations are described by the Taylor expansion applied to the phase Φ_j given by (1.4), in which only first three terms are included [10].

Using the normalized radial coordinate $\rho_N = \rho/\rho_h$, where ρ_h is the radius of the circularly bounded interference record, the total holographic aberration is given by

$$W = S\rho_N^4 + C\rho_N^3 \cos\varphi + A\rho_N^2 \cos^2\varphi + F\rho_N^2 + D\rho_N \cos\varphi, \tag{1.18}$$

where the coefficients S, C, A, F and D represent spherical aberration, coma, astigmatism, field curvature and distortion, respectively, and can be written as

$$S = -\frac{\rho_h^4}{8}\left(\frac{1}{z_{i0}^3} + \frac{1}{z_{r0}^3} - \frac{1}{z_{s0}^3} - \frac{1}{z_{c0}^3}\right), \qquad C = \frac{x_{s0}\rho_h^3}{2}\left(\frac{\beta}{z_{i0}^3} - \frac{1}{z_{s0}^3}\right),$$
$$A = -\frac{x_{s0}^2\rho_h^2}{2}\left(\frac{\beta^2}{z_{i0}^3} - \frac{1}{z_{s0}^3}\right), \qquad F = \frac{1}{2}A, \qquad D = \frac{x_{s0}^3\rho_h}{2}\left(\frac{\beta^3}{z_{i0}^3} - \frac{1}{z_{s0}^3}\right). \tag{1.19}$$

When the reconstruction wave matches the reference wave ($z_{c0} = z_{r0}$) the aberration-free image with the unitary magnification (1.8) is obtained ($z_i = z_{i0} = z_{s0}$, $\beta = 1$, hence $S = C = A = F = D = 0$). However, when the reconstructing wave differs from the reference wave ($z_{c0} \neq z_{r0}$) the influence of holographic aberrations have to be taken into account.

1.2 Optical performance of Gabor digital holography

In case of the circular aperture, the radius of Airy disc (1.11) is given as $AD_i = 0.61\lambda/NA_i$ where $NA_i = \rho_h/|z_{i0}|$. Considering the pinhole and a source of the reconstruction wave placed on the optical axis ($x_{j0} = y_{j0} = 0$, for $j = \{r, c\}$), the lateral resolution in the object space is then obtained using the lateral magnification β (1.8) as $AD_s = AD_i/|\beta|$, hence AD_s is inversely proportional to $NA_i|\beta| = \rho_h/(z_{r0} - \Delta)$ which is independent of z_{c0}. The theoretical lateral resolution in the object space thus remains unchanged when the different reconstruction waves are used. If the point interference record is bounded by the light area arising from the illumination of the reference wave, the radius ρ_h is given by the radius of pinhole ρ_p as $\rho_h = 0.61\lambda|z_{r0}|/\rho_p$. The resolution in the object space is then expressed in

the form

$$AD_s = \rho_p \left(1 - \frac{\Delta}{|z_{r0}|}\right), \tag{1.20}$$

where $\Delta > 0$ in the investigated in-line holographic geometry. On the other hand, the Fresnel number of the image space depends on the basic experimental parameters, but also changes with the reconstruction geometry. For limiting cases of the reconstruction it can be written as

$$N_i = \frac{0.61^2 \lambda \kappa}{\rho_p A D_s}, \tag{1.21}$$

where $\kappa = |z_{r0}|$ for the reconstruction wave exactly matched to the reference wave ($z_{c0} = z_{r0}$), while $\kappa = \Delta$ for the plane wave reconstruction ($z_{c0} \to -\infty$). In experiments, $|z_{r0}| \gg \Delta$ and the high N_i is reached with common geometrical parameters when reconstructing with $z_{c0} = z_{r0}$, guaranteeing a symmetrical profile of the axial PSF. Additionally, the diffraction limited image is obtained despite the reconstruction provide the unitary lateral magnification $\beta = 1$. If the zooming is achieved by mismatch between the parameters of the reconstruction and reference waves ($z_{c0} \neq z_{r0}$), the axial asymmetry of the PSF and holographic aberrations appear even when the ideal spherical waves are considered.

To obtain the magnified image, the reconstruction wave originating from a virtual source placed at the distances $z_{c0} \in (-\infty, z_{r0})$ from the recording plane is examined. The largest lateral magnification is for the established experimental parameters Δ and z_{r0} achieved for a plane wave reconstruction ($z_{c0} \to -\infty$). Axial symmetry of the PSF and the object space resolution are enhanced when increasing the pinhole-sample distance Δ [relations (1.20) and (1.21)], however demands on the correct sampling provided by the detector increase strongly. Considering the Nyquist-Shannon sampling theorem for the reconstruction using $z_{c0} \to -\infty$, the largest specimen to pinhole distance Δ permissible for the pixel size p_{CCD} is determined by the condition

$$\Delta \leq \frac{|z_{r0}| A D_s}{1.22 p_{CCD}}. \tag{1.22}$$

To investigate how the real imaging meets the theoretically predicted object space resolution limit (1.20) both the holographic aberrations and diffraction effects leading to the axially asymmetric profile of PSF must be included in the analysis.

1.3 Simulations

Before the measurement was realized, the aberration deterioration and axial asymmetry of the PSF was evaluated depending on the experimental parameters by adopting the criteria

imposed. In all demonstrated results, the monochromatic plane wave ($\lambda = 633$ nm) was considered as a reconstruction wave. The pinhole-detector distance $z_{r0} = -43.5$ mm, the pinhole radius $\rho_p = 2.75$ µm and the pixel size $p_{CCD} = 7.4$ µm of the camera chip are used in the simulations. The dependence of the Strehl ratio K on Δ evaluated in the optimal plane is plotted in Fig. 1.3 (black line), together with the diffraction-limited resolution (1.20) in the object space AD_s (green line), the resolution limit obtained by sampling conditions (1.22) (thin black line), the coefficient of asymmetry Q_s (red line) and the coefficient of spherical aberration S (1.19) (blue line). The asymmmetry coefficient in the object space Q_s is calculated exactly by applying the variable longitudinal magnification to transform the required distances from the image to the object space. The range of the evaluated distances between the pinhole and the sample $\Delta \in [0, 10\ \mathrm{mm}]$ is limited by the sampling conditions determined for CCD QImaging Retiga 4000R. For the greatest value of Δ, the best theoretical lateral resolution $AD_s \approx 3.3\lambda$ is obtained. Lateral resolution AD_s improves linearly with increasing Δ. The asymmetry and aberration coefficients Q_s and S exhibit mutually

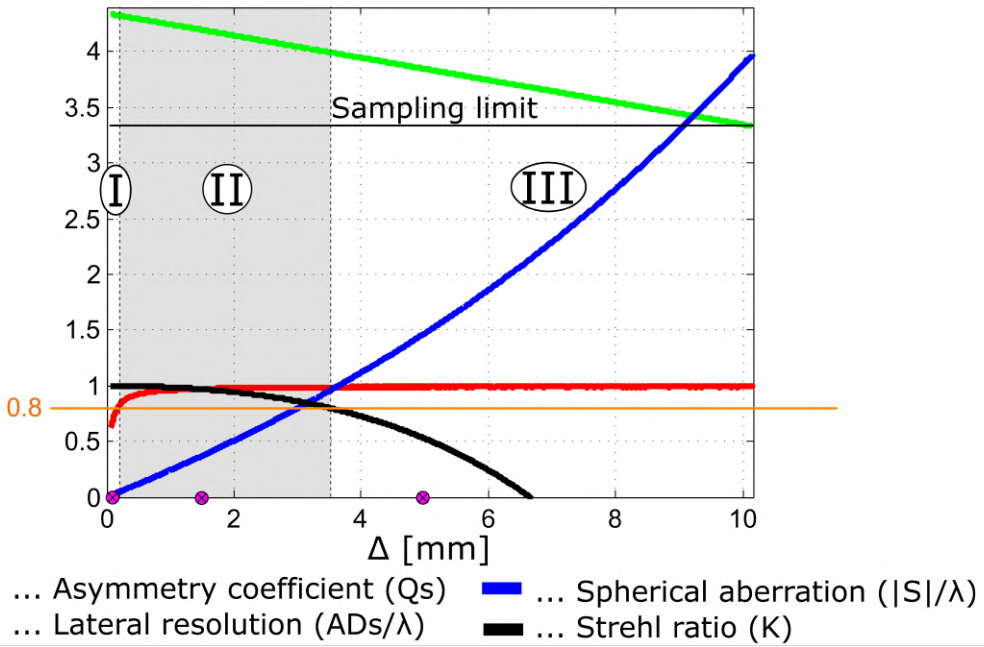

Figure 1.3: Dependence of the indicators of imaging performance on the pinhole to object distance Δ (evaluation performed for $z_{r0} = -43.5$ mm and $\rho_p = 2.75$ µm): object space diffraction-limited lateral resolution in multiples of λ, AD_s (green line), resolution limit in multiples of λ given by sampling conditions for CCD QImaging Retiga 4000R (thin black line), asymmetry coefficient, Q_s (red line), Strehl ratio for optimal image plane, K (black line) and coefficient of spherical aberration in multiples of λ, S (blue line). Ranges of parameters: I-axially asymmetric PSF, II-symmetric nearly diffraction-limited PSF ($Q_s \geq 0.8$, $K \geq 0.8$), III-strong spherical aberration.

opposite changes. The axial symmetry of the PSF with the coefficient $Q_s \approx 1$ is achieved, while the spherical aberration increases and the Strehl ratio drops sharply. Axial symmetry of the PSF and nearly aberration-free imaging are guaranteed if both the asymmetry coefficient and the Strehl ratio are close to unit value. With the conditions $Q_s \geq 0.8$ and $K \geq 0.8$, the range of applicable positions Δ can be determined for the fixed parameters z_{r0} and ρ_p defining three different areas in Fig. 1.3 marked as I, II and III. The area I defines the parameters resulting in diffraction-limited imaging with strong axial asymmetry of the PSF. The area II determines a low-aberration imaging with the nearly symmetrical 3D PSF. The area III indicates imaging strongly deteriorated by the spherical aberration. The optimal area II is defined by the limit values of the sample to pinhole distance $\Delta = 0.17$ mm and $\Delta = 3.5$ mm and corresponding lateral magnifications $\beta = 257$ and $\beta = 12.5$, respectively.

1.4 Experimental setup

The experimental arrangement implemented to demonstrate the imaging performance is illustrated in Fig. 1.4. The light beam emanated from the unpolarized helium–neon (He-Ne) laser (10 mW, $\lambda = 633$ nm) is spatially filtered by the single-mode fiber (Thorlabs P1-630A-FC-2, mode field diameter 3.6-5.3 mm) and collimated by the lens L_1 (achromatic doublet Thorlabs AC254-150-A, diameter 25.4 mm, focal length 150 mm). The beam generated passes through a linear polarizer (LP), a half-wave plate (HWP) and a beam splitter (BS)

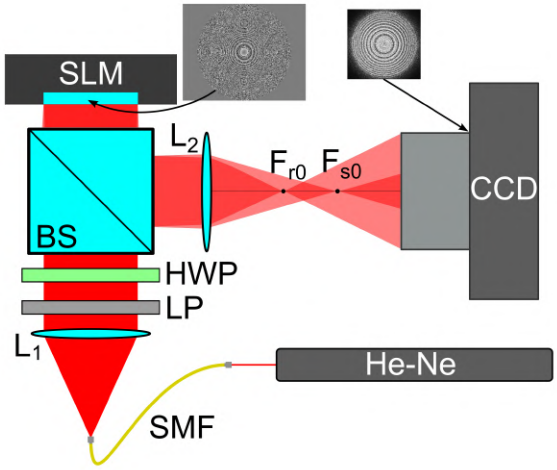

Figure 1.4: In-line holographic setup used for reconstruction of the 3D PSFs and image of the resolution target in testing an optimal design of geometric parameters: SMF...single-mode fiber, collimating lens (L_1), beam splitter (BS), linear polarizer (LP), half-wave plate (HWP), spatial light modulator (SLM) creating converging/diverging lenses with varying focal lengths, imaging lens (L_2).

towards the reflective spatial light modulator (SLM, Hamamatsu X10468, 800×600, pixel size 20 μm). Two different phase masks are simultaneously displayed on the SLM providing the converging and diverging lenses by a random pixel selection [11,12] and three different constant phase shifts θ_j are sequentially added to the phase creating the converging lens for purposes of the phase-shifting When implementing the lens L_2 with the focal distance $f_d = 38.1$ mm (achromatic doublet Edmund # $49 - 775$, diameter 12.7 mm), two focal points F_{r0} and F_{s0} are formed behind the lens L_2. The focal points represent sources of reference and signal waves that interfere and form a point interference record captured by a CCD (QImaging Retiga 4000R, 2048×2048 pixels, chip size 15×15 mm^2). During the measurements the flexibility of the SLM was advantageously utilized for positioning the spots F_{s0} and F_{r0} and achieving the mechanical free phase-shifting of the interfering waves. By recording and processing three mutually phase-shifted interference patterns, a complex holographic term corresponding to the virtual image was obtained and the 3D PSF reconstructed numerically. When reconstructing image of the resolution target, only one convergent lens was displayed on the SLM that created the reference wave in combination with the lens L_2. The signal wave was hence created by diffraction of the reference wave on the resolution target.

1.5 Results

The experimental results are shown in Fig. 1.5, Fig. 1.6 and Fig. 1.7. The positions of spots F_{s0}, F_{r0} (Fig. 1.5) determine the parameters corresponding to the Gabor holographic geometry including the pinhole-camera distance z_{r0}, the pinhole-sample distance Δ and the pinhole radius ρ_p (Fig. 1.3). In all three cases, the same position of the reference focal spot $z_{r0} = -43.5$ mm was used and the plane wave reconstruction of the PSF was done using the point interference records recorded with the same radius $\rho_h = 6.1$ mm. In the individual cases, the distance Δ corresponds to $\Delta = 0.1$ mm, 1.5 mm and 4.9 mm, respectively. The settings considered provides nearly identical theoretical lateral resolution in the object space $AD_s = 2.7$ μm, 2.65 μm and 2.4 μm, respectively. When considering the paraxial Debye approximation the obtained PSFs are symmetrical of the analytical form given by (1.16). The half-width of the longitudinal spot determined by the first zero point of the sinc function transformed into the object space by utilizing the axial magnification (1.9) are comparable in all three cases as $\Delta z^+_{sD} = \Delta z^+_{iD}/\gamma = 64$ μm, 60 μm and 56 μm, respectively, where Δz^+_{iD} is given by (1.17). Although the demonstrated image reconstructions provide nearly the same theoretical values of the lateral and the longitudinal resolutions in the paraxial Debye approximation, significant differences are found when the 3D PSFs

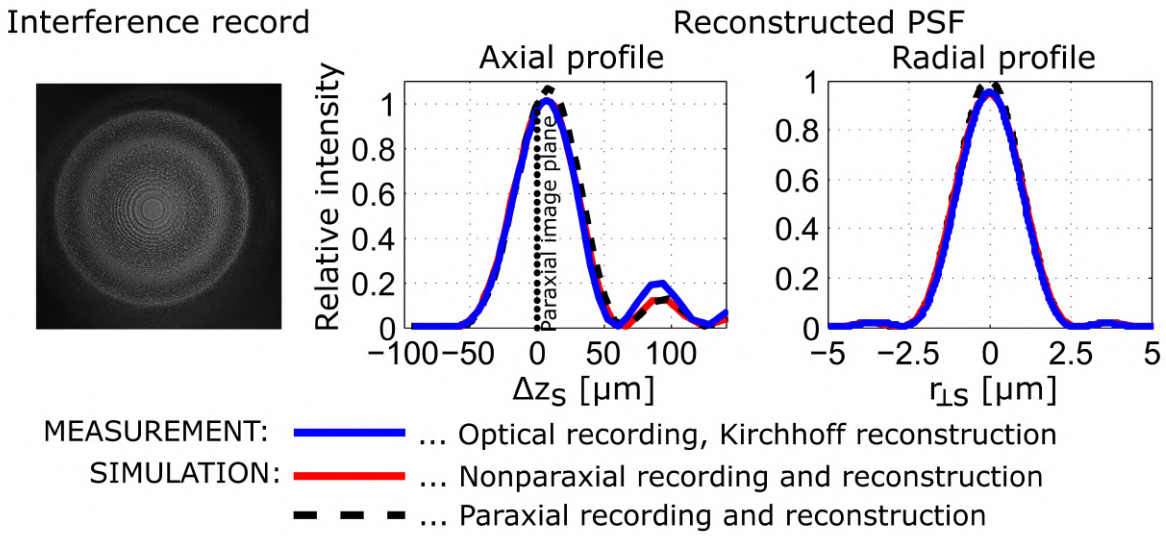

Figure 1.5: Diffraction-limited axially asymmetric PSF reconstructed by the plane wave from three phase-shifted point interference records taken with the geometric parameters belonging to the area I in Fig. 1.3 ($\rho_h = 6.1$ mm; $z_{r0} = -43.5$ mm; $\Delta = 0.1$ mm). The axial and radial PSF profiles obtained from experimental data were transformed into the object space and compared with numerical simulations.

are experimentally implemented and correctly evaluated. The 3D PSFs shown in Fig. 1.5, Fig. 1.6 and Fig. 1.7 can be assigned, according to the effects influencing their shape, to the areas I, II and III in Fig. 1.3.

The PSF shown in Fig. 1.5 was reconstructed from the interference records recorded with $\rho_h = 6.1$ mm, $z_{r0} = -43.5$ mm and $\Delta = 0.1$ mm. The parameters used correspond to the left violet dot in Fig. 1.3. With these parameters, the paraxial lateral and longitudinal resolutions $AD_s = 2.7$ μm and $\Delta z^+_{sD} = 64$ μm were obtained by combining a very low numerical aperture in the image space ($NA_i = 0.0003$) with extremely large lateral and longitudinal magnifications ($\beta = 435$, $\gamma = \beta^2$). Influence of holographic aberrations is in this case negligible due to low value of NA_i. On the other hand, very low value of the Fresnel number ($N_i = 3.1$) indicates a significant influence of diffraction effects causing an asymmetry of the axial PSF. The asymmetric axial PSF (blue line) was reconstructed from experimentally acquired interference records by the direct implementation of (1.1). To confirm accordance of the experimental results, the numerical simulations were performed including both, the recording with parameters of the real experiment and the reconstruction. The results obtained in the precise nonparaxial approach are illustrated by a red line while the use of the paraxial approximation corresponds to a black dashed line.

The PSF in Fig. 1.6 belongs to the area II in Fig. 1.3 and was obtained by reconstructing the records acquired with optimally selected parameters $\rho_h = 6.1$ mm, $z_{r0} = -43.5$ mm

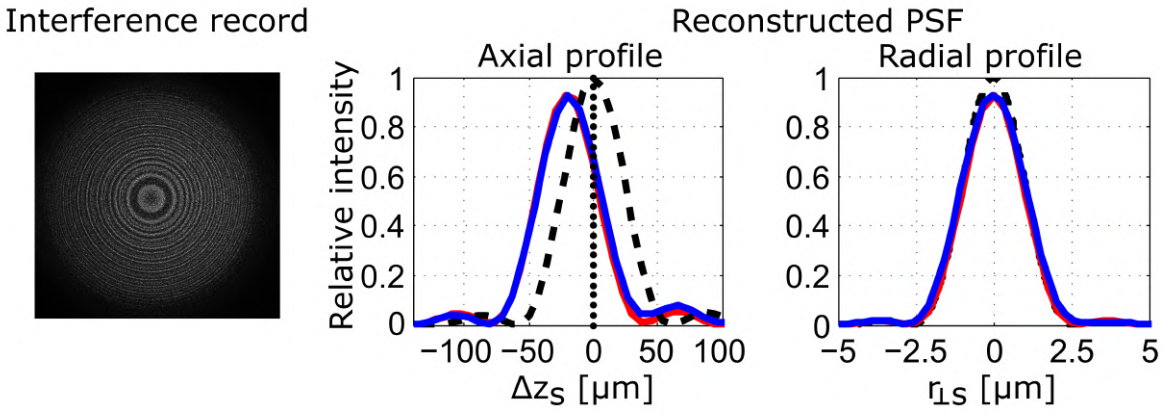

Figure 1.6: Symmetric low-aberration PSF reconstructed by the plane wave from three phase-shifted point interference records taken with the geometric parameters belonging to the area II in Fig. 1.3 ($\rho_h = 6.1$ mm; $z_{r0} = -43.5$ mm; $\Delta = 1.5$ mm).

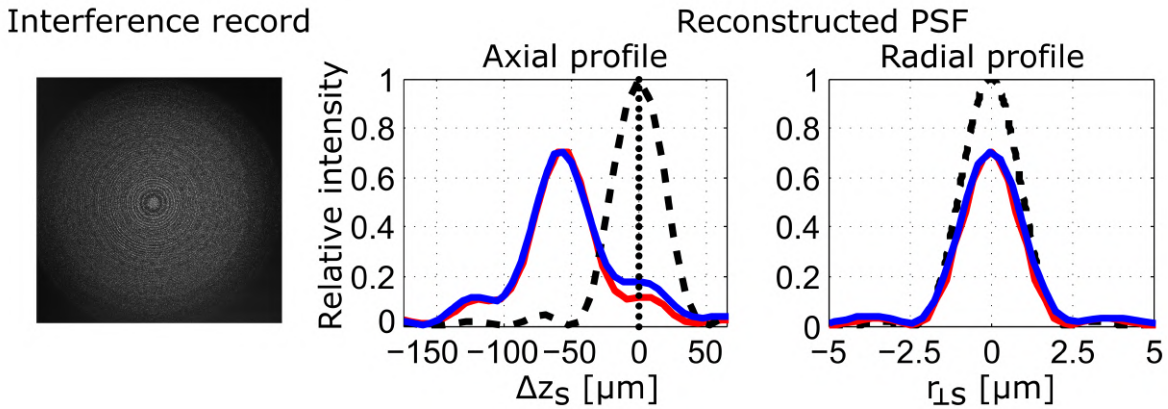

Figure 1.7: PSF deteriorated by a holographic aberration and reconstructed by the plane wave from three phase-shifted point interference records taken with the geometric parameters belonging to the area III in Fig. 1.3 ($\rho_h = 6.1$ mm; $z_{r0} = -43.5$ mm; $\Delta = 4.9$ mm).

and $\Delta = 1.5$ mm (middle violet dot in Fig. 1.3). Here, the paraxial lateral and the longitudinal resolutions $AD_s = 2.65$ μm and $\Delta z^+_{sD} = 60$ μm were achieved by an appropriate combination of the image numerical aperture ($NA_i = 0.005$) and the lateral and the longitudinal magnifications ($\beta = 29$, $\gamma = \beta^2$). High enough value of the Fresnel number ($N_i = 48.3$) ensures nearly symmetrical axial PSF while an influence of the spherical aberration remains small enough to provide nearly diffraction-limited imaging ($K \geq 0.8$).

The PSF shown in Fig. 1.7 belongs to the area III in Fig. 1.3 ($\rho_h = 6.1$ mm, $z_{r0} = -43.5$ mm, $\Delta = 4.9$ mm, right violet dot in Fig. 1.3), and corresponds to the paraxial lateral and the longitudinal resolutions $AD_s = 2.4$ μm and $\Delta z^+_{sD} = 56$ μm obtained with the high image space aperture ($NA_i = 0.017$) and the low lateral and longitudinal magnifications ($\beta = 8.9$, $\gamma = \beta^2$). High value of the Fresnel number ($N_i = 172$) confirms that the

asymmetrical PSF is not present, however the spherical aberration appears making both the lateral and longitudinal PSF profiles deteriorated. The experimental PSF (blue line) is again in a good agreement with the PSF obtained in the numerical model (red line) in which both the holographic recording and reconstruction were simulated in the nonparaxial approach.

Additional measurement was realized in the arrangement displayed in Fig. 1.4 with a positive line resolution target. In this case the distance z_{r0} between the camera and the reference focus F_{r0} was fixed, $z_{r0} = -46.4$ mm. Three interference patterns, that correspond to the three distinct positions of the resolution target relative to the reference focus $\Delta = 0.7$ mm, $\Delta = 3$ mm and $\Delta = 10$ mm, were recorded. Numerical reconstructions were accomplished by applying the monochromatic plane wave. Different positioning of the sample corresponds to various combinations of the reached magnification and the image space numerical aperture. Theoretical resolution, radius of Airy disc in the object space, is obtained as $AD_s = 0.61\lambda|z_{i0}|/(\rho_h\beta)$. It means that if the ρ_h remains fixed the object space resolution improves with the smaller $|z_{i0}|/\beta$ ratio. In the settings imposed, the reconstruction distances and the lateral magnifications reach values $z_{i0} = -3029$ mm, -671 mm and -169 mm, and $\beta = 66.3$, 15.5 and 4.6, respectively. The $|z_{i0}|/\beta$ ratio decreases in each of the examined cases, giving values $|z_{i0}|/\beta = 45.7$, 43.4 and 36.7, respectively.

The smallest group present in the target includes the lines of the 2.5 μm widths. Each of the reconstructions is shown in Fig. 1.8, where the enlarged cutout of the finest line group is present together with profiles of the average visibility of horizonzal and vertical lines calculated in the marked square areas. In Fig. 1.8a the reconstruction of the line target with the experimental setting providing a high lateral magnification and the low image space numerical aperture is shown. In this case the lateral resolution is limited by the $|z_{i0}|/\beta$ ratio, which is the highest of all the three cases. Moreover, axial asymmetry of the PSF occurs with these parameters. The reconstruction in the Fig. 1.8b belongs to the optimal configuration of experimental parameters where the image is nearly uneffected by the holographic aberrations and the resolution achieved meets the theoretical limit. In this case, the axial PSF provides practically perfect symmetry. Even that combination of the geometrical parameters in case of the reconstruction shown in Fig. 1.8c reaches the smallest $|z_{i0}|/\beta$ ratio predicting the best theoretical resolution, the influence of spherical aberration forbid its practical realization. The reduced lateral resolution and deteriorated axial profile of the PSF is achieved as was discussed in the text mentioned above.

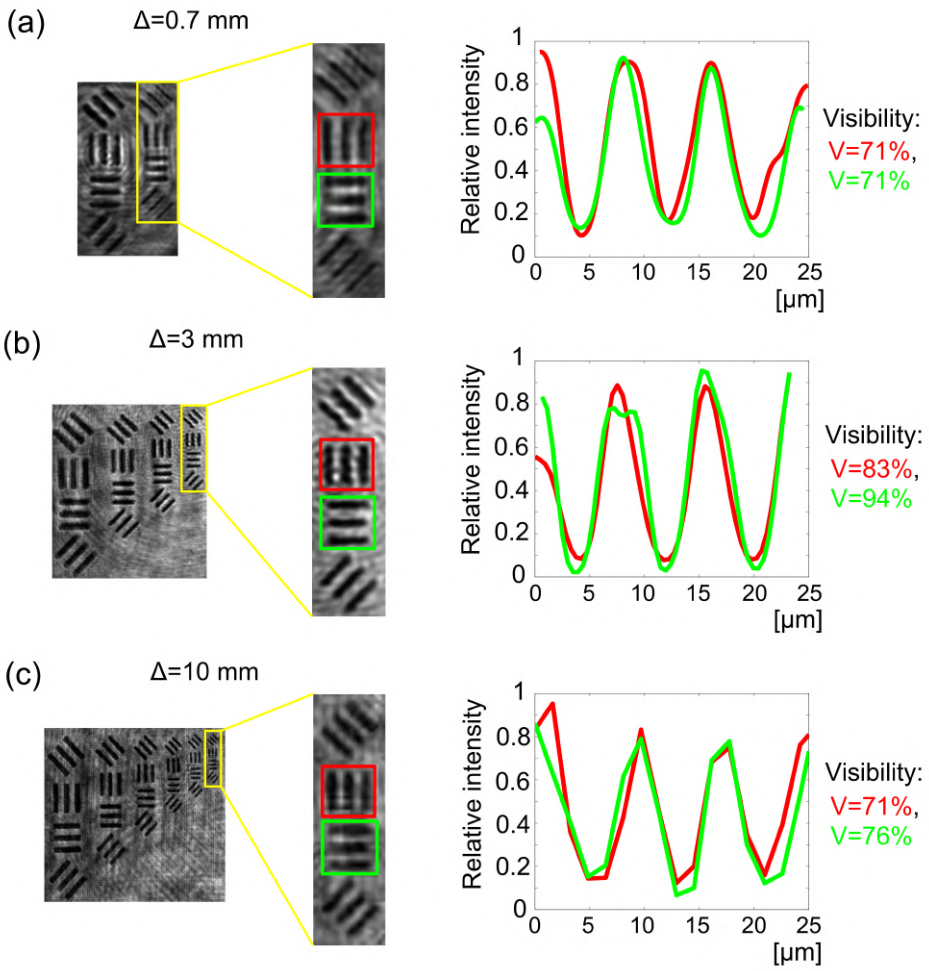

Figure 1.8: Plane wave reconstructions of the resolution target verifying an optimal choice of geometric parameters for recording: (a) aberration-free imaging with reduced diffraction-limited lateral resolution ($z_{r0} = -46.4$ mm, $\Delta = 0.7$ mm), (b) low-aberration imaging with optimal lateral resolution ($z_{r0} = -46.4$ mm, $\Delta = 3$ mm), (c) imaging with resolution reduced by holographic aberrations ($z_{r0} = -46.4$ mm, $\Delta = 10$ mm).

Chapter 2

Red blood cells as photomask for photorefractive writing into lithium niobate

This chapter is based on the following publication:

[2] L. Miccio, J. Behal, M. Mugnano, P. Memmolo, B. Mandracchia, F. Merola, S. Grilli, and P. Ferraro, "Biological lenses as a photomask for writing laser spots into ferroelectric crystals," *ACS Applied Bio Materials*, vol. 2, no. 11, pp. 4675–4680, 2019.

Red blood cells (RBCs) may behave as a sort of biolenses with optical parameters determined by their shape. This chapter demonstrates the exploitation of the biolensing effect to modulate the optical properties of the photo-activated and biocompatible substrate. Thus, performing the optical bio-photolithography (bio-PL) as a consequence. The chapter notably presents the possibility of imprinting information about red blood cells into the iron-doped x-cut $LiNbO_3$ crystal. The results achieved prove that different optical properties of discocytes and spherical-like RBCs imprint different phase discontinuities, which are characterized by the complex-amplitude propagation.

2.1 Red blood cells as biolenses

The biolensing effect was discovered and firstly demonstrated in [13], where RBCs were treated as transparent phase objects with corresponding magnification and focal length. The attribute mentioned corresponds to the fingerprint, which enables to discriminate various morphological types of the RBCs. For example, healthy RBCs surrounded by an environment with a hypotonic osmolarity change the shape fluently from disc-like RBCs (Discocytes) to spherical-like RBCs (Spherocytes). Amplitude cross-sections through two mutually orthogonal planes, including the optical axis, in the case of such RBCs whose

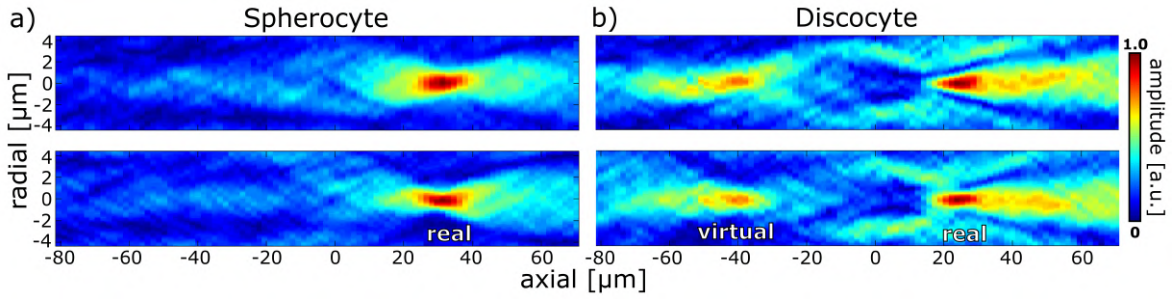

Figure 2.1: Absolute value of complex amplitude. Cross-sections through mutually orthogonal planes including the optical axis in case of a) Spherocyte, b) Discocyte.

interference patterns were measured experimentally, and the amplitudes were calculated numerically, are illustrated in the Fig. 2.1. Spherocytes include just one real focal point (Fig. 2.1a), while Discocytes produce both the real and the virtual focal spots (Fig. 2.1b) due to a convex-concave profile of the cells.

Various objects can be successfully localized, exploiting the contrast properties. The contrast is a measure characterizing the distribution of the bright and dark values in the image I. It can be evaluated in the meaning of the Tamura-coefficient approximation [14] defined as

$$TC = \sqrt{\frac{\sigma_I}{\langle I \rangle}}, \tag{2.1}$$

where $\langle I \rangle$ and σ_I are the mean value and standard deviation of the distribution evaluated, respectively. Absorbing objects often maximize the contrast, while transparent phase-like structures minimize the contrast in the sample's plane.

2.2 Experimental setup

Fig. 2.2a illustrates a Mach-Zehnder holographic microscope, and the scheme in Fig. 2.2b represents the optical bio-PL performed by an array of RBCs. Here, linearly polarized laser light (Melles Griot, $\lambda = 473$ nm, 15 mW, 0.67 mm beam diameter) is attenuated by an arrangement consisting of the half-wave plate HWP_1 and the linear polarizer LP_1, maintaining the output polarization. The sample illuminated by the laser light is placed in the signal arm of the interferometer on the vertical stage made of a beam splitter BS_1 and mirrors M_1 – M_3. The microscope objective MO_1 (Nikon, $20\times/0.30$) images the sample placed in a Petri Dish (PD) onto the conventional CMOS chip (1280×1024 pixels, 5.3 μm square pixels). Lateral magnification of the optical arrangement $43\times$ was measured by a standard amplitude resolution target (USAF 1951). Phase curvature induced by the objective MO_1 is compensated experimentally by the module placed in the reference arm, which consists

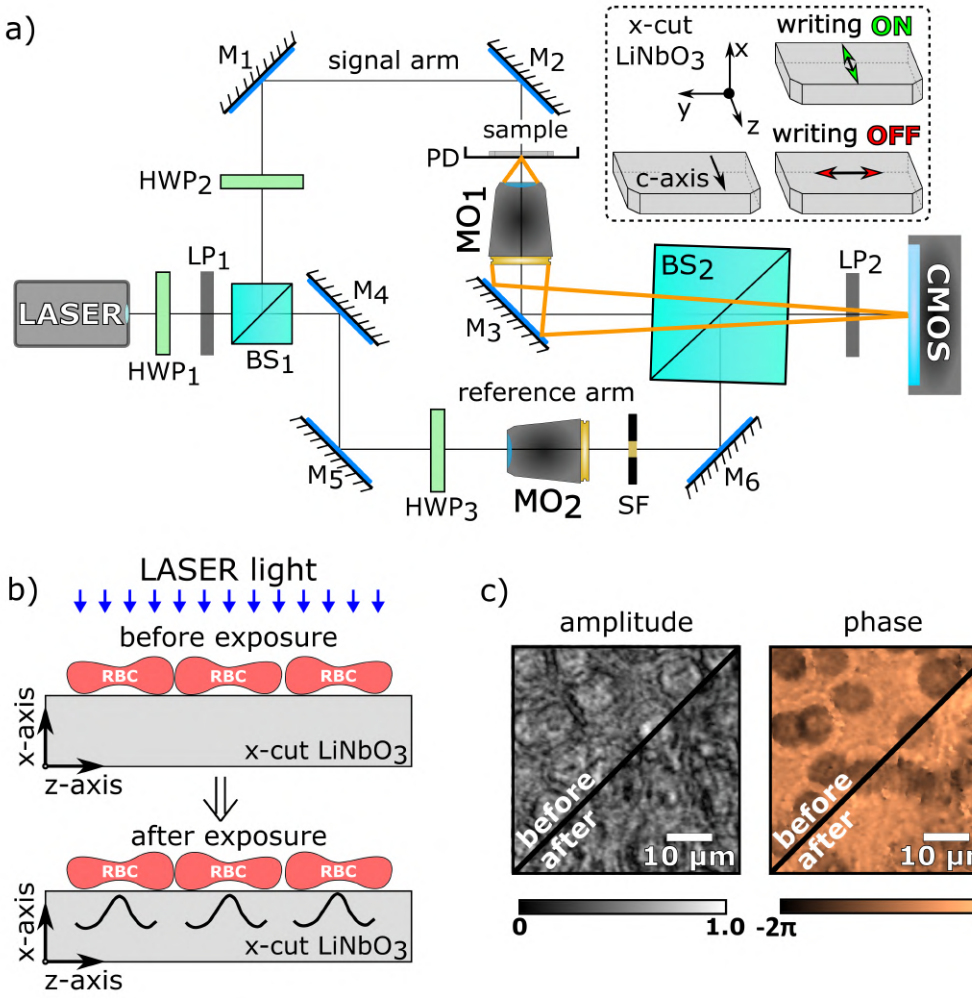

Figure 2.2: (a) Sketch of the experimental setup. Inserted image defines the coordinate system of the crystal and writing ON and writing OFF modes. Microscope objective (MO), half wave plate (HWP), mirror (M), linear polarizer (LP), beam Splitter (BS), Petri dish (PD). (b) Schematic view of bio-PL by RBC biolenses. (c) Quantitative phase map due to bio-PL writing on $LiNbO_3$, before and after exposure including RBCs.

of the spatial filter (SF) and the microscope objective MO_2 (Newport, $20\times$), generating the parabolic wave of comparable curvature as MO_1. The off-axis geometry is achieved by mixing the signal and the reference waves on the second beam splitter BS_2. The half-wave plate HWP_1 adjusts the polarization direction related to the sample plane. The half-wave plate HWP_2 ensures the collinearity of the output polarization states, and the linear polarizer LP_2 filters out the undesired residual polarization component. An x-cut iron-doped $LiNbO_3$ (Altechna, Fe:$LiNbO_3$ dopant level 0.05 %, 500µm thickness in x-axis, 10×10 mm in y-z plane) is placed into the PD, adopting the coordinate system from Fig. 2.2a. The optical arrangement works in two modalities, i.e., writing-on mode (polarization adjusted collinearly to the z-axis) and writing-off mode (polarization adjusted perpendicular to the z-axis). It is

possible to easily switch between the two modalities by 90° rotation of the linear laser light polarization. Writing-on mode allows the local modification of the refractive index while writing-off mode does not modify the refractive index, respectively. In the writing-off condition, it is possible to illuminate and analyze the $LiNbO_3$ sample using the same laser light without inducing the refractive index changes.

2.3 Measurement

The camera records the interference field originating from mixing a mutually coherent object beam, passing through the sample, and a separated reference wave. The interference patterns are recorded at different times and then numerically processed to retrieve the sample's complex amplitude, including quantitative phase maps.

Fig. 2.2c illustrates the amplitude and phase of the sample before and after the writing process. On the left-upper part of the phase map, the phase shift introduced by a few RBCs settled on the crystal is visible. The color-map goes from -2π to 0, and the image is retrieved in the writing-off mode. The cells exhibit a negative phase due to the adopted coordinate system (Fig. 2.2a). Then the laser light polarization is switched in the writing-on mode for 15 minutes. At the end of the process, the laser polarization is turned-off again. Another interference record is captured, and the corresponding phase map is shown on the right-bottom part of Fig. 2.2c. In this case, the measured phase map is the integral contribution of the phase shift of RBCs and local inhomogeneity induced inside the $LiNbO_3$.

The measurements were conducted on both types of RBCs, discocytes, and spherocytes, respectively. Initially, the light in the writing-off mode (Fig. 2.2a) illuminated the RBCs seeded on the top surface of the crystal, hence the first interference record close to the image plane was recorded before the PL writing started. In Fig. 2.3a and Fig. 2.3c, retrieved amplitude and quantitative phase maps are reported. Further, the optical power was set to 120 µW, and the polarization was adjusted in the writing-on mode (Fig. 2.2a) to imprint the cell structures into the crystal. After this procedure, the polarization was switched again into the writing-off mode. The sample was taken out from the signal arm. The RBCs were removed out of the surface of the crystal. Petri dish with the cleaned crystal was then placed back into the object plane of the microscope objective MO_1. The imprinted structures were localized in the identical FOV, and subsequently, the corresponding interference record was captured. Fig. 2.3b and Fig. 2.3d show the amplitude and the phase maps of the crystal without RBCs. The imprinted structures were imaged under writing-off-mode illumination of lower optical power, to minimize the possible deterioration.

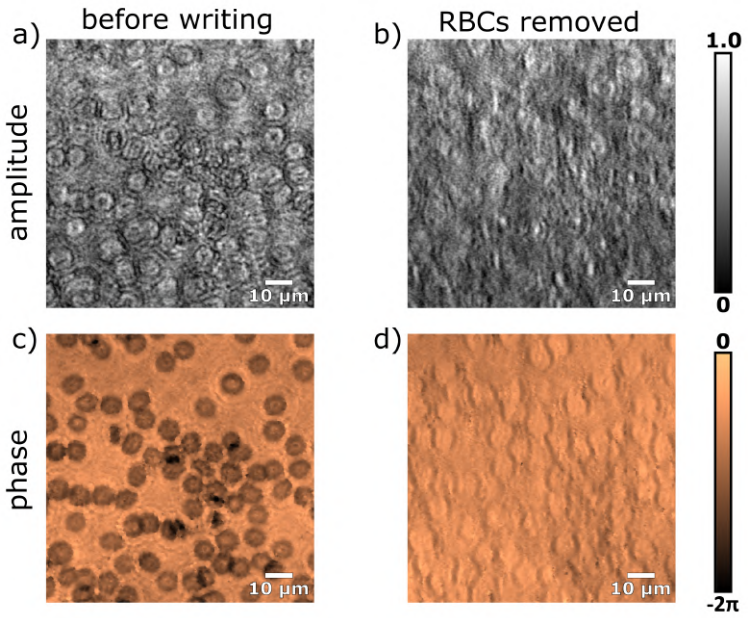

Figure 2.3: Reconstructed amplitude and phase of discocytes and the corresponding imprints. a), c) Cells before writing. b), d) Imprinted structures without cells.

2.4 Data processing, results and discussion

The useful holographic term was reconstructed, and the phase-background removed by fitting the entire FOV (Fig. **??**). The obtained complex amplitude was further propagated using the angular spectrum method. Thanks to DH features, axial reconstructions of the complex amplitude along the optical axis of the RBC biolenses were accomplished. The data presented in Fig. 2.4 and Fig. 2.5 were derived from the cell's properties and their corresponding imprints in the identical FOV.

The cells were localized using their focusing properties [13]. The radial coordinates of the amplitude maxima were found in the plane of the highest contrast calculated using the Tamura coefficient in the entire FOV [15]. The obtained amplitude profiles in x-y and x-z planes are shown in Fig. 2.4a and Fig. 2.5a. The zero axial coordinates correspond to the plane of the lowest local value of TC calculated in the plotted area (not shown in the figures), which not necessarily correspond to the local minimum of the amplitude profile. The focal distance of each cell was estimated as a position of the highest value of the axial amplitude. Histograms inserted in the figures represent the real and virtual focal distance distributions of the selected cells with the calculated values -28 ± 3 µm for the real foci in the case of spherical-like RBCs while, in case of discocytes, -42 ± 3 µm for the real foci and 27 ± 5 µm for the virtual foci (Fig. 2.4a, Fig. 2.5a).

In the adopted coordinate system, the real focus of the cells and the imprinted structures

are situated in the negative part of the propagation axis. The interference records of the imprinted structures without RBCs were processed similarly as the interference records of the RBCs due to analogous focusing properties. The obtained average amplitude profiles in x-y and x-z planes for spherical-like RBCs and discocytes are plotted in Fig. 2.4b and Fig. 2.5b, respectively. Spherical-like cells and their imprints contain just one significant focal point. The position of the real foci of 35 spherical-like cells -28 ± 3 µm is equal to the position of the real foci of the corresponding imprints -28 ± 3 µm. In the case of discocytes, it can be observed that imprints exhibit bi-focal properties, thus replicating the intrinsic double-focal property of discocytes. The external toroidal shape of the discocyte is responsible for the real-focus, while the central part produces a negative focus. The real and the virtual foci for 24 discocyte cells were established as -42 ± 3 µm and 27 ± 5 µm, respectively. The real and the virtual foci of the imprints were established as -42 ± 2 µm and 39 ± 12 µm, respectively. Real focal distances exhibit comparable standard deviations for the cells and the imprints, whereas the position of virtual focal distances of the imprints

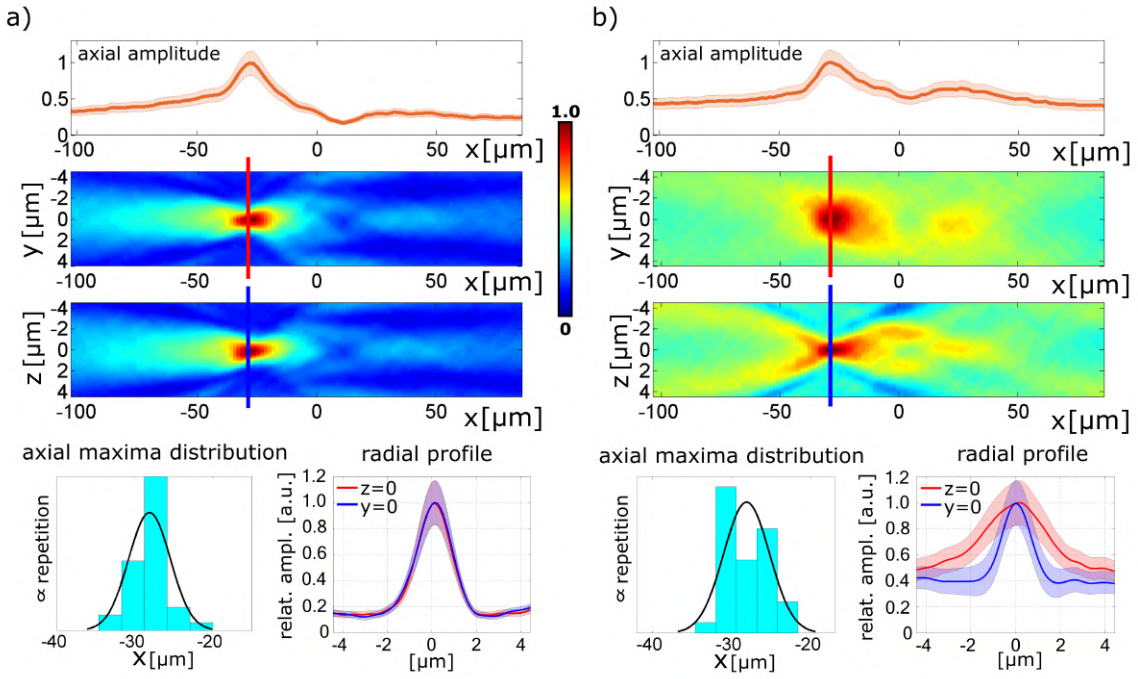

Figure 2.4: Average data obtained from 35 spherocytes and corresponding imprints. a) Axial amplitude and 2D amplitude plots in x-y and x-z planes of the cells with the real focal distance -28 ± 3 µm. b) Axial amplitude and 2D amplitude plots in x-y and x-z planes of the corresponding imprints with the real focal distance -28 ± 3 µm. Histograms represent focal-plane distribution for the real focal distance by means of the highest value of the axial amplitude [equal x-axis range 25 µm]. The radial profiles are the intersections through the marked lines. The error curves are calculated from the ensemble of 35 cells as a range of one standard deviation.

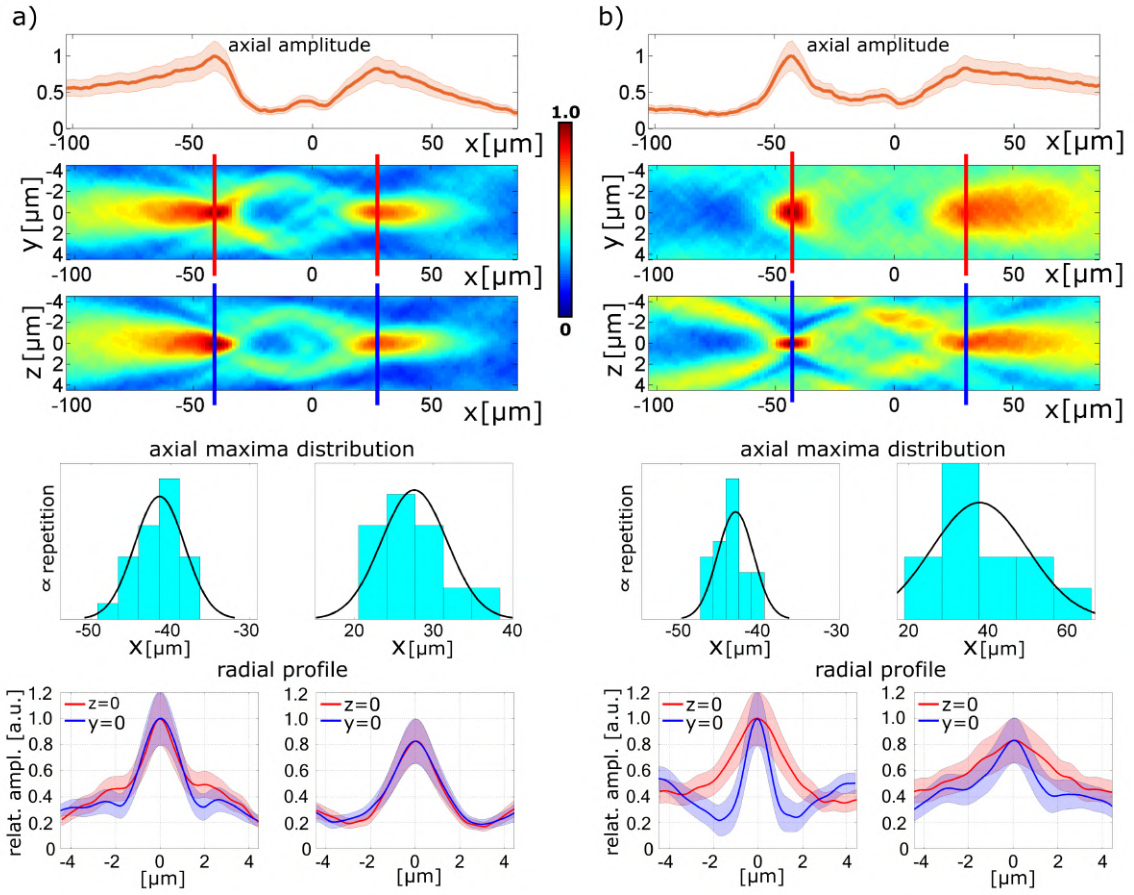

Figure 2.5: Average data obtained from 24 discocytes and corresponding imprints. a) Axial amplitude and 2D amplitude plots in x-y and x-z planes of the cells with the real focal distance -42 ± 3 μm and the virtual focal distance 27 ± 5 μm. b) Axial amplitude and 2D amplitude plots in x-y and x-z planes of the corresponding imprints with the real focal distance -42 ± 2 μm and the virtual focal distances 39 ± 12 μm. Histograms represent focal-plane distribution for the real and the virtual focal distances by means of the highest value of the axial amplitude [equal x-axis range 25 μm in all cases except virtual foci of the imprints (60 μm)]. The radial profiles are the intersections through the marked lines. The error curves are calculated from the ensemble of 24 cells as a range of one standard deviation.

is blurred. Nevertheless, the absolute distance between both focal points in the case of the discocytes and the imprints is equal in a range of the calculated standard deviations. All the mentioned values are summarized in the Tab. 2.1.

Amplitudes of the imprints exhibit asymmetrical behavior in x-y and x-z planes in both cases because the imprinted structures are also asymmetrical (Fig. 2.3b, Fig. 2.3d), even though amplitude plots of cells are symmetrical. This effect appears due to light-induced spatial distribution of the electric charges generated in PR materials by inhomogeneous illumination distribution [16, 17]. The asymmetry of the focal spots in the radial plane is

		Real foci (values in µm)			Virtual foci (values in µm)		
		position	FM_{x-y}	FM_{y-z}	position	FM_{x-y}	FM_{y-z}
Disco. (24 cells)	cells	-42 ± 3	1.5 ± 0.3	1.7 ± 0.3	27 ± 5	1.8 ± 0.3	1.9 ± 0.3
	imprints	-42 ± 2	2.4 ± 0.5	1.0 ± 0.3	39 ± 12	4.0 ± 1.1	2.0 ± 0.8
Spher. (35 cells)	cells	-28 ± 3	1.4 ± 0.2	1.4 ± 0.2	/	/	/
	imprints	-28 ± 3	3.4 ± 0.6	1.6 ± 0.4	/	/	/

Table 2.1: Characteristics in the focal regions for RBCs and the corresponding imprinted structures. FWHMs (denoted as FM_{x-y} and FM_{y-z}) are calculated from the intensity profiles.

characterized by a coefficient $\chi \in [0, 1]$ calculated as a ratio of two full widths at half maxima (FWHMs) in mutually orthogonal planes, i.e., x-y and y-z planes in our case, thus

$$\chi = \min\left\{\frac{\mathrm{FWHM}_{x-y}}{\mathrm{FWHM}_{x-z}}, \frac{\mathrm{FWHM}_{x-z}}{\mathrm{FWHM}_{x-y}}\right\}. \tag{2.2}$$

The real focal spots of the cells exhibit symmetrical behavior in both cases, discocytes ($\chi \approx 0.9$), and spherical-like cells ($\chi \approx 1.0$) as expected. In contrast, the imprints in the case of discocytes ($\chi \approx 0.4$) and spherical like RBC ($\chi \approx 0.4$) are significantly asymmetrical (Fig. 2.4, Fig. 2.5). Even values achieved in the virtual focal spots confirm the symmetry of discocytes ($\chi \approx 1.0$) and the asymmetry of the imprints ($\chi \approx 0.5$).

Moreover, numerical simulations are performed to understand the formation of refractive-index distribution induced by RBCs via a PR effect in $LiNbO_3$. The closed-form formula of the generated steady-state intrinsic electric-intensity field E_{sc} for circularly symmetric beams reaches the form [18]

$$\begin{aligned} E_{sc}(r,\varphi) = E_0\sqrt{\frac{1+I_\infty}{1+I}}\{2\cos^2\varphi - \cos 2\varphi\sqrt{\frac{1+I}{1+I_\infty}} - \\ - \frac{2}{r^2}\left(\cos 2\varphi + r\cos^2\varphi\frac{\mathrm{d}\ln\sqrt{1+I}}{\mathrm{d}r}\right)\int_0^r \rho\left(1-\sqrt{\frac{1+I(\rho)}{1+I_\infty}}\right)\mathrm{d}\rho\}, \end{aligned} \tag{2.3}$$

where (r, φ) are polar coordinates, E_0 is the transverse dc internal field in the crystal, I is intensity profile of the illumination beam, and $I_\infty = \lim_{r\to\infty} I(r)$. The equation (2.3) reaches a scalar form because the released electric charges tend to migrate along the crystal axis ($c-$axis). Here, the expression (2.3) is adopted to clarify the results observed (Fig. 2.5). Discocytes seeded on top of the crystal modify the profile of the laser-light illumination. Hence, the intensity illuminating surface of the crystal can be in principle obtained by numerical refocusing the reconstructed complex-amplitude map (Fig. 2.3a,c) of $\sim$ 3 µm. The distribution calculated is approximately radially symmetrical due to the shape of RBCs

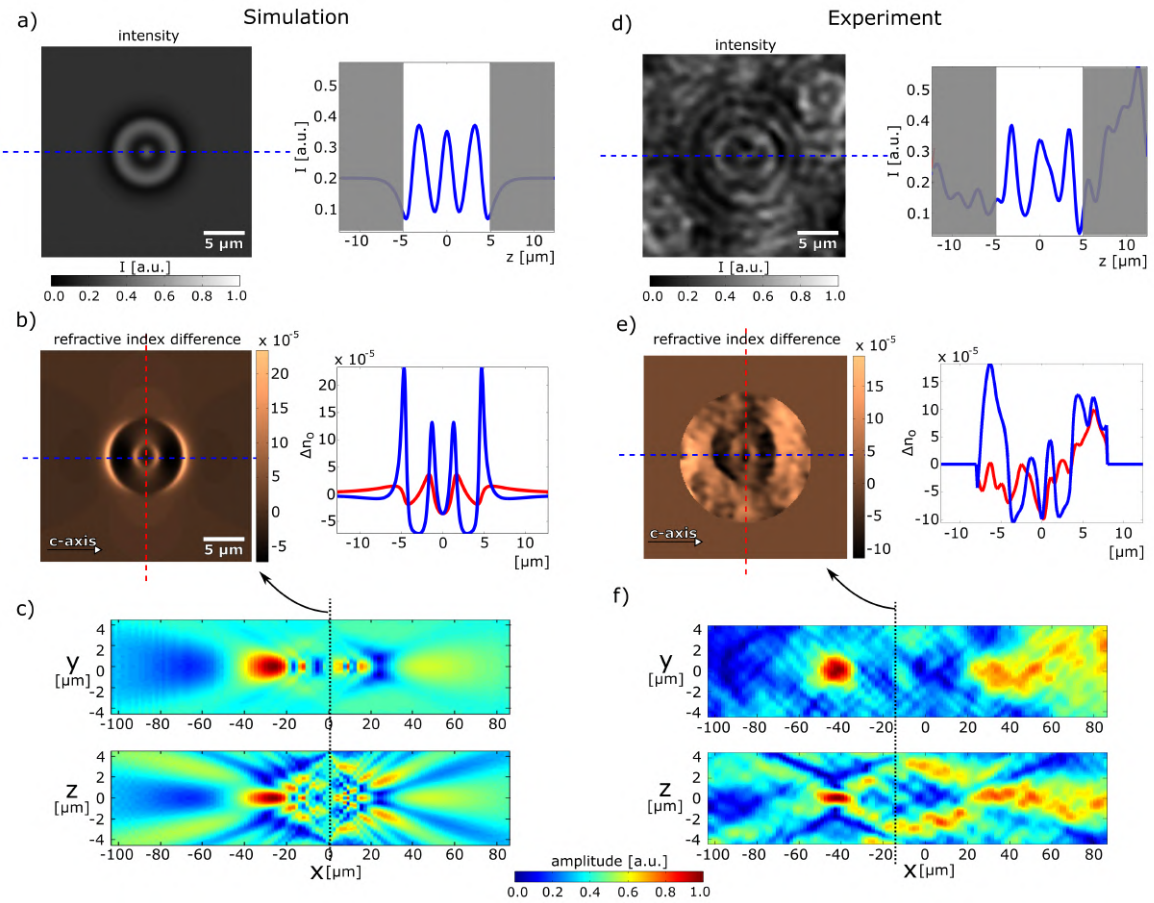

Figure 2.6: Parameters af the selected RBC and the corresponding imprint. a) Theoretical intensity profile illuminating the surface of the iron-doped x-cut $LiNbO_3$ crystal of parameters (2.4) $\kappa_1 = 0.38, \kappa_2 = 1.9, \kappa_3 = -1.5 \cdot 10^{43}, \kappa_4 = -2.9, \kappa_5 = -9.9^{11}, \kappa_6 = 1.4, \kappa_7 = -9.9^{12}, \kappa_8 = 0.20$. (Physical units of the coefficients are omitted for simplicity). b) Evaluated refractive-index distribution according to (2.5) with maintained parameters except $\kappa_1 = 300$ and $\kappa_1 = 150$ due to experimental conditions, $n_o = 2.35$, $r_{13} = 11$ pm V^{-1}, $E_0 = 20$ kV cm^{-1}. c) Cross-sections through the amplitude obtained by numerical propagation. d) Intensity profiles obtained by processing the experimenal data (refocusing the reconstructed complex amplitude of the RBC of $\sim$ 3 µm). e) Experimentally obtained refractive-index distribution. f) Cross-sections through the amplitude obtained by numerical propagation.

and can be roughly expressed as

$$I = \kappa_1 \left(\kappa_2 \exp\{\kappa_3 r^8\} + \kappa_4 \exp\{\kappa_5 r^2\} + \kappa_6 \exp\{\kappa_7 r^2\}\right) + \kappa_8, \tag{2.4}$$

where r is a radial coordinate, and $\kappa_j, j = \{1, ..., 8\}$ are real coefficients. The defocused intensity distribution of the selected discocyte is illustrated in Fig. 2.6d, together with its approximate form (Fig. 2.6a) obtained according to equation (2.4). Coefficients

$\kappa_j, j = \{1, ..., 8\}$ are specified in the caption of the figure. The coefficients κ_1, κ_8 were subsequently changed (in contrast to Fig. 2.6a) to 300 and 150, respectively, to approximately estimate real experimental conditions. Hence, the peak intensity of the light illuminating the crystal's surface reaches $\sim$ 300 W m^{-2}. The formula obtained for I is further substituted into the equation (2.3) to predict the intrinsic electric field E_{sc} induced by space-charge distribution inside the crystal. Finally, the refractive-index map predicted by the measurement is calculated according to

$$\Delta n_o = -0.5 n_o^3 r_{13}(E_0 - E_{sc}), \tag{2.5}$$

because the measurements were performed with illumination polarized orthogonally to the $c-$axis=$z-$axis, where $n_o = 2.35$, $r_{13} = 11$ pm V^{-1}, and E_0 is estimated as 20 kV cm^{-1}, which lies in the range of expected values [19]. Predicted distribution of the induced refractive-index is illustrated in Fig. 2.6b with corresponding plots through the horizontal and vertical coordinates. The central part reaches local minimum followed by two symmetrically displaced local maxima, two local minima and two maxima in a periphery. Cross-sections through the amplitude, similar to those observed in Fig. 2.5b, were subsequently calculated by numerical propagation of the phase profile corresponding to the derived refractive-index map (Fig. 2.6c). Furthermore, amplitude cross-sections through the complex amplitude of the measured imprint are illustrated in Fig. 2.6f. The theoretical predictions (Fig. 2.6c) are in good accordance with the experimental measurements (Fig. 2.6f), although positions of the amplitude maxima are mutually shifted in the $z-$direction of $\sim$ 15 µm. Hence, the simulated refractive-index distribution (Fig. 2.6b) was compared to the correspondingly shifted experimental one (Fig. 2.6e).

For detailed quantitative evaluation, more precise optical measurements, including speckle-free homogeneous illumination, should be provided with an in-depth characterization of the used crystal. Here approximate characteristics of Fe:$LiNbO_3$ were used to evaluate the theoretical photorefractive change induced by the living RBC (Fig. 2.6). Moreover, temporarily stable optical illumination, together with an accurately defined beam profile, should be used to study the interaction of light and photorefractive material. However, the theoretical model of the proposed interaction was out of the scope of this work. In our case, living cells, dynamically evolved systems [20, 21], were used as optical elements that fluctuate in their positions and induced optical properties. To prove the possibility of imprinting structures of cells into the photorefractive material and to study the possibility of their mutual distinguishing was the primary motivation of this work. Both of the properties were proved satisfyingly.

Chapter 3

Optimized implementation of the double-exposure method in common-path self-referencing digital holographic microscopy

This chapter is based on the following publication:

[3] J. Běhal, "Quantitative phase imaging in common-path cross-referenced holographic microscopy using double-exposure method," *Scientific Reports*, vol. 9, no. 9801, 2019.

This chapter presents the optimized implementation of the double-exposure method with emphasis on the uniformity and the minimization of residual phase imperfections in common-path self-referencing DHM. The required holographic terms are retrieved from single-shot records. Quantitative phase maps obtained are further processed to reduce phase defects originating from the imperfections of the optical path. Firstly, common-path lateral-shearing self-referencing DHM is implemented in a microscope configuration supplemented by a Sagnac interferometer to achieve duplication and further shearing of the waves. Utilization of the averaging process, which enhances the precision of QPI reconstruction, applicable in the methods with a doubled FOV, is also presented. The application potential is demonstrated by the imaging of biological samples, including the cheek and sperm cells. Moreover, another common-path self-referencing DHM is realized in a microscope arrangement with the added mirror to obtain the self-referencing. The initial measurements are performed, and the optimized implementation of the double-exposure method is demonstrated by imaging the glass beads.

3.1 Double-exposure method

Various types of phase inhomogeneities without the need of their exact knowledge can be eliminated utilizing the double exposure method [22]. The method is based on processing two interference records, with and without the sample, respectively (Fig. 3.1). The phase image restored from the pattern acquired with the specimen reveals a background-phase degradation, making the quantitative phase assessment of the image difficult (Fig. 3.1b). Hence, the sample is moved out of the field of view to take the reference snapshot (Fig. 3.1c). The phase map restored (Fig. 3.1d) is then subtracted from the original phase image. By this operation, the phase image of the cell is obtained in which the phase background approaches the zero phase level (Fig. 3.1e).

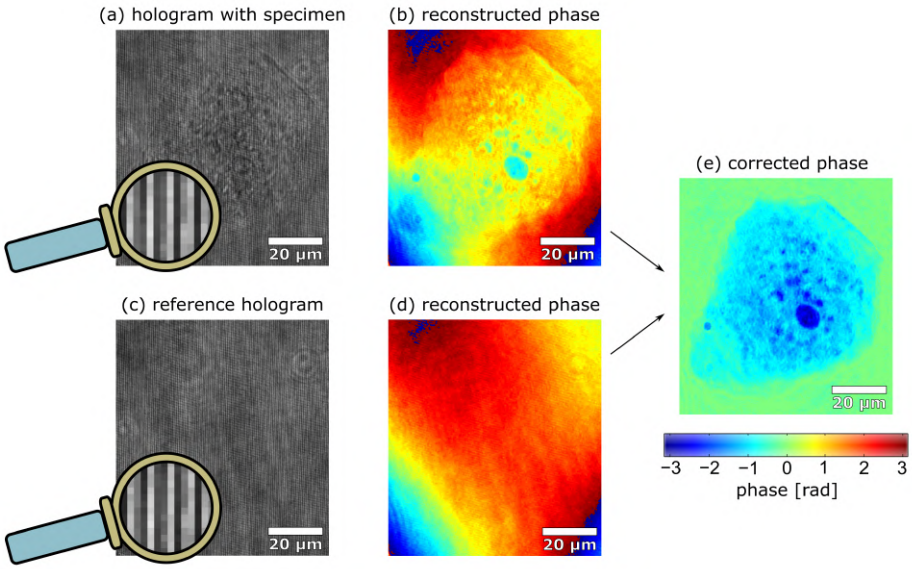

Figure 3.1: Background phase corrected by the double-exposure method exploiting the reference interference record. (a) Interference record including the specimen. (b) Quantitative phase image of the specimen reconstructed from the record. (c) Reference snapshot recorded without the specimen. (d) Quantitative phase map reconstructed from the reference record. (e) Corrected quantitative phase image of the cell.

3.2 Common-path lateral-shearing self-referencing digital holographic microscopy

The signal and the reference waves in the DH configurations with the common-path interferometer pass through a single-arm and share identical optical components. Hence the temporal stability of the system is enhanced by comparing the geometries with two spatially

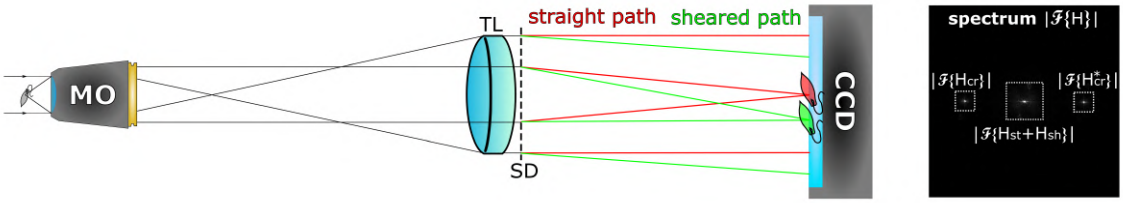

Figure 3.2: Illustration of straight and sheared optical paths in standard microscope supplemented by a shearing device. microscope objective (MO), tube lens (TL), shearing device (SD), camera (CCD). Typical Fourier amplitude spectrum on the right part of the figure.

independent arms. The signal and the reference waves in a common-path lateral-shearing self-referencing DHM, leave a standard microscope arrangement with a microscope objective (MO) and a tube lens (TL). The lateral shear required between the straight and sheared copies of the FOV (Fig. 3.2) is achieved by inserting a proper optical component, called a shearing device (SD), between the TL and detector (CCD). Various types of shearing devices were used to achieve the lateral shear, such as a beam splitter [23], a thick glass plate [24], a Wollaston prism [25], a calcite crystal [26], a Fresnel biprism [27], or gratings [28]. The choice of suitable shearing device depends on the requirements of a particular application. The spatial frequency introduced between the interfering paths advantageously enables a single-shot holographic reconstruction ideal for the real-time experimental observations.

3.3 Arrangement with Sagnac interferometer

Common-path lateral-shearing self-referencing DHM was realized in the microscope arrangement with incorporated Sagnac interferometer operating as a fluently adjustable shearing device (Fig. 3.3). The monochromatic light beam emerging from unpolarized He-Ne laser (10 mW, $\lambda = 633$ nm) is coupled into a single-mode optical fiber by collimation and focusing optics. The spatially filtered light arising from the fiber is captured by an aspheric lens L_0 and focused in proximity to a rotating diffuser (RD). The light scattered by RD is condensed by lens L_1 and subsequently illuminates the studied specimen. Using a microscope objective MO (UPlanFL N, NA $= 0.75$) and a tube lens TL (achromatic doublet, effective focal distance 400 mm) the specimen's magnified image (lateral magnification $89\times$) is created on a CCD (Retiga 4000R, 7.4 µm pixel size, 2048×2048 pixels). Relay lenses L_2 and L_3 (both achromatic doublets, effective focal distance 50 mm) are used to image the field iris diaphragm (FID) to the CCD plane.

The Sagnac interferometer module is situated between the TL and the CCD. It contains a polarizing beam splitter (PBS), three mirrors M_4-M_6, and two diagonally oriented linear polarizers LP_1 and LP_2 in the input and the output of the PBS to enhance the contrast of

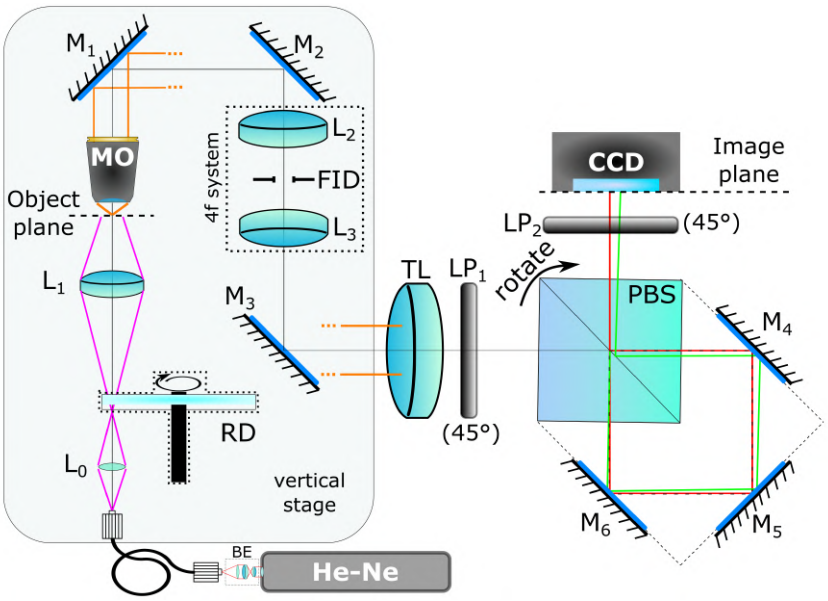

Figure 3.3: Setup for implementation of the common-path lateral-shearing self-referencing digital holographic microscopy with the incorporated Sagnac interferometer used as a shearing device. Collimation and focusing lenses (BE), aspheric lens (L_0), rotating diffuser (RD), condenser lens (L_1), microscope objective (MO), mirrors (M_1-M_4), relay lenses (L_2, L_3), field iris diaphragm (FID), tube lens (TL), linear polarizers (LP_1, LP_2), polarizing beam splitter (PBS), camera (CCD).

interference fringes created at the CCD. The lateral shear Δx between the interfering waves is adjusted by a slight rotation of the PBS, which is illustrated in Fig. 3.3. The used tube lens (focal distance 400 mm) enables easy access to the Sagnac module built with optical components of commonly available parameters. In case when coupling the microscope objective with the standard tube lenses (focal distance ≈ 200 mm) is required, dimensions of PBS and used mirrors (M_4-M_6) should decrease correspondingly.

3.3.1 Initial measurements

The distance between the light spot created by the lens L_0 and the rotating diffuser allows the adjustment of spatial coherence of illuminating light and reducing speckle noise in the image plane when imaging the sample [29, 30]. Moreover, the temporal stability of the system was measured without the presence of any specimen. Period of interference fringes was adjusted to three pixels of the CCD, and a sequence of 240 snapshots was recorded for 2 minutes (the detector rate of 2 Hz). Each of the saved interference records was filtered in the Fourier space, and a phase map was further restored. The standard deviation calculated in the area 8.3×8.3 μm^2 was determined as $\sigma_{mean} = 0.018$ rad in a case when the rotating diffuser was inactive. The measurement realized with the rotating diffuser results in the

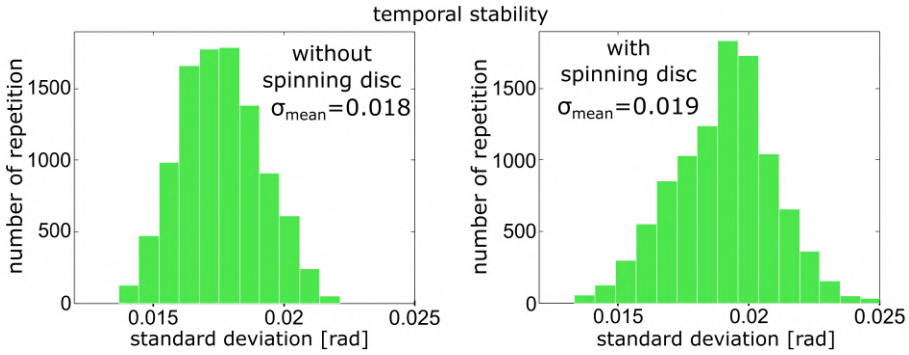

Figure 3.4: Measurement of the temporal stability carried out with and without rotating diffuser.

standard deviation value of $\sigma_{mean} = 0.019$ rad, meaning that the diffuser spins have low importance on the temporal stability of the system. The results obtained are illustrated in Fig. 3.4.

3.3.2 Results and discussion

For practical utilization of the method, cheek cells as a specimen were used. The cells were taken from inside the mouth by a toothpick, diluted in a drop of water, and sandwiched between the ground glass and the cover glass. The interference record of a single cheek cell was stored. Subsequently, the reference snapshot was recorded after the cell was moved away from the FOV by mechanically translating the stage. The phase-maps were retrieved from corresponding records and mutually deducted to eliminate the phase background. The reconstructed doubled phase images, with a flat background reaching the zero phase value, are shown in Fig. 3.5a.

Results obtained by the double-exposure method were compared to the polynomial background phase fitting (Fig. 3.5b). The reconstructed phase was unwrapped and fitted by the second-order polynomial to reduce residual offsets, tilts, and curvatures. The phase map corrected by fitting is compared to the result achieved by the double-exposure method in the same area (16.6×24.9 μm^2) in proximity to the observed cell reaching the standard deviations $\sigma_{mean} = 0.208$ rad and $\sigma_{mean} = 0.066$ rad, respectively. These results confirm an efficient background phase correction in the experimental configuration considered. Although the background phase can be fitted by higher-order polynomials or more sophisticated mathematical models, local phase inhomogeneities can barely be suppressed. As an example, multiple reflections from optical surfaces cause local ring-like interference circles, which deteriorate the overall sample phase-map. These local defects influence both amplitude and phase distributions (Fig. 3.5b) and are effectively eliminated by the double-

exposure method (Fig. 3.5b).

Homogeneity of the phase background is examined by quantifying the changes of standard deviations when expanding the region for evaluation. The standard deviations calculated in two small laterally displaced areas of the size 4.2×4.2 µm^2 are established as 0.030 rad and 0.038 rad, respectively. When the areas are enlarged from 4.2×4.2 µm^2 to 12.5×12.5 µm^2, the standard deviations are increased to 0.057 rad and 0.059 rad revealing

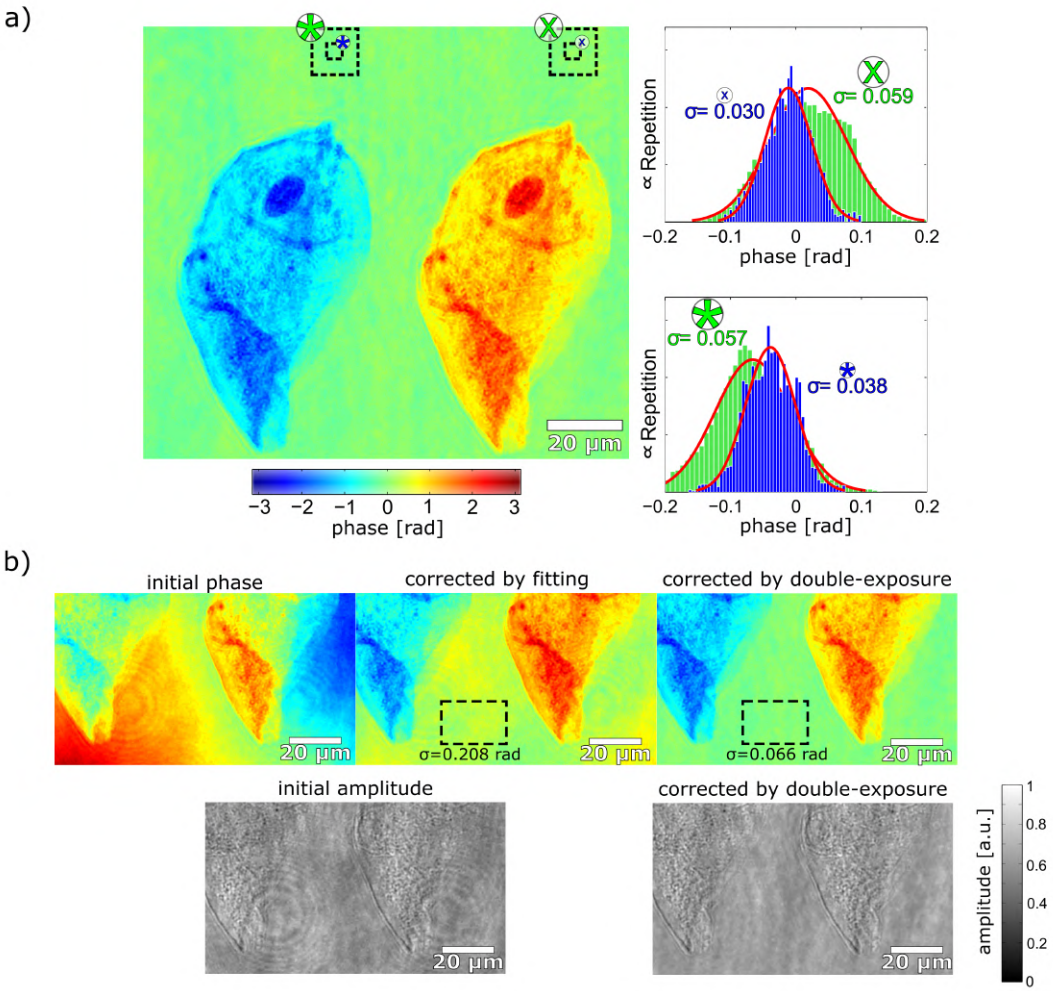

Figure 3.5: a) Quantitative phase image of the cheek cell with demonstration of nonuniformity of the phase background in the two laterally displaced areas. The standard deviations were increased from 0.038 rad to 0.057 rad and from 0.030 rad to 0.059 rad when evaluation areas expanded from 4.2×4.2 µm^2 (blue line histograms) to 12.5×12.5 µm^2 (green line histograms). b) Comparison of background phase correction achieved by fitting and double-exposure method. Standard deviations calculated in dashed rectangles embedded (16.6×24.9 µm^2) reach values 0.208 rad and 0.066 rad, respectively. Local circ-like structures originating from multiple reflections are effectively eliminated in both amplitude and phase distributions by double-exposure method.

irregularity of the phase background. The inhomogeneity of phase background is illustrated by blue and green histograms associated with the smaller and larger regions. In addition to the enlarged standard deviations, even a shift of mean values is evident comparing the histograms of smaller and larger areas. The indicated inhomogeneity of the background phase in Fig. 3.5a is a consequence of a mechanical translation of the specimen to achieve the empty FOV when recording the reference snapshot. The shape of the phase background changes when the specimen is mechanically removed. Consequently, the remaining phase nonuniformities influence the quality of the phase background, even the double-exposure method is applied (Fig. 3.5a).

The correction of the phase background is much more accurate when the specimen is removed without external mechanical interventions. The approach mentioned is feasible to demonstrate in the experiment with a semen sample diffused in water and sandwiched between the ground and the cover glass. The stage was slightly tilted from a horizontal position to achieve moving of the specimen by flowing a surrounding medium. In this case, the reference interference record can be captured after the sample is freely removed outside of FOV. The doubled phase images of the semen cell restored from the records appear on the opposite sides of the FOV in Fig. 3.6a. The standard deviations calculated in two laterally displaced areas of the size 4.2×4.2 μm^2, providing values of 0.024 rad and 0.022 rad. When expanding the areas from 4.2×4.2 μm^2 to 12.5×12.5 μm^2, the values of standard deviation stayed practically unchanged, 0.029 rad and 0.026 rad, respectively. The homogeneity of phase background is well illustrated by the blue and the green histograms associated with the smaller area and the larger area, respectively (Fig. 3.6a). Note that the range of the values displayed is different compared to Fig. 3.5a.

The fact that the field of view in common-path lateral-shearing DHM is reduced intrinsically can be exploited to enhance the imaging performance. Quality of the quantitative phase image restored is further improved when the straight and the sheared images $\Delta\Phi_{st}(x)$ and $\Delta\Phi_{sh}(x-\Delta x)$, respectively, are present in the FOV. The lateral shear between the duplicated images is eliminated during the numerical processing, hence averaging of the phases $-\Delta\Phi_{st}(x)$ and $+\Delta\Phi_{sh}(x)$ is possible to carry out. Significant advantages of the averaging are demonstrated in measurement with the sperm specimen, where both doubled images of the cell fit inside the FOV. The result obtained after applying the averaging procedure is shown in Fig. 3.6b with the standard deviation of the background decreased to 0.019 rad and 0.023 rad, in the regions studied, respectively. The quasi-surface plot of the phase image restored, including the sperm cell, is available in Fig. 3.6d, where the homogeneous background enables clear recognition of the sperm-cell tail.

The terms $+\Delta\Phi_{st}(x)$ and $+\Delta\Phi_{sh}(x-\Delta x)$ contain identical information about the sample but differ in residual phase imperfections rising from the sheared and the straight

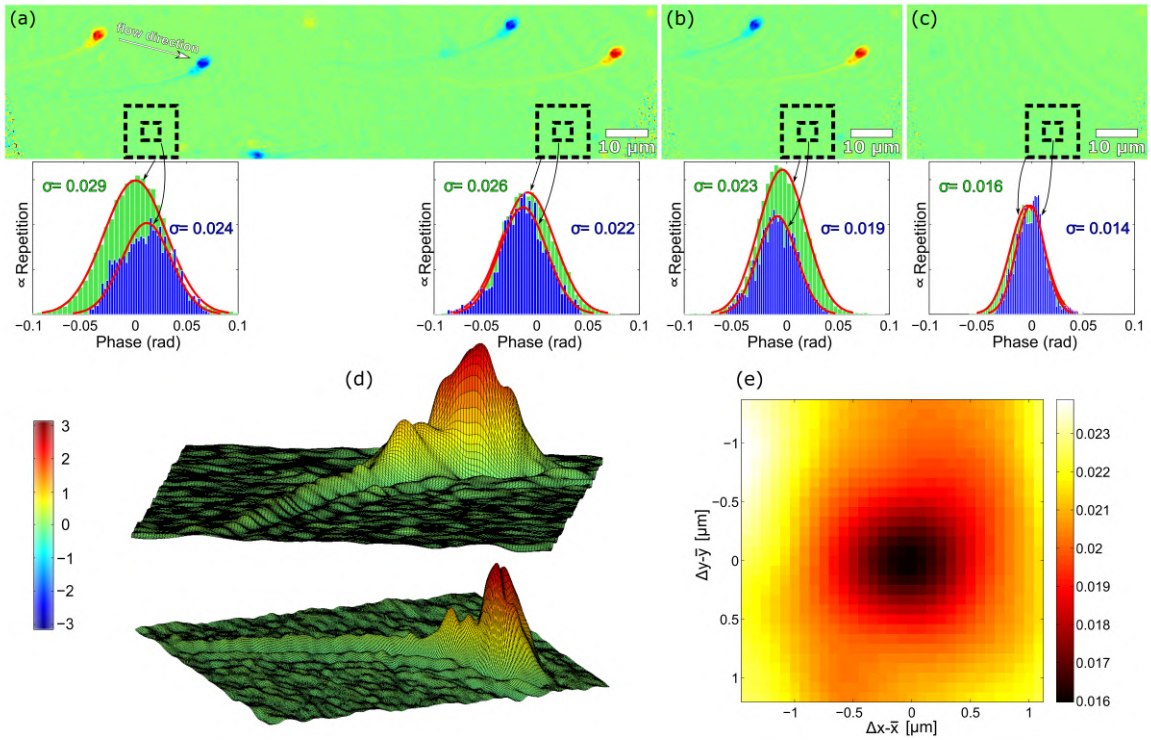

Figure 3.6: Quantitative phase imaging of the sperm cell. (a) Doubled phase image of the cell with demonstration of the background uniformity. The standard deviation is less dependent on the size and lateral position of the evaluation areas than in the previous case (size of areas 4.2×4.2 µm^2 and 12.5×12.5 µm^2). (b) The phase image with decreased standard deviation provided by the averaging procedure. (c) The phase map of imperfections added by the cross-referenced waves and standard deviations calculated in the marked areas. (d) Surface plot of the cell. (e) Standard deviation of $[\Delta\Phi_{st}(x,y) + \Delta\Phi_{sh}(x - \Delta x + \overline{x}, y - \Delta y + \overline{y})]/2$ when eliminating the lateral shear Δx in x-direction and Δy in y-direction.

cross-reference waves, respectively. The feature mentioned was exploited when numerically eliminating a lateral shear. The sheared image is localized, shifted towards the straight image by $\overline{x}$, and both areas are averaged. The lateral shear is canceled when a standard deviation of the averaged image $[\Delta\Phi_{st}(x) + \Delta\Phi_{sh}(x - \Delta x + \overline{x})]/2$ reaches its minimum (i. e., in case when $\overline{x} = \Delta x$) because the information about the sample is just reduced. This property is evaluated by a standard deviation calculated inside the larger area 12.5×12.5 µm^2 without the cells (Fig. 3.6e). The lateral shear is canceled with precision $\propto$ 0.08 µm, which is lower than the radius of Airy disc $\propto$ 0.5 µm in the object space. After removing the lateral shear, the phase differences $+\Delta\Phi_{st}(x)$ and $+\Delta\Phi_{sh}(x)$ can be averaged which enables to estimate the amount of phase fluctuations added into the area of interest by the straight and the sheared reference waves, passing through the surrounding medium. Fig. 3.6c illustrates the result with the standard deviations of the background 0.014 rad and 0.016 rad,

which simultaneously estimate the precision of the quantitative phase reconstruction in the evaluation areas. These values converted into OPD result in 1.4 nm and 1.6 nm, respectively. These imperfections can be minimized, and the common-path lateral shearing self-referencing DHM imaging performance further enhanced in microfluidic applications using channels. Here the reference record can be captured without mechanical movements, and the straight and the sheared reference waves pass through the areas out of the channel without the surrounding medium. This implementation reduces the added phase fluctuations naturally.

3.4 Arrangement with additional mirror

Another example of a quasi-common-path experimental arrangement is illustrated in Fig. 3.7a. Instead of incorporating the shearing device replicating FOV, just an additional mirror is used to create an off-axis geometry by reflecting a part of the object beam on itself. Particularly, He-Ne laser ($10\mathrm{mW}$, $\lambda = 633$ nm) is coupled into a single-mode fiber by collimation and focusing optics (BE). Light emerging from the fiber illuminates the sample whose magnified image (lateral magnification $25\times$) is created close to the camera's chip (CCD, Retiga 4000R, 7.4 µm pixel size, 2048×2048 pixels) by the microscope objective (MO). The mirror (M) positioned in the image space of the MO reflects part of initially unemployed light for self-referencing. Hence, off-axis geometry is achieved by mixing both mutually coherent optical fields with fluent adjustment of the fringe period allowed by a tilt of the mirror M.

Firstly, 240 interference images without any specimen were recorded for 120 seconds (the detector rate of 2 Hz) to test the temporal stability of the system. The saved images were numerically processed to reconstruct phase maps of the corresponding complex amplitudes. The average standard deviation evaluated in the region of the entire camera chip $\sim 600 \times 600$ µm^2 reaches $\sigma_{mean} = 0.028$ rad. Histogram of the values obtained is illustrated in Fig. 3.7b.

It can be noticed in the experiment with phase target USAF 1951 (Fig. 3.7c), that phase background contains residual curvatures even when the spatial carrier frequency is eliminated because the interfering waves are of close, however unequal, curvatures. Hence, the unwrapped phase background can be corrected accurately by the second-order polynomial fitting (Fig. 3.7c). Although the phase background is fixed, the higher-frequency fringes originating from parasitic interference of multiple reflections remain preserved. The residual fringes are eliminated more effectively by the double-exposure method with the reference acquisition obtained when the target is translated out of the field of view. The average

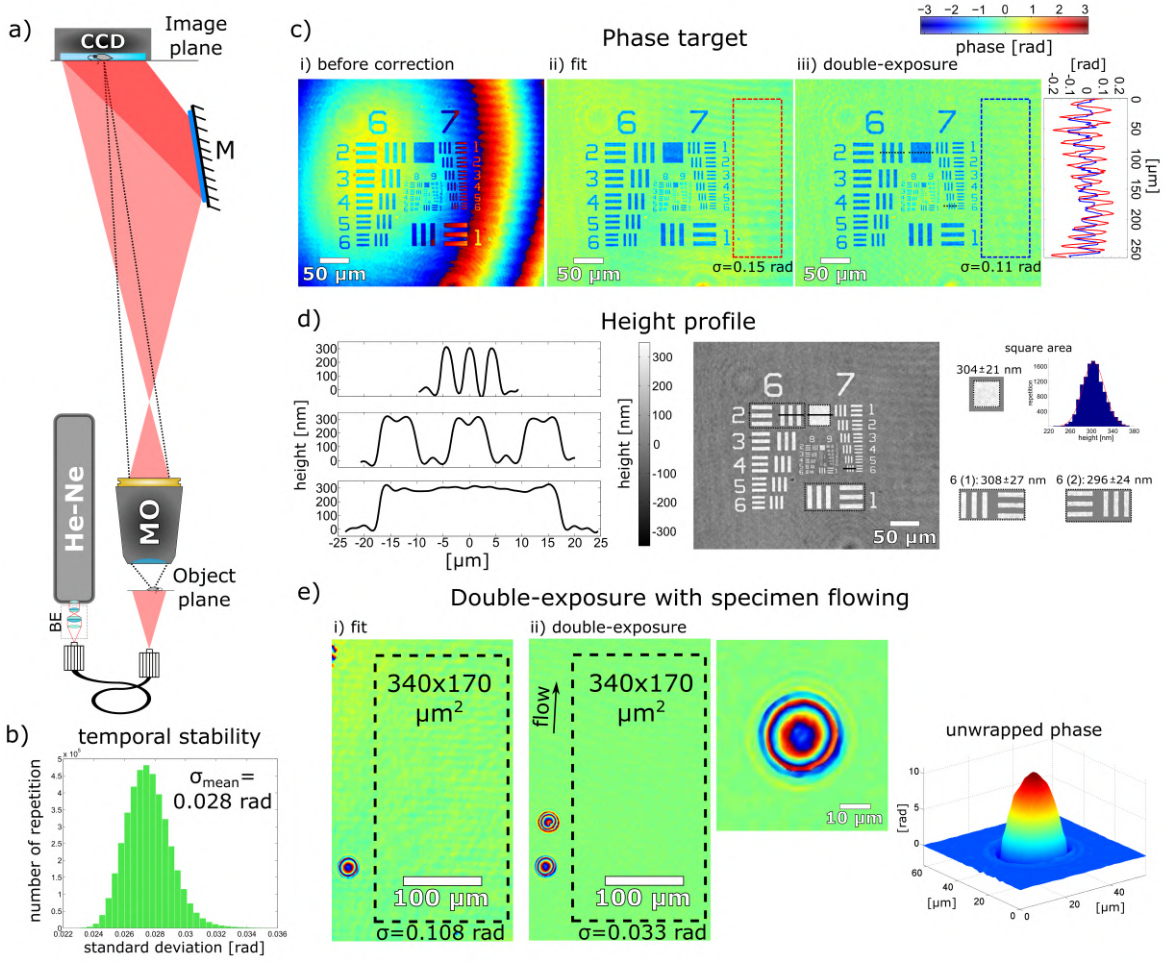

Figure 3.7: a) Experimental arrangement. Collimation and focusing lenses (BE), microscope objective (MO), a mirror (M), and camera (CCD). b) Temporal stability evaluated in the area of $\sim 600 \times 600$ μm^2 from a 2-minute interference record captured by frequency of 2 Hz. c) Phase target USAF 1951. i) The reconstructed phase before correction. ii) Phase corrected by the second-order polynomial fitting. iii) Phase corrected by double-exposure method. d) Reconstructed height map with plots along the marked lines. Ground-truth height of the target is 321 nm. e) Comparison of the double-exposure method with second-order polynomial fitting in case of a self-moving sample.

profile of fringes inside the highlighted area is plotted in Fig. 3.7c and reaches standard deviations $\sigma = 0.15$ rad in case of the map corrected by fitting and $\sigma = 0.11$ rad in the case of the double-exposure method, respectively. Furthermore, the height profile is evaluated according to equation $h(x) = \Delta\Phi_{st}(x)/[k(n-1)]$, where the refractive index of the glass $n = 1.52$ is used. Plots through the square, line group 6 element 2, and line group 7 element 6 of the resolution target transformed into the heights are also shown in Fig. 3.7d (black solid lines). Oscillations near sharp edges appear again as a result of filtering out the high spatial frequencies of the resolution target by the optical system. The height calculated in

the area of $\sim 30 \times 30$ μm^2 inside the large square of the phase target reaches 304 ± 21 nm. Subsequently, the heights of different line groups of comparable lateral dimensions present in mutually distant areas were evaluated. Especially, height of the line group 6 element 1 and line group 6 element 2 (highlighted by dotted rectangles in Fig. 3.7d) achieve similar results 308 ± 27 nm and 296 ± 24 nm, respectively.

The correction of phase background is even more efficient when the sample observed is self-moving or driven by the flow. In such the case, both interference records with and without the sample, respectively, can be recorded without external mechanical manipulation by the sample. The approach mentioned is demonstrated in the experiment with glass beads ($10 - 30$ μm, Polyscience, $\#07688$) diffused in distilled water and sandwiched between the ground and the cover glass. The stage was slightly tilted from a horizontal position to achieve moving of the specimen by flowing in the flow. In this case, the reference snapshot can be captured after the sample is freely removed outside of the FOV. The reconstructed phase is illustrated in Fig. 3.7e, where the background phase homogeneity is evaluated in the area of the size 340×170 μm^2, where the standard deviation reaches $\sigma = 0.033$ rad. The predictable shape of the background phase map also enables its more sufficient correction by a second-order polynomial fitting, in comparison to Fig. 3.5b. Initially, the phase is unwrapped, fitted, corrected, and the result obtained is illustrated in the left part of Fig. 3.7e. Furthermore, the standard deviation $\sigma = 0.108$ rad is obtained inside the same area, as in the case of the double-exposure method, which enables the direct comparison of results obtained by both approaches. Hence, the reference snapshot captured without mechanical interventions enables efficient correction of the whole background phase. Therefore the double-exposure method is used as a reference to confirm the effectiveness of other phase-compensation methods [31–33]. The conclusions reached in the current experimental arrangement are in good accordance with the results achieved in the previous experiment, where the Sagnac interferometer was used as a shearing device.

Chapter 4

Polarization-sensitive digital holographic imaging with enhanced temporal stability

Enhanced temporal stability of the common-path Sagnac interferometer, discussed in the previous chapter, is utilized for generation of the temporarily correlated beams. The experimental arrangement, being examined (sketched in Fig. 4.1), basically represents a digital holographic microscope with the Mach-Zehnder interferometer with the incorporated polarization-sensitive Sagnac module in the reference arm for generation of two orthogonally polarized reference beams. This idea was firstly introduced in the work [34]. However detailed analysis of the setup have not been discussed yet, according to our knowledge. The experimental configuration presented served for imaging homogeneous anisotropic samples producing uniform polarization distribution (linear polarizer, quarter-wave plate), except residual deviations from the expected values. Here, the temporal stability is quantified and the ability of reconstructing spatially variable polarization states confirmed by imaging the S-wave plate, which is a half-wave plate with the spatially-dependent orientation of the local axis.

4.1 Direct Jones matrix reconstruction in digital holography

The polarized light is advantageously characterized by the Jones matrix formalism developed in the 1940s [35]. Jones vector of the optical beam propagated along the z-axis is written as

$$\mathbf{U} = \begin{bmatrix} U_x \\ U_y \end{bmatrix} = \begin{bmatrix} A_x \exp(i\Phi_x) \\ A_y \exp(i\Phi_y) \end{bmatrix}. \tag{4.1}$$

The Jones matrix of an arbitrary object transforming the polarization state is defined as

$$\mathbb{T} = \begin{bmatrix} T_{xx} & T_{xy} \\ T_{yx} & T_{yy} \end{bmatrix}, \tag{4.2}$$

where $T_{xx}, T_{xy}, T_{yx}, T_{yy}$ are complex elements in general. Elements of the matrix can be obtained directly from the measurement provided by the two orthogonal polarization states of the illuminating light. For example, when the measurement is sequentially performed by the diagonal ($\mathbf{U^d}$) and antidiagonal ($\mathbf{U^a}$) illumination, given as

$$\mathbf{U^d} = \frac{1}{\sqrt{2}} \begin{bmatrix} 1 \\ 1 \end{bmatrix}, \quad \mathbf{U^a} = \frac{1}{\sqrt{2}} \begin{bmatrix} 1 \\ -1 \end{bmatrix}, \tag{4.3}$$

and the corresponding output polarization states

$$\overline{\mathbf{U}}^{\mathbf{d}} = \mathbb{T}\mathbf{U^d}, \quad \overline{\mathbf{U}}^{\mathbf{a}} = \mathbb{T}\mathbf{U^a} \tag{4.4}$$

are measured, the required elements of the Jones matrix $\mathbb{T}$ are recovered as

$$\mathbb{T} = \begin{bmatrix} T_{xx} & T_{xy} \\ T_{yx} & T_{yy} \end{bmatrix} = \frac{1}{\sqrt{2}} \begin{bmatrix} \overline{U}_x^d + \overline{U}_x^a & \overline{U}_x^d - \overline{U}_x^a \\ \overline{U}_y^d + \overline{U}_y^a & \overline{U}_y^d - \overline{U}_y^a \end{bmatrix}. \tag{4.5}$$

Till now, the exploitation of the DH was considered working for the scalar waves. However, each of the components in equation (4.1) can be mixed with the mutually coherent equally polarized beam generating the scalar interference field. The polarization imaging is consequently possible by measuring the phase differences for multiple polarization modes. Especially, the horizontally $\overline{\mathbf{U}}_{\mathbf{r1}}$ and vertically polarized reference waves $\overline{\mathbf{U}}_{\mathbf{r2}}$ are considered, which are simultaneously mixed with the arbitrarily polarized signal wave $\overline{\mathbf{U}}_{\mathbf{s}}$, given as

$$\overline{\mathbf{U}}_{\mathbf{r1}} = \begin{bmatrix} \overline{U}_{r1,x} \\ 0 \end{bmatrix}, \quad \overline{\mathbf{U}}_{\mathbf{r2}} = \begin{bmatrix} 0 \\ \overline{U}_{r2,y} \end{bmatrix}, \quad \overline{\mathbf{U}}_{\mathbf{s}} = \begin{bmatrix} \overline{U}_{s,x} \\ \overline{U}_{s,y} \end{bmatrix}. \tag{4.6}$$

In this case, two interference fields are created and summarized incoherently. When significant spatial frequencies are introduced between the interfering waves, the correct single-shot reconstruction is feasible, providing the complex amplitudes $\overline{U}_{s,x}\overline{U}^{*}_{r1,x}$, and $\overline{U}_{s,y}\overline{U}^{*}_{r2,y}$. For the known parameters of the reference waves, even the complex amplitudes $\overline{U}_{s,x}$ and $\overline{U}_{s,y}$ are additionally obtained, and the polarization-state distribution is recovered. Reconstruction of the Jones matrix is possible when the sample is illuminated by orthogonally polarized waves. When diagonally and antidiagonally polarized illumination beams are used, the output Jones vectors $\overline{\mathbf{U}}_{\mathbf{s}}^{\mathbf{d}}$ and $\overline{\mathbf{U}}_{\mathbf{s}}^{\mathbf{a}}$ are reconstructed, and the Jones matrix,

determined by equation (4.5), is recovered.

4.2 Experimental setup

Experimental arrangement is illustated in the Fig. 4.1, where the beam from an unpolarized He-Ne laser (10 mW, $\lambda = 633$ nm) is coupled into a single-mode optical fiber, decoupled, collimated by the lens L_0, and polarized along the horizontal direction related to the optical table by a linear polarizer (LP). The beam generated is divided into two paths by the first beam splitter (BS_1) of the Mach-Zehnder interferometer. The lenses L_1 and L_2 placed in the reference arm serve as a beam expander followed by the Sagnac module which consists of the polarizing beam splitter (PBS_1) and three mirrors (M_1-M_3). The half-wave plate (HWP_1) balance the intensity ratio between the output orthogonally polarized beams. A slight ro-

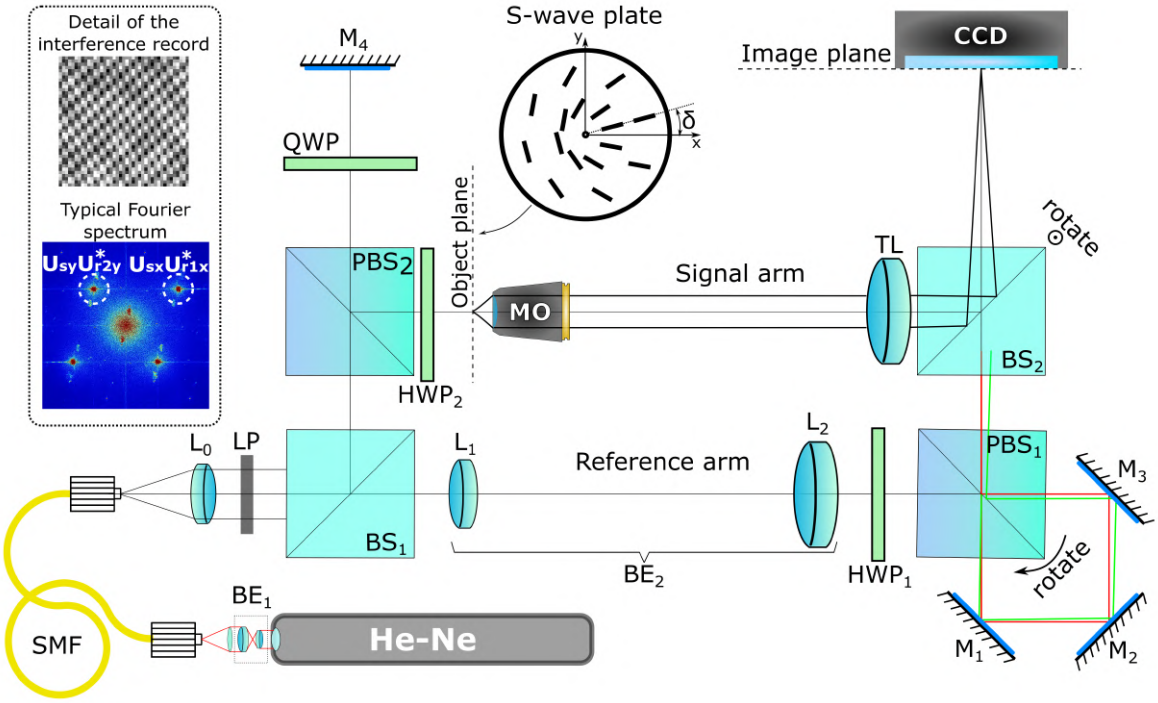

Figure 4.1: Mach-Zehnder configuration with the Sagnac interferometer incorporated in the reference arm to perform the polarization-sensitive imaging by DH. Beam expander and focusing lens (BE_1), single mode fiber (SMF) collimating lens (L_0), linear polarizer (LP), beam splitter (BS_1, BS_2), beam expander (BE_2), half-wave plate (HWP_1, HWP_2), polarizing beam splitter (PBS_1, PBS_2), mirrors (M_1-M_4), quarter-wave plate (QWP), microscope objective (MO), tube lens (TL), camera (CCD). The detail of the interference record and a typical Fourier spectrum are set in the inset figure. Arrows in proximity to PBS_1 and BS_2 point out the tilt direction clockwise and toward the reader, respectively. Lines in the aperture of the S-wave plate indicate orientation of the local axis.

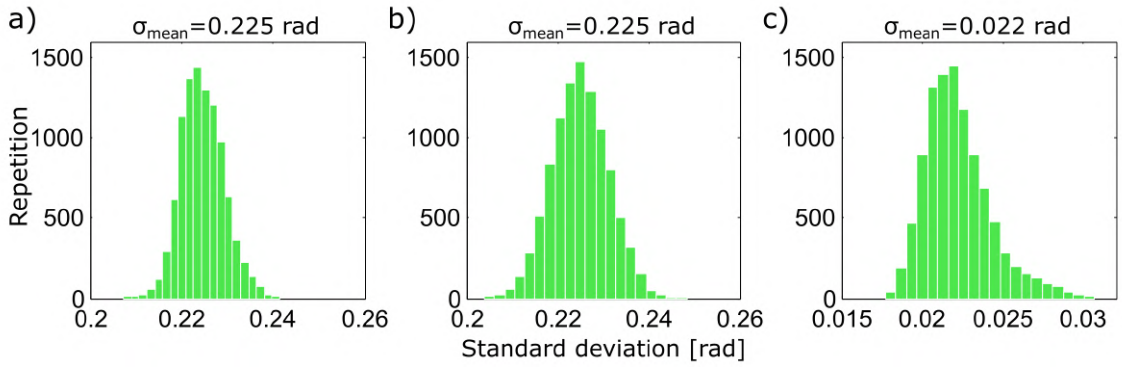

Figure 4.2: Simultaneously measured temporal stability of the: a) QPI performed by the horizontally polarized component, b) QPI performed by the vertically polarized component, c) polarization-state reconstruction. The calculations were accomplished in the area of 0.3×0.3 mm^2 from the 240 interference records captured by the 2 Hz frequency.

tation of the PBS_1 induces a tilt between the noninterfering but temporarily correlated output beams which leave the Mach-Zehnder interferometer after the transmission through the last beam splitter (BS_2). The polarizing beam splitter (PBS_2), quarter wave (QWP) and mirror (M_4) serve as OPD compensator in the signal arm, and the half-wave plate (HWP_2) adjusts the linear polarization direction of the beam illuminating the specimen. The sample is imaged by the microscope objective (MO, Olympus, $4\times$ Plan N, NA$= 0.1$) and the tube lens (TL, achromatic doublet, effective focal distance 100 mm) into the camera plane (CCD, Retiga 4000R, 7.4 µm pixel size, 2048×2048 pixels) with the lateral magnification $2.2\times$. The optical beams formed in the signal and the reference arm are mixed by the BS_2 which introduce spatial carrier frequency between the signal beam and the reference waves. As a result the horizontal component of the signal wave interferes with the horizontally polarized reference beam while the vertical component of the signal wave interferes with the vertically polarized reference beam. Both the interference fields are incoherently summed and detected by the CCD. An example of the recorded checkerboard like structure and the Fourier spectrum are shown in the inset in Fig. 4.1.

4.3 Measurements and results

In the arrangement described, the horizontal and vertical components of the signal wave, interfere with the horizontal and vertical reference waves, respectively. Hence the temporal stability of the interferometer can be evaluated for both polarizations simultaneously. Particularly, a diagonal polarization of the signal wave was adjusted, and a sequence of 240 interference records was measured during 120 seconds with the frequency 2 Hz without any sample incuded in the signal arm. The phase map corresponding to the horizontal

component was retrieved from 240 records, and the standard deviation was evaluated in the area of 0.3×0.3 mm^2 as 0.225 rad (Fig. 4.2a). Moreover, the equal set of interference records enabled to calculate the temporal stability of the vertical polarization with the identical standard deviation of 0.225 rad (Fig. 4.2b). Hence, both distributions reach similar parameters. Indeed, temporal stability of the polarization-state reconstruction by the digital holography, i.e., a standard deviation of the phase differences induced between the horizontal and the vertical polarization components, reaches 0.022 rad (Fig. 4.2c). The Mach-Zehnder configuration determines the stability of the quantitative phase imaging independently for the horizontal and vertical polarization. However, their fluctuations are mutually correlated due to the Sagnac interferometer providing an order of magnitude improvement of the temporal stability in the polarization imaging compared to the temporal stability of QPI in horizontal and vertical components in Mach-Zehnder interferometer separately. To sum up, the presented arrangement can be advantageously used for the polarization imaging by DH with an enhanced temporal stability.

Known object producing the spatially variable polarization distribution was used as a specimen to test the practical utilization of the method. Specifically, a structured HWP-like component with a spatially-dependent orientation of the local fast axis, called S-wave plate (SWP), was used. Jones matrix of the SWP of a unitary topological charge is mathematically expressed as

$$\mathbb{T}_{SWP}(\delta) = \begin{bmatrix} \cos(\varphi+\delta) & \sin(\varphi+\delta) \\ \sin(\varphi+\delta) & -\cos(\varphi+\delta) \end{bmatrix}, \tag{4.7}$$

where the orientation of local axis η in the circular aperture of the SWP satisfies equation $\eta = \varphi/2$ with the azimuthal coordinate $\varphi \in [0, 2\pi]$. δ is the rotation angle between the horizontal axis of the system and the position, where the SWP local-axis orientation is collinear to the radial direction. The situation is illustrated in Fig. 4.1. This component is usually used for the generation of radially or azimuthally polarized beams from the linearly polarized illumination or optical vortices from the circularly polarized light.

The SWP used (RCP-632-04) was placed into the object plane of the MO and two independent interference patterns were recorded, corresponding to the diagonal and antidiagonal illumination, respectively. Firstly, the interference pattern under the diagonal illumination was captured, numerically processed, and the output Jones vector $\overline{\mathbf{U}}_{\mathbf{s}}^{\mathbf{d}}$ was retrieved as a result. Secondly, the same process was repeated for antidiagonally polarized illumination. Parameters of the reconstructed polarization states $\overline{\mathbf{U}}_{\mathbf{s}}^{\mathbf{d}}$ and $\overline{\mathbf{U}}_{\mathbf{s}}^{\mathbf{a}}$ are visualized in Fig. 4.3.

Subsequently, the Jones matrix of the SWP was reconstructed directly from the $\overline{\mathbf{U}}_{\mathbf{s}}^{\mathbf{d}}$ and $\overline{\mathbf{U}}_{\mathbf{s}}^{\mathbf{a}}$ by applying equation (4.5). The absolute values of the complex amplitudes are illustrated in Fig. 4.4a, which are compared to the theoretical predictions. The correlation

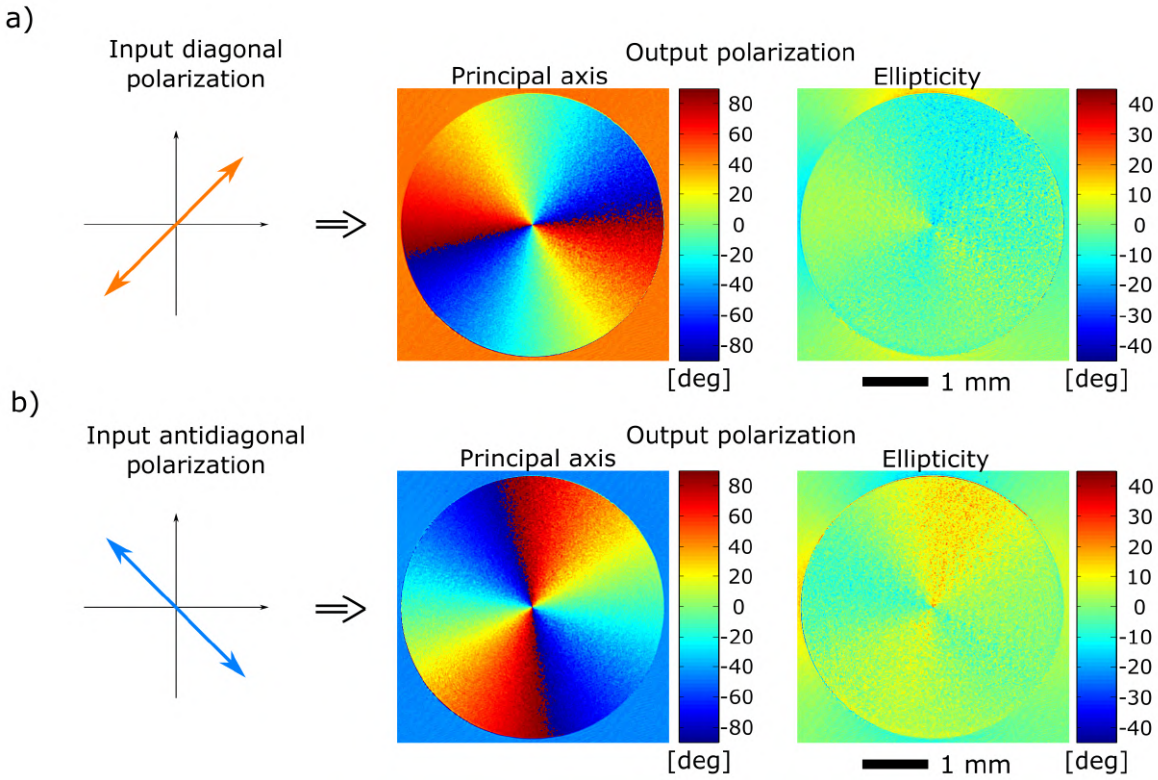

Figure 4.3: Principal axis orientation and ellipticity of the reconstructed output polarization states for diagonally (a) and antidiagonally (b) polarized input illumination beam.

coefficients (CCs) of the T_{xx}, T_{xy}, T_{yx}, and T_{yy} are calculated to estimate the similarity reaching the values 0.91, 0.97, 0.96, and 0.95, respectively. Phases of the Jones-matrix elements (Fig. 4.4b) are also compared calculating the CCs with the results 0.93, 0.93, 0.93, and 0.94, respectively. All the CCs are obtained from the evaluations provided inside the whole square areas, except phases of T_{xy}, T_{yx}, where CCs are calculated from the area inside the circular aperture of the SWP. Phases obtained in the area out of this aperture are irrelevant for the quantification because the retrieved amplitudes reach zero levels.

To be complete, two Sagnac modules were additionally exploited in a configuration used for a single-shot Jones matrix reconstruction [36]. The first module was incorporated in the signal arm to simultaneously generate two orthogonally polarized mutually tilted illuminating beams, while the second was situated in the reference arm to generate two orthogonally polarized mutually tilted reference beams as in [34]. The working principle was proved, however, based on the synthetic-aperture principle, mutually tilted illumination beams provide imaging from different parts of the spatial-frequency spectral domain. Hence the method may provide insufficient results for the selected applications.

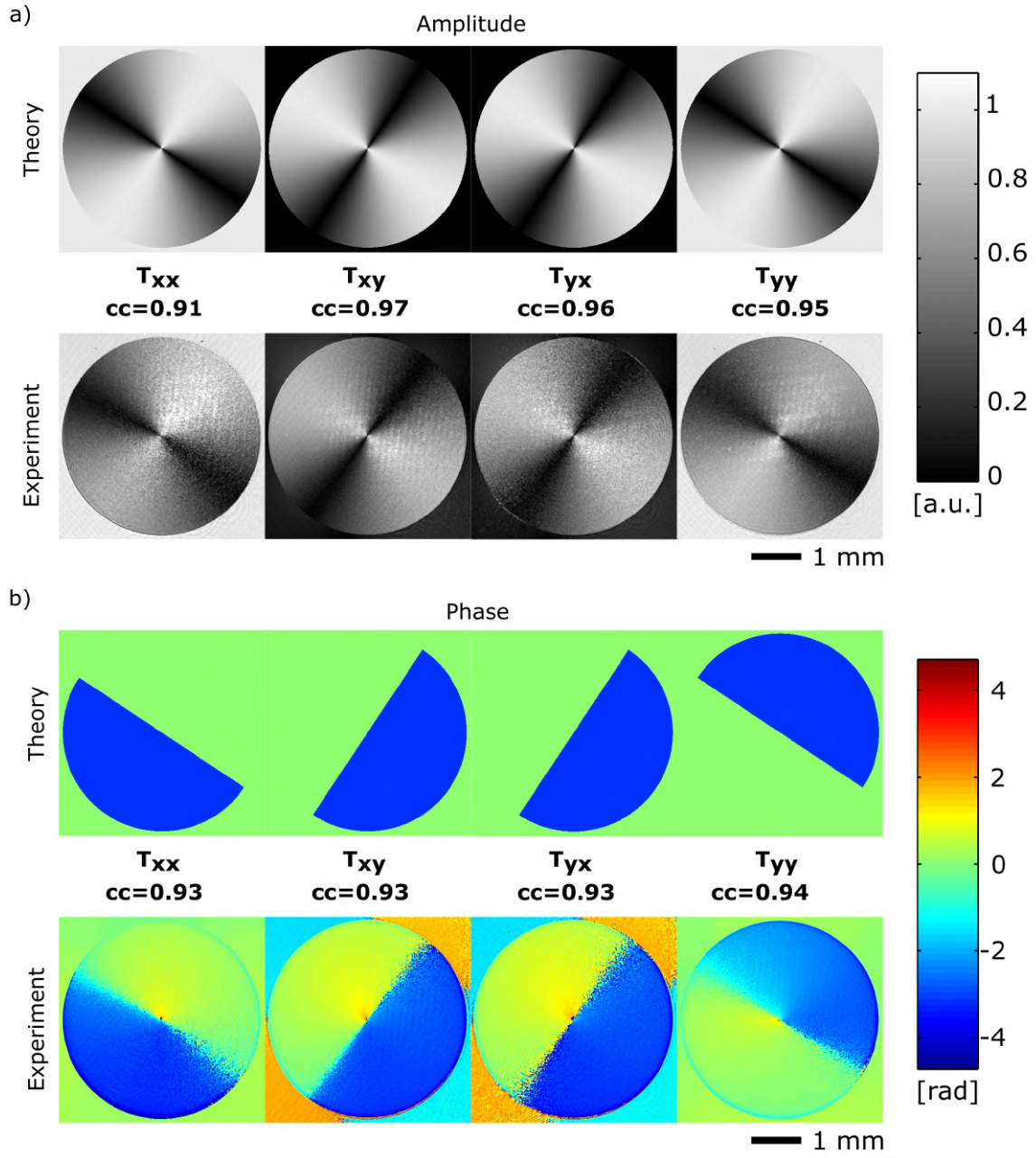

Figure 4.4: Jones matrix of the SWP. The upper rows represent the theoretical predictions and the bottom rows represent the reconstructions obtained by processing the experimantal data. a) Absolute values of the T_{xx}, T_{xy}, T_{yx}, and T_{yy} with the corresponding correlation coefficients (CCs) 0.91, 0.97, 0.96, and 0.95, respectively. b) Phases of the T_{xx}, T_{xy}, T_{yx}, and T_{yy} with the corresponding CCs 0.93, 0.93, 0.93, and 0.94, respectively. All the CCs are evaluated in the displayed areas except the phases of T_{xy}, T_{yx}, which are evaluated just in the circular aperture of the SWP. Phase values out of the aperture are irrelevant because the amplitudes from a) are close to zero.

Conclusion

In this thesis, the primary outcomes of my Ph.D. studies were discussed. All the investigated problems benefit from and further develop the advantages of digital holography, which serves as a subject of investigation itself as well as an instrument to study and quantify the observed phenomena.

In chapter 1, based on publication [1], the imaging performance of the magnified lensless coherent digital holographic microscopy was investigated. The primary intent aimed to provide experimental parameters appropriate for observing the specimen's enlarged image while preserving the quality of the imaging performance. Initially, a three-dimensional point spread function was designed considering deteriorations originating from the influence of holographic aberrations and the diffraction effects, respectively. The desired magnification was achieved by the mismatch between the parameters of the reference and the reconstruction waves. It was shown that plane wave holographic reconstructions with the expected comparable theoretical resolutions produce very different results based on the various experimental adjustments. In this context, the focal shift effect and asymmetry of the axial point spread function was discussed for the first time in the digital holography according to our best knowledge. The combination of a low Fresnel number and high magnifications in image space cause the axial asymmetry, and intensity maximum shifted out of the paraxial image plane. In contrast, higher Fresnel numbers and lower magnifications enlarge the deterioration of the three-dimensional point spread function by the spherical aberration. The theoretical criteria were formulated to assess the influence of both effects and were further used to optimize the holographic reconstruction. Indeed, the predictions were approved experimentally by the reconstructed three-dimensional point spread functions from the point holographic records and the measurements realized with the line resolution target.

In chapter 2, based on publication [2], the living cells were employed as optical elements to perform the photolithography into the photoactivable and biocompatible substrate. The main ambition was to create and fix the optical fingerprints of the biological specimen whose properties correlate with its morphology into such material. Notably, red blood cells, lacking any internal organelles, were successfully employed as biolenses. The standard off-

axis digital holography arrangement was used, which served simultaneously as an instrument for the realization and characterization of the bio-photolithographic performance. Cells seeded on the top of the x-cut lithium niobate crystal were exposed directly. The structures inside the crystal arose without changing its topography, just reversibly modifying the refractive index distribution. The structures were further investigated through the propagation of a complex amplitude. Similarities and differences between the cells and corresponding imprints were analyzed concerning the anisotropy of the photorefractive effect. Besides, disc-like and spherical-like red blood cells were used due to their different morphologies. The results obtained confirmed the replication of a single layer of both cell types. Hence, exhibiting bi-focal and mono-focal structures for disc-like and spherical-like cells, respectively.

Chapter 3, based on publication [3], proposed the phase-background compensation employing the double-exposure method. Notably, its implementation in common-path self-referencing digital holographic microscopy was introduced, suggesting the optimal concept of phase-background elimination with emphasis on reducing the residual phase defects. Thus the performance of the double-exposure method was extended, whose practical utilization was demonstrated observing various samples. The first experiment was realized in the configuration with a microscope objective, a tube lens, and an integrated Sagnac interferometer used as a shearing device duplicating the field of view. Here, interference of the signal and the reference waves with their replicas were utilized for a single-shot holographic reconstruction, whose phase background was further corrected in the post-processing procedure. The averaging process of the duplicated phase images also contributed to improving the quality of the final reconstruction. The analysis concluded that the advantageous implementation of the double-exposure method is possible when imaging the self-moving or driven-by-a-flow sparse specimens. It was found that further enhancement of the reconstructed phase-map is feasible in microfluidic applications. The second investigated experimental arrangement represented quasi-common-path geometry. Instead of incorporating the shearing device replicating field of view, just an additional mirror was used to create an off-axis geometry by reflecting a part of the initially unemployed object beam on itself. Firstly, calibration measurements verifying the accuracy of the quantitative reconstruction and the high temporal stability of the interferometer were approved. Furthermore, the experimental measurements with glass beads as a specimen confirmed the previous conclusions valid for optimal implementation of the double-exposure method.

Finally, in chapter 4, the polarization-sensitive imaging by digital holography performed in the Mach-Zehnder experimental arrangement with the incorporated Sagnac module was presented. The method exploited the angular multiplexing principles in the off-axis geometry, and it was realized using common optical elements. Improvement of the

temporal stability in the polarization-state reconstruction was quantified and compared to the standard Mach-Zehnder configuration of the identical parameters used for the quantitative phase imaging. Moreover, the imaging capacity was mostly qualitatively tested in measurements carried with the sample generating the spatially variable polarization state distribution. Quantifying the accuracy of this proof-of-concept arrangement is a subject of future experiments.

Stručné shrnutí v češtině

Předložená práce shrnuje hlavní výsledky dosažené během mého doktorského studia. Všechny studované problémy využívají principů digitální holografie, ať už v kontextu designu vlastního experimentálního uspořádání, nebo jako nástroje pro studium a kvantifikaci studovaných jevů.

Kapitola 1, která je založená na publikaci [1], se zabývá zobrazením v bezčočkové koherentní digitální holografické mikroskopii. Hlavním přínosem práce je nalezení experimentálních parametrů, které umožňují pozorování zvětšeného obrazu s přípustným vlivem holografických aberací a co nejlepší zachovanou rozlišovací schopností. Nejprve byla studována trojrozměrná bodová rozptylová funkce s uvážením vlivu holografických aberací a difrakčních efektů. V tomto kontextu byly poprvé studovány asymetrie axiální bodové rozptylové funkce a posun maxima osová intenzity mimo paraxiální obrazovou rovinu v digitální holografii. Zvětšení nezbytné pro pozorování mikroskopických objektů zde bylo získáno nesouladem mezi parametry referenční a rekonstrukční vlny. Digitální rekonstrukce byla speciálně provedena pro případ rovinné rekonstrukční vlny se zjištěním, že různá volba experimentálních parametrů vede k odlišným výsledkům, a to i v případě srovnatelné teoretické rozlišovací meze. Kombinace nízké hodnoty Fresnelova čísla a relativně velkého zvětšení v obrazovém prostoru vedou k asymetrii PSF v důsledku difrakce, zatímco vysoké hodnoty Fresnelova čísla a relativně malého zvětšení způsobují degradaci odrazu sférickou aberací. Rozmezí přípustných hodnot experimentálních parametrů bylo určeno pomocí numerických simulací a aproximativních kritérií. Teoretické predikce byly též experimentálně ověřeny rekonstrukcí trojrozměrné bodové rozptylové funkce z bodových holografických záznamů a rekonstrukcí plošného předmětu – amplitudového čárového testu.

V další části práce, která je založená na publikaci [2], bylo studováno využití živých buněk jako optických elementů pro fotolitografický zápis do fotorefraktivního a biokompatibilního materiálu. Hlavním cílem bylo vytvoření a fixace otisků biologického vzorku, s rozdílnými optickými vlastnostmi v závislosti na jejich morfologické stavbě. Jelikož lze červeným krvinkám přiřadit například ohniskovou vzdálenost a zvětšení, naskytla se otázka, zda je možné využít těchto buněk jako optických elementů pro vytvoření fotoli-

tografického otisku. Vrstva krvinek proto byla nanesena na lithium niobátový krystal a exponována laserovým světlem. Otisky krvinek vznikly v krystalu díky lokální modifikaci indexu lomu světla bez změny topologie povrchu. Vlastnosti buněk a struktur byly studované numerickým šířením komplexní amplitudy, která byla rekonstruovaná z interferenčního obrazce zaznamenaného ve standardním dvoucestném digitálním holografickém uspořádání s mimoosovou geometrií. Analogie a rozdíly mezi optickými vlastnostmi krvinek a vzniklých otisků byly analyzovány s uvážením anisotropie fotorefraktivního efektu v lithium niobátovém krystalu. Krvinky diskovitého a sférického tvaru byly dále použity pro jejich odlišnou morfologii. Dosažené výsledky prokazují, že vzniklé struktury vykazují obdobné fokusační vlastnosti, jako původní buňky – v obou případech. A tak vykazují jedno-ohniskovou strukturu v případě sférických a dvoj-ohniskovou v případně diskovitých červených krvinek.

Kapitola 3, která je založená na publikaci [3], prezentuje optimální využití metody dvojí expozice v interferometrech se společnou optickou cestou a mimoosovou geometrií. Tato metoda je založena na zpracování dvou holografických záznamů a umožňuje kompenzaci fázového pozadí bez znalosti jeho přesného numerického modelu. Hlavní přínos této práce spočívá v určení podmínek pro zvýšení kvality rekonstruované fáze s důrazem na potlačení nehomogenit zbytkového fázového pozadí. Praktické využití metody dvojité expozice bylo zkoumáno při pozorování různých vzorků. První experiment byl realizovaný v konfiguraci s objektivem a tubusovou čočkou doplněnou o Sagnacův interferometr, který duplikoval zorné pole a zaváděl střih mezi interferujícími vlnami. Vzniklé duplikované zorné pole bylo u řídkých vzorků též využito pro vylepšení kvality rekonstruovaného obrazu. Analýza dat zjistila, že implementace metody dvojí expozice je výhodná v aplikacích s pohybujícími se či plovoucími řídkými vzorky. Další vylepšení je dále myslitelné v aplikacích s mikrofluidními kanálky. Druhé experimentální uspořádání reprezentovalo geometrii bez duplikovaného zorného pole s blízkými optickými cestami. Místo komponenty zavádějící střih zde bylo použito přídavné zrcátko. To zajišťovalo mimoosovou geometrii smícháním signální vlny s původně nevyužitou částí předmětového zorného pole. Kalibrační měření potvrdila vysokou časovou stabilitu konfigurace a správnost fázové rekonstrukce. Praktické využití metody bylo konkrétně demonstrováno v měřeních se skleněnými kuličkami a potvrdilo závěry získané z předchozího experimentálního uspořádání se Sagnacovým interferometrem.

Kapitola 4 se zabývá polarizačně citlivým zobrazením s využitím principů digitální holografie. Experimentální uspořádání využívá mimoosové geometrie Mach-Zehnderova interferometru se Sagnacovým modulem vloženým do referenčního ramene. Princip metody spočívá v nekoherentním skládání dvou ortogonálně polarizovaných optických polí, které (každé zvlášť) reprezentují skalární interferenční záznamy. U rekonstrukce po-

larizačního stavu je prokázaná zvýšená časová stabilita vzhledem k časové stabilitě kvantitativního fázového zobrazování provedeného ve standardním Mach-Zehnderově interferometru shodných optických parametrů. Metoda je převážně kvalitativně testována s využitím anizotropního vzorku jako předmětu, který generuje prostorově závislé rozložení polarizace. Přesnost rekonstrukce tohoto 'proof-of-principle' experimentálního uspořádání bude předmětem následujících zkoumání.

Bibliography

[1] J. Běhal and Z. Bouchal, "Optimizing three-dimensional point spread function in lensless holographic microscopy," *Optics Express*, vol. 25, pp. 29026–29042, 2017.

[2] L. Miccio, J. Behal, M. Mugnano, P. Memmolo, B. Mandracchia, F. Merola, S. Grilli, and P. Ferraro, "Biological lenses as a photomask for writing laser spots into ferroelectric crystals," *ACS Applied Bio Materials*, vol. 2, no. 11, pp. 4675–4680, 2019.

[3] J. Běhal, "Quantitative phase imaging in common-path cross-referenced holographic microscopy using double-exposure method," *Scientific Reports*, vol. 9, no. 9801, 2019.

[4] J. W. Goodman, *Introduction To Fourier Optics*. McGraw-Hill, 1996.

[5] U. Schnars and W. P. O. Juptner, "Digital recording and numerical reconstruction of holograms," *Measurement Science and Technology*, vol. 13, pp. R85–R101, 2002.

[6] P. Ferraro, A. Wax, and Z. Zalevsky, *Coherent Light Microscopy*. Springer-Verlag, 2011.

[7] T. Kreis, *Handbook of Holographic Interferometry*. Wiley-Vch, 2005.

[8] Y. Li and E. Wolf, "Focal shift in diffracted converging spherical waves," *Optics Communications*, vol. 39, pp. 211–215, 1981.

[9] M. Gu, *Advanced Optical Imaging Theory*. Springer-Verlag, 2000.

[10] R. W. Meier, "Magnification and third-order aberrations in holography," *Journal of the Optical Society of America*, vol. 55, pp. 987–992, 1965.

[11] J. Rosen and G. Brooker, "Digital spatially incoherent fresnel holography," *Optics Letters*, vol. 32, pp. 912–914, 2007.

[12] B. Katz, J. Rosen, R. Kelner, and G. Brooker, "Enhanced resolution and throughput of fresnel incoherent correlation holography (FINCH) using dual diffractive lenses on a spatial light modulator (SLM)," *Optics Express*, vol. 20, pp. 9109–9121, 2012.

[13] L. Miccio, P. Memmolo, F. Merola, P. A. Netti, and P. Ferraro, "Red blood cell as an adaptive optofluidic microlens," *Nature Communications*, vol. 6, no. 6502, 2015.

[14] P. Memmolo, C. Distante, M. Paturzo, A. Finizio, P. Ferraro, and B. Javidi, "Automatic focusing in digital holography and its application to stretched holograms," *Optics Letters*, vol. 36, pp. 1945–1947, 2011.

[15] P. Memmolo, L. Miccio, M. Paturzo, G. D. Caprio, G. Coppola, P. A. Netti, and P. Ferraro, "Recent advances in holographic 3D particle tracking," *Advances in Optics and Photonics*, vol. 7, pp. 713–755, 2015.

[16] C. Arregui, J. B. Ramiro, Á. Alcázar, Á. Méndez, H. Burgos, Á. García-Cabañes, and M. Carrascosa, "Optoelectronic tweezers under arbitrary illumination patterns: theoretical simulations and comparison to experiment," *Optics Express*, vol. 22, pp. 29099–29110, 2014.

[17] C. Bernert, R. Hoppe, F. Wittwer, T. Woike, and C. G. Schroer, "Ptychographic analysis of the photorefractive effect in $LiNbO_3$:Fe," *Optics Express*, vol. 25, pp. 31640–31650, 2017.

[18] G. F. Calvo, F. Agulló-López, M. Carrascosa, M. R. Belić, and W. Królikowski, "Locality vs. nonlocality of $(2+1)$-dimensional light-induced space-charge field in photorefractive crystals," *Europhysics Letters (EPL)*, vol. 60, no. 6, pp. 847–853, 2002.

[19] P. Gunter and J. P. Huignard, *Photorefractive Materials and Their Applications*. Springer-Verlag, 2006.

[20] G. Popescu, T. Ikeda, R. R. Dasari, and M. S. Feld, "Diffraction phase microscopy for quantifying cell structure and dynamics," *Optics Letters*, vol. 31, pp. 775–777, 2006.

[21] G. Popescu, K. Badizadegan, R. R. Dasari, and M. S. Feld, "Observation of dynamic subdomains in red blood cells," *Journal of Biomedical Optics*, vol. 11, no. 040503, 2006.

[22] P. Ferraro, S. D. Nicola, A. Finizio, G. Coppola, S. Grilli, C. Magro, and G. Pierattini, "Compensation of the inherent wave front curvature in digital holographic coherent microscopy for quantitative phase-contrast imaging," *Applied Optics*, vol. 42, pp. 1938–1946, 2003.

[23] M. León-Rodríguez, J. A. Rayas, R. R. Cordero, A. Martínez-García, A. Martínez-Gonzalez, A. Téllez-Quiñones, P. Yañez-Contreras, and O. Medina-Cázares, "Dual-plane slightly off-axis digital holography based on a single cube beam splitter," *Applied Optics*, vol. 57, pp. 2727–2735, 2018.

[24] T. O'Connor, A. Doblas, and B. Javidi, "Structured illumination in compact and field-portable 3D-printed shearing digital holographic microscopy for resolution enhancement," *Optics Letters*, vol. 44, pp. 2326–2329, 2019.

[25] K. Lee and Y. Park, "Quantitative phase imaging unit," *Optics Letters*, vol. 39, pp. 3630–3633, 2014.

[26] J. Di, Y. Li, K. Wang, and J. Zhao, "Quantitative and dynamic phase imaging of biological cells by the use of the digital holographic microscopy based on a beam displacer unit," *IEEE Photonics Journal*, vol. 10, pp. 1–10, 2018.

[27] V. Singh, S. Tayal, and D. S. Mehta, "Highly stable wide-field common path digital holographic microscope based on a fresnel biprism interferometer," *OSA Continuum*, vol. 1, pp. 48–55, 2018.

[28] J. Á. Picazo-Bueno and V. Micó, "Opposed-view spatially multiplexed interferometric microscopy," *Journal of Optics*, vol. 21, no. 035701, 2019.

[29] M. G. Somekh, C. W. See, and J. Goh, "Wide field amplitude and phase confocal microscope with speckle illumination," *Optics Communications*, vol. 174, pp. 75–80, 2000.

[30] F. Dubois, M.-L. N. Requena, C. Minetti, O. Monnom, and E. Istasse, "Partial spatial coherence effects in digital holographic microscopy with a laser source," *Applied Optics*, vol. 43, pp. 1131–1139, 2004.

[31] L. Miccio, D. Alfieri, S. Grilli, P. Ferraro, A. Finizio, L. D. Petrocellis, and S. D. Nicola, "Direct full compensation of the aberrations in quantitative phase microscopy of thin objects by a single digital hologram," *Applied Physics Letters*, vol. 90, no. 041104, 2007.

[32] Y. Liu, Z. Wang, J. Li, J. Gao, and J. Huang, "Total aberrations compensation for misalignment of telecentric arrangement in digital holographic microscopy," *Optical Engineering*, vol. 53, no. 112307, 2014.

[33] D. Deng, W. Qu, W. He, Y. Wu, X. Liu, and X. Peng, "Off-axis tilt compensation in common-path digital holographic microscopy based on hologram rotation," *Optics Letters*, vol. 42, pp. 5282–5285, 2017.

[34] N. K. Soni, A. S. Somkuwar, and R. K. Singh, "Jones matrix imaging for transparent and anisotropic sample," in *International Conference on Optics and Photonics 2015* (K. Bhattacharya, ed.), vol. 9654, SPIE, 2015.

[35] R. C. Jones, "A new calculus for the treatment of optical systems," *Journal of the Optical Society of America*, vol. 31, pp. 488–493, 1941.

[36] A. V., N. K. Soni, V. R. V., and R. K. Singh, "Anisotropy imaging using polarization and angular multiplexing," in *Quantitative Phase Imaging III* (G. Popescu and Y. Park, eds.), vol. 10074, SPIE, 2017.